

Atmospheric Partitioning of Polycyclic Aromatic Hydrocarbons (PAH) and Oxygenated PAH

by

Jonathan O. Allen

Submitted to the Department of Chemical Engineering
in partial fulfillment of the requirements for the degree of

Doctor of Science
[Doctor of Philosophy]
at the

MASSACHUSETTS INSTITUTE OF TECHNOLOGY

February, 1997

© Massachusetts Institute of Technology 1997. All rights reserved.

Author
Department of Chemical Engineering
January 23, 1997

Certified by
Adel F. Sarofim
Lammot du Pont Professor of Chemical Engineering Emeritus
Thesis Supervisor

Certified by
Kenneth A. Smith
Edwin R. Gilliland Professor of Chemical Engineering
Thesis Supervisor

Accepted by
Robert E. Cohen
St. Laurent Professor of Chemical Engineering
Chairman, Committee for Graduate Students

MASSACHUSETTS INSTITUTE
OF TECHNOLOGY

APR 28 1997

ARCHIVES

LIBRARIES

Atmospheric Partitioning of Polycyclic Aromatic Hydrocarbons (PAH) and Oxygenated PAH

by

Jonathan O. Allen

Submitted to the Department of Chemical Engineering on
January 23, 1997, in partial fulfillment of the requirements for
the degree of Doctor of Science in Chemical Engineering.

Abstract

Polycyclic aromatic hydrocarbons (PAH) and oxygenated PAH (OPAH) are mutagenic air pollutants formed as by-products of combustion. After formation and emission, these compounds partition between the gas phase and atmospheric aerosols. The environmental fate of PAH and OPAH depends, in part, on their distribution between the gas and particulate phases and among particle size fractions. Particle size affects the removal rate of the associated PAH from the atmosphere by dry and wet deposition. The mechanism and location of deposition of particulate phase compounds in the lung are also affected by particle size. The large particles tend to impact on the upper regions of the lung and small particles diffuse to the surface of the alveoli. The goal of this work is a better understanding of the atmospheric partitioning of PAH and OPAH necessary to determine the environmental fate of, and human exposure to, these pollutants.

Size-segregated atmospheric aerosols were collected from urban and rural locations in Massachusetts using a micro-orifice inertial impactor. The samples were analyzed for PAH and OPAH using gas chromatography/mass spectrometry. In the urban samples, PAH were distributed among aerosol size fractions based on molecular weight. PAH with molecular weights between 178 and 202 were approximately evenly distributed between the fine (aerodynamic diameter, $D_p < 2 \mu\text{m}$) and coarse ($D_p > 2 \mu\text{m}$) particles. PAH with molecular weights greater than 228 were associated primarily with the fine aerosol fraction. In the rural samples, low and high molecular weight PAH were associated with both the fine and coarse aerosols. PAH are primarily emitted by combustors with fine particles. Slow mass transfer by vaporization and sorption is proposed to explain the observed PAH partitioning among aerosol size fractions.

OPAH were also generally distributed among aerosol size fractions based on molecular weight in the urban aerosol. Compounds with molecular weights between 168 and 208 were approximately evenly distributed between the fine and coarse particles. OPAH with molecular weights of 248 and greater were associated primarily with the fine aerosol fraction. Most OPAH were distributed with particle size in a broad, unimodal hump similar to the the distributions observed for PAH in the same samples. These results indicate that OPAH were initially associated with fine particles following emission by combustors or formation by gas phase photooxidation. OPAH then re-distributed from fine particles to larger particles by vaporization and sorption. Two OPAH were distributed in bimodal distributions with peaks at $D_p \approx 0.2 \mu\text{m}$ and

$D_p \approx 2.5 \mu\text{m}$. The bimodal distributions suggest that these compounds have solution behavior very different from PAH and other OPAH.

Size-segregated atmospheric aerosols were collected on oiled impaction media in this work to prevent particle bounce during sampling. The use of the oiled impaction media, however, may have introduced another sampling artifact — the absorption of species from the gas phase. Such absorption would artificially increase the amount of PAH attributed to the aerosol and possibly distort the measured size distributions. Absorption of pyrene from the gas phase to the oiled impaction media was measured in the laboratory. The amounts absorbed were approximately equal for the impactor stages, indicating that, in the worst case, the absorption artifact resulted in a small increase in the amount of PAH collected and no qualitatively significant distortion in the measured size distribution.

The experimental measurements of the absorption artifact are valid only for the impactor design and impaction media used in this work. A model of the absorption artifact, based on the laminar impinging jet mass transfer literature, was developed to predict the absorption artifact for other impactor designs and impaction media. The model predictions compared well to experimental measurements for the first four impactor stages. The model overpredicted absorption on the last four stages, probably due to the tight packing of impinging jets on these stages. A lower estimate of absorption on these stages was made by considering the mass transfer from a single jet. The experimental results were bracketed by the array of jets and single jet models.

A widely circulated hypothesis holds that PAH-particle associations can be described as adsorption and that the association is in equilibrium. This hypothesis was examined and found to be inconsistent with available atmospheric data. In place of the adsorptive partitioning hypothesis, we propose that PAH partitioning in the atmosphere is best explained as non-equilibrium absorptive partitioning. This explanation is consistent with the observation that the apparent enthalpy of gas-particle partitioning is greater than the enthalpy of vaporization. It is also consistent with the observations that, in urban aerosols, lower molecular weight PAH partition to both fine and coarse particles while higher molecular weight PAH partition mainly to fine particles. This description was implemented as a Lagrangian model of aerosol partitioning in an urban environment. The model results match well the measured distributions of low and intermediate molecular weight PAH ($M < 278$) with particle size. These results indicate that association of organic compounds with aerosols is by absorption and that, in the urban atmosphere, these compounds do not attain equilibrium partitioning.

Thesis Supervisors: Adel F. Sarofim

Lammot du Pont Professor of Chemical Engineering Emeritus

Kenneth A. Smith

Edwin R. Gilliland Professor of Chemical Engineering

Acknowledgments

I extend heartfelt thanks to all those who aided and instructed me in this work which has been a collaborative effort throughout. First among these are my advisors, Adel Sarofim and Ken Smith. The affectionate care and guidance these men have given was beyond my experience or expectation. The truest description of their roles is that of the German expression, *Doktorvater*. I thank the members of my thesis committee, Art Lafleur, Greg Rutledge, and Greg McRae, for their comments and advice.

A number of MIT undergraduates made important contributions to this work. Learning from, and working with these talented students was a great reward of this project. Olivia Siu ran many of the soot desorption experiments. Rana Biswas assisted in assembling and testing the atmospheric sampling system. Nameeta Dookeran worked on all aspects of the atmospheric aerosol sampling project. She assisted in the collection of the size-segregated aerosol samples, and in HPLC and GC/MS method development. She performed many of the HPLC separations and much of the PAH and OPAH identification and quantification. John Paschkewitz set up the absorption artifact experiment and ran a number of these experiments. He also assisted with the early development of the absorption artifact model. Jill Depto assisted in the soot desorption work and absorption artifact experiments. Ingrid Ulbrich collected the photoionization data presented in Chapter 4.

All of the analytic chemistry work described herein was performed at the Core Laboratory for Analytic Chemistry, part of MIT's Center for Environmental Health Sciences. The Core Labs staff gave freely of their time and talents to instruct and guide the analytical chemistry portions of this research. Art Lafleur shared his expertise on methods development and data analysis. Koli Taghizadeh collaborated in the development of GC/MS methods to identify and quantify trace amounts of PAH and OPAH in the atmospheric samples. She ran many of the samples on the GC/MS and assisted in the identification of analytes. Elaine Plummer developed the HPLC quantification method used in the absorption artifact experiment. She ran many of these samples and assisted in the quantification of pyrene. She also assisted in the development of the HPLC separation technique used for the atmospheric samples.

Thanks are due to many other colleagues at MIT. Lenore Rainey assisted with the collection of atmospheric particles for electron microscopy. She performed the electron microscopic analyses of these samples. Angelo Kandas assisted in the photography of absorbed pyrene fluorescence. He created the first version of Figure 8-7. Tony Modestino provided advice on operation of the thermogravimetric analyzer, design of the absorption artifact experimental apparatus, and construction of the atmospheric

sampling system. John Durant discussed the identification of PAH and OPAH by GC/MS and kindly shared his preliminary analyses of atmospheric aerosol extracts. Mike Hannigan shared his experience in the design of the atmospheric sampler. Daniel Pedersen collaborated on the collection of photoionization data. Andreas Tschöpe and Doron Levin ran the surface area and pore volume analyses of thermally desorbed soot samples. I thank the support staff, Gabrielle Joseph, Marcia Ross, Linda Mousseau, Bhengy Jackson, and especially Emmi Snyder, for their assistance.

I gratefully acknowledge the National Institute of Environmental Health Sciences and the S. C. Johnson Wax Company which funded this research. I thank the staff of the Massachusetts Department of Environmental Protection who provided access to the sampling sites at Kenmore Square and Quabbin Summit. They also provided ambient data collected at these sites.

I thank my family for their encouragement and support. I am grateful for the friendship of Angelo Kandas, Mary Jane O'Rourke, Radha Nayak, Nameeta Dookeran, John Paschkewitz, Koli Taghizadeh, Hong Bin Ni, Alysia Hammond, Talid Sinno, Howard Covert, David de Sola, Ayal Naor, Fred & Antonia von Gottberg, Tom & Alyson Preston, and Anthony van Niel. They have shared their lives with me, and made my years in Cambridge joyful and worthwhile. Finally, I thank Anne Foerst.

But he that doeth truth cometh to the light,
that his deeds may be made manifest,
that they are wrought in God.

John 3:21

Contents

1	Introduction	31
1.1	Health Effects Motivation	31
1.1.1	Particulate Matter	31
1.1.2	Mutagenic Organic Species	32
1.2	Atmospheric Particles	34
1.3	PAH and OPAH in the Atmosphere	42
1.4	Atmospheric Partitioning	47
1.4.1	Effect of Partitioning on Atmospheric Fate	47
1.4.2	Effect of Partitioning on Human Exposure	51
1.4.3	Measurements of Gas—Particle Distribution	52
1.4.4	Models of Atmospheric Partitioning	54
1.4.5	Measurements of Distribution with Particle Size	57
1.5	Thesis Objectives	59
2	Collection and Analysis of Size-segregated Aerosols	63
2.1	Introduction	63
2.2	Sample Collection	65
2.3	Sample Analysis	70
2.3.1	Materials	70
2.3.2	Sample Extraction and Storage	71
2.3.3	Sample Preparation by HPLC	73
2.3.4	Reference Standards	74
2.3.5	GC/MS Operation	82
2.3.6	Species Identification and Quantification	86
2.3.7	Limits of Quantification	94
2.4	Sample Contamination	96
2.5	Conclusions	98
3	PAH and OPAH in Size-segregated Aerosols	101
3.1	Introduction	101
3.2	PAH in Urban Boston Aerosol	102
3.3	PAH in Rural Massachusetts Aerosol	114
3.4	OPAH in Urban Boston Aerosol	120
3.4.1	PAH Ketones	121
3.4.2	PAH Diones	128

3.4.3	PAH Dicarboxylic Acid Anhydrides	132
3.5	Qualitative Discussion of PAH Partitioning	135
3.6	Qualitative Discussion of OPAH Partitioning	138
3.7	Conclusions	143
4	Absorption Artifact Experiment	145
4.1	Introduction	145
4.2	Experimental Method	147
4.2.1	Apparatus	147
4.2.2	Sample Analysis	149
4.2.3	Saturator Performance	150
4.3	Results	151
4.3.1	Saturation Concentration of PAH in Oil	151
4.3.2	Absorption Artifact Measurements	152
4.3.3	Empirical Absorption Model	160
4.4	Apparent Distribution with Particle Size Due to Absorption	165
4.4.1	Absorption Artifact at Short and Long Times	165
4.4.2	Absorption Artifact Using Gas—Particle Distribution Ratios	167
4.4.3	Upper Limit for Absorption Artifact	171
4.4.4	Comparison of Gas—Particle Distribution Ratios	174
4.5	Conclusions	177
5	Absorption Artifact Model	179
5.1	Introduction	179
5.2	Cascade Impactors	180
5.3	Impinging Jet Mass Transfer	181
5.3.1	Impinging Jet Flow	181
5.3.2	Stagnation Region	184
5.3.3	Wall Jet Region	186
5.3.4	Transition Region	186
5.3.5	Correction for Arrays of Impinging Jets	187
5.4	Absorption without Gas Phase Denuding	188
5.5	Absorption with Gas Phase Denuding	191
5.6	Comparison with Experimental Results	195
5.7	Conclusions	198
6	Adsorptive Partitioning	199
6.1	Introduction	199
6.2	Equilibrium Adsorptive Partitioning	200
6.3	Single Particle Mass Transfer	200
6.4	Comparison with Atmospheric Data	203
6.4.1	Surface Coverage	203
6.4.2	Observed Enthalpies of Gas—Particle Association	207
6.4.3	Distribution of PAH with Particle Size	209
6.5	Conclusions	210

7	Absorptive Partitioning	213
7.1	Introduction	213
7.2	Equilibrium Absorptive Partitioning	215
7.3	Single Particle Mass Transfer	218
7.3.1	Gas Phase Diffusion	218
7.3.2	Liquid Phase Diffusion	219
7.3.3	Gas—Liquid Equilibration	219
7.4	Aerosol Partitioning Model	224
7.4.1	Model Description	224
7.4.2	Sorbent Evolution	225
7.4.3	PAH Evolution	231
7.4.4	Model Implementation	233
7.5	Predictions for Combustion Products in Urban Air	234
7.5.1	Distributions with Particle Size	234
7.5.2	Gas Phase Concentration	242
7.6	Conclusions	242
8	Other Experiments	247
8.1	Atmospheric Particle Imaging	247
8.1.1	Introduction	247
8.1.2	Sample Collection	249
8.1.3	Electron Microscopy	251
8.1.4	Conclusions	255
8.2	Surface Study of Thermally Desorbed Soot	257
8.2.1	Introduction	257
8.2.2	Soot Desorption	259
8.2.3	Surface Area Measurements	263
8.2.4	Conclusions	266
	Bibliography	267
A	Tabulated GC/MS Data for Size-segregated Aerosol Samples	283
B	Tabulated Absorption Artifact Experimental Data	297
C	Absorption Artifact Model Code	299
D	PAH Physical Properties	309
D.1	Introduction	309
D.2	Boiling Point	310
D.3	Critical Properties	313
D.4	Lennard-Jones Parameters	315
D.5	Diffusivity in Air	315
D.6	Melting Behavior	318
D.7	Heat Capacity	320
D.8	Sublimation Pressure	325

D.9 Vapor Pressure Above Liquid	330
D.10 Activity Coefficients	335
E Atmospheric Partitioning Model Code	339

List of Figures

1-1	Number distribution with particle size of a typical urban aerosol. . . .	38
1-2	Surface area and volume distributions for typical urban aerosol. . . .	39
1-3	Transmission electron micrograph image of submicron particles collected from the atmosphere in Cambridge, MA.	41
1-4	High resolution transmission electron micrograph image of a soot particle collected from the atmosphere in Cambridge, MA.	43
1-5	Estimated emissions of organic carbon, elemental carbon, and PAH in Los Angeles by source category.	44
1-6	Total concentration of 16 PAH in the atmosphere.	46
1-7	Proposed mechanism for the nitration of pyrene.	48
1-8	PAH fluxes into Siskiwit Lake.	50
1-9	PAH fluxes out of Siskiwit Lake.	51
1-10	Deposition of particles in the respiratory tract for mouth breathing as a function of particle size.	52
1-11	Measured gas—particle distribution of pyrene as a function of $1/T$	54
1-12	Distributions of elemental carbon, pyrene, and benzo[<i>a</i>]pyrene with particle size in a highway tunnel.	59
1-13	Distributions of elemental carbon, pyrene, and benzo[<i>a</i>]pyrene with particle size at Pico Rivera, CA, in winter.	60
2-1	Schematic diagram of atmospheric aerosol sampling system.	67
2-2	Separation of some PAH from dibutyl phthalate by HPLC.	75
2-3	Total ion chromatogram using PAH SIM program for Kenmore Square stage 7 sample.	87
2-4	Total ion chromatogram using OPAH SIM program for Kenmore Square stage 7 sample.	89
2-5	Calibration of fluoranthene to pyrene- <i>d</i> ₁₀ MSD response.	91
2-6	Decay of PAH concentration eluting from HPLC with time.	97
3-1	Acenaphthene distribution with particle size in Kenmore Square aerosol.	105
3-2	Fluorene distribution with particle size in Kenmore Square aerosol. . .	105
3-3	Phenanthrene distribution with particle size in Kenmore Square aerosol.	106
3-4	Anthracene distribution with particle size in Kenmore Square aerosol.	106
3-5	Fluoranthene distribution with particle size in Kenmore Square aerosol.	107
3-6	Pyrene distribution with particle size in Kenmore Square aerosol. . .	107

3-7	Benzo[ghi]fluoranthene distribution with particle size in Kenmore Square aerosol.	108
3-8	Benz[a]anthracene distribution with particle size in Kenmore Square aerosol.	108
3-9	Chrysene/triphenylene distribution with particle size in Kenmore Square aerosol.	109
3-10	Benzofluoranthenes distribution with particle size in Kenmore Square aerosol.	109
3-11	Benzo[e]pyrene distribution with particle size in Kenmore Square aerosol.	110
3-12	Benzo[a]pyrene distribution with particle size in Kenmore Square aerosol.	110
3-13	Perylene distribution with particle size in Kenmore Square aerosol. . .	111
3-14	PAH-276a distribution with particle size in Kenmore Square aerosol. . .	111
3-15	Indeno[1,2,3- <i>cd</i>]pyrene distribution with particle size in Kenmore Square aerosol.	112
3-16	Dibenzanthracenes distribution with particle size in Kenmore Square aerosol.	112
3-17	Benzo[ghi]perylene distribution with particle size in Kenmore Square aerosol.	113
3-18	Coronene distribution with particle size in Kenmore Square aerosol. . .	113
3-19	Fluoranthene distribution with particle size in Quabbin Summit aerosol.	115
3-20	Pyrene distribution with particle size in Quabbin Summit aerosol. . .	116
3-21	Benzo[ghi]fluoranthene distribution with particle size in Quabbin Summit aerosol.	116
3-22	Benz[a]anthracene distribution with particle size in Quabbin Summit aerosol.	117
3-23	Chrysene/triphenylene distribution with particle size in Quabbin Summit aerosol.	117
3-24	Benzofluoranthenes distribution with particle size in Quabbin Summit aerosol.	118
3-25	Benzo[e]pyrene distribution with particle size in Quabbin Summit aerosol.	118
3-26	Indeno[1,2,3- <i>cd</i>]pyrene distribution with particle size in Quabbin Summit aerosol.	119
3-27	Benzo[ghi]perylene distribution with particle size in Quabbin Summit aerosol.	119
3-28	1-Acenaphthenone distribution with particle size in Kenmore Square aerosol.	122
3-29	9-Fluorenone distribution with particle size in Kenmore Square aerosol.	123
3-30	11 <i>H</i> -Benzo[a]fluoren-11-one distribution with particle size in Kenmore Square aerosol.	123
3-31	7 <i>H</i> -Benzo[<i>c</i>]fluoren-7-one distribution with particle size in Kenmore Square aerosol.	124
3-32	11 <i>H</i> -Benzo[<i>b</i>]fluoren-11-one distribution with particle size in Kenmore Square aerosol.	124
3-33	Benzanthrone distribution with particle size in Kenmore Square aerosol.	125
3-34	OPAH-254a distribution with particle size in Kenmore Square aerosol.	125

3-35	6 <i>H</i> -Benzo[<i>cd</i>]pyrene-6-one distribution with particle size in Kenmore Square aerosol.	126
3-36	OPAH-280a distribution with particle size in Kenmore Square aerosol.	126
3-37	OPAH-280b distribution with particle size in Kenmore Square aerosol.	127
3-38	OPAH-208a distribution with particle size in Kenmore Square aerosol.	129
3-39	Phenanthrenequinone distribution with particle size in Kenmore Square aerosol.	129
3-40	OPAH-208b distribution with particle size in Kenmore Square aerosol.	130
3-41	5,12-Naphthacenequinone distribution with particle size in Kenmore Square aerosol.	130
3-42	Benzo[<i>a</i>]pyrene-6,12-dione distribution with particle size in Kenmore Square aerosol.	131
3-43	1,8-Naphthalic anhydride distribution with particle size in Kenmore Square aerosol.	133
3-44	OPAH-248a distribution with particle size in Kenmore Square aerosol.	133
3-45	OPAH-272a distribution with particle size in Kenmore Square aerosol.	134
3-46	Fraction of PAH associated with coarse particles ($D_p > 1.9 \mu\text{m}$) in the Kenmore Square (\circ) and Quabbin Summit (\times) samples.	136
3-47	Fraction of PAH and OPAH associated with coarse particles ($D_p > 1.9 \mu\text{m}$) in an urban aerosol.	142
4-1	Experimental apparatus to measure absorption of pyrene in greased impaction media.	148
4-2	Fluorescence image of pyrene absorbed on stage 3 of the MOI after 6 hours.	154
4-3	Fluorescence image of pyrene absorbed on stage 5 of the MOI after 6 hours.	155
4-4	Experimental data and empirical model for pyrene absorption on stage 0 of the MOI.	156
4-5	Experimental data and empirical model for pyrene absorption on stage 1 of the MOI.	156
4-6	Experimental data and empirical model for pyrene absorption on stage 2 of the MOI.	157
4-7	Experimental data and empirical model for pyrene absorption on stage 3 of the MOI.	157
4-8	Experimental data and empirical model for pyrene absorption on stage 4 of the MOI.	158
4-9	Experimental data and empirical model for pyrene absorption on stage 5 of the MOI.	158
4-10	Experimental data and empirical model for pyrene absorption on stage 6 of the MOI.	159
4-11	Experimental data and empirical model for pyrene absorption on stage 7 of the MOI.	159
4-12	Experimental data and empirical model for pyrene absorption on stage 8 of the MOI.	160

4-13	Apparent distribution with particle size of absorbed species at short times.	168
4-14	Apparent distribution with particle size of absorbed species at long times.	168
4-15	Measured distribution of phenanthrene with particle size in Kenmore Square aerosol and predicted absorption artifact.	172
4-16	Measured distribution of pyrene with particle size in Kenmore Square aerosol and predicted absorption artifact.	172
4-17	Measured distribution of chrysene/triphenylene with particle size in Kenmore Square aerosol and predicted absorption artifact.	173
4-18	Measured distribution of benzo[<i>a</i>]pyrene with particle size in Kenmore Square aerosol and predicted absorption artifact.	173
4-19	Photoionization detector response at Kenmore Square, September 11 and 12, 1996.	177
5-1	MOI impactor stage design.	181
5-2	Schematic of flow for a round impinging jet.	183
5-3	Mass transfer coefficient (<i>k</i>) versus radial position (<i>r</i>) for pyrene in MOI stages 0–8.	187
5-4	Prediction of absorption in MOI versus time for stages 2, 4, 6, and 8 without denuding.	191
5-5	Dimensionless denuding, ζ , versus dimensionless time, τ , in the MOI.	193
5-6	Prediction of absorption in MOI versus time for stages 2, 4, 6, and 8 with denuding.	194
5-7	Measured and predicted pyrene absorption in MOI after 6 hours.	196
5-8	Measured and predicted pyrene absorption in MOI after 24 hours.	197
5-9	Measured and predicted pyrene absorption in MOI after 73 hours.	197
6-1	Characteristic time for equilibration between the gas phase and spherical adsorbate particles for some PAH at 25°C.	204
7-1	Characteristic time for equilibration between the gas phase and <i>n</i> -octanol particles for some PAH at 25°C.	223
7-2	Distributions of total and sorbent mass with particle size in rural aerosol.	228
7-3	Distributions of total and sorbent mass with particle size in urban aerosol.	229
7-4	Net addition of aerosol sorbent and PAH by emissions and deposition.	230
7-5	Predicted distributions of PAH with particle size for $\log K = 9$ –18.	234
7-6	Comparison of the distributions of fluoranthene with particle size as measured in an urban aerosol and predicted by the absorptive partitioning model.	237
7-7	Comparison of the distributions of pyrene with particle size as measured in an urban aerosol and predicted by the absorptive partitioning model.	238

7-8	Comparison of the distributions of benz[<i>a</i>]anthracene with particle size as measured in an urban aerosol and predicted by the absorptive partitioning model.	238
7-9	Comparison of the distributions of chrysene/triphenylene with particle size as measured in an urban aerosol and predicted by the absorptive partitioning model.	239
7-10	Comparison of the distributions of benzo[<i>e</i>]pyrene with particle size as measured in an urban aerosol and predicted by the absorptive partitioning model.	239
7-11	Comparison of the distributions of benzo[<i>a</i>]pyrene with particle size as measured in an urban aerosol and predicted by the absorptive partitioning model.	240
7-12	Comparison of the distributions of perylene with particle size as measured in an urban aerosol and predicted by the absorptive partitioning model.	240
7-13	Comparison of the distributions of dibenzanthracenes with particle size as measured in an urban aerosol and predicted by the absorptive partitioning model.	241
7-14	Comparison of the distributions of benzo[<i>ghi</i>]perylene with particle size as measured in an urban aerosol and predicted by the absorptive partitioning model.	241
7-15	Evolution of gas phase and total particulate phase concentrations with time for $\log K = 12$ and partial gas phase emissions.	243
7-16	Evolution of gas phase and total particulate phase concentrations with time for $\log K = 12$ and no gas phase emissions.	243
7-17	Predicted distributions of PAH with particle size for $\log K = 12$ at various times.	244
8-1	Intermediate magnification TEM image of a carbonaceous aggregate particle collected on a carbon grid.	248
8-2	Low magnification TEM image of atmospheric particles collected on a lacey grid.	250
8-3	Intermediate magnification TEM image of a carbonaceous aggregate particle collected on a lacey grid.	252
8-4	Low magnification TEM image of mixed aggregate particle collected on a lacey grid.	254
8-5	Intermediate magnification STEM image of aggregate particle collected on a lacey grid.	256
8-6	High magnification STEM image of aggregate particle collected on a lacey grid.	258
8-7	Schematic of Cahn System 113 thermogravimetric analyzer.	260
8-8	Temperature programmed desorption of diesel particulate matter, 150°C final temperature.	261
8-9	Temperature programmed desorption of diesel particulate matter, 300°C final temperature.	262

8-10	Temperature programmed desorption of diesel particulate matter, 450°C final temperature.	262
8-11	Distribution of pore volume with pore size for diesel particulate matter thermally desorbed at 150°C.	264
8-12	Distribution of pore volume with pore size for diesel particulate matter thermally desorbed at 300°C.	265
8-13	Distribution of pore volume with pore size for diesel particulate matter thermally desorbed at 450°C.	265
D-1	Linear fit of boiling point with retention time.	312
D-2	Heat capacity at saturated conditions for solid and liquid fluoranthene.	324
D-3	Solid heat capacities, $C_{sat,S}$, of PAH at $T = 298$ K.	325
D-4	Comparison of vapor pressure estimation techniques.	334

List of Tables

1.1	PAH Structures	35
1.1	36
1.1	37
1.2	Particulate Phase PAH Concentrations in Urban Air Sampled by Fil- tration.	45
1.3	$\Delta H_{obs} - \Delta H_{vap}$ Estimated from Gas—Particle Distribution Data. . .	56
2.1	Air Conditions during Sampling.	66
2.2	Operating Characteristics of MOI.	69
2.3	HPLC Retention Volumes for PAH and OPAH.	74
2.4	PAH Reference Standards.	77
2.4	78
2.5	Oxygenated PAH Reference Standards.	80
2.5	81
2.6	PAH Selected Ion Monitoring Program.	84
2.7	OPAH Selected Ion Monitoring Program.	85
2.8	Sample Peak Attribution for Kenmore Square Stage 7.	88
2.9	PAH Response Factors Relative to Deuterated PAH	90
2.10	PAH:dPAH MSD Responses for Different Ion Monitoring Programs. .	93
2.11	OPAH Response Factors Relative to Deuterated PAH.	93
3.1	PAH Identified in Kenmore Square Samples.	103
3.2	PAH Identified in Quabbin Summit Samples.	115
3.3	OPAH Identified in Kenmore Square Samples.	120
3.4	OPAH Tentatively Identified by GC/MS.	121
4.1	Characteristic Times, τ , and Overall Mass Transfer Coefficients, \bar{k} , for Absorption to Impaction Media in MOI.	163
4.2	Gas—Particle Distribution Ratios.	171
5.1	Characteristics of MOI Stages.	182
7.1	Equilibrium Gas—Sorbent Partition Coefficients (K).	235
8.1	Summary of Soot Desorption Experiments.	263

A.1	Amounts of naphthalene, acenaphthylene, and acenaphthene in Kenmore Square aerosol samples.	284
A.2	Amounts of fluorene, phenanthrene, and anthracene in Kenmore Square aerosol samples.	284
A.3	Amounts of fluoranthene, pyrene, and benzo[ghi]fluoranthene in Kenmore Square aerosol samples.	285
A.4	Amounts of benz[a]anthracene, chrysene/triphenylene, and benzofluoranthenes in Kenmore Square aerosol samples.	285
A.5	Amounts of benzo[e]pyrene, benzo[a]pyrene, and perylene in Kenmore Square aerosol samples.	286
A.6	Amounts of 276a, indeno[1,2,3-cd]pyrene, and dibenzanthracenes in Kenmore Square aerosol samples.	286
A.7	Amounts of benzo[ghi]perylene, and coronene in Kenmore Square aerosol samples.	287
A.8	Amounts of naphthalene, acenaphthylene, and acenaphthene in Quabbin Summit aerosol samples.	288
A.9	Amounts of fluorene, phenanthrene, and anthracene in Quabbin Summit aerosol samples.	288
A.10	Amounts of fluoranthene, pyrene, and benzo[ghi]fluoranthene in Quabbin Summit aerosol samples.	289
A.11	Amounts of benz[a]anthracene, chrysene/triphenylene, and benzofluoranthenes in Quabbin Summit aerosol samples.	289
A.12	Amounts of benzo[e]pyrene, benzo[a]pyrene, and perylene in Quabbin Summit aerosol samples.	290
A.13	Amounts of 276a, indeno[1,2,3-cd]pyrene, and dibenzanthracenes in Quabbin Summit aerosol samples.	290
A.14	Amounts of benzo[ghi]perylene, and coronene in Quabbin Summit aerosol samples.	291
A.15	Amounts of 1,4-naphthoquinone, OPAH-168a, and OPAH-168b in Kenmore Square aerosol samples.	292
A.16	Amounts of 1-acenaphthenone, 9-fluorenone, and 1,8-naphthalic anhydride in Kenmore Square aerosol samples.	292
A.17	Amounts of OPAH-208a, phenanthrenequinone, and OPAH-208b in Kenmore Square aerosol samples.	293
A.18	Amounts of 11H-benzo[a]fluoren-11-one, 7H-benzo[c]fluoren-7-one, and 11H-benzo[b]fluoren-11-one in Kenmore Square aerosol samples.	293
A.19	Amounts of benzanthrone, 5,12-naphthacenequinone, and OPAH-248a in Kenmore Square aerosol samples.	294
A.20	Amounts of OPAH-254a, 6H-benzo[cd]pyrene-6-one, and OPAH-230a in Kenmore Square aerosol samples.	294
A.21	Amounts of OPAH-272a, OPAH-280a, and benzo[a]pyrene-6,12-dione in Kenmore Square aerosol samples.	295
A.22	Amounts of OPAH-280b in Kenmore Square aerosol samples.	295
B.1	Amounts of Pyrene in Absorption Artifact Experiments.	298

B.2	Amounts of Pyrene in Recovery Test Samples.	298
B.3	Amounts of Pyrene in Saturation Experiment Samples.	298
B.4	Amounts of Pyrene in Solvent Trap Experiment.	298
D.1	Experimental and Estimated Values of PAH Boiling Points.	311
D.2	Estimated Values for PAH Critical Properties and Lennard—Jones Parameters.	314
D.3	Literature Values for PAH Critical Properties.	314
D.4	Joback Group Contributions for Critical Properties.	314
D.5	Gas Phase Diffusivities for PAH Estimated by the Method of Fuller et al. and a Revised Method.	317
D.6	Thermodynamic Properties for PAH Melting.	319
D.7	Ideal Gas Heat Capacities for PAH.	321
D.8	Solid Heat Capacities of PAH.	322
D.9	Liquid Heat Capacities of PAH.	323
D.10	Sublimation Pressure Correlations for PAH at Experimental Temperatures.	327
D.11	Sublimation Pressure Correlations for PAH Corrected to 298 K.	329
D.12	Subcooled Liquid Vapor Pressures for PAH.	333
D.13	Enthalpy of Vaporization and Activity Coefficients for PAH at 298 K.	337

List of Symbols

A	Surface area.
$\sum_{ext} A$	External surface area of aerosol.
b	Energy of adsorption parameter.
C	Concentration.
C_0	Initial concentration.
C_{abs}	Amount absorbed per volume of air sampled.
C_{filter}	Atmospheric concentration collected on a filter.
C_i	Concentration in aerosol size fraction i on a volume of air basis.
C_{meas}	Measured amount per volume of air sampled.
$C_{o,i}$	Concentration of organic sorbent in aerosol size fraction i on a volume of air basis.
C_p	Heat capacity at constant pressure.
C_{part}	Amount associated with particles per volume of air sampled.
$C_{sat,S}$	Heat capacity of solid in equilibrium with saturated vapor.
$C_{sat,L}$	Heat capacity of solid in equilibrium with saturated vapor.
$C_{sat,G}$	Heat capacity of vapor in equilibrium with condensed phase.
C_B	Concentration in bulk gas phase.

$C_{B,0}$	Concentration in bulk gas phase at inlet.
C_G	Concentration in gas phase.
C_L	Concentration in liquid phase.
$C_{L,eq}$	Concentration in liquid phase at equilibrium.
$C_{L,i}$	Concentration in liquid phase of aerosol size fraction i .
C_{PUF}	Atmospheric concentration collected in an absorbent.
C_S	Concentration in gas phase at surface.
C'	Cunningham slip correction.
D	Impactor nozzle diameter.
D_p	Aerodynamic diameter of particle.
D_{p50}	Aerodynamic diameter for which 50% of particles are collected on an impaction stage.
D_{AB}	Binary diffusion coefficient.
\mathcal{D}_G	Diffusion coefficient in air.
\mathcal{D}_L	Diffusion coefficient in liquid.
EC	Atmospheric concentration of elemental carbon.
G_L	Gibbs free energy of pure liquid.
G_S	Gibbs free energy of pure solid.
H	Height of nozzle above surface.
ΔH_{abs}	Enthalpy of absorption.
ΔH_{ads}	Enthalpy of adsorption.
ΔH_{fus}	Enthalpy of fusion.
ΔH_{mix}	Enthalpy of mixing.

ΔH_{obs}	Observed enthalpy of particle association.
ΔH_{sub}	Enthalpy of sublimation.
ΔH_{vap}	Enthalpy of vaporization.
k	Mass transfer coefficient.
\bar{k}	Overall mass transfer coefficient.
k'	Mass transfer coefficient corrected for array of jets.
k'_0	Mass transfer coefficient corrected for array of jets at center of impinging jet.
K	Equilibrium partition coefficient between liquid and gas phases.
K_{oa}	Equilibrium partition coefficient between oil and air.
K_{ow}	Equilibrium partition coefficient between <i>n</i> -octanol and water.
L	Nozzle length.
L_e	Entrance length for fully developed laminar flow.
M	Molecular weight.
M_i	Mass of particles in size bin <i>i</i> .
M_o	Molecular weight of organic sorbent.
M_{oil}	Molecular weight of oil.
M^+	Molecular ion.
$(M+1)^+$	Molecular ion plus 1 amu.
$(M-CO)^+$	Molecular ion less a CO group.
$(M-2CO)^+$	Molecular ion less two CO groups.
$(M-CO_2)^+$	Molecular ion less a CO ₂ group.

$(M-CO_2-CO)^+$	Molecular ion less CO ₂ and CO groups.
n	Number of moles adsorbed.
n_{eq}	Number of moles adsorbed at equilibrium.
$n(D_p)$	Number distribution of particles with size.
n_A	Mass flux of species A.
N	Total number of particles in a size mode.
N_{jet}	Number of jets in array.
N_s	Moles sorbed per surface area for monolayer coverage.
N_{st}	Number of stages in impactor.
OC	Atmospheric concentration of organic carbon.
OF	Fraction of organic material.
p	Partial pressure.
p_L	Saturation pressure over pure liquid.
p_S	Saturation pressure over pure solid.
P	Total pressure.
P_0	Total pressure at inlet.
P_c	Critical pressure.
P_j	Total pressure at stage j .
PM10	Atmospheric concentration of particles smaller than 10 μm .
Q	Volumetric flow rate.
r	Dimensionless distance from center of impinging jet.
R	Ideal gas constant.

R_p	Radius of particle.
Re	Reynolds number.
RF	Response factor.
RI	Retention index.
RT	Retention time.
Sc	Schmidt number.
Sh	Sherwood number.
St_{50}	Stokes number corresponding to D_{p50} .
ΔS_{fus}	Entropy of fusion.
$\Delta S_{fus,TP}$	Entropy of fusion at triple point.
t	Time.
t_{res}	Residence time.
T	Temperature.
T_a	Ambient temperature.
T_b	Boiling point.
T_c	Critical temperature.
T_{exp}	Experimental temperature.
T_m	Melting point.
T_{TP}	Triple point temperature.
U_0	Average velocity of jet exiting nozzle.
V	Volume.
V_{air}	Volume of air sampled.

V_c	Critical volume.
V_i	Volume of particles in size bin i .
V_{oil}	Volume of oil.
V_L	Volume of liquid.
V_{PM10}	Volume of particles smaller than 10 μm .
V_S	Volume of solid.
x	Mole fraction.
α	Ratio of the rural to urban atmospheric concentration of PAH.
α_S	Intercept of linear fit of $C_{sat,S}$ with T .
α_L	Intercept of linear fit of $C_{sat,L}$ with T .
β_S	Slope of linear fit of $C_{sat,S}$ with T .
β_L	Slope of linear fit of $C_{sat,L}$ with T .
γ	Activity coefficient.
δ	Oil layer thickness.
ζ	Dimensionless measure of denuding.
η	Mass adsorbed.
η_∞	Mass adsorbed in monolayer.
θ	Surface coverage.
θ	Dimensionless concentration.
$\bar{\theta}$	Average dimensionless concentration.
θ_J	Surface area of particles per volume air.
κ	Dimensionless mass transfer coefficient.

μ	Viscosity.
Π	Dimensionless pressure.
ρ	Density.
ρ_o	Density of organic sorbent.
ρ_{oil}	Density of oil.
ρ_p	Density of particle.
σ	Surface tension.
σ	Standard deviation.
σ_{EC}	Surface area of elemental carbon.
σ_{OC}	Surface area required to accommodate a monolayer of organic carbon.
τ	Characteristic time.
τ	Dimensionless time.
τ_{eq}	Characteristic time for gas—particle equilibration.
τ_i	Characteristic time for mass input.
τ_k	Characteristic time for mass transfer.
τ_G	Characteristic time for diffusion in gas phase.
τ_L	Characteristic time for diffusion in liquid phase.
ϕ	Gas—particle distribution.
ϕ_{tim}	Largest value of gas—particle distribution consistent with size-segregated sampling data.
ϕ_Y	Gas—particle distribution measured by Yamasaki et al.
ψ	Ratio of vapor pressure over a drop to that over a flat surface.

List of Abbreviations

BaP	Benzo[<i>a</i>]pyrene.
BET	Brunauer, Emmett and Teller [theory of adsorption].
DBP	Dibutyl phthalate.
DCAA	Dicarboxylic acid anhydride.
DCM	Dichloromethane.
DEP	Department of Environmental Protection.
DMSO	Dimethyl sulfoxide.
dPAH	Deuterated polycyclic aromatic hydrocarbons.
EC	Elemental carbon.
ESP	Electrostatic precipitator.
GC/MS	Gas chromatography/mass spectrometry.
HP	Hewlett Packard.
HPLC	High pressure liquid chromatography.
MOI	Micro-orifice impactor.
MSD	Mass selective detector.
NIST	National Institute of Standards and Technology.
OC	Organic carbon.

OPAH	Oxygenated polycyclic aromatic hydrocarbons.
PAH	Polycyclic aromatic hydrocarbons.
PM10	Particulate matter smaller than 10 μm .
PTFE	Polytetrafluorethylene.
RI	Retention index.
RT	Retention time.
SIM	Selected ion monitoring.
SRM	Standard reference material.
STEM	Scanning transmission electron microscope.
STP	Standard temperature and pressure.
TEM	Transmission electron microscope.
TGA	Thermogravimetric analyzer.
TSP	Total suspended particulate matter.

Chapter 1

Introduction

1.1 Health Effects Motivation

1.1.1 Particulate Matter

Epidemiological studies in six U.S. cities found positive correlations between the concentration of particles in the air and daily mortality [1]. These studies also suggest that daily rates of respiratory illness, and mortality from respiratory and cardiovascular disease correlate with the concentration of particles in urban air. These conclusions have been extrapolated to suggest that approximately 50,000 die prematurely in the U.S. due to particulate pollution. A reanalysis of these data has supported the conclusions similar of the original investigators [2].

Epidemiological studies of humans exposed to high levels of combustion generated particles have also found links between particulate air pollution and human health. Elevated lung cancer rates among women in rural China have been attributed to emis-

sions from their coal-fired stoves [3]. Studies of populations occupationally exposed to diesel emissions data suggest that there is an association between this exposure and lung cancer [4, 5]. The carcinogenic activity of diesel emissions has also been demonstrated in rats; however carbon black, which is similar to diesel soot but lacks the associated organic compounds, was also found to cause cancer in rats [6].

The mechanism by which particles cause adverse health effects is a subject of active debate. One hypothesis holds that particles themselves induce health effects. A second hypothesis holds that respirable particles deposit harmful chemicals in the lung. This second hypothesis is the motivation for this work which examines the association of toxic and mutagenic organic compounds with particles in the atmosphere.

1.1.2 Mutagenic Organic Species

Likely agents of harmful health effects are species which are associated with atmospheric particles and, by themselves, are toxic or mutagenic. PAH and related compounds have been shown to cause mutations in cells and cancer in animals. The toxic and mutagenic effects of these compounds have been reviewed [7, 8, 9, 10, 11, 12].

Bioassay-directed chemical analysis is a useful technique to identify mutagenic species in environmental samples [13, 14, 15]. In this technique, extracts from air particle samples are fractionated and the fractions tested for biological activity in bacterial or human cell assays. Fractions which are mutagenic are then subfractionated and these subfractions further tested using bioassays. This reductive procedure is repeated until the most active subfractions are subdivided to include a relatively

small set of chemical species. The final subfractions are then analyzed for individual species to determine which species are the cause of the toxic or mutagenic effect of the subfraction. The chemical species are then tested individually using the same bioassay. The goal is to attribute the mutagenicity of a subfraction, and ultimately the whole particle extract, to particular mutagenic species. This approach assumes that the mutagenic effect of the species are linearly additive to the mutagenicity of the complex mixture.

Durant and coworkers have recently analyzed extracts of an urban aerosol sample from Washington, DC, by human cell bioassay-directed chemical analysis [15]. The non-polar organic fraction containing PAH and the semi-polar fraction containing oxygenated PAH (OPAH) were both found to be human cell mutagens. Related work to test individual compounds for human cell mutagenicity found a number of PAH and OPAH to be human cell mutagens [16].

This work is focused on the association of PAH and OPAH with atmospheric particles. PAH were chosen because of they account for a large fraction of the mutagenicity of air particle extracts [15]. There is also a vast literature on the analytic techniques, ambient concentrations, atmospheric partitioning, and thermodynamic properties of PAH. Reviews of this literature are available [17, 18, 19, 20, 21]. This literature will be used to test proposed mechanisms of partitioning and to generalize the results for application to other semi-volatile pollutants. PAH discussed in this work are listed in Table 1.1 with their chemical structures.

OPAH were chosen because they are recently identified human cell mutagens representative of the mutagenic semi-polar fraction. Relatively little is known about

these compounds in the atmosphere. Therefore measurements of their partitioning in the atmosphere will be novel and will serve as a test of the generalized description of partitioning of semi-volatile compounds in the atmosphere.

1.2 Atmospheric Particles

In the late 1970s, Whitby and coworkers synthesized numerous measurements of atmospheric particle size distributions to describe the distribution of particle sizes in atmospheric aerosols [22, 23]. In the Whitby paradigm, atmospheric particles are grouped into ultrafine, accumulation and coarse size modes. Ultrafine particles have an aerodynamic diameter (D_p) less than $\approx 0.1 \mu\text{m}$; they are emitted from combustors and formed in the atmosphere by homogeneous nucleation. Accumulation particles are in the approximate range $0.1 < D_p < 2.0 \mu\text{m}$; they are formed by the coagulation of and condensation on smaller particles. Coarse particles, those larger than $\approx 2 \mu\text{m}$, are generated by mechanical attrition of solids and the break up of liquid surfaces.

The number of particles in each mode is represented by a log-normal distribution with respect to D_p . The number of particles in the size range D_p to $D_p + dD_p$, $n(D_p)$, is

$$n(D_p) = \frac{N}{\sqrt{2\pi}D_p \ln \sigma} \exp \left[\frac{-(\ln D_p - \ln \overline{D_p})^2}{2(\ln \sigma)^2} \right] \quad (1.1)$$

where $\overline{D_p}$ is the geometric mean particle size, and σ is the geometric standard deviation of particle size. Figure 1-1 shows the the number particles per volume of air for the average urban aerosol with the contributions of the three modes.

By assuming that the particles are spherical, one can calculate the volume of an

Table 1.1: PAH Structures

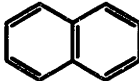
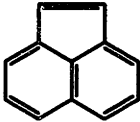
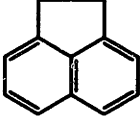
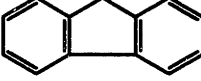
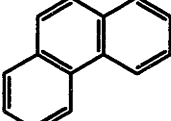
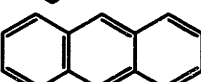
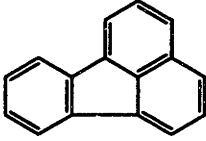
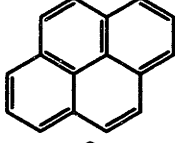
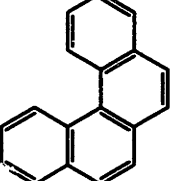
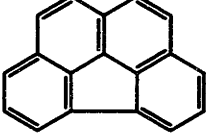
Name	Formula	Molecular Weight	Structure
Naphthalene	$C_{10}H_8$	128	
Acenaphthylene	$C_{12}H_8$	152	
Acenaphthene	$C_{12}H_{10}$	154	
Fluorene	$C_{13}H_{10}$	166	
Phenanthrene	$C_{14}H_{10}$	178	
Anthracene	$C_{14}H_{10}$	178	
Fluoranthene	$C_{16}H_{10}$	202	
Pyrene	$C_{16}H_{10}$	202	
Benzo[<i>c</i>]phenanthrene	$C_{18}H_{12}$	228	
Benzo[<i>ghi</i>]fluoranthene	$C_{18}H_{10}$	226	

Table 1.1: PAH Structures, continued

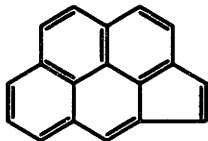
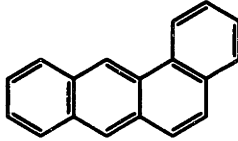
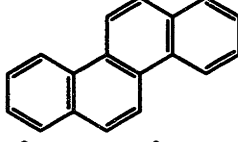
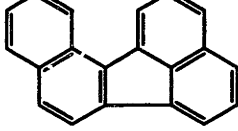
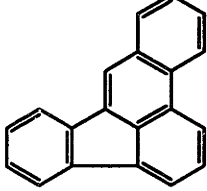
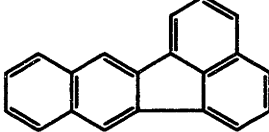
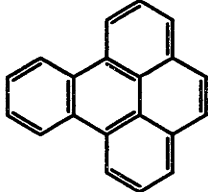
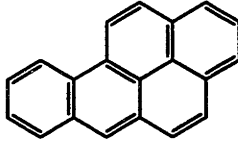
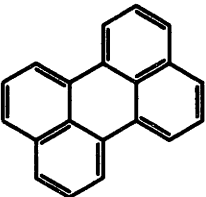
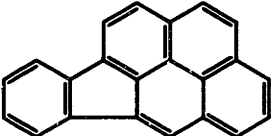
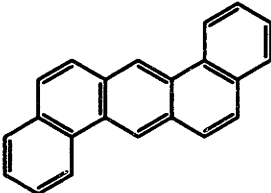
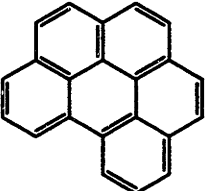
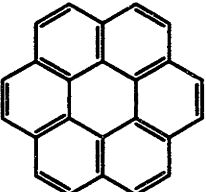
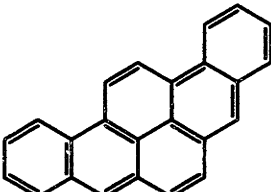
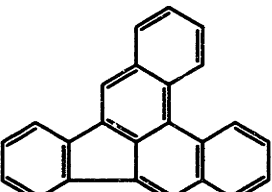
Name	Formula	Molecular Weight	Structure
Cyclopenta[<i>cd</i>]pyrene	$C_{18}H_{10}$	226	
Benz[<i>a</i>]anthracene	$C_{18}H_{12}$	228	
Chrysene	$C_{18}H_{12}$	228	
Benzo[<i>j</i>]fluoranthene	$C_{20}H_{12}$	252	
Benzo[<i>b</i>]fluoranthene	$C_{20}H_{12}$	252	
Benzo[<i>k</i>]fluoranthene	$C_{20}H_{12}$	252	
Benzo[<i>e</i>]pyrene	$C_{20}H_{12}$	252	
Benzo[<i>a</i>]pyrene	$C_{20}H_{12}$	252	

Table 1.1: PAH Structures, continued

Name	Formula	Molecular Weight	Structure
Perylene	$C_{20}H_{12}$	252	
Indeno[1,2,3- <i>cd</i>]pyrene	$C_{22}H_{12}$	276	
Dibenz[<i>a,h</i>]anthracene	$C_{22}H_{14}$	278	
Benzo[<i>ghi</i>]perylene	$C_{22}H_{12}$	276	
Coronene	$C_{24}H_{12}$	300	
Dibenzo[<i>a,i</i>]pyrene	$C_{24}H_{14}$	302	
Dibenzo[<i>b,e</i>]fluoranthene	$C_{24}H_{14}$	302	

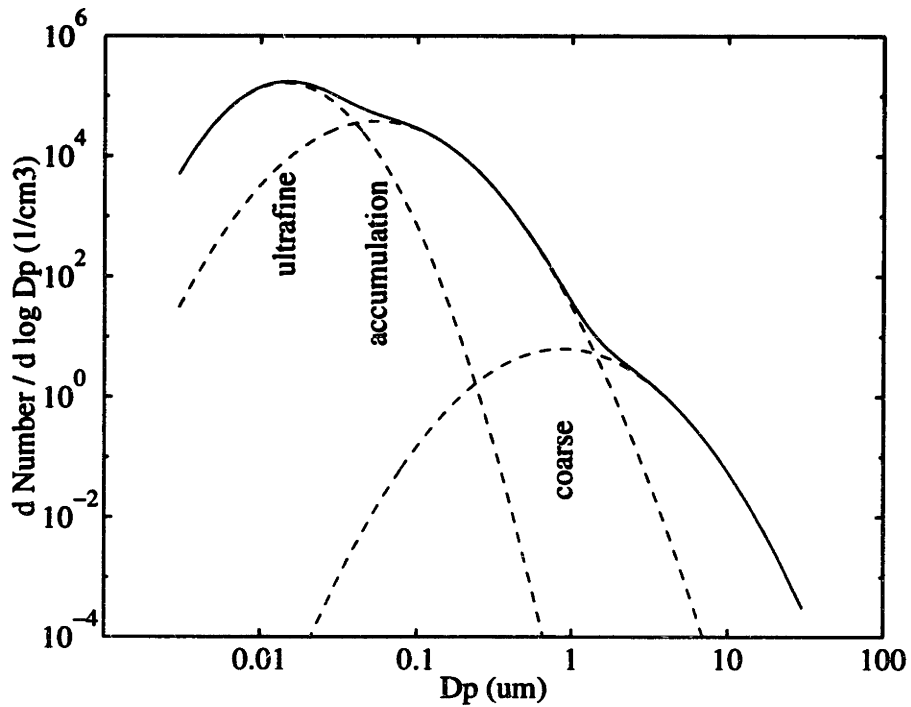


Figure 1-1: Number distribution with particle size for a typical urban aerosol [22].

aerosol size fraction as the third moment of the number distribution as

$$V = \frac{\pi}{6} \int D_p^3 n(D_p) dD_p \quad (1.2)$$

The surface area of an aerosol can be calculated similarly, as the second moment of the number distribution. Figure 1-2 shows the surface area and volume distributions with particle size for Whitby's typical urban aerosol. The surface area distribution is unimodal with a peak at $D_p \approx 0.2 \mu\text{m}$. The volume distribution is bimodal with peaks at $D_p \approx 0.3 \mu\text{m}$ and $D_p \approx 6 \mu\text{m}$.

Recent mass spectral analyses of fragment ions laser ablated from atmospheric particles has found that the composition of these particles, even particles of the same size, varies greatly [24, 25]. Some of the particle types were identified by the Prather

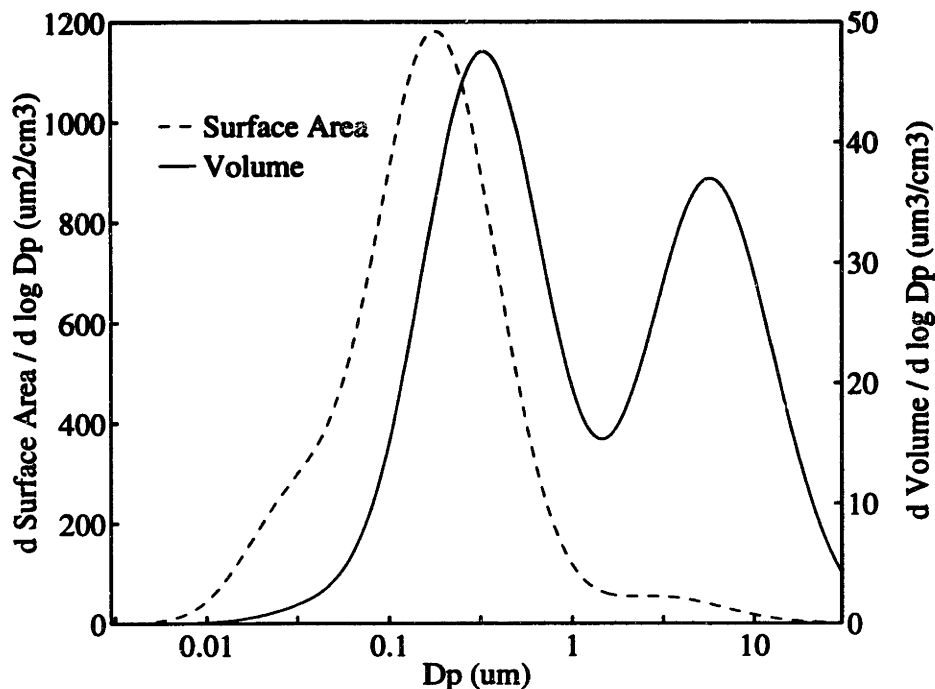


Figure 1-2: Surface area and volume distributions for typical urban aerosol [22].

group as “organic/nitrate”, “organic/inorganic”, “hydrocarbon”, “elemental carbon”, “inorganic oxide”, “marine”, “nitrate” and “nitrate/sulfate” [25]. The various particle types are presumed to have different sources and formation mechanisms.

The observation that atmospheric aerosols are mixtures of different types of particles is also observed by electron microscopy [26, 27, 28]. Figure 1-3 is a transmission electron micrograph (TEM) image of submicron particles collected in Cambridge, MA. The collection and microscopy methods are given in Chapter 8. Three distinct particle types are visible; they are:

1. Solid carbonaceous aggregates identified as particles A, B and C in Figure 1-3.

STEM analysis shows that these particles are composed primarily of carbon.

High resolution TEM shows that the structure is that of graphitic crystallites.

These particles resemble, and are believed to be, soot particles from combustors.

2. Particles D, E, and F in Figure 1-3 are visible circular deposits which evaporated when exposed to the electron beam. These are probably liquid droplets containing high boiling point organic compounds.
3. Particles G and H in Figure 1-3 are faint circular deposits. These are probably the residue from aqueous particles which were dried while the sample was stored in a desiccator prior to analysis.

Mixtures of these basic particle types are also visible, e.g. particles I and J in Figure 1-3.

Soots are carbonaceous aggregates formed by combustion which are composed of aggregated primary particles which are approximately spherical. Figure 1-4 shows soot from the same sample at a higher magnification. The turbostratic structure of the carbonaceous aggregates is apparent with ordered graphitic structures over limited length scales. Soots have carbon structures very similar to carbon blacks, the main difference between soot and carbon black is that soot includes a significant fraction of extractable organics and carbon black does not. Some investigators have used carbon blacks as soot analogs to determine the nature of the PAH—soot association [29, 30, 31].

Cass and coworkers have developed an inventory of aerosol emissions for the Los Angeles air shed. Hildemann et al. sampled 16 source types estimated to be the largest contributors to organic carbon emissions to the Los Angeles air [32]. These samples were analyzed for a range of elements and organic compounds including elemental carbon and 32 PAH [32, 33, 34, 35, 36]. The total emissions from each type of source

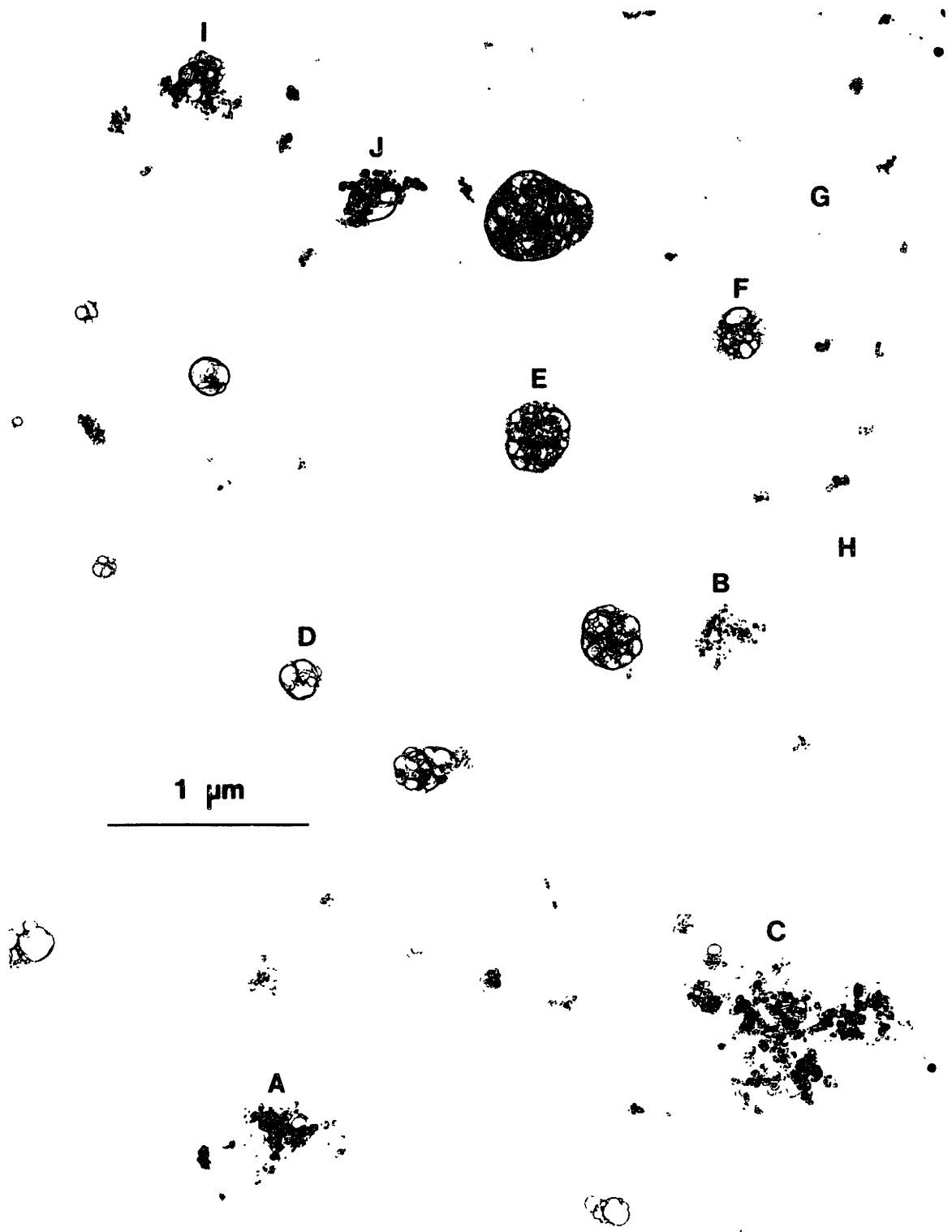


Figure 1-3: Transmission electron micrograph image of submicron particles collected from the atmosphere in Cambridge, MA.

were estimated by multiplying the emission factors, e. g. ng PAH/km driven, by the extent of the source, e. g. km driven. Figure 1-5 shows the estimated contributions to total organic carbon, elemental carbon and PAH fine particle emissions in greater Los Angeles by source type. Organic carbon is defined as the carbon which volatilizes at temperatures less than 525°C. Elemental carbon is defined as the remaining carbon as determined by oxidation of the volatilized sample. For the fine particles, $D_p < 2 \mu\text{m}$, collected in this study, soots are expected to be the main contributor to elemental carbon. Diesel vehicles dominate the production of soot, while gasoline vehicles without catalysts emit the most PAH.

1.3 PAH and OPAH in the Atmosphere

PAH are a class of chemical compounds formed as combustion by-products and of environmental concern due to their demonstrated mutagenicity and carcinogenicity. The physical properties and biological activity of PAH vary widely. For example, the room temperature vapor pressure of naphthalene is 11 orders of magnitude higher than that of benzo[*a*]pyrene (BaP) [20]. BaP caused significant mutations in human cells at concentrations of 14.9 ng/mL while pyrene showed no mutagenic activity at 100,000 ng/mL [16]. Because the biological activity of PAH and PAH reaction products vary by orders of magnitude, the mutagenicity of a sample depends greatly on the relative concentrations of the PAH present.

Urban particulate phase PAH concentrations have been measured in numerous filter sampling studies [37, 38, 39, 40, 41, 42, 43, 44, 45, 46, 47, 48, 49, 50, 51]. Table 1.2



Figure 1-4: High resolution transmission electron micrograph image of a soot particle collected from the atmosphere in Cambridge, MA.

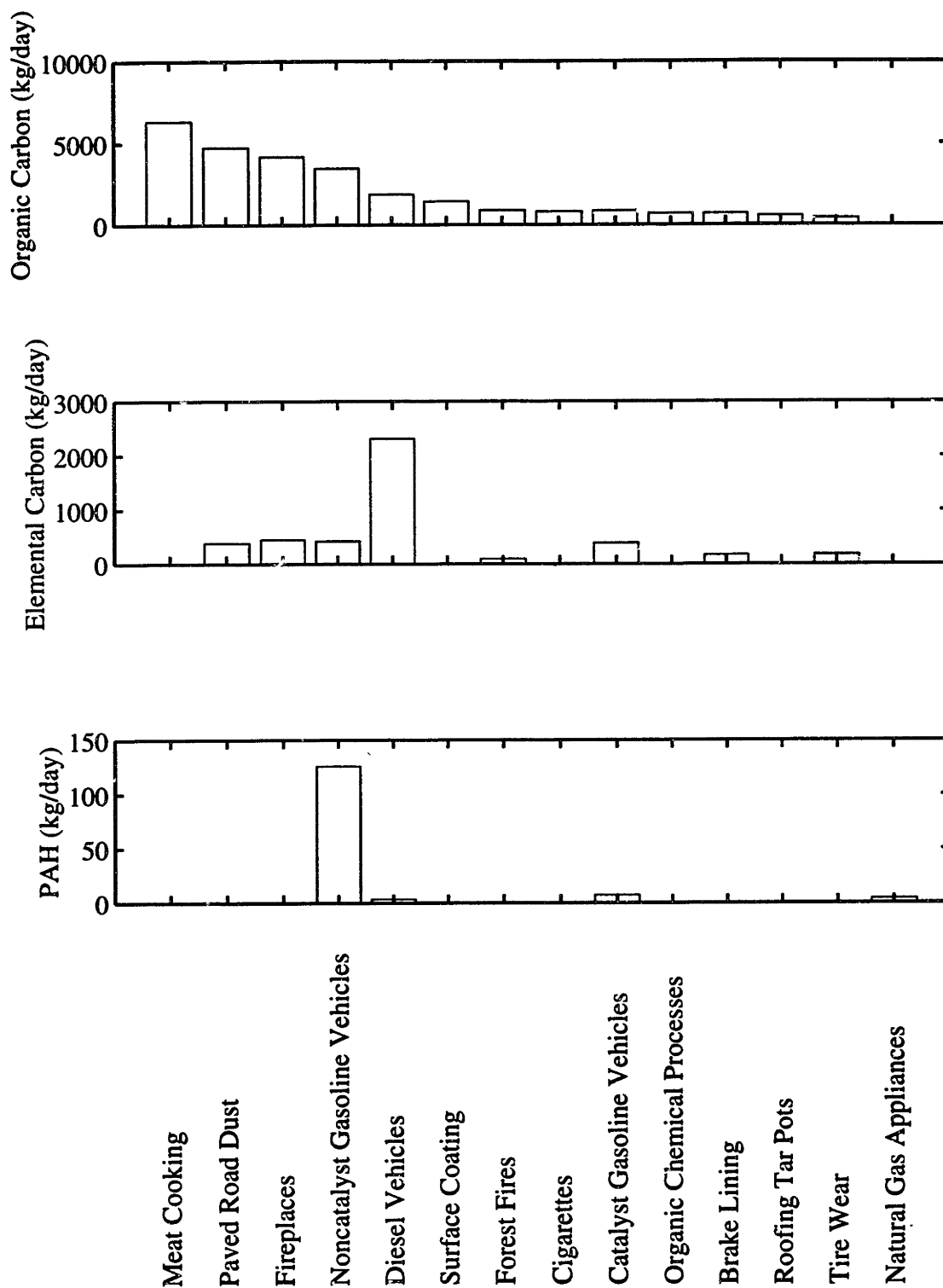


Figure 1-5: Estimated emissions of organic carbon, elemental carbon, and PAH in Los Angeles by source category [32, 33, 34, 36].

Table 1.2: Particulate Phase PAH Concentrations in Urban Air Sampled by Filtration.

Location	This Work Boston USA (ng/m ³)	Cautreels and Van Cauwenberghe (1978) Antwerp Belgium (ng/m ³)	Yamasaki et al. (1982) Osaka Japan (ng/m ³)	Pyysalo et al. (1987) Kokkola Finland (ng/m ³)	Barale et al. (1991) La Spezia Italy (ng/m ³)
Phenanthrene and Anthracene	14.52	0.54–1.70	0.22–2.01	0.2–0.5	0.19–4.3
Fluoranthene	14.70	1.09–4.33	0.36–7.30	0.2–1.1	0.16–7.7
Pyrene	8.07	0.85–3.17	0.37–8.52	0.2–1.5	0.56–16.8
Benz[<i>a</i>]anthracene and Chrysene/Triphenylene	3.44	4.90–25.3	0.95–23.7	0.4–3.5	0.20–14.7
Benzofluoranthenes	3.21	8.92–39.9	2.69–29.1	0.2–3.1	0.27–18.0
Benzo[<i>e</i>]pyrene and Benzo[<i>a</i>]pyrene	2.51	8.63–36.1 ^a	2.64–28.4	0.2–3.1	0.32–12.7
Dibenzanthracenes	0.15	—	—	0.1–0.2	0.11–2.5
Benzo[<i>ghi</i>]perylene	0.82	—	1.83–17.2 ^b	0.2–3.5	0.12–14.9
Coronene	0.11	—	—	0.2–2.4	—

^aIncludes picene.

^bIncludes anthanthrene.

lists selected filter sampling results along with the total particulate concentrations found in this work (see Chapter 3). PAH concentrations are generally in the range 0.1–30 ng/m³. These concentrations vary greatly between sampling sites and over time at the same sites.

PAH emissions will vary by region and over time. In colder regions, home heating combustors will be a more significant source of soot and PAH in addition to emissions by vehicles which were found to dominate emissions in Los Angeles. Analyses of ambient air samples from Japan collected over a full year showed that concentrations of PAH increase in the winter (see Figure 1-6) [40]. This is due to 1) the increase in combustion for heating, 2) lower temperatures, which lower PAH vapor pressures, 3) the reduced rate of photooxidation, and 4) lower mixing heights in winter. The concentration of PAH in the environment depends on many factors including proximity to sources, source types, source performance, wind direction, wind speed, tempera-

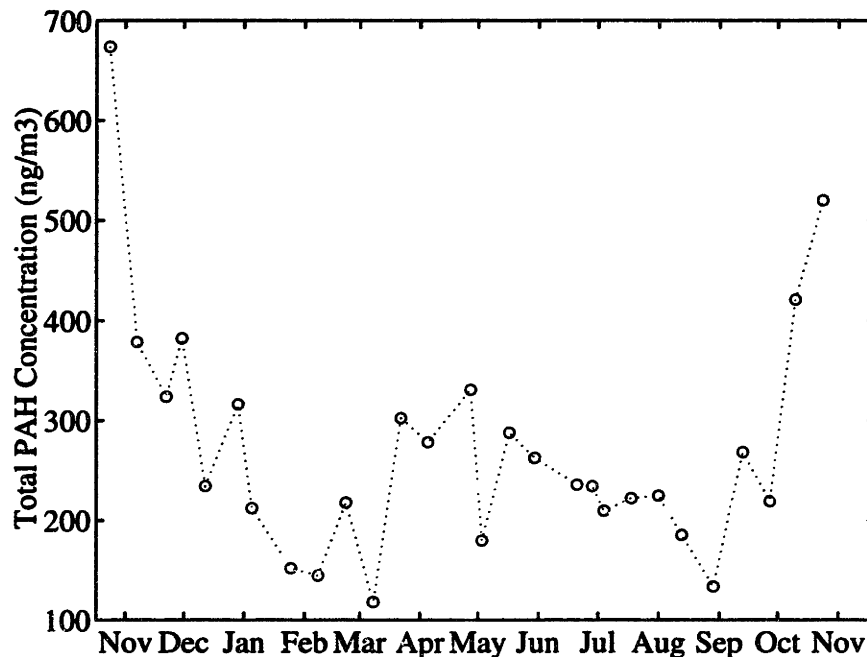


Figure 1-6: Total concentration of 16 PAH in the atmosphere [40].

ture, concentration of other pollutants, and precipitation. These factors introduce a great deal of variability to the sampling of PAH in the environment.

OPAH are semi-volatile organic air pollutants of concern because of their demonstrated genotoxic effects. Studies of OPAH in bacterial and human cell mutation assays have found some of these compounds to be mutagenic [52, 53, 54, 55, 56, 57, 16]. In addition, OPAH are compounds characteristic of the semi-polar fractions of atmospheric particulate extracts; fractions which are highly mutagenic in bacterial and human cells [56, 16, 58]

OPAH have been identified in source samples from gasoline, diesel, coal, wood, and municipal waste combustion [59, 60, 61, 56, 57]. Photooxidation of PAH has also been found to produce OPAH [62]. Atmospheric sampling studies of OPAH have found concentrations in the approximate range 0.1 to 10 ng/m³ for a number of OPAH [61,

63, 64, 65, 66, 56, 67, 57]. A study of OPAH associated with size-segregated particles found approximately half of the benzantrone and perinaphtenone (phenalen-1-one) associated with particles smaller than $3.0 \mu\text{m}$ in summer, and two-thirds in winter [68].

1.4 Atmospheric Partitioning

“Atmospheric partitioning” is used broadly in this work to mean both the distribution of species between the gas and particulate phases, and among particles in the atmospheric aerosol. Estimates of equilibrium partitioning are required to determine these distributions. The equilibrium partitioning of PAH depends on the ambient temperature, concentration of particles, and chemical affinity for the particles. But the distributions cannot be assumed to be at equilibrium without justification as the urban atmosphere is itself in a state of disequilibrium. Dynamic processes, including emissions, photochemical reactions, and deposition, also effect the fate of PAH in the atmosphere. To address the problem of atmospheric partitioning requires analyses of both the equilibrium state and transient processes.

1.4.1 Effect of Partitioning on Atmospheric Fate

Atmospheric Reactions of PAH

Reactive species are formed in the atmosphere by photolysis and subsequent reactions with atmospheric pollutants. PAH in the gas and particulate phases react with these species, most notably $\text{OH}\cdot$, O_3 and NO_3 [69, 70]. The effect of the atmospheric

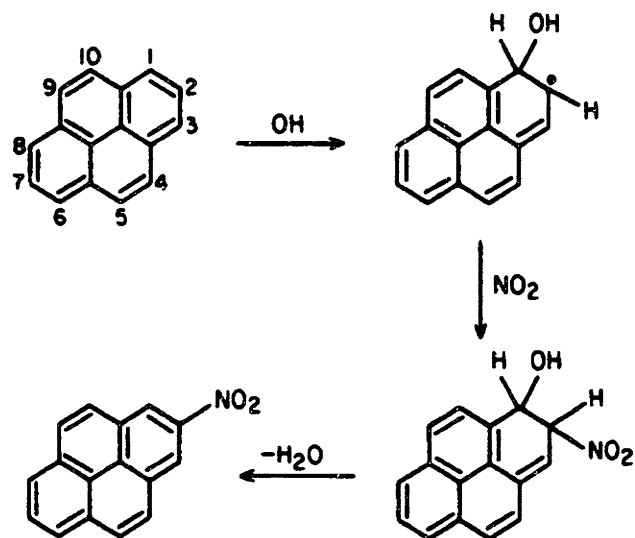


Figure 1-7: Proposed mechanism for the nitration of pyrene [75].

reactions is to react PAH toward CO_2 and H_2O . However, rather stable intermediates may be more active mutagens than the original PAH [71, 72, 73, 74].

From smog chamber studies, Atkinson et al. concluded that the primary reaction of gas phase PAH is with $\text{OH}\cdot$ radicals [76]. In polluted atmospheres $[\text{OH}\cdot]$ is of the order 10^6 molecules/ cm^3 [23]. This results in half lives on the order of 4 hours for unsubstituted PAH like naphthalene, fluoranthene and pyrene. The gas phase reaction rates of higher molecular weight PAH have not been determined. However, structurally similar PAH should react with $\text{OH}\cdot$ at approximately the same rate. Subsequent reactions can produce nitro-PAH as shown in Figure 1-7 [75]. Similar studies of the reactions of acenaphthalene showed that the reaction with $\text{OH}\cdot$ proceeded approximately twice as fast as for pyrene [77].

Ozone reacts readily with the unsaturated carbons in the acenaphthalene cy-

clopenta group. This reaction results in a half life for acenaphthalene of 0.5 hours in the presence of 30 ppb O_3 . Typical polluted urban air concentrations of O_3 are on the order of 100 ppb [23]. PAH without external cyclopenta groups do not readily react with O_3 . Therefore, O_3 reactions decrease the concentration of PAH with external cyclopenta groups relative to other PAH in the atmosphere.

Behymer and Hites studied the photolysis of PAH sorbed on carbon black, fly ash and silica gel [78]. In contrast with the gas phase reactions, fluoranthene and pyrene sorbed on carbon black had half lives of greater than 1000 hours. The rate of photolysis of PAH associated with fly ash correlated with the amount of carbon in the sorbate. The reaction rates for PAH on carbon black and high-carbon fly ash were uniformly low. For some PAH, photolysis on these sorbates was not detectable. In contrast, the half lives of PAH on silica ranged from 0.6 to 268 hours. The reactions of PAH sorbed on carbonaceous particles are 2 to 3 orders of magnitude slower than when the PAH is in the gas phase [79, 78]. The type of photochemical reaction and the rates of those reactions therefore depend greatly on whether the PAH are sorbed or in the gas phase.

Reaction products of PAH, including nitro-PAH, OPAH, and nitrodibenzopyranones, have significantly lower vapor pressures than the parent PAH. These compounds may then be preserved by sorption onto particles [73, 75]. This can have a great effect on the ultimate mutagenicity of PAH emitted to the atmosphere.

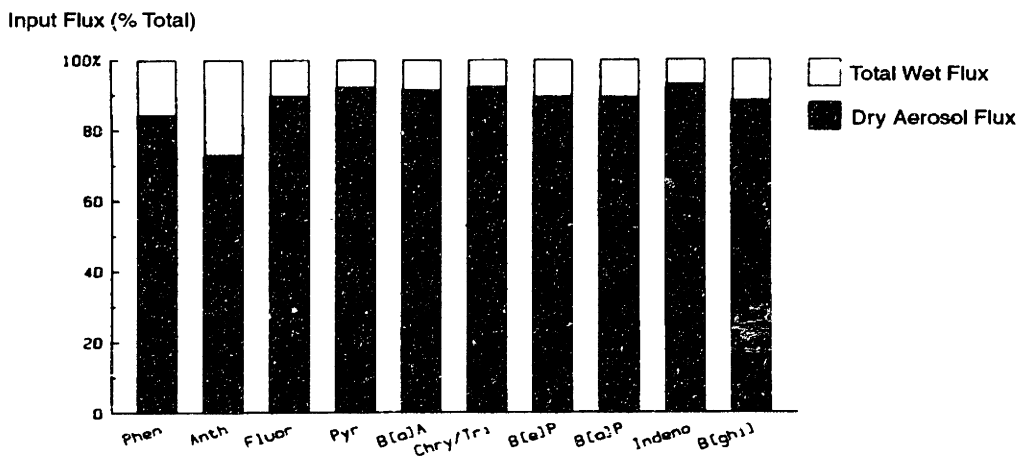


Figure 1-8: PAH fluxes into Siskiwit Lake [80].

Deposition of PAH

McVetty and Hites studied the total flux of PAH for a remote lake over the course of a year by sampling PAH concentrations in atmospheric particulate and gas phases, precipitation, and sediment [80]. The authors defined the washout ratio as the concentration of PAH in precipitation divided by the total concentration of PAH in the air. They found that particle-bound PAH have washout ratios 2 orders of magnitude greater than PAH present primarily in the gas phase.

Dry deposition of aerosol particles is another mechanism to remove PAH from the atmosphere. McVetty and Hites found that this flux accounted for $\approx 90\%$ of the flux of each PAH species with the remainder of the input flux from wet deposition (see Figure 1-8). Figure 1-9 shows the flux of PAH out of the lake studied [80]. The flux of PAH from the lake due to evaporation is greater than that due to condensation from the gas phase to the lake. For more volatile PAH evaporation accounts for 80% of the flux from the lake. Particle size also affects the removal rate of the associated PAH

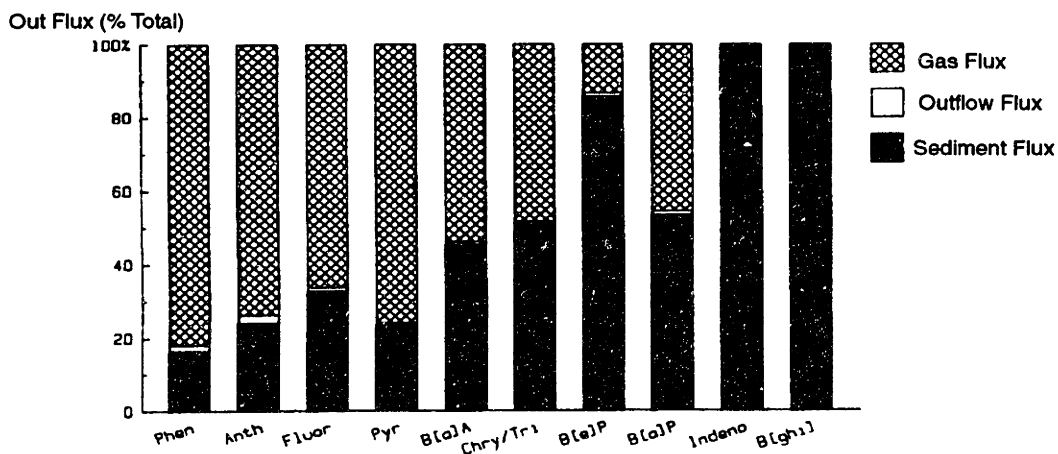


Figure 1-9: PAH fluxes out of Siskiwit Lake [80].

from the atmosphere by dry and wet deposition [81, 82]. In sum, particle bound PAH are removed from the atmosphere by dry and wet deposition 2–3 orders of magnitude more quickly than are gas phase PAH. This selective deposition affects which PAH are deposited to crops and sediments, as well as which remain in the atmosphere.

1.4.2 Effect of Partitioning on Human Exposure

The mechanism and location of deposition of particulate phase PAH in the lung are also affected by particle size. The large particles tend to impact on the upper regions of the lung and small particles diffuse to the surface of the alveoli (see Figure 1-10) [83]. Particles in the accumulation mode size range have the lowest fraction deposited in the lung.

Sun and coworkers studied the fate of BaP in animal lungs. The authors administered tritium-labeled BaP aerosol to rats by nose inhalation. The BaP was removed from rat lungs in 2 hours [84]. The most likely mechanisms for fast removal of pure BaP are 1) metabolism in the lung and 2) diffusion of BaP into the blood.

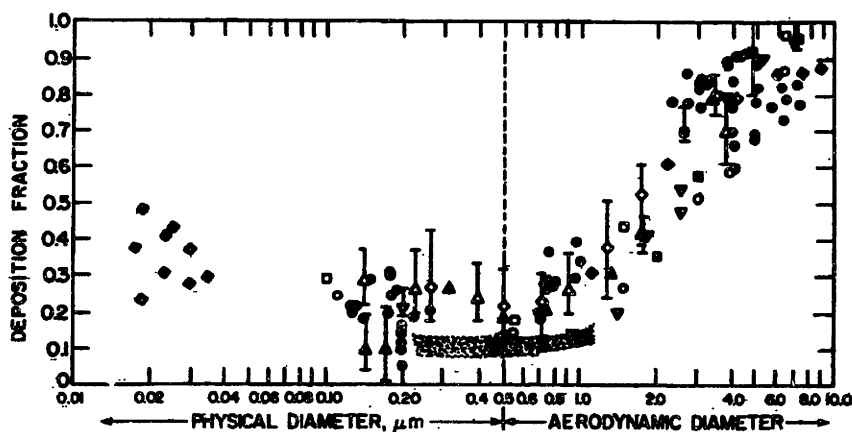


Figure 1-10: Deposition of particles in the respiratory tract for mouth breathing as a function of particle size [83].

BaP metabolites formed in the lung were excreted in urine and bile. Once in the blood, BaP may be stored in fatty tissues, however the majority of BaP is probably metabolized in the liver and excreted in bile. It is reasonable to expect that other PAH inhaled as vapors to be quickly sorbed and distributed in the body in a similar manner.

The same group sorbed tritium-labeled BaP on diesel exhaust which was then inhaled by rats. In this study approximately 50% of the inhaled labeled BaP was cleared from the respiratory tract within 1 hour. The other half of the BaP and BaP metabolites remain in the lung with a half life of 18 days. Therefore PAH sorbed on soot are removed at a much slower rate from the lung than pure PAH.

1.4.3 Measurements of Gas—Particle Distribution

Westerholm et al. sampled diluted gasoline engine exhaust and analyzed the particulate and gas phases for PAH [85]. PAH from naphthalene through fluorene were detected only in the gas phase. Intermediate molecular weight PAH, from phenan-

threne through benz[*a*]anthracene, triphenylene and chrysene, were detected in both the gas and particulate phase exhaust. The particulate phase contained all of the PAH with molecular weights greater than 252. While the general trend of partitioning between the gas and particulate phases is well explained by PAH molecular weight, there are exceptions; 1-methylanthracene and 1-methylphenanthrene are present only in the gas phase and cyclopenta[*cd*]pyrene is present only in the particulate phase. As in gasoline emissions, PAH in diesel exhaust partition between the gas and particulate phases mainly as a function of molecular weight [86].

The gas—particle distribution ratios for PAH in the atmosphere have been measured by a number of investigators [40, 48, 80, 64]. The measured distribution, ϕ , is

$$\phi = \frac{C_{\text{PUF}}}{C_{\text{filter}}} \quad (1.3)$$

where C_{filter} is the the atmospheric concentration of PAH collected on the filter and C_{PUF} that collected in an absorbent (often polyurethane foam) downstream of the filter. Note that some authors designate this ratio K ; in this work K is reserved for equilibrium partition coefficients.

Yamasaki et al. collected an extensive set of ϕ data for a range of temperatures at an urban site in Japan [40]. The distribution ratios reported in this data set are comparable to later measurements [21]. Figure 1-11 shows ϕ versus $1/T$ for pyrene. Ambient temperature variations of 25°C resulted in order of magnitude changes in ϕ .

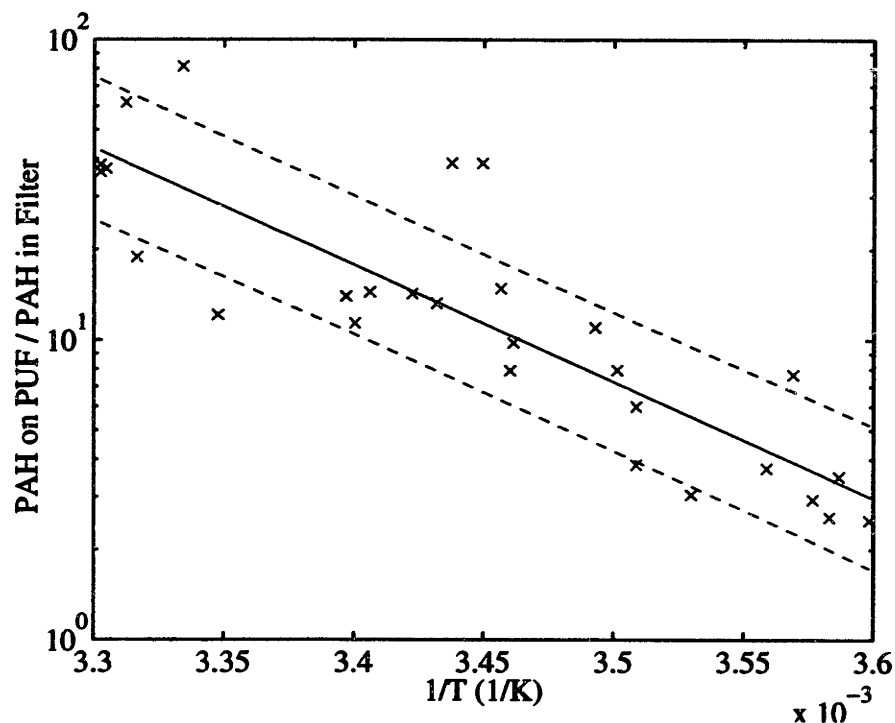


Figure 1-11: Measured gas—particle distribution of pyrene as a function of $1/T$ [40].

1.4.4 Models of Atmospheric Partitioning

Clausius—Clapeyron Fit of Gas—Particle Distribution Data

A number of authors, beginning with Yamasaki et al., have assumed a Clausius-Clapeyron type relation for the gas—particle distributions of PAH. The logarithm of the measured ϕ values were plotted versus $1/T$ as in Figure 1-11. If the PAH are assumed to be in equilibrium with the particles, the slope of this line is the observed enthalpy of gas—particle association, ΔH_{obs} .

Langmuir Adsorption Model

Junge and Yamasaki et al. proposed to model PAH partitioning as non-competitive Langmuir type adsorption [87, 40]. For species at low concentration in the gas phase

[88]

$$\phi = \frac{1}{bRT\theta_J N_s} \quad (1.4)$$

where

b parameter, $b \propto e^{\frac{\Delta H_{ads}}{RT}}$

θ_J surface area of particles per volume air

N_s moles sorbed per surface area

ΔH_{ads} enthalpy of adsorption

Assuming values for θ_J and N_s , one can estimate ΔH_{ads} from atmospheric partitioning data. The resulting values from literature data are presented in Table 1.3. The data from Yamasaki et al. and Ligocki and Pankow show large errors and do not agree in the case of pyrene. The disagreements may be due to variations in the actual versus the assumed values for θ_J , which neither group measured. They may also be due to non-equilibrium conditions or differences in the particles collected in the two studies. Gas—particle distribution data may provide useful rough estimates of ΔH_{ads} , limited by 1) assumed values for θ_J , 2) experimental errors due to the low concentration of PAH in the atmosphere, and 3) inability to detect very low concentrations of higher molecular weight PAH in the gas phase.

BET Adsorption Model

Pankow estimated the heat of adsorption for PAH on atmospheric particles by applying the BET adsorption model to atmospheric partitioning data [88]. The BET

Table 1.3: $\Delta H_{obs} - \Delta H_{vap}$ Estimated from Gas—Particle Distribution Data.

PAH	$\Delta H_{ads} - \Delta H_{vap}$ (kcal/mol)	Reference
Phenanthrene/anthracene	2.9–3.9	[40]
Fluoranthene	3.0–3.5	[40]
Pyrene	3.6–4.3	[40]
Benzo[<i>a</i>]pyrene/ Benzo[<i>e</i>]pyrene	1.9–3.9	[40]
Anthracene	2.5–3.0	[64]
Phenanthrene	2.4–3.0	[64]
Fluoranthene	2.4–3.0	[64]
Pyrene	2.7–3.2	[64]
Benzo[<i>a</i>]anthracene	3.3–3.8	[64]
Chrysene	2.8–3.0	[64]

adsorption isotherm was expressed as

$$\frac{\eta}{\eta_{\infty}} = \frac{bp}{(p_L - p)[1 + (b - 1)p/p_L]} \quad (1.5)$$

where

- η mass sorbed
- η_{∞} mass sorbed in monolayer
- b parameter, $b \propto e^{\frac{\Delta H_{ads} - \Delta H_{vap}}{RT}}$
- p partial pressure of PAH
- p_L vapor pressure of pure liquid
- ΔH_{vap} enthalpy of vaporization

Pankow showed that for low concentrations typical of those in the atmosphere and

$\Delta H_{ads} - \Delta H_{vap} < 7$ kcal/mol at $T = 300$ K, Equation 1.5 reduces to Equation 1.4.

Both the Langmuir and BET models have been used to describe the gas—particle partitioning of PAH in the atmosphere. These descriptions require a number of assumptions. The most important of these are 1) the gas—particle distribution is at equilibrium, 2) competitive adsorption of other species can be neglected, and 3) the adsorption is “liquid like”, that is, the enthalpy of adsorption is a few kJ/mol greater than the enthalpy of vaporization from pure subcooled liquid.

Absorption model

The association of PAH with atmospheric particle has also been explained as absorptive partitioning [89]. In this case the sorbent is the organic fraction of the atmospheric aerosol. The partial pressure of PAH is then

$$p = x\gamma p_L \quad (1.6)$$

where x is the mole fraction of PAH in the organic fraction, γ is the activity coefficient, and p_L is the subcooled liquid vapor pressure. For the assumption of equilibrium gas—particle distribution, this description has been shown to give reasonable values for ϕ [89]. This description is unable to account for $\Delta H_{obs} > \Delta H_{vap}$ since for PAH in organic solvents γ is generally greater than 1 [20, 90, 91].

1.4.5 Measurements of Distribution with Particle Size

Since 1975 measurements of the distribution of PAH with particle size have been performed in and around Toronto, Los Angeles, Antwerp, Barcelona, and Paris [68,

92, 93, 94, 95, 96, 97, 98, 99, 100]. In these studies, PAH were found predominantly in association with fine particles ($D_p < 2.0 \mu\text{m}$). PAH of the same molecular weight were observed to partition similarly among atmospheric aerosols [96, 94]. PAH were also found to partition to larger aerosols in warmer periods [68, 93, 94, 95] and at sites away from emission sources [68, 96, 99].

Studies by the Friedlander group used uv fluorescence to attain detection limits for PAH in the 2–40 pg range [94]. These low detection limits allowed sampling of only 3.6 m³ air through a 1 L/min flow inertial impactor. While uv fluorescence gives very sensitive detection of PAH, it is limited to compounds like PAH with excellent fluorescence properties. Quantification by gas chromatography/mass spectrometry (GC/MS) is applicable to a wider range of compounds, but is generally less sensitive than uv fluorescence. In the recent study of Sicre et al., GC/MS detection limits for PAH were about 300 pg [99]. The lower sensitivity of GC/MS methods requires that large volumes of air, greater than 2000 m³, be sampled. The high flow rate impactors used in these studies cannot segregate particles smaller than 0.5 μm .

Venkataraman recently sampled Los Angeles air with a low pressure impactor [101, 94]. The size-segregated particles were analyzed for PAH. Figure 1-12 shows the distributions of elemental carbon, pyrene and BaP with particle size for a sample obtained in a highway tunnel. This sample represents the soot and PAH as emitted from vehicles. This study and others show that the emissions of soot and PAH from combustion sources are emitted as particles with approximately 0.1 μm diameter [32].

Figure 1-13 shows the distributions of elemental carbon, pyrene and BaP with particle size for ambient air samples collected in greater Los Angeles [94]. The dis-

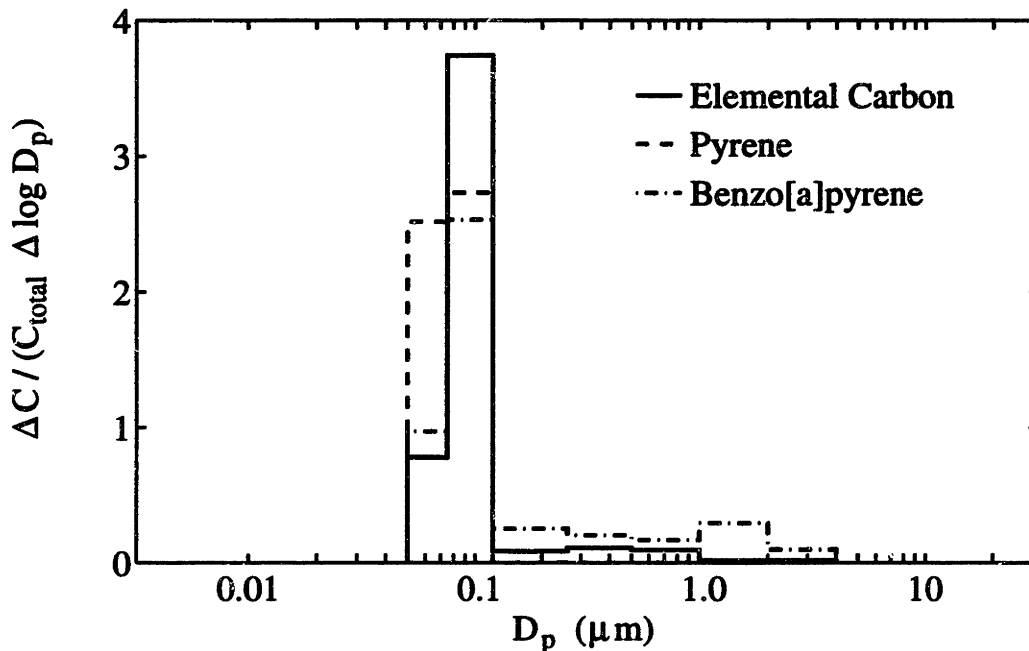


Figure 1-12: Distributions of elemental carbon, pyrene, and benzo[*a*]pyrene with particle size in a highway tunnel [101].

tribution of elemental was bimodal. The second mode (0.5-2 μm) is not present in emission source samples and is due to condensation and particle aggregation in the atmosphere. The distribution of BaP with particle size is similar to that of elemental carbon, implying that BaP largely remains bound to particles. The size distribution of pyrene, however, differs significantly from those of elemental carbon and BaP. This suggest that pyrene enters the gas phase and condenses on larger particles.

1.5 Thesis Objectives

Measurements and predictions of FAH partitioning, both between the gas and particulate phases and among particles, are necessary for a complete understanding of the environmental fate of, and human exposure to, PAH. This work is an attempt to

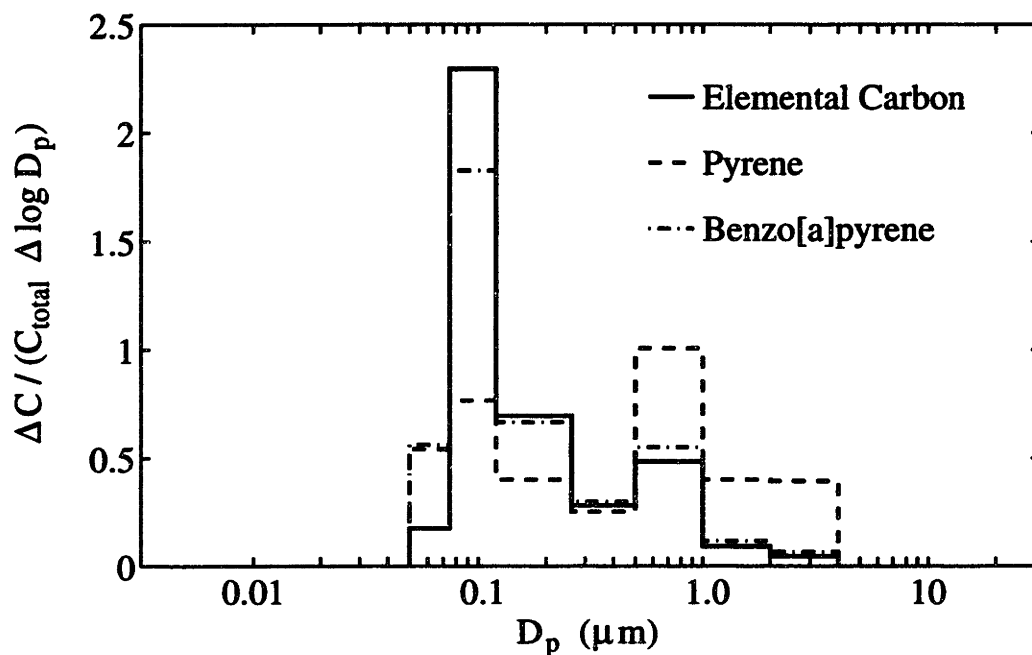


Figure 1-13: Distributions of elemental carbon, pyrene, and benzo[a]pyrene with particle size at Pico Rivera, CA, in winter [94].

improve both the measurements of partitioning with particle size and the prediction of partitioning in general.

One objective of this work was to apply recent advances in aerosol sampling and analysis techniques to develop an improved method for measuring PAH and OPAH associated with size-segregated atmospheric aerosols. In the present study aerosols were collected with a micro-orifice impactor (MOI) from sites in Boston and rural Massachusetts. This impactor is designed to segregate particles as small as 0.08 μm . One half of the samples were analyzed for PAH by gas chromatography/mass spectrometry (GC/MS). The other half were analyzed for OPAH using a similar analytic procedure. This analytic technique is able to quantify a wide variety of organic species; it is not limited to compounds like PAH which have excellent fluorescent

properties. Chapter 2 discusses these sampling and analysis techniques. Chapter 3 presents the distributions of PAH and OPAH with particle size as measured by these techniques.

Size-segregated atmospheric aerosols were collected on oiled impaction media in this work to prevent particle bounce during sampling. The use of the oiled impaction media, however, may have introduced another sampling artifact — the absorption of species from the gas phase. Such absorption would artificially increase the amount of PAH attributed to the aerosol and possibly distort the measured size distributions. An experimental examination of this artifact is presented in Chapter 4. A more general model of the absorption artifact is developed in Chapter 5.

Existing models of the atmospheric partitioning of PAH and, more generally, semi-volatile atmospheric pollutants, have assumed that the pollutants are uniformly distributed among the airborne particles, and that equilibrium partitioning is attained in the atmosphere [87, 40, 88, 102]. Recent data on the distribution of PAH with particle size have shown that PAH were not uniformly distributed among aerosol size fractions [94, 103]. These recent data demonstrate that the assumption of uniform distribution of PAH within an aerosol is incorrect, and cast doubt on the assumption of equilibrium partitioning.

The second main objective of this work was to describe the partitioning of PAH in an atmospheric aerosol consistent with the available atmospheric data. This description relaxed the assumptions of uniform distribution and equilibration. The approach was to examine partitioning by the mechanisms of adsorption and absorption, both of which have been proposed as the dominant mechanisms of PAH—particle association.

The equilibrium gas—particle partitioning and characteristic times for mass transfer were estimated for both adsorption and absorption. Comparisons of these estimates with atmospheric data were used to evaluate the proposed mechanisms of PAH partitioning in the atmosphere. In Chapter 6 the adsorptive partitioning mechanism is presented; in Chapter 7, the absorptive partitioning mechanism.

Chapter 2

Collection and Analysis of Size-segregated Aerosols

2.1 Introduction

Since 1975 measurements of the distribution of PAH with particle size have been performed in and around Toronto, Los Angeles, Antwerp, Barcelona, and Paris [68, 92, 93, 94, 95, 96, 97, 98, 99, 100]. The challenge of this type of sampling is to collect enough material for quantitative analysis while maintaining an accurate size segregation of atmospheric particles. PAH concentrations in the atmosphere are in the range 0.1 to 10 ng/m³ range, therefore, large volumes of air must be sampled and sensitive analytic techniques used to quantify the association of PAH with size-segregated aerosols. The general strategy used has been to collect particle deposits of differing aerodynamic diameters (D_p) with cascade impactors then to chemically analyze the deposits. The size ranges of the particles collected is determined by the

impactor design. Impactor operation — the impaction media used, sample location and sampling times — affect the types of particles sampled and the efficiency of the particle collection. After collection PAH were separated from other extractable compounds by liquid or gas chromatography and quantified by uv fluorescence or mass spectrometry.

One objective of this thesis was to apply recent advances in aerosol sampling and analysis techniques to develop an improved method for measuring PAH and other organic compounds associated with size-segregated atmospheric aerosols. Particles were collected with a micro-orifice impactor (MOI) from sites in Boston and rural Massachusetts. The MOI has the advantages of relatively high flow rates (30 L/min), segregation of particles as small as $D_p = 0.08 \mu\text{m}$, and relatively high operating pressures ($P > 0.65 \text{ atm}$) [104]. Samples were prepared for analysis by high performance liquid chromatography (HPLC) and analyzed by gas chromatography/mass spectrometry (GC/MS). This analytic technique is able to quantify a wide variety of organic species; it is not limited to compounds like PAH which have excellent fluorescence properties. One half of the samples were analyzed for PAH and the other half were analyzed for OPAH.

This chapter describes only the collection and analysis of these samples. The results are presented in Chapter 3. The results of the PAH work have been published [103]; the results of the OPAH work have been submitted for publication [105].

2.2 Sample Collection

Urban and rural aerosol samples were collected from the roofs of National Ambient Air Quality Standards monitoring stations operated by the Massachusetts Department of Environmental Protection (DEP). At both sampling sites the air inlet was located 4 m above ground level. Urban samples were collected at the Kenmore Square sampling site which is located 1.5 km west of downtown Boston, MA, at 590 Commonwealth Avenue (42:20:54 N, 71:05:57 W). This site is on a traffic island in the center of a divided 6-lane street near a major intersection. A bus station is located 170 m away. Rural samples were collected at the Quabbin Summit site which is located on the 81,000 acre Quabbin Reservation in central Massachusetts (42:17:54 N, 72:20:05 W). The nearest urban center is Springfield, MA, located 30 km to the southwest. This site was chosen to sample rural air typical of that which enters the Boston airshed from the west.

A total of five 24 hour samples were collected at each sampling site on an alternate day schedule. Samples and field blanks were collected for 24 hours from midnight to midnight. The Kenmore Square samples were collected on five days between June 16 and 24, 1994. A total of 188 m³ of air were collected over 120 hours. The Quabbin Summit samples were collected on five days between July 19 and 31, 1994. A total of 189 m³ of air were collected over 119 hours. All samples were retrieved the morning following the sampling period and stored in a freezer at -20°C. Table 2.1 shows the average air temperature and pollutant levels during the sampling periods as measured by the Massachusetts DEP.

Table 2.1: Air Conditions during Sampling.

Location	Date	Temperature ^a (°C)	NO _x ^a (ppm)	O ₃ ^a (ppm)	PM10 ^b (μg/m ³)
Kenmore Square	16 Jun 94	23	0.071		33
	18 Jun 94	29	0.015		
	20 Jun 94	24	0.066		
	22 Jun 94	25	0.033		
	24 Jun 94	21	0.100		
Quabbin Summit	19 Jul 94	24	0.008	0.063	23
	21 Jul 94	26	0.007	0.059	
	25 Jul 94	25	0.005	0.062	
	29 Jul 94	22	0.005	0.045	
	31 Jul 94	23	0.006	0.036	

^aDaily average measured by Massachusetts DEP

^bMonthly average measured by Massachusetts DEP

The sampling train consisted of an inlet tube and cascade impactor followed by a regulating valve, rotameter and vacuum pump (see Figure 2-1). The sampler inlet was a straight 0.6 m polytetrafluoroethylene (PTFE) lined tube with an inside diameter of 0.95 cm. The cascade impactor used was a micro-orifice impactor (MOI) manufactured by MSP Corporation (Minneapolis, MN) [104]. The MOI collects size-segregated aerosols by impaction on nine stages. A 25 mm quartz after filter downstream of the impactor collected particles which were not collected on the impactor stages. A Gast Manufacturing Corporation (Benton Harbor, MI) model DAA-111-EB diaphragm pump was used. The entire sampling system was placed in a weather-proof enclosure. For the Kenmore Square sampling, the system was turned on and off manually; for the Quabbin Summit sampling, a 7-day timer controlled the system. An hour counter recorded the elapsed sample collection times.

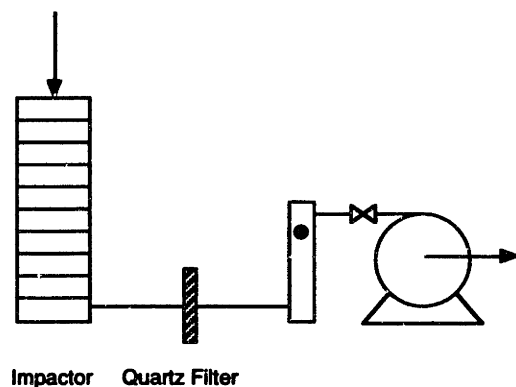


Figure 2-1: Schematic diagram of atmospheric aerosol sampling system.

The inlet tube and all parts of the MOI were carefully cleaned with DCM before placement in the field. The impactor was tested for clogged nozzles in the laboratory by monitoring the downstream pressure. Before each day's sampling, the system was checked for leaks in the field by sealing the inlet and monitoring the flow rate. The regulating valve was adjusted to a flow of 27 L/min at the inlet before each sample collection. Rotameter readings were recorded before and after each sample collection. The sample flow rate was determined to be the average of the beginning and ending flow rates.

The size of particles collected on the impaction plates is a function of the flow rate and operating pressures of the MOI. The diaphragm pump maintained an average sampling flow rate of 26.3 L/min at standard temperature and pressure — less than the design flow rate of 30 L/min. This reduction in air flow and pressure drops across the impactor stages changed the sizes of particles collected. The aerodynamic diameter for which 50% of particles are collected on an impaction stage (D_{p50}) depends

on the design and operation of the impaction jets as

$$D_{p50} = \sqrt{\frac{9\mu D St_{50}}{\rho_p C' U_0}} \quad (2.1)$$

where

μ air viscosity

D nozzle diameter

St_{50} Stokes number corresponding to D_{p50} (≈ 0.22 [106])

ρ_p density of particle

C' Cunningham slip correction

U_0 average velocity of jet exiting nozzle

Of these variables only U_0 depends on the volumetric flow rate (Q) and C' depends on the operating pressure (P). Pressure drops for a flow rate of 26.3 L/min were measured and actual D_{p50} values subsequently calculated as

$$D_{p50 \text{ actual}} = D_{p50 \text{ design}} \left(\frac{C'(P_{\text{design}}) Q_{\text{design}}}{C'(P_{\text{actual}}) Q_{\text{actual}}} \right)^{1/2} \quad (2.2)$$

Operating the MOI with a 26.3 L/min flow rate increased the cut-off diameters to approximately 1.07 times the design values. Table 2.2 lists D_{p50} for the design and actual flow rates. Changes in flow during and between sample collections would introduce variability in the size of particles collected on each impactor stage. The flow measured at the beginning and end of each run differed by less than 10%. This variation would cause a change of approximately 5% in the impactor stage cut-off

Table 2.2: Operating Characteristics of MOI.

Stage	Number of Orifices	Orifice Diameter (mm)	Cut-off Diameter (μm)	
			Design Flow	Actual Flow
0	1	10.	18.	19.2
1	10	3.80	5.62	6.00
2	10	2.47	3.16	3.38
3	20	1.37	1.78	1.90
4	40	0.72	1.00	1.07
5	80	0.4376	0.585	0.626
6	900	0.1361	0.320	0.343
7	2000	0.0594	0.131	0.141
8	2000	0.0514	0.080	0.087

sizes. Because the flow was not recorded during sampling and these sampling errors introduce only minor variations in D_{p50} , for the remainder of this work the air flow is taken to be constant.

A PTFE membrane with an underlay of aluminum foil was placed on each stage of the MOI to collect particles for analysis. The PTFE membranes used in this work were Millipore (Bedford, MA) Mitex, 10 μm pore size membranes. PTFE membranes were cleaned by sonication in DCM for 5 minutes. The aluminum was cleaned with DCM in a Soxhlet extractor for 24 hours. Each impaction medium was coated with approximately 0.1 mL of 20% dibutyl phthalate solution in cyclohexane to reduce particle bounce [107]. The after filters were Pallflex (Putnam, CT) Tissuquartz 2500 QAT-UP quartz fiber filters which were baked by the manufacturer. The filters were sonicated in DCM for 5 minutes. Impaction and filter media blanks were prepared in the same manner as the sampling media.

2.3 Sample Analysis

The sample analysis steps can be summarized as

1. Extract analytes from collection media by sonication in dichloromethane.
2. Separate analyte fraction by high performance liquid chromatography (HPLC).
3. Inject concentrated analyte solution in gas chromatograph/mass spectrometer (GC/MS).
4. Quantify analytes by comparing MS response to that of deuterated PAH internal standards.

One half of the samples were extracted and analyzed for PAH in the summer and fall of 1994. The second half of the samples were analyzed for OPAH in the spring of 1996.

2.3.1 Materials

All glassware was cleaned in detergent, rinsed with deionized water, methanol, and then dichloromethane (DCM). For the PAH sample analysis, newly purchased glassware was only rinsed with DCM. Only ground glass stoppers and PTFE lined screw tops were used. The solvents used were glass distilled OmniSolv DCM, 99.99% purity, and HPLC grade Aldrich cyclohexane, 99.9% purity. Aldrich dibutyl phthalate (DBP), 99+% purity, was used. The analyte reference standards are discussed below.

2.3.2 Sample Extraction and Storage

Samples from the impactor stages and the after filter were split in half; then the halves from each of the five collection days were composited for analysis. Prior to extraction, the composited sampling media were spiked with 10 μL of a 4 $\mu\text{g}/\text{mL}$ solution of deuterated PAH (dPAH) internal standards. The dPAH were naphthalene- d_8 , acenaphthene- d_{10} , phenanthrene- d_{10} , pyrene- d_{10} , chrysene- d_{12} , perylene- d_{12} , dibenz[*a,h*]anthracene- d_{14} and coronene- d_{12} . The impaction media were then covered with approximately 15 mL of DCM and sonicated for 30 min. The particle/liquid suspension and additional DCM used to rinse the jar were then filtered by syringe using a 0.2 μm PTFE filter. The filter was discarded and the filtrate evaporated under N_2 to a volume of approximately 1 mL.

It is generally accepted that isotopically labeled isomeric standards experience losses similar to the analyte throughout a work-up procedure. However, the internal standards were added to the sampling medium prior to extraction and they may have been extracted with a higher efficiency than compounds in the complex environmental matrix. A comparison of extraction efficiencies was not performed in this work due to the small sample size. Using urban air particulate matter, Burford and coworkers found extraction efficiencies of at least 80% for native PAH and 100% for spiked dPAH using 30 minute sonication in DCM [108]. To test the efficacy of the extraction protocol, the Kenmore Square impactor stage 7 sample was extracted twice. For all quantified PAH, the second extraction contained less than 3% of the amount initially recovered. Based on these results, we assume that the extraction efficiencies of the

native analytes and spiked internal standards were identical in this study.

For PAH analyses, samples from each site were processed in three batches with a method blank in each batch. One batch consisted of the odd stages; another the even stages plus the field blank. The zeroth stage and after filter samples were processed together; method blanks for both types of sampling media were analyzed with these samples. Samples were stored in a freezer and analyzed within 90 days of collection. The time between final preparation and completion of the GC/MS injections was less than two weeks.

In that time, however, there was a noticeable decrease in the amount of naphthalene and naphthalene- d_8 in some samples. This was probably due to evaporation through the pierced septum of the sample vial. Some samples were reanalyzed after 60 days of further storage. Unlike the original samples, the aged samples did not have quantifiable amounts of PAH with molecular weights from 128 to 166. Therefore, naphthalene, acenaphthylene, acenaphthene, and fluorene could not be accurately quantified by this method. The amounts of other PAH in the aged samples were within the range of experimental results from the original GC/MS runs.

Samples from the urban site were analyzed for OPAH in two batches with a method blank in each batch. One batch consisted of the odd stages; the other the even stages plus the field blank. Samples were stored in a freezer on the original sampling media for 14 months. The samples were extracted and stored for an additional 6 months in solution with DBP. The initial GC/MS runs of all the samples were made within 2 weeks of final preparation by HPLC. Final GC/MS runs were made after the samples had been stored for an additional 4 months. As with the higher molecular weight

PAH ($M > 166$), the concentrations of all OPAH measured by GC/MS after storage were comparable with the concentrations measured before storage.

2.3.3 Sample Preparation by HPLC

Analyte fractions of the samples were separated from other pollutants and dibutyl phthalate by high performance liquid chromatography (HPLC). The HPLC system was a Beckman System Gold equipped with a Programmable Solvent Module 126 and a Programmable Detector Module 166 controlled by System Gold software running on a personal computer. The separation was accomplished by two Jordi-Gel poly(divinylbenzene) columns in series. The columns were 500 mm long, 10 mm inside diameter, packed with 5 μm particle size, 500 Å pore size divinylbenzene polymer. They were purchased from Jordi Associates (Billingham, MA). The PAH separation was performed isocratically with 1.0 mL/min flow of DCM at a pressure of approximately 700 psi. For the OPAH separation, a flow rate of 0.8 mL/min was used. The separation of phthalates and PAH using this type of column has been previously reported [109].

The uv detector used was unable to detect the amounts of PAH and OPAH present in the samples, on the order of 10 ng. The collection times for the analyte fractions were therefore determined by injecting concentrated solutions of DBP and PAH or OPAH. Figure 2-2 is a chromatogram which shows a typical separation of a concentrated solution of PAH from DBP. Table 2.3 lists the elution volumes of the tested compounds. Note that the HPLC columns used for the PAH and OPAH separations

Table 2.3: HPLC Retention Volumes for PAH and OPAH.

Standard	Retention Volume (mL)
HPLC columns used for PAH separation	
dibutyl phthalate	49.8
naphthalene	58.7
pyrene	59.0
coronene	68.0
HPLC columns used for OPAH separation	
dibutyl phthalate	53.6
5,12-naphthacenequinone	59.7
benzanthrone	62.4
7 <i>H</i> -dibenz[<i>d,ej</i>]anthracen-7-one	64.3

were of the same design, but not identical. The elution volumes shown on Figure 2-2 and Table 2.3 are different because the figure shows HPLC separation of PAH using the columns which were used for OPAH separation. The elution times were somewhat variable; for example, the inception of the DBP peak in the samples varied by up to 1 minute and the peak lasted for up to 4 minutes. The HPLC operating procedures were designed to collect the analytes at least 2 minutes after the end of the DBP peak. For PAH the HPLC effluent volume from 57.0 to 77.0 mL was collected. For OPAH the HPLC effluent volume from 57.6 to 77.6 mL was collected.

2.3.4 Reference Standards

Species in the samples were identified by comparing GC retention indices and monitored ion mass to charge ratios to those of reference standards. The GC retention times and mass spectra of reference standards were determined by preparing solutions with dPAH and injecting these identification solutions into the GC/MS. The same

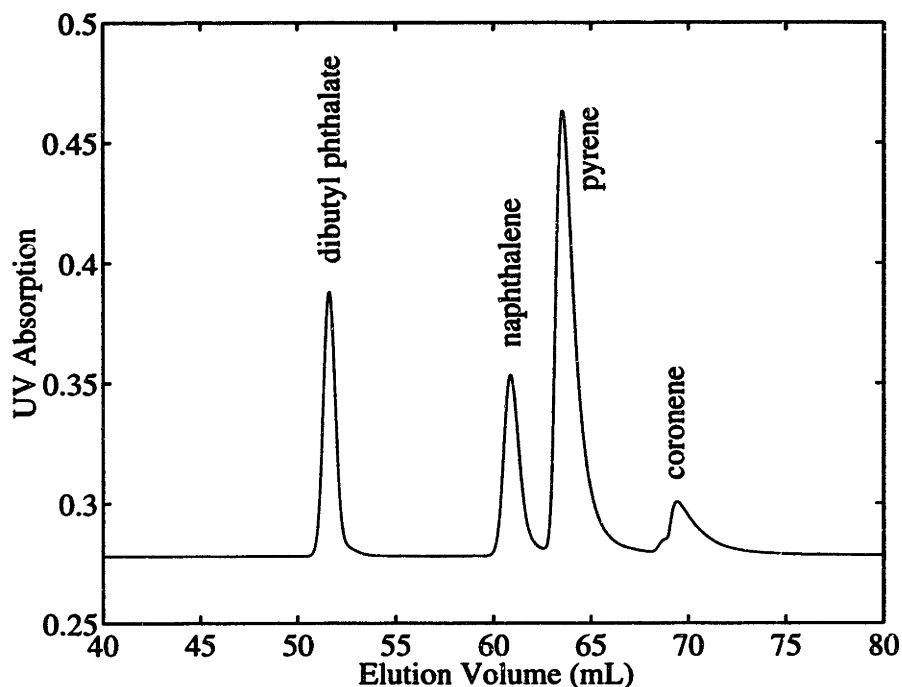


Figure 2-2: Separation of some PAH from dibutyl phthalate by HPLC.

GC temperature program was used for the identification standards and samples. Tables 2.4 and 2.5 summarize results of the reference standard work. The reference standards were purchased from AccuStandard (New Haven, CT), Aldrich (Milwaukee, WI), Cambridge Isotope Labs (CIL) (Andover, MA), Chem Service (West Chester, PA), Chemicals Procurement Laboratories (CPL) (College Point, NY), Chemsyn Science Laboratories (Lenexa, KS), Columbia Organic Chemicals (COC) (formerly of Columbia, SC), European Community Bureau of Reference (ECBR) (Brussels, Belgium), Midwest Research Institute (MRI) (Kansas City, MO), MSD Isotopes (Montreal, Canada), and PAH Research Institute (PAHRI) (Greifenberg, Germany).

Retention indices were calculated so that GC elution times from different samples could be compared. These retention indices are analogous to those published by Lee et al. [110]. Lee et al. assigned retention indices of 200, 300, 400 and 500 to naph-

thalene, phenanthrene, chrysene, and picene, respectively. Other PAH were assigned retention indices by linear interpolation of retention times. We assigned retention indices compatible with those of Lee et al. by linear interpolation of retention times relative to dPAH internal standards. Naphthalene- d_8 , phenanthrene- d_{10} , chrysene- d_{12} , dibenz[*a,h*]anthracene- d_{14} , and coronene- d_{12} were assigned retention indices of 199.49, 299.34, 399.15, 494.24 and 549.71, respectively. Tables 2.4 and 2.5 list the retention times and retention indices of the PAH and OPAH reference standards. The small differences between our retention indices and those obtained by Lee et al. may be due to differences in the injector port temperature and column material used.

The retention indices in this work were very repeatable. The standard deviations of retention indices for PAH in 16 sample injections were less than 0.2 for all PAH except fluoranthene and pyrene. The retention index standard deviations for fluoranthene and pyrene were 1.8 and 0.8, respectively. This greater variability may be due to the elution of residual dibutyl phthalate a short time before fluoranthene. Fluoranthene and pyrene were readily identified because pyrene- d_{10} eluted between them and there were no interfering peaks with a mass to charge ratio of 202. Note that the retention times listed in Tables 2.4 and 2.5 may be for samples injected at different times and are not directly comparable. This is because whenever GC separation performance deteriorated approximately 10 cm were removed from the top of the column, causing slightly shorter retention times for samples injected at later times.

Analytes with retention indices differing by 1 unit have completely separated peaks and can be separately quantified by this method. Isomers which did not com-

Reference Standard	Supplier	Primary Ion	Secondary Ion	Ion Ratio	Retention Time (min)	Retention Index	
						Experimental	Literature
naphthalene- <i>d</i> ₈	AccuStandard	136	137	0.115	12.23	199.49	
naphthalene	AccuStandard	128	129	0.112	12.27	200.06	200.00
acenaphthylene	AccuStandard	152	153	0.133	18.17	248.43	244.63
acenaphthene- <i>d</i> ₁₀	AccuStandard	164	165	0.131	18.79	253.37	
acenaphthene	AccuStandard	154	155	0.124	18.90	254.43	251.29
fluorene	AccuStandard	166	167	0.145	20.85	270.39	268.17
phenanthrene- <i>d</i> ₁₀	AccuStandard	188	189	0.157	24.39	299.34	
phenanthrene	AccuStandard	178	179	0.154	24.47	300.12	300.00
anthracene	AccuStandard	178	179	0.157	24.61	301.78	301.69
fluoranthene	AccuStandard	202	203	0.177	29.34	344.76	344.01
pyrene- <i>d</i> ₁₀	MSD Isotopes	212	213	0.176	29.96	351.87	
pyrene	AccuStandard	202	203	0.176	30.02	352.56	351.22
benzo[<i>ghi</i>]fluoranthene	ECBR	226	227	0.189	33.80	390.86	389.60
benzo[<i>c</i>]phenanthrene	Aldrich	228	229	0.153	33.69	391.23	391.39
cyclopenta[<i>cd</i>]pyrene	Chemsyn	226	227		34.37	397.88	396.54
benz[<i>a</i>]anthracene	AccuStandard	228	229	0.196	34.58	398.66	398.50
chrysene- <i>d</i> ₁₂	AccuStandard	240	241	0.206	34.70	399.15	
triphenylene	Aldrich	228	229	0.158	34.58	400.05	400.00
chrysene	AccuStandard	228	229	0.194	34.78	400.17	400.00
naphthacene	Aldrich	228	229	0.159	34.95	404.08	408.30
benzo[<i>b</i>]fluoranthene	AccuStandard	252	253	0.218	38.48	443.20	441.74
benzo[<i>j</i>]fluoranthene	AccuStandard	252	253	0.215	38.39	443.70	440.92
benzo[<i>k</i>]fluoranthene	AccuStandard	252	253	0.224	38.55	444.11	442.56
benzo[<i>e</i>]pyrene	Aldrich	252	253	0.219	39.35	453.13	450.73
benzo[<i>a</i>]pyrene	AccuStandard	252	253	0.224	39.50	454.84	453.44

Table 2.4: PAH Reference Standards.

Reference Standard	Supplier	Primary Ion	Secondary Ion	Ion Ratio	Retention Time (min)	Retention Index Experimental	Retention Index Literature
perylene- <i>d</i> ₁₂	AccuStandard	364	265	0.224	39.70	456.97	
perylene	Aldrich	252	253	0.225	39.78	457.92	456.22
indeno[1,2,3- <i>cd</i>]fluoranthene	ECBR	276	277	0.236	42.08	485.35	
dibenz[<i>a,j</i>]anthracene	MRI	278	279		42.60	491.36	481.87
indeno[1,2,3- <i>cd</i>]pyrene	AccuStandard	276	277	0.249	42.92	493.78	
dibenz[<i>a,h</i>]anthracene- <i>d</i> ₁₄	CIL	292	293	0.228	42.96	494.24	
dibenz[<i>a,c</i>]anthracene	Chem Service	278	279	0.232	42.95	495.10	495.01
dibenz[<i>a,h</i>]anthracene	AccuStandard	278	279	0.240	43.04	495.27	495.45
benzo[<i>b</i>]chrysene	COC	278	279	0.236	43.22	498.26	497.66
picene	CPL	278	279	0.223	43.29	499.39	500.00
benzo[<i>ghi</i>]perylene	AccuStandard	276	277	0.237	43.58	501.32	501.32
anthanthrene	ECBR	278	279	0.238	43.82	505.56	
naphtho[1,2- <i>k</i>]fluoranthene	PAHRI	302	303	0.253	46.51	537.20	
naphtho[2,3- <i>b</i>]fluoranthene	PAHRI	302	303	0.180	46.69	538.95	
dibenzo[<i>a,l</i>]pyrene	ECBR	302	303	0.253	46.74	539.35	
dibenzo[<i>b,k</i>]fluoranthene	PAHRI	302	303	0.183	46.72	539.41	
naphtho[2,3- <i>k</i>]fluoranthene	PAHRI	302	303	0.245	47.12	543.62	
coronene- <i>d</i> ₁₂	CIL	312	313	0.235	47.81	549.71	
coronene	Aldrich	300	301	0.270	47.88	550.44	
dibenzo[<i>a,e</i>]pyrene	COC	302	303		47.80	551.77	
dibenzo[<i>e,l</i>]pyrene	PAHRI	302	303	0.241	47.84	552.84	
naphtho[2,3- <i>a</i>]pyrene	Aldrich	302	303	0.251	48.11	555.10	
dibenzo[<i>a,i</i>]pyrene	ECBR	302	303	0.211	48.22	556.78	
dibenzo[<i>cd,l</i>]pyrene	Chem Service	302	303	0.251	48.26	556.78	
dibenzo[<i>a,h</i>]pyrene	ECBR	302	303	0.257	48.50	560.00	

Table 2.4: PAH Reference Standards (continued).

pletely separate were quantified together. For example, benzo[*b*]fluoranthene and benzo[*k*]fluoranthene are quantified together as benzofluoranthenes.

Characteristic mass spectra of PAH contain prominent peaks for the molecular ion (M^+) and doubly charged molecular ion (M^{2+}) because PAH do not readily fragment under electron impactation [111]. Additional peaks at nearby mass to charge ratios appear as a result of proton loss or naturally occurring isotopes. For PAH we chose the molecular ion as the primary ion and $(M+1)^+$ as the confirming ion. The $(M+1)^+$ to M^+ ion ratios closely matched the expected ratio of molecular masses due to the presence of ^{13}C . Assuming that the number of molecules with two or more ^{13}C is negligible, this ratio can be calculated as

$$\frac{(M+1)^+}{M^+} = \frac{(p-1)^{n-1} p \frac{n!}{(n-1)!}}{1 - (p-1)^{n-1} p \frac{n!}{(n-1)!}} \quad (2.3)$$

where p is the probability that a C atom is ^{13}C ($p = 0.011$), and n is the number of C atoms. Table 2.4 shows the experimentally measured $(M+1)^+ : M^+$ ratio which was generally within a few percent of the calculated value.

Unlike PAH, OPAH do readily fragment upon electron impactation. Prominent fragmentation ions are $(M-\text{CO})^+$ for ketones, $(M-\text{CO})^+$ and $(M-2\text{CO})^+$ for diones, and $(M-\text{CO}_2)^+$ and $(M-\text{CO}_2-\text{CO})^+$ for dicarboxylic acid anhydrides. Table 2.5 shows the experimentally measured ratios of these characteristic secondary ions to the molecular ions for the OPAH reference standards.

Reference Standard	Supplier	Primary Ion	Secondary Ion	Ion Ratio	Retention Time (min)	Retention Index
1-acenaphthenone	Chemsyn	168.06	140.06	0.997	21.99	282.03
1,2-naphthoquinone	Aldrich	130.04	102.05	0.766	21.14	275.04
1,4-naphthoquinone	Aldrich	158.04	130.04	0.385	17.32	243.59
9-fluorene	Aldrich	180.06	102.05	0.549		
1,2-naphthalic anhydride	Chemsyn	198.03	152.06	0.435	23.41	293.72
			154.04	1.045	25.17	309.88
acenaphthenequinone	Aldrich	182.04	126.05	1.918		
			154.04	2.012	25.75	315.56
2,3-naphthalic anhydride	Chemsyn	198.03	126.05	2.075		
			154.04	1.257	26.63	324.17
anthraquinone	Aldrich	208.05	126.05	2.502		
			180.06	0.931	27.36	331.32
			152.06	0.762		
1,8-naphthalic anhydride	Aldrich	198.03	154.04	1.863	28.28	341.61
			126.05	1.734		
phenanthrenequinone	Aldrich	180.06	208.05	0.130	30.55	362.54
			152.06	0.370		
11 <i>H</i> -benzo[<i>a</i>]fluoren-11-one	PAHRI	230.07	202.08	0.218	32.94	385.93
7 <i>H</i> -benzo[<i>c</i>]fluoren-7-one	PAHRI	230.07	202.08	0.637	33.35	389.94
11 <i>H</i> -benzo[<i>b</i>]fluoren-11-one	PAHRI	230.07	202.08	0.224	33.77	394.05
benzanthrone	Aldrich	230.07	202.08	0.597	34.83	405.29
aceanthrenequinone	Aldrich	232.05	204.06	2.126	35.42	412.02
			176.06	1.998		

Table 2.5: Oxygenated PAH Reference Standards.

Reference Standard	Supplier	Primary Ion	Secondary Ion	Ion Ratio	Retention Time (min)	Retention Index
benz[<i>a</i>]anthracene-7,12-dione	Aldrich	258.07	230.07	0.372	36.06	419.32
1,4-chrysenquinone	Aldrich	258.07	202.08	0.610	36.86	428.44
5,12-naphthacenequinone	Aldrich	258.07	202.08	0.453	37.05	430.60
6H-benzo[<i>cd</i>]pyrene-6-one	PAHRI	254.07	226.08	0.333	39.16	454.66
benzo[<i>k</i>]fluoranthene-7,12-dione	MRI	282.07	254.07	0.666	40.17	466.18
dibenzofluorenone-a	PAHRI	280.09	226.08	0.663	40.75	472.79
13 <i>H</i> -dibenzo[<i>a,i</i>]fluoren-13-one	PAHRI	280.09	252.10	0.131	41.14	477.24
dibenzofluorenone-b	PAHRI	280.09	252.10	0.282	42.09	488.07
7 <i>H</i> -dibenzo[<i>c,g</i>]fluoren-7-one	PAHRI	280.09	252.10	0.445	42.49	492.63
dibenzofluorenone-c	PAHRI	280.09	252.10	0.177	42.82	496.47
7 <i>H</i> -dibenz[<i>d,e</i>]anthracen-7-one	PAHRI	280.09	252.10	0.187	42.88	497.17
benzo[<i>a</i>]pyrene-6,12-dione	MRI	282.07	254.07	0.975	42.95	498.00
dibenzofluorenone-d	PAHRI	280.09	226.08	0.436	43.16	500.48
benzo[<i>a</i>]pyrene-1,6-dione	MRI	282.07	254.07	0.411	43.70	506.85
benzo[<i>a</i>]pyrene-3,6-dione	MRI	282.07	226.08	0.377	43.85	508.62
benzo[<i>a</i>]pyrene-4,5-dione	MRI	282.07	226.08	0.471	44.21	512.86
benzo[<i>e</i>]pyrene-4,5-dione	MRI	282.07	226.08	0.724	44.32	514.16
			254.07	3.091		
			226.08	0.739		

Table 2.5: Oxygenated PAH Reference Standards (continued).

2.3.5 GC/MS Operation

Analytes were identified and quantified on a Hewlett Packard GC/MS system consisting of an HP Model 5890 Series II Plus gas chromatograph (GC) and an HP model 5972 mass selective detector (MSD). The MSD operated in electron impact mode with electron energies of 70 eV. The GC column was a 30 m HP-5 0.25 mm i.d. capillary column coated with 0.25 μm film thickness 5% cross-linked phenyl methyl siloxane stationary phase. The GC temperature was held at 50°C for 1.5 minutes then ramped to 310°C at 6°C/min. The final temperature was held for 10 minutes. The injector port temperature was maintained at 280°C. The GC/MS was controlled and data collected by HP ChemStation software running on a personal computer.

The MSD was run in selected ion monitoring (SIM) mode. The SIM programs were designed to monitor primary and secondary ions of a group of analytes which elute at times near one of the dPAH internal standards. For PAH the primary ion was the molecular ion (M^+) and the qualifying ion was the ^{13}C isotope ion $[(M+1)^+]$. For OPAH the primary ion was generally the molecular ion; the qualifying ions were $(M-\text{CO})^+$ for ketones, $(M-\text{CO})^+$ and $(M-2\text{CO})^+$ for diones, and $(M-\text{CO}_2)^+$ and $(M-\text{CO}_2-\text{CO})^+$ for dicarboxylic acid anhydrides. Tables 2.6 and 2.7 show the SIM programs and analytes detected in each time window. The MSD dwell time for each mass was between 20 and 50 ms to maximize the dwell time while maintaining a scan rate of 200 scans per minute. This scan rate allowed collection of at least 20 data points for typical peaks. At least ten data points were collected for peaks at the lower limit of detection.

The PAH SIM program monitored integral mass to charge ratios. As discussed below, this led to PAH:dPAH response ratios different from the expected value of approximately 1.0. The SIM program for OPAH was developed later and monitored mass to charge ratios with masses of the OPAH ions, to the nearest 0.05 mass units.

The MSD was tuned at the start of a series of runs using the HP ChemStation AutoTune routine with perfluorotributylamine. Additionally, the HP ChemStation QuickTune routine was run at the start of each day. A midrange calibration standard containing 3 or 10 ng/ μ L of the dPAH was also run at the start of each day of PAH analysis to confirm system performance.

Before each sample injection, DCM blanks were run until the monitored ion signals were reduced to background levels. The GC temperature program for blank runs was accelerated to save instrument time. The temperature was 50°C held for 1.5 min, then ramped to 310°C at a rate of 30°C/min, and held at 310°C for 10 minutes. The SIM program times were adjusted for the faster temperature program used for the blank injections.

At least three duplicate GC/MS injections were made for each sample. For the first GC/MS analysis of a sample, the HPLC column effluent was evaporated under N₂ at room temperature to a volume of approximately 5 μ L. One μ L of the sample solution was injected to the GC/MS. For subsequent injections 5 μ L of DCM was added to the samples because they evaporated to dryness when stored for 24 hours.

Table 2.6: PAH Selected Ion Monitoring Program.

Time after Injection (min)	Eluting Compounds		Monitored Ions	
	Internal Standard	PAH		
8.0–15.2	naphthalene- <i>d</i> ₈	naphthalene	128	129
			136	137
15.2–22.6	acenaphthylene- <i>d</i> ₁₀	acenaphthene	152	153
		acenaphthene	154	155
		fluorene	164	165
			166	167
22.6–26.8	phenanthrene- <i>d</i> ₁₀	phenanthrene	178	179
		anthracene	188	189
26.8–32.2	pyrene- <i>d</i> ₁₀	fluoranthene	202	203
		pyrene	212	213
32.2–36.6	chrysene- <i>d</i> ₁₂	benzo[<i>ghi</i>]fluoranthene	226	
		benzo[<i>c</i>]phenanthrene	227	
		cyclopenta[<i>cd</i>]pyrene	228	
		benz[<i>a</i>]anthracene	229	
		chrysene	240	
		triphenylene	241	
		naphthacene		
36.6–40.8	perylene- <i>d</i> ₁₂	benzo[<i>b</i>]fluoranthene	252	
		benzo[<i>k</i>]fluoranthene	253	
		benzo[<i>j</i>]fluoranthene	264	
		benzo[<i>e</i>]pyrene	265	
		benzo[<i>a</i>]pyrene		
		perylene		
40.8–45.5	dibenz[<i>a,h</i>]anthracene- <i>d</i> ₁₄	indeno[1,2,3- <i>cd</i>]fluoranthene	276	
		indeno[1,2,3- <i>cd</i>]pyrene	277	
		dibenz[<i>a,j</i>]anthracene	278	
		dibenz[<i>a,c</i>]anthracene	279	
		dibenz[<i>a,h</i>]anthracene	292	
		benzo[<i>b</i>]chrysene	293	
		picene		
		benzo[<i>ghi</i>]perylene		
		anthanthrene		
45.5 ^a –55.0	coronene- <i>d</i> ₁₂	naphtho[1,2- <i>k</i>]fluoranthene	300	
		naphtho[2,3- <i>b</i>]fluoranthene	301	
		naphtho[2,3- <i>k</i>]fluoranthene	302	
		dibenzo[<i>b,k</i>]fluoranthene	303	
		naphtho[2,3- <i>a</i>]pyrene	312	
		dibenzo[<i>a,l</i>]pyrene	313	
		dibenzo[<i>a,e</i>]pyrene		
		dibenzo[<i>e,l</i>]pyrene		
		dibenzo[<i>a,i</i>]pyrene		
		dibenzo[<i>a,h</i>]pyrene		
		coronene		

^aChanged to 44.5 for Quabbin Summit samples.

Table 2.7: OPAH Selected Ion Monitoring Program.

Time after Injection (min)	Internal Standard	Eluting Compounds OPAH	Monitored Ions
15.2–22.8	phenanthrene- <i>d</i> ₁₀	1,4-naphthoquinone	162.05
		1,2-naphthoquinone	130.05
		1-acenaphthenone	140.05
			158.05
			164.10
			168.06
22.8–27.0	phenanthrene- <i>d</i> ₁₀	9-fluorenone	126.05
		1,2-naphthalic anhydride	152.05
		acenaphthenequinone	154.05
		2,3-naphthalic anhydride	180.05
			182.05
			188.15
	198.05		
27.0–31.8	pyrene- <i>d</i> ₁₀	anthraquinone	126.05
		1,8-naphthalic anhydride	152.05
		phenanthrenequinone	154.05
			180.05
			198.05
			208.05
	212.15		
31.8–35.8	chrysene- <i>d</i> ₁₂	11 <i>H</i> -benzo[<i>a</i>]fluoren-11-one	176.05
		7 <i>H</i> -benzo[<i>c</i>]fluoren-7-one	202.05
		11 <i>H</i> -benzo[<i>b</i>]fluoren-11-one	204.05
		benzanthrone	226.05
		aceanthrenequinone	230.05
			240.15
			248.05
			254.05
			258.05
			264.15
35.8–40.0	perylene- <i>d</i> ₁₂	benz[<i>a</i>]anthracene-7,12-dione	176.05
		1,4-chrysenequinone	202.05
		5,12-naphthacenequinone	204.05
		6 <i>H</i> -benzo[<i>cd</i>]pyrene-6-one	226.05
			230.05
			248.05
			254.05
			258.05
	264.15		
40.0–47.0	dibenz[<i>a,h</i>]anthracene- <i>d</i> ₁₄	benzo[<i>k</i>]fluoranthene-7,12-dione	200.05
		13 <i>H</i> -dibenzo[<i>a,i</i>]fluoren-13-one	226.05
		7 <i>H</i> -dibenzo[<i>c,g</i>]fluoren-7-one	228.05
		7 <i>H</i> -dibenz[<i>de,j</i>]anthracen-7-one	252.10
		benzo[<i>a</i>]pyrene-6,12-dione	254.05
		benzo[<i>a</i>]pyrene-1,6-dione	272.05
		benzo[<i>a</i>]pyrene-3,6-dione	280.10
		benzo[<i>a</i>]pyrene-4,5-dione	282.05
		benzo[<i>e</i>]pyrene-4,5-dione	292.20

2.3.6 Species Identification and Quantification

An analyte was deemed identified if the confirming ion ratio(s) and retention time matched a reference standard. These species were quantified if, in addition to being identified, the signal to noise ratio was greater than 20 (response > 10,000 in arbitrary units). This analytical technique cannot distinguish between isomers which coelute. This is a particular problem for PAH of molecular weight 302 because of the large number of isomers. In cases where a number of PAH isomers have similar elution times, e.g. benzo[*b*]fluoranthene and benzo[*k*]fluoranthene, the isomers were quantified together. All the OPAH isomers were well separated, with retention indices for isomers differing by at least 1 unit.

Figure 2-3 is a representative chromatogram showing the abundance of all the monitored ions using the PAH SIM program for the Kenmore Square impactor stage 7 sample. All of the prominent peaks are identifiable as either PAH or dPAH. Table 2.8 shows retention indices and attributed PAH for the peaks for this sample. This sample is used as an example because it had the largest number of distinct peaks. PAH were assigned to peaks as discussed above. Retention times were deemed to match if the retention indices were within ± 0.2 units. Peaks which may be PAH but which match none of the available reference standards are designated "PAH-xy", where "x" is the molecular weight and "y" is a letter designation to distinguish isomers.

Figure 2-4 is a representative chromatogram showing the abundance of all the monitored ions using the OPAH SIM program for the Kenmore Square impactor

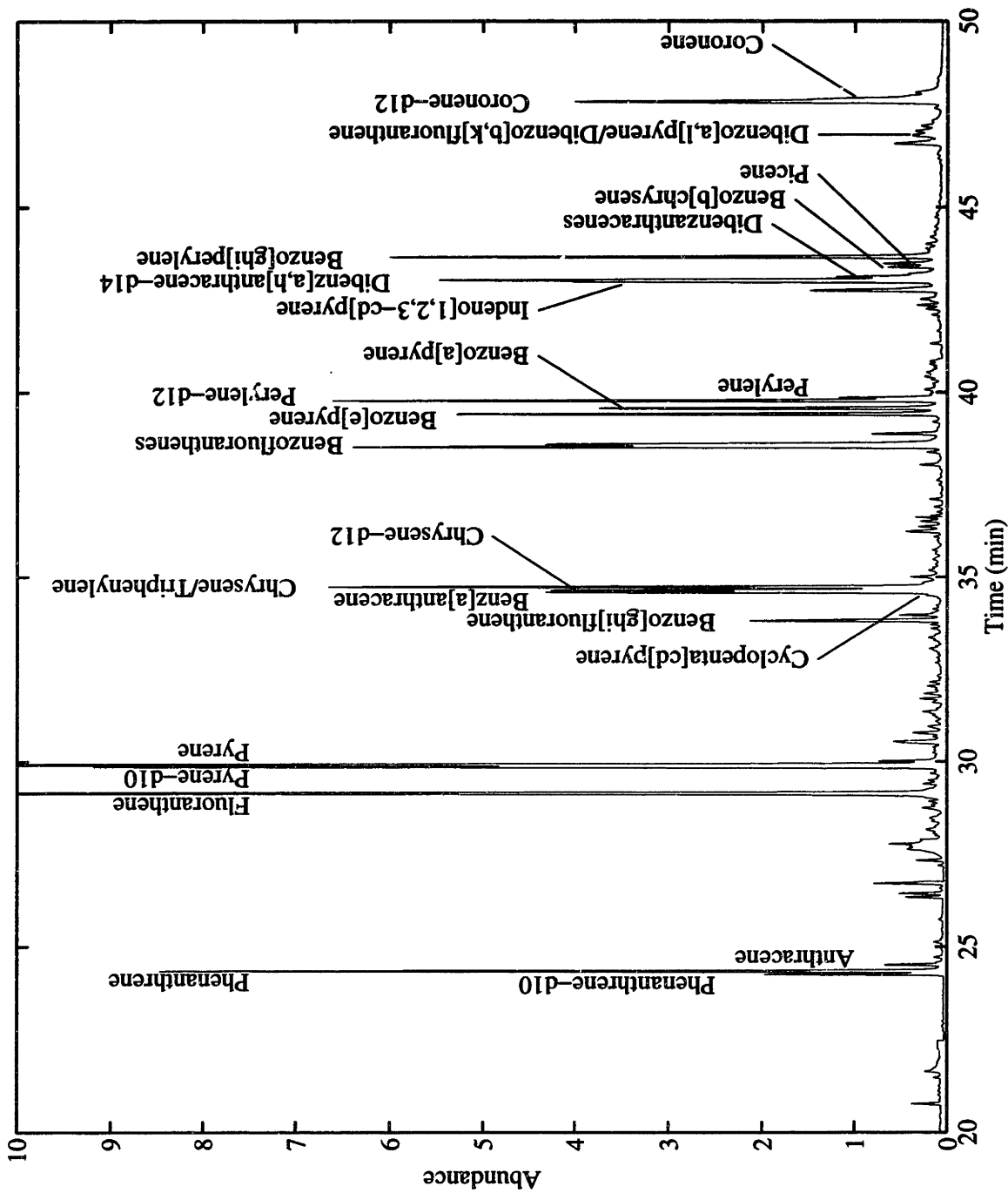


Figure 2-3: Total ion chromatogram using PAH SIM program for Kenmore Square stage 7 sample.

Table 2.8: Sample Peak Attribution for Kenmore Square Stage 7.

PAH	Retention Time (min)	Retention Index
naphthalene- <i>d</i> ₈	12.21	199.42
naphthalene	12.28	200.00
acenaphthylene	18.17	248.29
acenaphthene- <i>d</i> ₁₀	18.78	253.45
acenaphthene	18.89	254.36
fluorene	20.84	270.39
phenanthrene- <i>d</i> ₁₀	24.36	299.34
phenanthrene	24.44	300.00
anthracene	24.61	301.66
fluoranthene	29.15	345.91
pyrene- <i>d</i> ₁₀	29.84	352.63
pyrene	29.90	353.22
benzo[<i>ghi</i>]fluoranthene	33.77	390.94
cyclopenta[<i>cd</i>]pyrene	34.47	397.81
benz[<i>a</i>]anthracene	34.55	398.58
chrysene- <i>d</i> ₁₂	34.61	399.12
PAH-228a	34.68	399.94
chrysene	34.70	400.00
benzofluoranthenes	38.47	443.06
PAH-252a	38.81	446.95
benzo[<i>e</i>]pyrene	39.34	453.00
benzo[<i>a</i>]pyrene	39.49	454.72
perylene- <i>d</i> ₁₂	39.69	457.00
perylene	39.77	457.91
PAH-278a	41.22	474.45
PAH-278b	42.01	483.48
PAH-278c	42.26	486.33
PAH-278d	42.43	448.27
PAH-276a	42.67	491.02
indeno[1,2,3- <i>cd</i>]pyrene	42.91	493.78
dibenz[<i>a,h</i>]anthracene- <i>d</i> ₁₄	42.95	494.21
dibenzanthracenes	43.04	495.27
benzo[<i>b</i>]chrysene	43.30	498.23
picene	43.39	499.26
benzo[<i>ghi</i>]perylene	43.57	501.32
PAH-302a	46.66	536.76
dibenzo[<i>a,l</i>]pyrene/ dibenz[<i>b,k</i>]fluoranthene	46.88	539.28
PAH-302c	46.99	540.54
PAH-302d	47.62	547.76
coronene- <i>d</i> ₁₂	47.79	549.52
coronene	47.87	550.44
PAH-302e	48.04	552.58

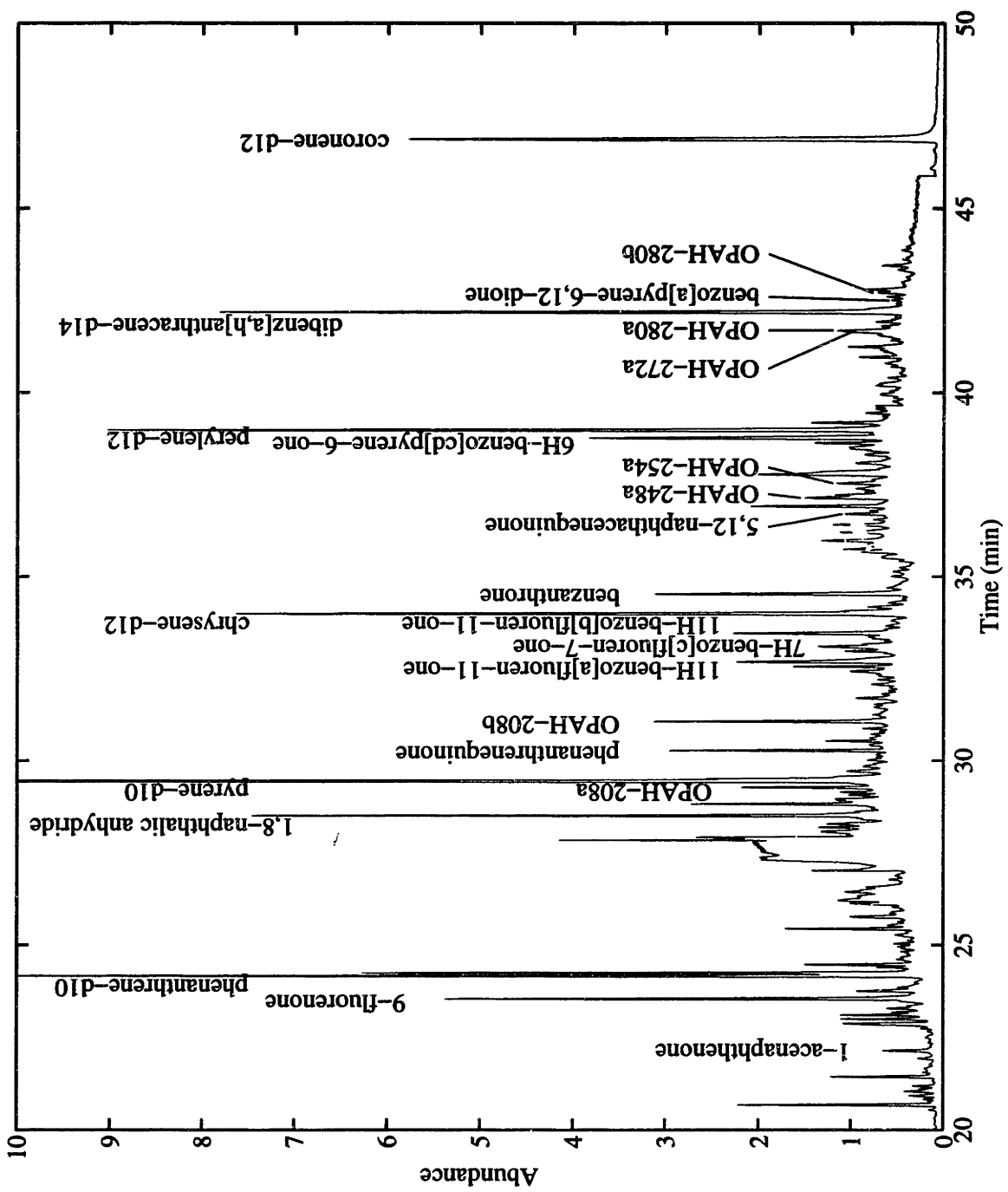


Figure 2-4: Total ion chromatogram using OPAH SIM program for Kenmore Square stage 7 sample.

Table 2.9: PAH Response Factors Relative to Deuterated PAH

PAH	Internal Standard	Response Factor	
		Slope	Intercept
naphthalene	naphthalene- <i>d</i> ₈	1.065	0.187
acenaphthylene	acenaphthene- <i>d</i> ₁₀	1.121	0.504
acenaphthene	acenaphthene- <i>d</i> ₁₀	1.094	0.317
fluorene	acenaphthene- <i>d</i> ₁₀	1.173	0.361
phenanthrene	phenanthrene- <i>d</i> ₁₀	1.066	0.308
anthracene	phenanthrene- <i>d</i> ₁₀	1.156	0.242
fluoranthene	pyrene- <i>d</i> ₁₀	1.075	0.092
pyrene	pyrene- <i>d</i> ₁₀	0.995	0.208
benzo[<i>ghi</i>]fluoranthene	chrysene- <i>d</i> ₁₂	1.123	0.320
benz[<i>a</i>]anthracene	chrysene- <i>d</i> ₁₂	1.097	0.253
chrysene	chrysene- <i>d</i> ₁₂	1.030	0.371
benzofluoranthenes	perylene- <i>d</i> ₁₂	1.150	0.240
benzo[<i>e</i>]pyrene	perylene- <i>d</i> ₁₂	1.132	0.243
benzo[<i>a</i>]pyrene	perylene- <i>d</i> ₁₂	1.169	0.241
perylene	perylene- <i>d</i> ₁₂	1.006	0.362
indeno[1,2,3- <i>cd</i>]pyrene	dibenz[<i>a,h</i>]anthracene- <i>d</i> ₁₄	1.067	0.324
dibenz[<i>a,h</i>]anthracene	dibenz[<i>a,h</i>]anthracene- <i>d</i> ₁₄	1.003	0.424
benzo[<i>ghi</i>]perylene	dibenz[<i>a,h</i>]anthracene- <i>d</i> ₁₄	0.991	0.547
coronene	coronene- <i>d</i> ₁₂	0.984	0.257

stage 7 sample. Many of the prominent peaks are not fully characterized.

PAH were quantified by comparing the MSD response for the primary ion to the response of the dPAH internal standard in the same SIM program time window. PAH to dPAH responses were calibrated by injecting standards containing PAH concentrations in the range 100 to 0.03 ng/μL and dPAH at a fixed concentration of 2.2 ng/μL. The amount of PAH in a sample was calculated as

$$\text{PAH (ng)} = 10^{-b/m} \times \text{Deuterated PAH (ng)} \left(\frac{\text{PAH Response}}{\text{Deuterated PAH Response}} \right)^{1/m} \quad (2.4)$$

The constants *m* and *b* in Equation 2.4 are the slope and intercept of a line fit to the logarithm of relative responses versus the logarithm of relative amounts of PAH

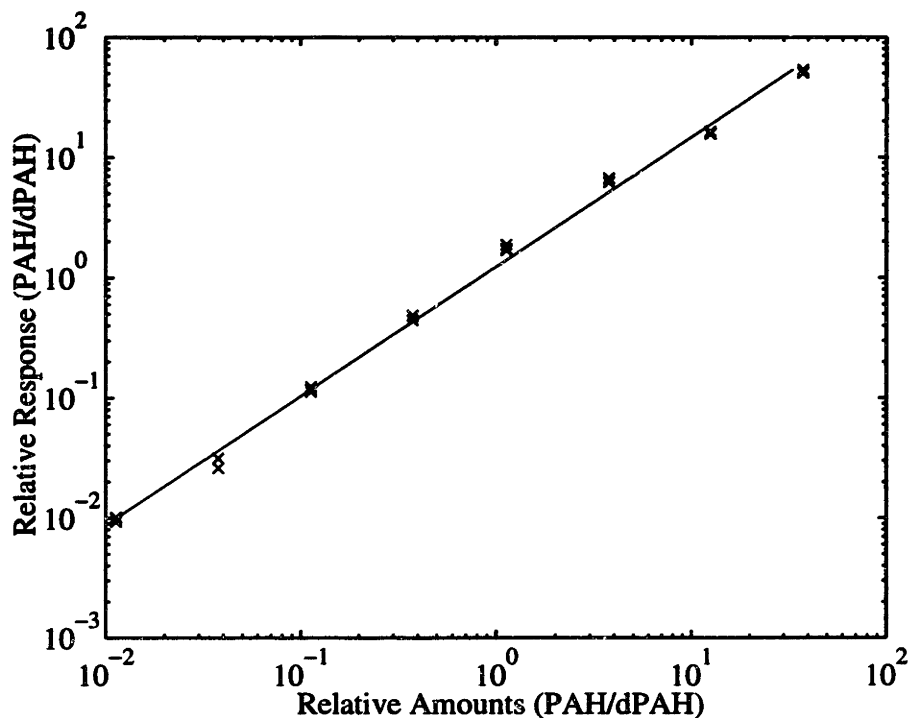


Figure 2-5: Calibration of fluoranthene to pyrene- d_{10} MSD response.

and dPAH (see Table 2.9). In all cases the linear fit was good, with $R^2 \geq 0.977$ (see Figure 2-5).

The MSD responses for an equal number of PAH and dPAH molecules was expected to be approximately equal. Instead, the calibration curves show that the dPAH molar response is one half to one third of the PAH response. The PAH SIM method monitored ions of integral mass to charge ratios (see Table 2.6). In fact ^{12}C , ^{16}O , ^1H , and ^2H have masses of 12.0000, 15.9949, 1.0078, and 2.0140, respectively. As a result, the molecular weight of a pyrene containing the most common isotopes is 202.0783 while for pyrene- d_{10} it is 212.1400. Deuterated compounds, therefore, will be detected less efficiently when the MSD is positioned to detect ions of integral mass. In the case of pyrene, the center of the ion beam for the deuterated analog will be 0.07 mass units further away from the detector than the undeuterated species.

To test the hypothesis that monitoring ions of integral mass units leads to less efficient detection of dPAH, a calibration standard containing 1.0 $\mu\text{g}/\text{mL}$ of PAH and 2.2 $\mu\text{g}/\text{mL}$ dPAH was injected into the GC/MS. The MSD responses were measured by three methods. The first ran the MSD in scan mode, in which case the MSD was not positioned at particular masses. The second method monitored integral mass to charge ratios; this was the method used to quantify PAH in the aerosol samples. The third method monitored ions of mass to charge ratios at the calculated fractional mass of the ions. The precision of the monitored mass to charge ratio is 0.05 mass units. Table 2.10 shows the relative responses for PAH and the dPAH internal standards using the three methods. The data show that the PAH to deuterated PAH relative responses for the fractional mass unit SIM program are near the relative responses from the scan mode and near unity.

The unequal responses from the integral mass unit SIM were repeatable, as evidenced by the small variations in duplicate injections of the calibration standards. Therefore the integral mass SIM program, although it did not yield the expected equal molar response for PAH and dPAH, can be used with confidence for PAH quantification.

OPAH were generally quantified by comparing their molecular ion peak areas to the molecular ion peak area of an internal standard. Phenanthrenequinone, which had a weak molecular ion response, was instead quantified using the $(\text{M}-\text{CO})^+$ ion. OPAH to deuterated PAH response factors, RF , were determined by triplicate injections of standards containing 3 $\text{ng}/\mu\text{L}$ OPAH and deuterated PAH. The amount of OPAH in

Table 2.10: PAH:dPAH MSD Responses for Different Ion Monitoring Programs.

Compound	PAH:dPAH Relative Molar Response		
	Scan Mode	Integral Mass Unit SIM	Fractional Mass Unit SIM
naphthalene	1.19	1.25	1.10
acenaphthene	1.28	1.72	1.25
acenaphthylene	2.01	2.49	1.87
fluorene	1.51	1.93	1.52
phenanthrene	1.27	1.69	1.29
anthracene	1.21	1.41	1.20
fluoranthene	0.94	1.13	0.90
pyrene	1.10	1.54	1.14
chrysene	1.31	2.01	1.34
benzo[ghi]fluoranthene	1.28	1.69	1.31
benz[a]anthracene	1.17	1.37	1.20
benzofluoranthenes	1.26	1.72	1.26
benzo[e]pyrene	1.34	1.81	1.40
benzo[a]pyrene	0.92	1.28	0.96
perylene	1.16	2.08	1.21
dibenz[a,h]anthracene	1.26	2.85	1.25
indeno[1,2,3-cd]pyrene	1.14	1.68	1.29
benzo[ghi]perylene	1.52	4.63	1.55
coronene	0.98	1.53	1.00

Table 2.11: OPAH Response Factors Relative to Deuterated PAH.

OPAH	Internal Standard	Response Factor
1,4-naphthoquinone	phenanthrene- <i>d</i> ₁₀	0.113
1-acenaphthenone	phenanthrene- <i>d</i> ₁₀	0.376
9-fluorenone	phenanthrene- <i>d</i> ₁₀	0.736
1,8-naphthalic anhydride	pyrene- <i>d</i> ₁₀	0.094
OPAH-208a	pyrene- <i>d</i> ₁₀	1.000
phenanthrenequinone	pyrene- <i>d</i> ₁₀	0.205
OPAH-208b	pyrene- <i>d</i> ₁₀	1.000
11 <i>H</i> -benzo[a]fluoren-11-one	chrysene- <i>d</i> ₁₂	0.649
7 <i>H</i> -benzo[c]fluoren-7-one	chrysene- <i>d</i> ₁₂	0.486
11 <i>H</i> -benzo[b]fluoren-11-one	chrysene- <i>d</i> ₁₂	0.536
benzanthrone	chrysene- <i>d</i> ₁₂	0.359
5,12-naphthacenequinone	perylene- <i>d</i> ₁₂	0.197
OPAH-248a	perylene- <i>d</i> ₁₂	1.000
OPAH-254a	perylene- <i>d</i> ₁₂	1.000
6 <i>H</i> -benzo[cd]pyrene-6-one	perylene- <i>d</i> ₁₂	0.362
OPAH-272a	dibenz[a,h]anthracene- <i>d</i> ₁₄	1.000
OPAH-280a	dibenz[a,h]anthracene- <i>d</i> ₁₄	0.333
benzo[a]pyrene-6,12-dione	dibenz[a,h]anthracene- <i>d</i> ₁₄	0.191
OPAH-280b	dibenz[a,h]anthracene- <i>d</i> ₁₄	0.173

a sample was calculated as

$$\text{OPAH (ng)} = \frac{\text{Deuterated PAH (ng)}}{RF} \left(\frac{\text{OPAH Response}}{\text{Deuterated PAH Response}} \right) \quad (2.5)$$

*RF*s ranged from 0.09 to 0.74 and were repeatable, with relative standard deviations less than 20% (see Table 2.11). A *RF* of 1.0 was generally assumed for OPAH for which a reference standard was not available. OPAH-280a and OPAH-280b matched impurities in the the 7*H*-dibenzo[*c,g*]fluoren-7-one reference standard. The *RF* for these compounds were calculated from injections of this reference standard. The relative amounts of 7*H*-dibenzo[*c,g*]fluoren-7-one, OPAH-280a, and OPAH-280b in the reference standard were assumed to be in proportion to the ratio of the sum of all ion signals measured by the MSD in scan mode.

2.3.7 Limits of Quantification

The limit of quantification depends on the sensitivity of the analytical equipment and the level of contamination in blank samples. Peaks with a signal to noise ratio smaller than 20 could not be reliably integrated. From the calibration standards, the detectable amount of PAH is 0.03 ng/ μ L in the injected sample. Because $\approx 10\%$ of the total sample is injected for each analysis, the sensitivity for PAH in a 200 m³ air sample is 1.5 pg/m³ for each aerosol size fraction. Peaks with a signal to noise ratio between 10 and 20 could be identified but not quantified. Thus the limit of detection was ≈ 0.8 pg/m³. For an OPAH with *RF* = 0.3, the limit of quantification in a 200 m³ air sample was ≈ 5 pg/m³ in each size fraction sample.

Blank samples were analyzed to quantify sample contamination from materials and equipment used in the collection and analysis of the samples. With each set of samples, one blank sample was carried to the field and three additional method blanks were made in the laboratory. No systematic difference was noticed between the field and method blanks, indicating that contamination did not occur during sample collection and transport. The amount of PAH found in the blanks was low but variable. For example, the average amount of pyrene was 2.09 ng with a standard deviation of 1.26 ng in the seven impaction media blanks. For the Kenmore Square samples, the amounts found in the blank samples were generally less than 5% of the amount in any sample. However, for some PAH in the Quabbin Summit samples, the amounts found on the blanks were comparable to the amounts found in the samples. This is a particular problem for phenanthrene, anthracene, pyrene, and coronene. The next section discusses the experiments to determine the source of the blank sample contamination.

All reported PAH concentrations have been blank-corrected by subtracting the mean blank concentration from the sample concentration, and summing the sample and blank variances. Compounds were considered identified in the whole aerosol sample if they were identifiable in at least one size fraction sample. The analytes were considered quantified in the whole aerosol sample if the sum of the blank-corrected concentrations over all impactor stages was positive by at least two standard deviations.

2.4 Sample Contamination

The hypothesis that high levels of PAH in some of the sample blanks was the result of cross contamination in the HPLC was tested. In this experiment a concentrated solution of DBP, naphthalene, pyrene, and coronene was initially injected into the HPLC. Seventy-seven minutes after this injection, a solution of deuterated PAH internal standards was injected. The effluent from this injection was collected from 57 to 77 minutes after injection as was done for the prepared aerosol samples. Injections of the deuterated PAH solution were repeated every 77 minutes for 8 hours, during which period six samples were collected. The amounts of PAH in the collected effluent samples were quantified by GC/MS as described above. Figure 2-6 shows the decay of naphthalene, pyrene and coronene concentrations over the course of the experiment. Fluoranthene was not present in the concentrated solution; it was quantified to monitor baseline contamination. The first data point is the total mass initially injected; this is reasonably assumed since only a small fraction of the injected PAH was subsequently detected. The PAH concentrations show an initial rapid decay to a constant final value. There was no detectable amount of naphthalene in the last samples. The first order time constants for the initial rapid concentration decay are 11.6, 9.9, and 8.9 min for naphthalene, pyrene and coronene, respectively. The final values for the PAH are near the limits of quantification for both compounds and typical of "clean" blank samples.

The maximum cross contamination of samples would occur if a sample with high concentrations of PAH were prepared with the HPLC immediately before a blank

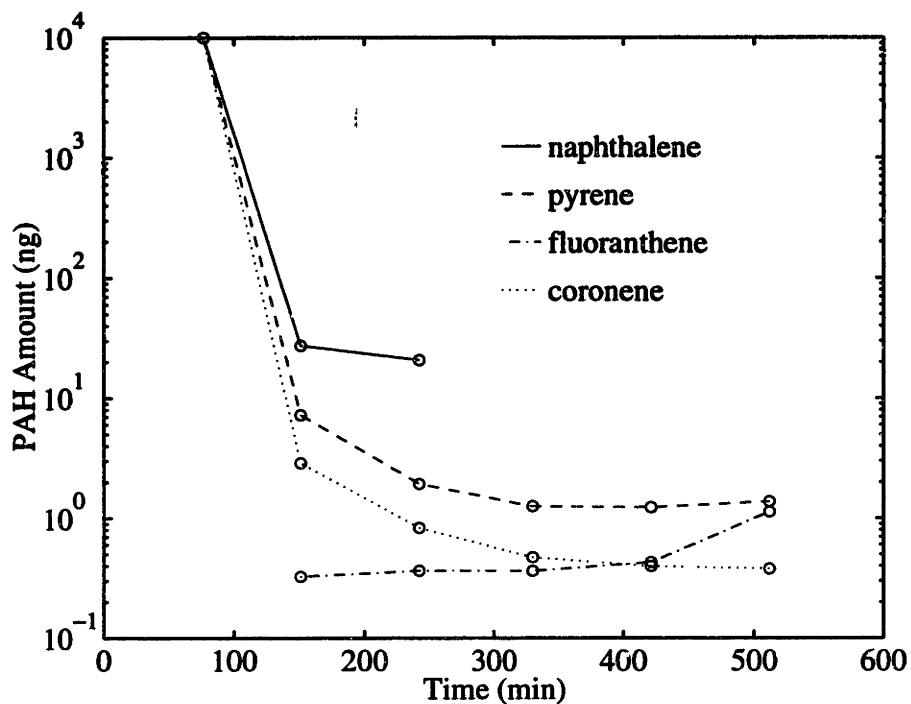


Figure 2-6: Decay of PAH concentration eluting from HPLC with time.

sample. The expected carry over to the blank sample would be

$$C = C_0 e^{-t/\tau} \quad (2.6)$$

For the case of pyrene, a PAH present in high concentrations, $C_0 \approx 100 \text{ ng}/\mu\text{L}$ and $\tau \approx 10 \text{ min}$, C is approximately $0.03 \text{ ng}/\mu\text{L}$. This is near the limit of detection for pyrene. Therefore we conclude that high levels of PAH in some of the blank samples are not the result of sample cross contamination through the HPLC columns.

The source of the blank contamination remains unknown. Cross contamination of samples may have occurred in the HPLC injection port. For the preparation of OPAH samples, the HPLC injection port was rinsed three times before each sample injection and the columns were purged with 70 mL DCM between sample injections. With the

exception of 9-fluorenone, detectable amounts of OPAH in the blank samples were rare. This suggests that the revised HPLC method successfully reduced sample cross contamination in the HPLC.

2.5 Conclusions

We have developed an integrated aerosol sampling and analysis procedure to collect size-segregated atmospheric particles in 9 samples with D_p in the range 0.087–19.2 μm . The particle bounce artifact is minimized by using oiled PTFE membrane impaction media. Very low detection limits, 1.5–5 pg/m^3 , in samples collected from relatively small volumes of air, 200 m^3 , were possible by using deuterated PAH internal standards and highly concentrated aerosol extracts.

Using this sample preparation and analysis technique we were able to quantify 15 PAH or PAH isomer groups in the air samples collected at Kenmore Square and Quabbin Summit. Four low molecular weight PAH were present in quantifiable amounts but could not be accurately quantified due to significant evaporation during sample preparation and storage. We identified four additional PAH or PAH isomer groups which were present in amounts too small to quantify. Eleven more peaks which may be PAH were not identified due to a lack of reference standards. We also quantified 12 OPAH in the Kenmore Square air sample. Seven additional compounds with mass spectra typical of OPAH were tentatively identified due to a lack of reference standards. These results are repeatable and consistent with the work of other researchers.

The technique quantifies trace organic compounds by mass spectroscopy. Be-

cause the analysis does not depend on the uncommon properties of the analytes, e.g. fluorescence, it is general, and with further development, it could be used to determine the concentrations of other trace pollutants in the size-segregated atmospheric aerosol samples. The developments necessary to extend the method to other compound classes are the development of preparatory techniques to remove the oil used to prevent particle bounce and a GC/MS SIM program.

As more sensitive MS detectors become available, these methods could be modified to collect air samples over a shorter time. Alternatively, with more sensitive detectors, the final volume of the samples could be increase above 5 μL , allowing the use of an autoinjector and a more complete analysis using multiple SIM programs.

Chapter 3

PAH and OPAH in Size-segregated Aerosols

3.1 Introduction

In previous measurements of the distribution of PAH with particle size, PAH were found predominantly in association with fine particles ($D_p < 2.0 \mu\text{m}$) [68, 92, 93, 94, 95, 96, 97, 98, 99, 100]. PAH of the same molecular weight were observed to partition similarly among atmospheric aerosols [96, 94]. PAH were also found to partition to larger aerosols in warmer periods [68, 93, 94, 95] and at sites away from emission sources [68, 94, 96, 99].

Atmospheric sampling studies of OPAH have found concentrations in the approximate range 0.1 to 10 ng/m³ for a number of OPAH [61, 63, 64, 65, 66, 56, 67, 57]. A study of OPAH associated with size-segregated particles found approximately half of the benzanthrone and perinaphtenone (phenalen-1-one) to be associated with par-

ticles smaller than $3.0 \mu\text{m}$ in summer, and two-thirds in winter [68].

The main experimental objective of this thesis was to determine the distribution of PAH and OPAH with particle size in atmospheric aerosols. In this work OPAH includes ketones, diones and dicarboxylic acid anhydrides of PAH. Particles were collected with a micro-orifice impactor (MOI) from sites in Boston and rural Massachusetts. The compounds were identified and quantified by gas chromatography/mass spectrometry (GC/MS) as described in the previous chapter. Possible mechanisms of partitioning will be examined qualitatively in light of the measured distributions of PAH and OPAH with particle size.

3.2 PAH in Urban Boston Aerosol

Deposits were visible on all of the Kenmore Square impactor stages: fibers on stage 0, brownish deposits on stages 1 through 3, black deposits on stages 4 through 8, and grey deposits on the after filter. A total of 23 PAH were identified in the Kenmore Square samples, of these 15 were quantifiable (see Table 3.1). PAH listed in Table 2.6 but not in Table 3.1 were not identified in these samples. The total measured PAH concentrations fall within the range of urban particulate phase PAH concentrations as measured by numerous filter sampling studies (see Table 1.2) [37, 38, 39, 40, 41, 42, 43, 44, 45, 46, 47, 48, 49, 50, 51]. The fraction of PAH collected on stage 8 and the after filter ($D_p < 0.14 \mu\text{m}$) is referred to as the ultrafine fraction in Table 3.1. PAH collected on impactor stages 4 through 7 ($0.14 < D_p < 1.9 \mu\text{m}$) is the accumulation fraction. The sum of ultrafine and accumulation fractions is referred to as the fine

fraction. PAH collected on stages 1, 2 and 3 ($1.9 < D_p < 19 \mu\text{m}$) is the coarse fraction.

Table 3.1: PAH Identified in Kenmore Square Samples.

PAH	Molecular Weight	Concentration with Aerosol (ng/m^3)	Fraction with Aerosol Modes		
			Ultrafine	Accumulation	Coarse
naphthalene	128	Identified			
acenaphthylene	154	Identified			
acenaphthene	152	0.377 ± 0.104	-0.009	0.320	0.689
fluorene	166	2.530 ± 0.309	0.032	0.250	0.719
phenanthrene	178	13.699 ± 0.680^a	0.037	0.360	0.604
anthracene	178	1.212 ± 0.071	0.052	0.424	0.524
fluoranthene	202	14.706 ± 0.410	0.063	0.478	0.459
pyrene	202	8.107 ± 0.209	0.065	0.504	0.431
benzo[ghi]fluoranthene	226	0.883 ± 0.043	0.100	0.609	0.291
cyclopenta[cd]pyrene	226	Identified			
benz[a]anthracene	228	1.636 ± 0.077	0.107	0.726	0.167
chrysene/triphenylene	228	1.767 ± 0.101	0.103	0.707	0.190
benzofluoranthenes	252	3.204 ± 0.102	0.164	0.740	0.096
benzo[e]pyrene	252	1.318 ± 0.031	0.193	0.717	0.091
benzo[a]pyrene	252	1.141 ± 0.022	0.181	0.748	0.072
perylene	252	0.208 ± 0.008	0.143	0.800	0.057
PAH-276a	276	0.591 ± 0.026	0.284	0.670	0.047
indeno[1,2,3-cd]pyrene	276	1.019 ± 0.051	0.253	0.680	0.067
dibenzanthracenes	278	0.133 ± 0.011	0.171	0.780	0.049
benzo[b]chrysene	278	Identified			
picene	278	Identified			
benzo[ghi]perylene	276	0.809 ± 0.048	0.366	0.578	0.056
dibenzo[a,l]pyrene/ dibenzo[b,k]fluoranthene	302	Identified			
coronene	300	0.439 ± 0.051	0.516	0.440	0.045

^aOne standard deviation.

Figures 3-1 through 3-18 show the normalized distribution of PAH with particle size. Dashed lines at $D_p = 0.14$ and $1.9 \mu\text{m}$ show the ultrafine—accumulation and accumulation—coarse fraction divisions. The error bars show one standard deviation from the mean analysis results. The lower limit of particle size collected on the after filter, $D_p = 0.01 \mu\text{m}$, has been arbitrarily selected. Calculations of the aspiration efficiency of our sampler using the semi-empirical correlation of Tsai and Vincent show

that for a wind velocity of 1 m/s, particles with $D_p = 19.2 \mu\text{m}$ have an aspiration efficiency of 47% [112]. PAH collected on stage 0 are not reported because of the low collection efficiencies for particles larger than $19.2 \mu\text{m}$.

The distributions of PAH with molecular weight 252 (benzofluoranthenes, benzo[*e*]pyrene, benzo[*a*]pyrene, and perylene) with particle size are nearly identical (see Figures 3-10 through 3-13). This trend is observed for all PAH of similar molecular weight, as the fractions of PAH found with each particle size range show (see Table 3.1). Others have also observed that PAH of the same molecular weight have similar distributions with particle size [96, 94]. The distributions of PAH show an increase in the fraction of PAH associated with larger particles as molecular weight decreases. Venkataraman and Friedlander also found a preferential accumulation of lower molecular weight PAH ($M \leq 228$) compared to higher molecular weight PAH in larger particles ($0.5 < D_p < 2.0 \mu\text{m}$), in qualitative agreement with the present findings [94].

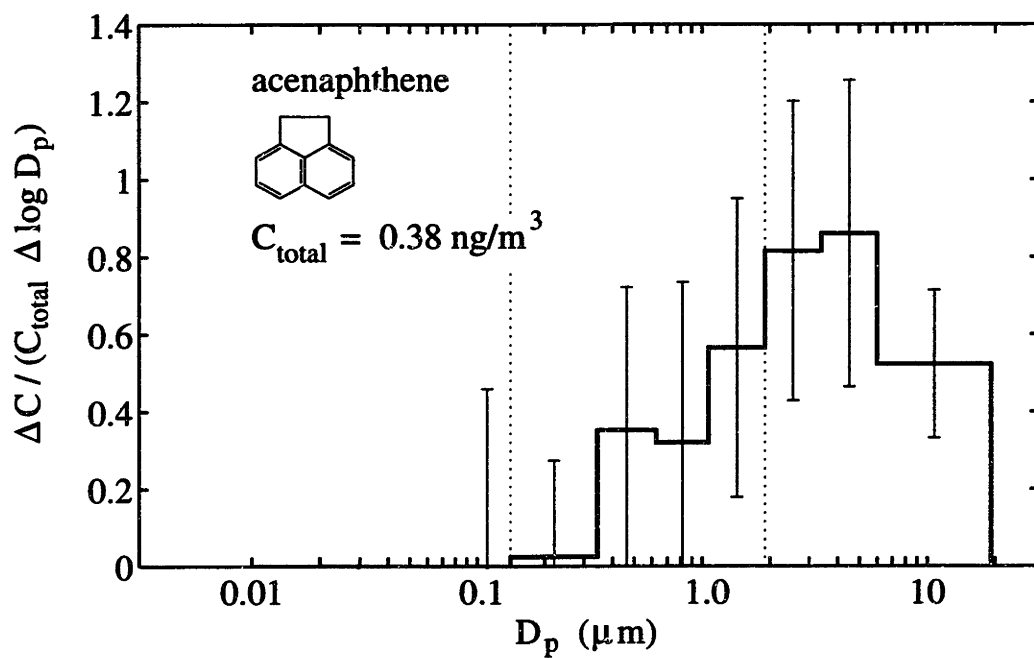


Figure 3-1: Acenaphthene distribution with particle size in Kenmore Square aerosol.

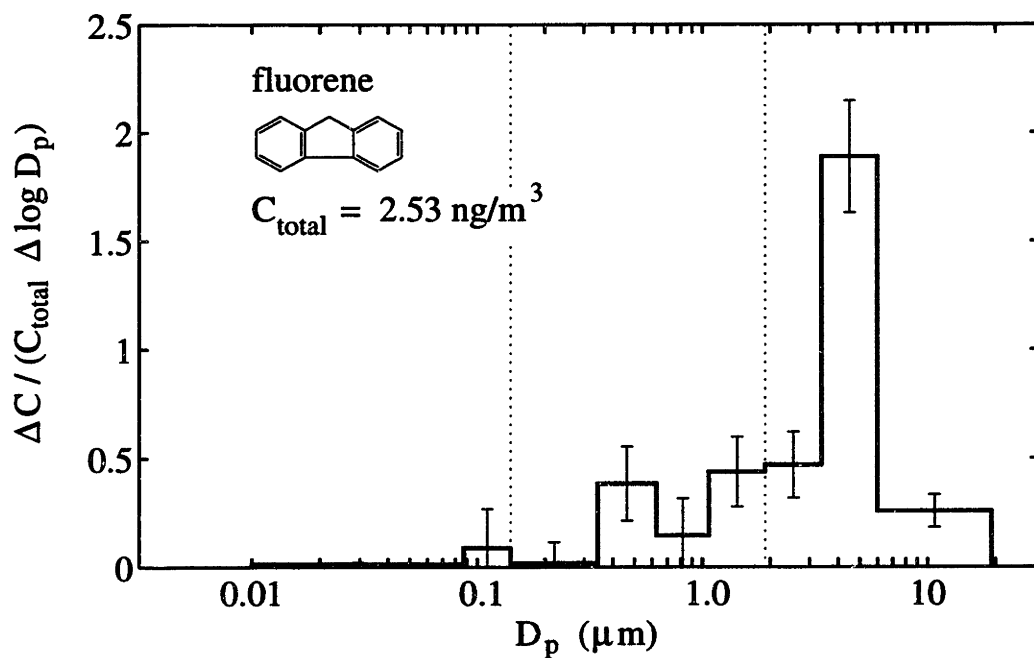


Figure 3-2: Fluorene distribution with particle size in Kenmore Square aerosol.

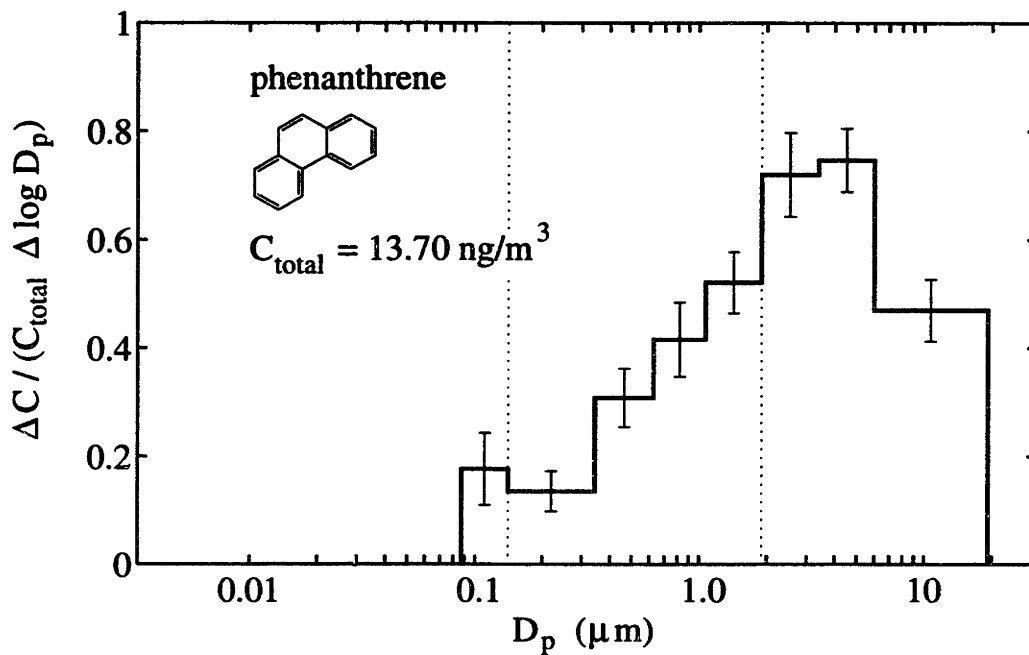


Figure 3-3: Phenanthrene distribution with particle size in Kenmore Square aerosol.

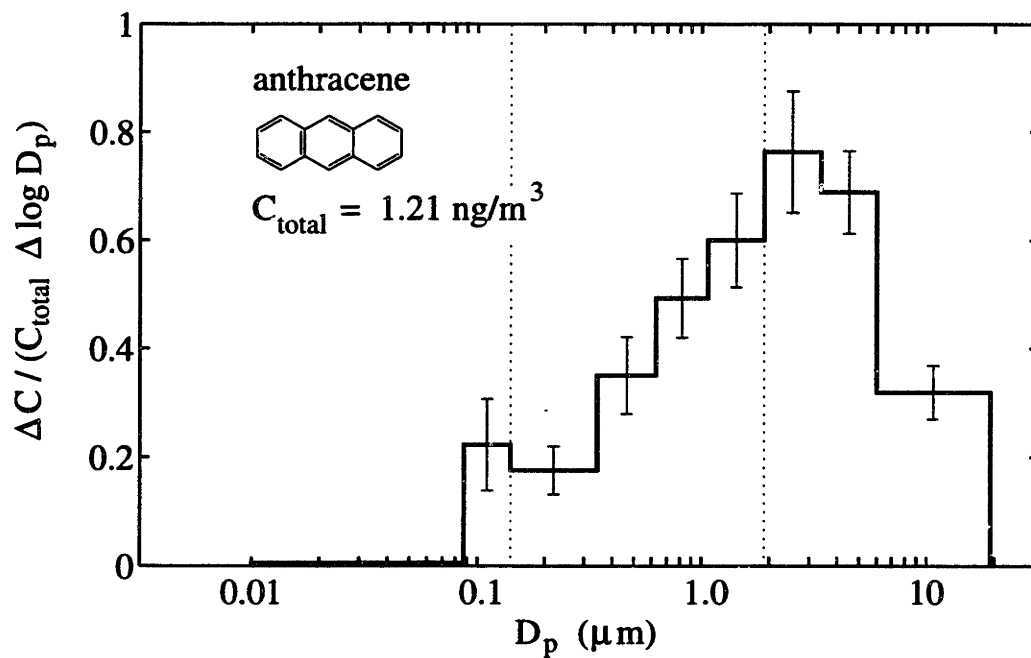


Figure 3-4: Anthracene distribution with particle size in Kenmore Square aerosol.

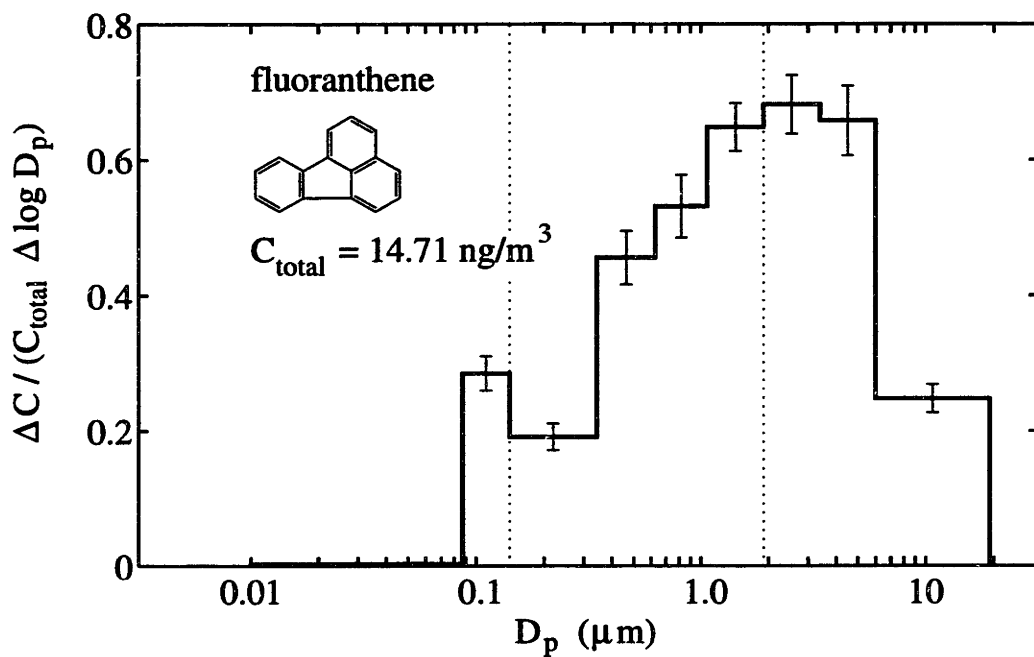


Figure 3-5: Fluoranthene distribution with particle size in Kenmore Square aerosol.

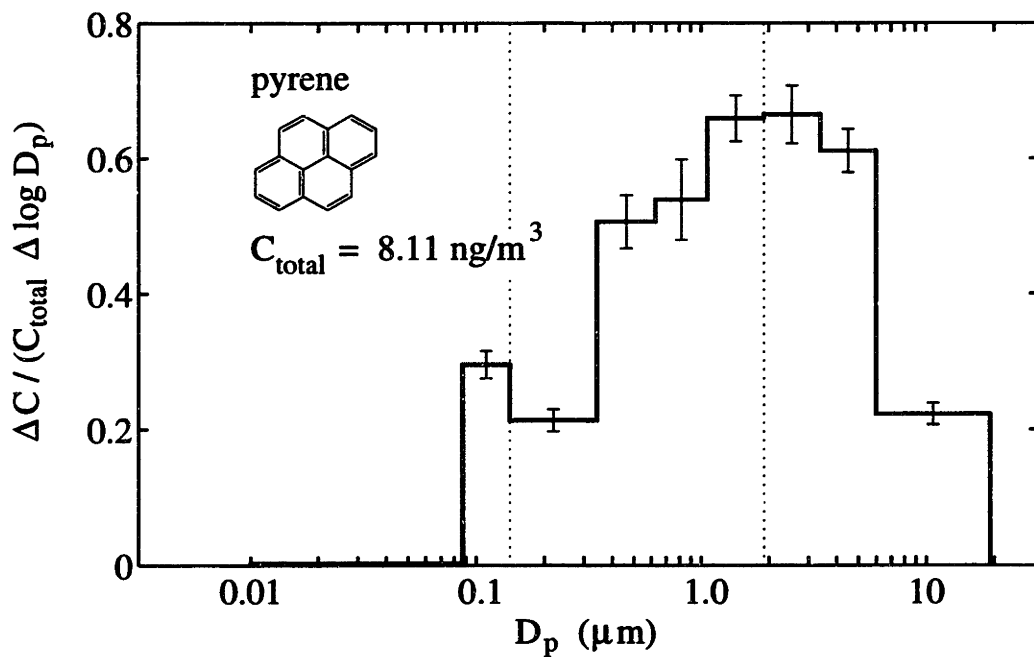


Figure 3-6: Pyrene distribution with particle size in Kenmore Square aerosol.

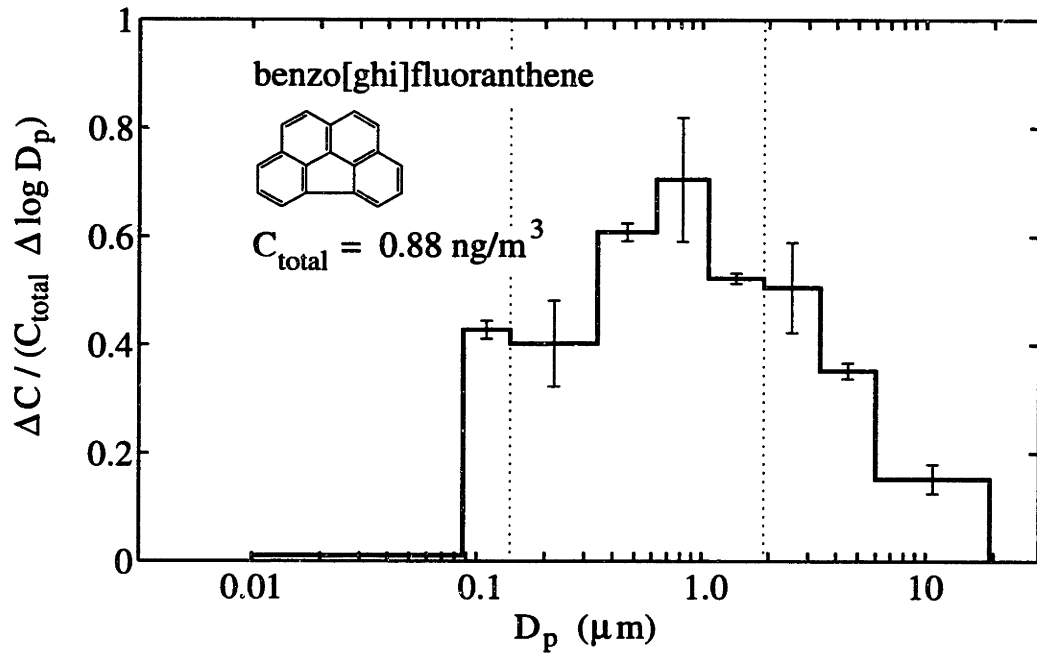


Figure 3-7: Benzo[*ghi*]fluoranthene distribution with particle size in Kenmore Square aerosol.

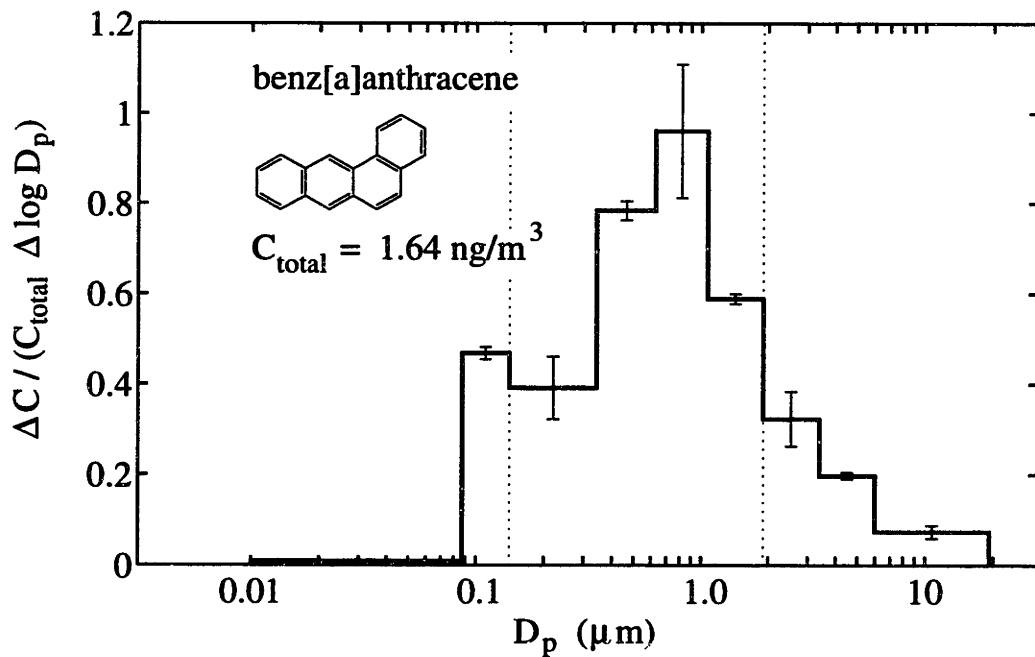


Figure 3-8: Benz[*a*]anthracene distribution with particle size in Kenmore Square aerosol.

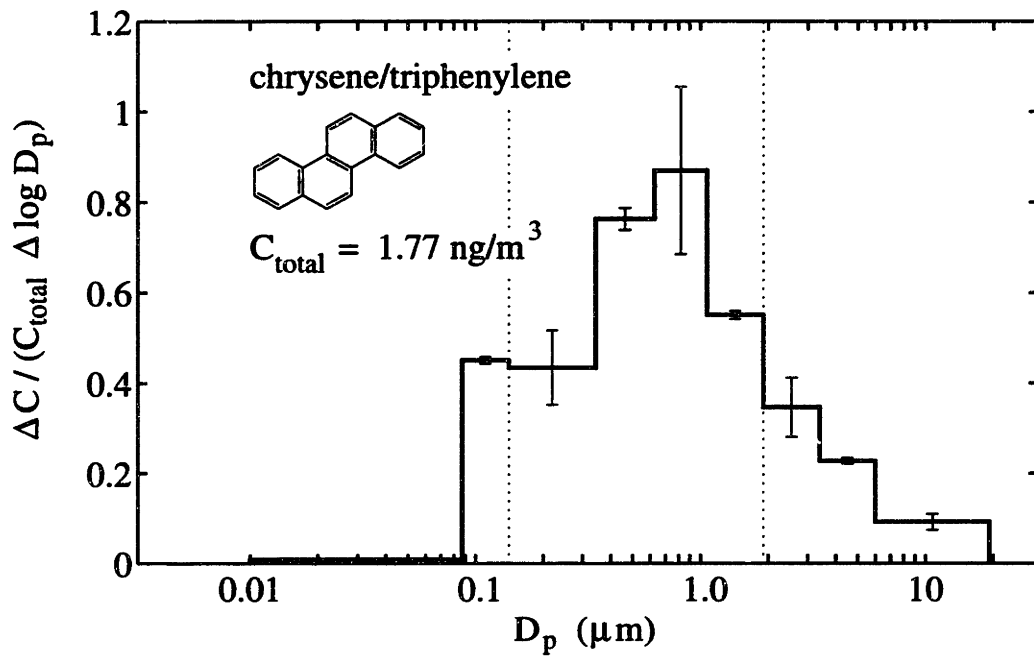


Figure 3-9: Chrysene/triphenylene distribution with particle size in Kenmore Square aerosol.

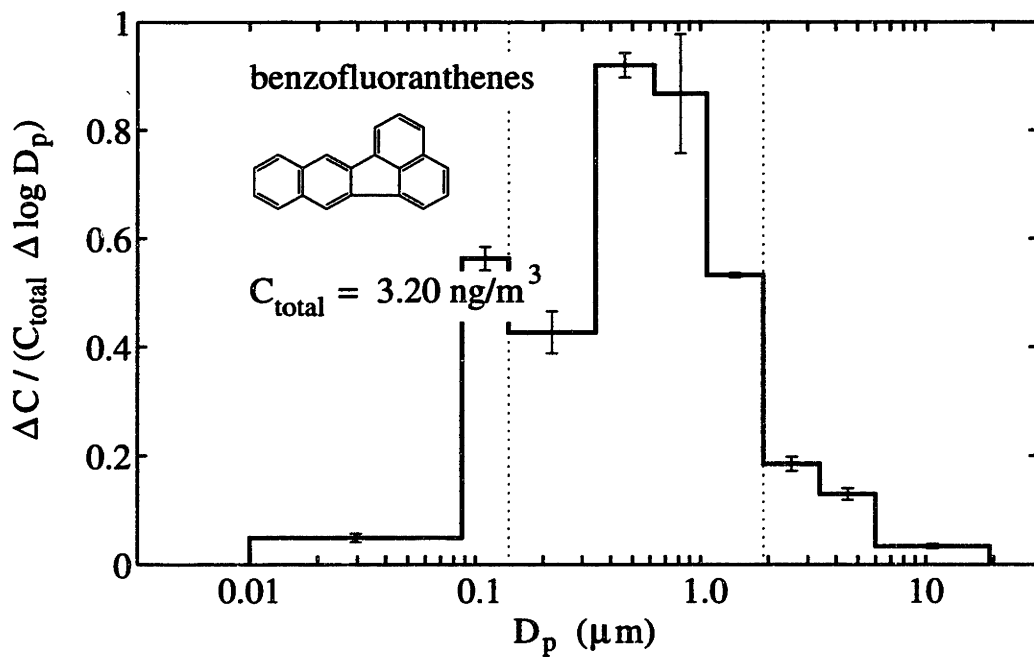


Figure 3-10: Benzofluoranthenes distribution with particle size in Kenmore Square aerosol.

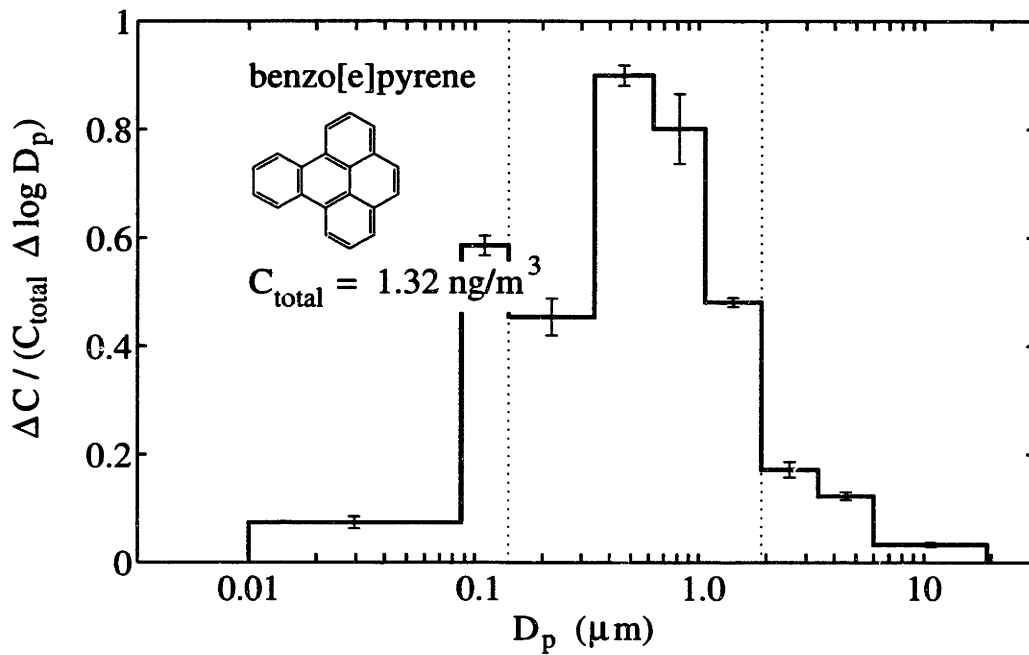


Figure 3-11: Benzo[e]pyrene distribution with particle size in Kenmore Square aerosol.

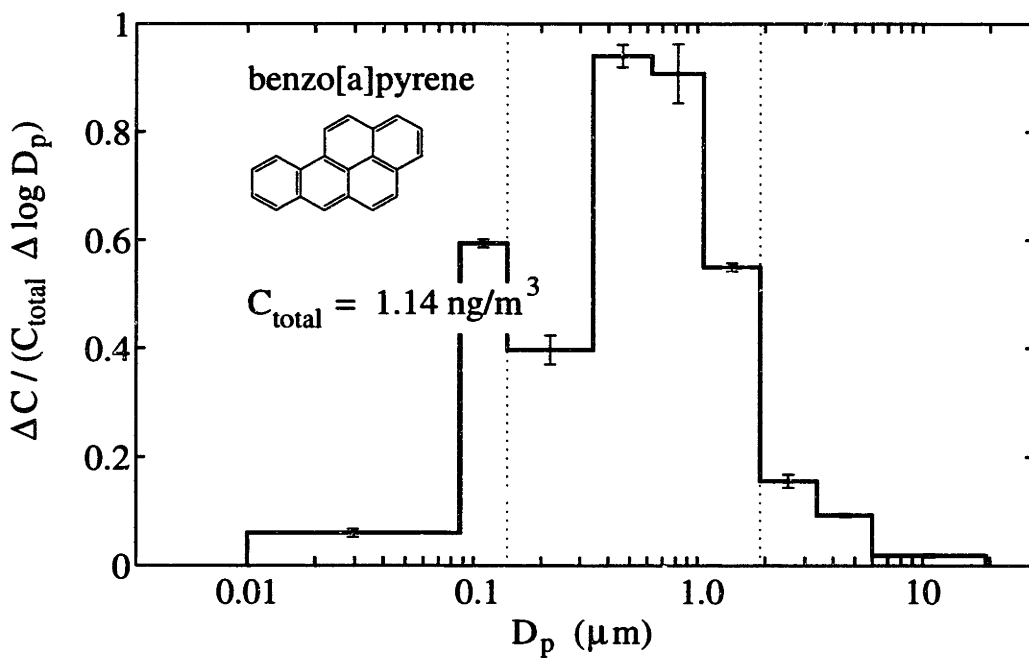


Figure 3-12: Benzo[a]pyrene distribution with particle size in Kenmore Square aerosol.

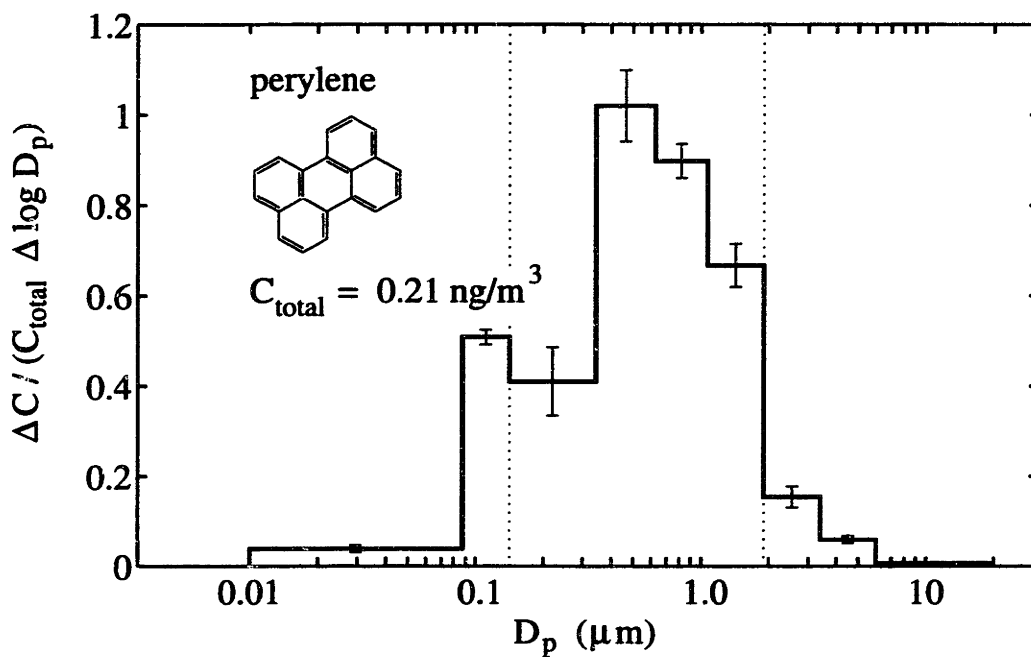


Figure 3-13: Perylene distribution with particle size in Kenmore Square aerosol.

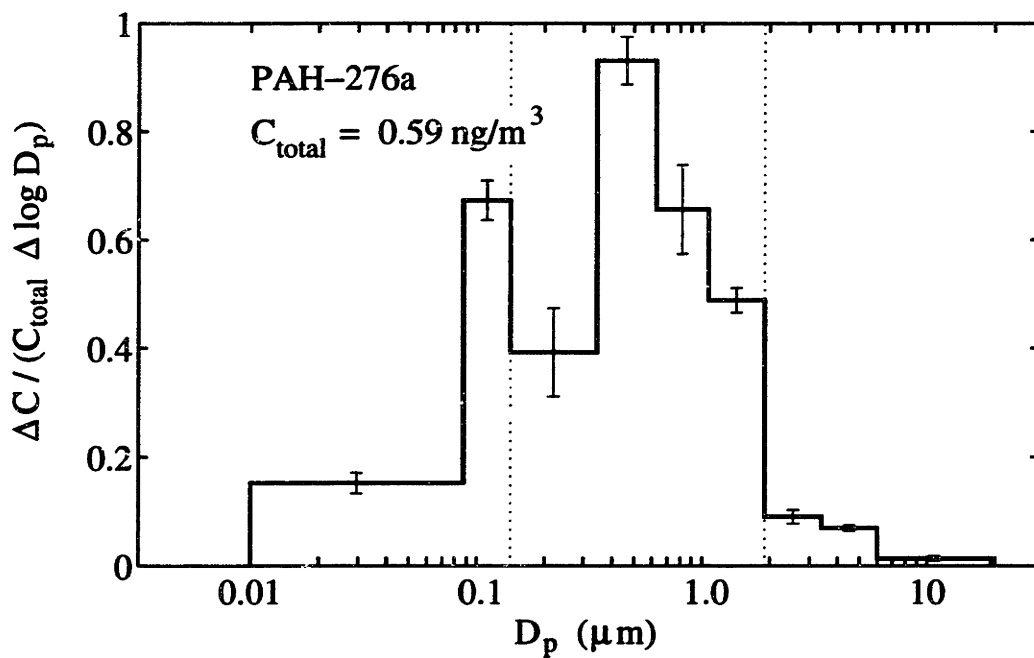


Figure 3-14: PAH-276a distribution with particle size in Kenmore Square aerosol.

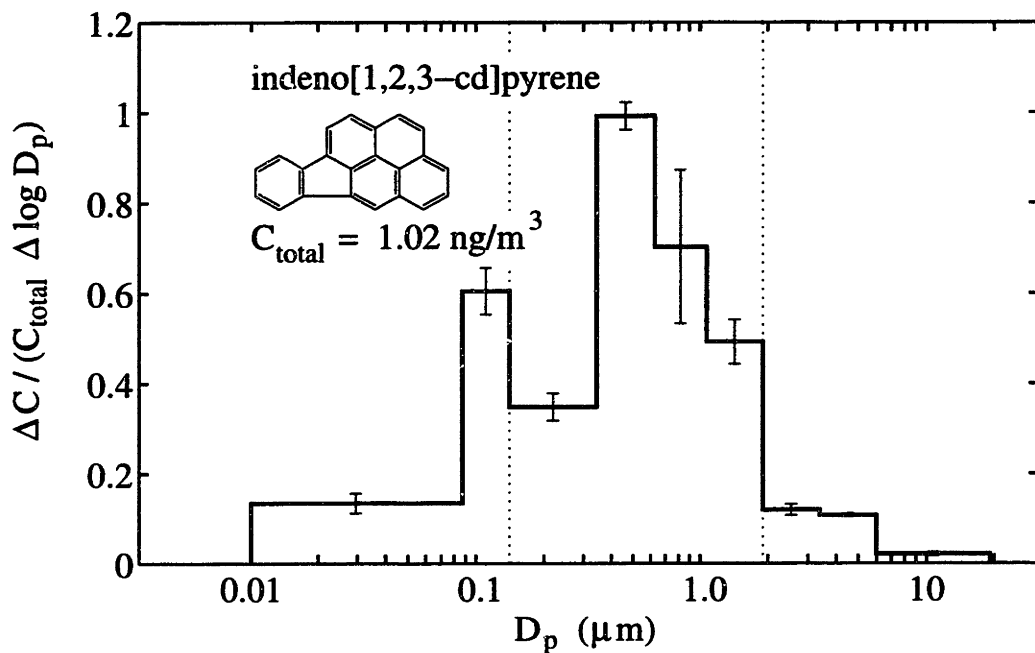


Figure 3-15: Indeno[1,2,3-*cd*]pyrene distribution with particle size in Kenmore Square aerosol.

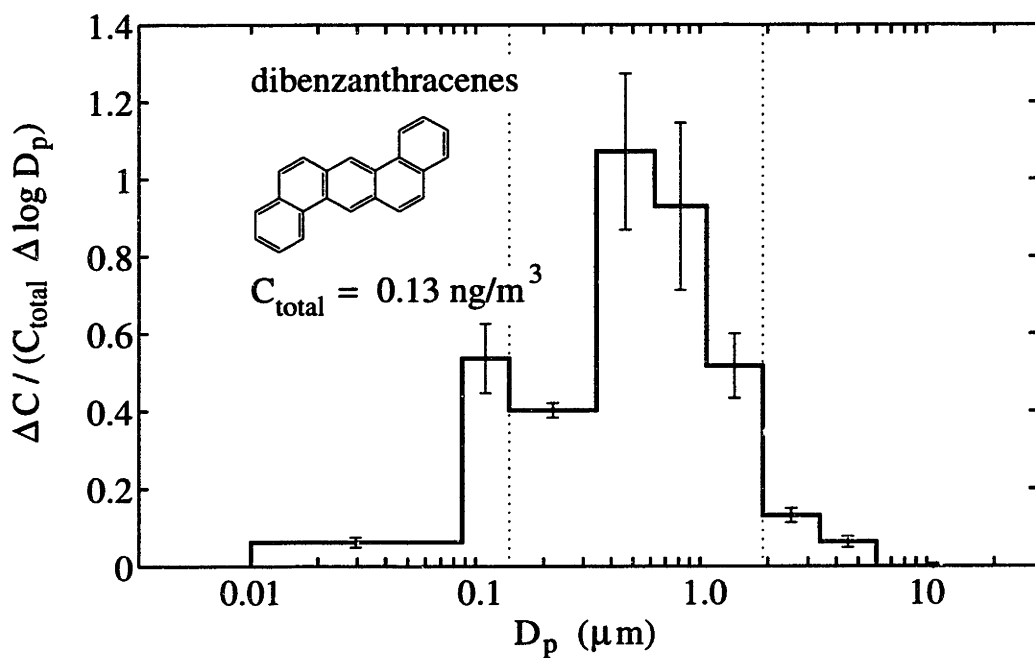


Figure 3-16: Dibenzanthracenes distribution with particle size in Kenmore Square aerosol.

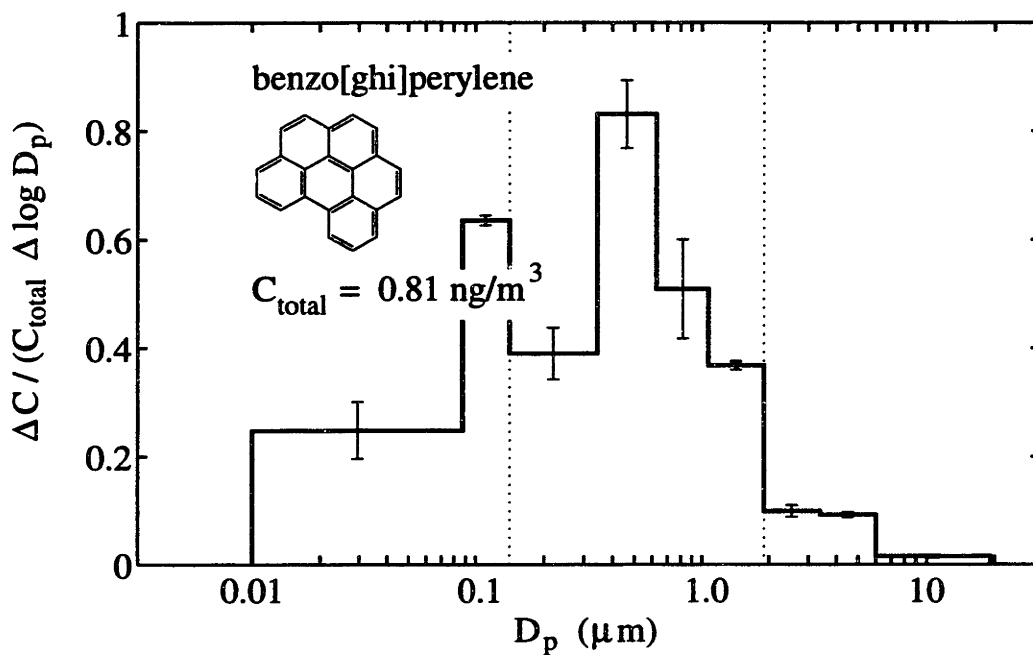


Figure 3-17: Benzo[ghi]perylene distribution with particle size in Kenmore Square aerosol.

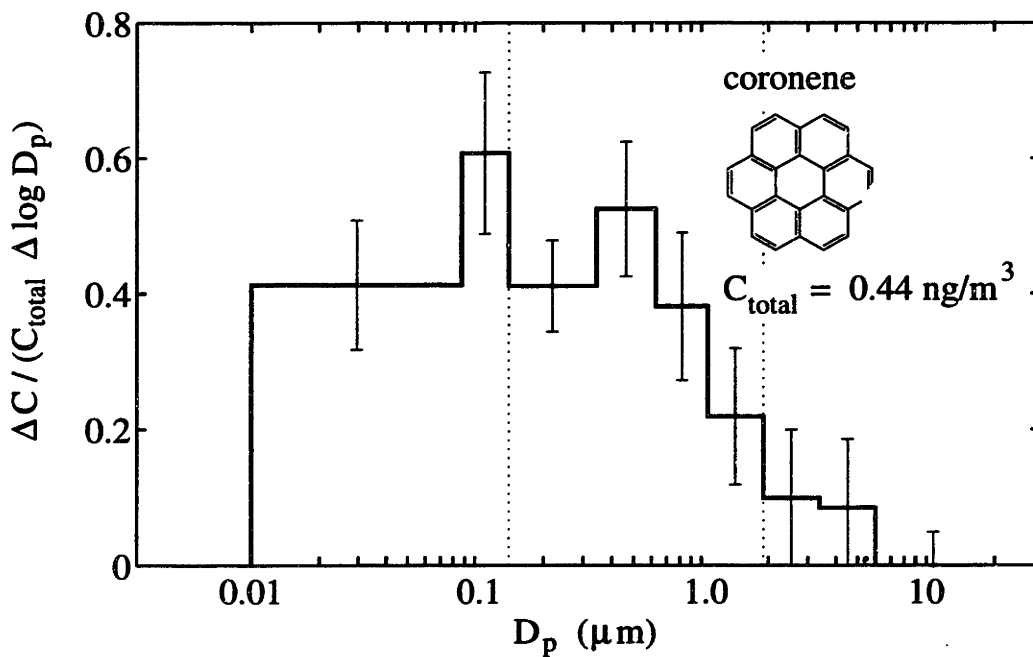


Figure 3-18: Coronene distribution with particle size in Kenmore Square aerosol.

3.3 PAH in Rural Massachusetts Aerosol

The rural impactor sample deposits were visibly lighter than those collected in Kenmore Square and there were no visible deposits on the after filter. The total concentration of each PAH found in the Quabbin Summit samples was approximately an order of magnitude lower than the concentration found at Kenmore Square. The amounts of many PAH in the rural samples were comparable to the amounts found in the method blanks, making accurate quantification impossible. PAH were considered quantified only if the sum of the blank-corrected concentrations over all stages was positive by at least two standard deviations. Table 3.2 lists the PAH identified and quantified along with the total concentrations and distributions among the aerosol size fractions.

The distribution of quantifiable PAH among particle sizes is qualitatively different for the urban and rural samples. Figures 3-19 through 3-27 show the distributions of PAH with particle size in the rural aerosol. PAH in the rural samples were associated with the coarse aerosols to a greater degree than in the urban samples, e.g. the distribution of benzo[*e*]pyrene shown in Figures 3-11 and 3-25. This is in qualitative agreement with other impaction sampling studies which found that PAH collected at sites away from emissions sources tend to partition to larger particles [68, 94, 96, 99].

Table 3.2: PAH Identified in Quabbin Summit Samples.

PAH	Molecular Weight	Concentration with Aerosol (ng/m ³)	Fraction with Aerosol Modes		
			Ultrafine	Accumulation	Coarse
fluoranthene	202	0.511 ± 0.157 ^a	0.076	0.444	0.480
pyrene	202	0.152 ± 0.041	0.073	0.567	0.360
benzo[ghi]fluoranthene	226	0.066 ± 0.002	0.118	0.659	0.223
benz[a]anthracene	228	0.010 ± 0.003	-0.043	0.187	0.856
chrysene/triphenylene	228	0.129 ± 0.005	0.089	0.504	0.407
benzofluoranthenes	252	0.174 ± 0.018	0.071	0.297	0.632
benzo[e]pyrene	252	0.056 ± 0.007	0.074	0.297	0.628
benzo[a]pyrene	252	Identified			
indeno[1,2,3-cd]pyrene	276	0.020 ± 0.004	-0.077	0.123	0.954
dibenzanthracenes	278	Identified			
benzo[ghi]perylene	276	0.008 ± 0.003	-0.077	0.232	0.846

^aOne standard deviation.

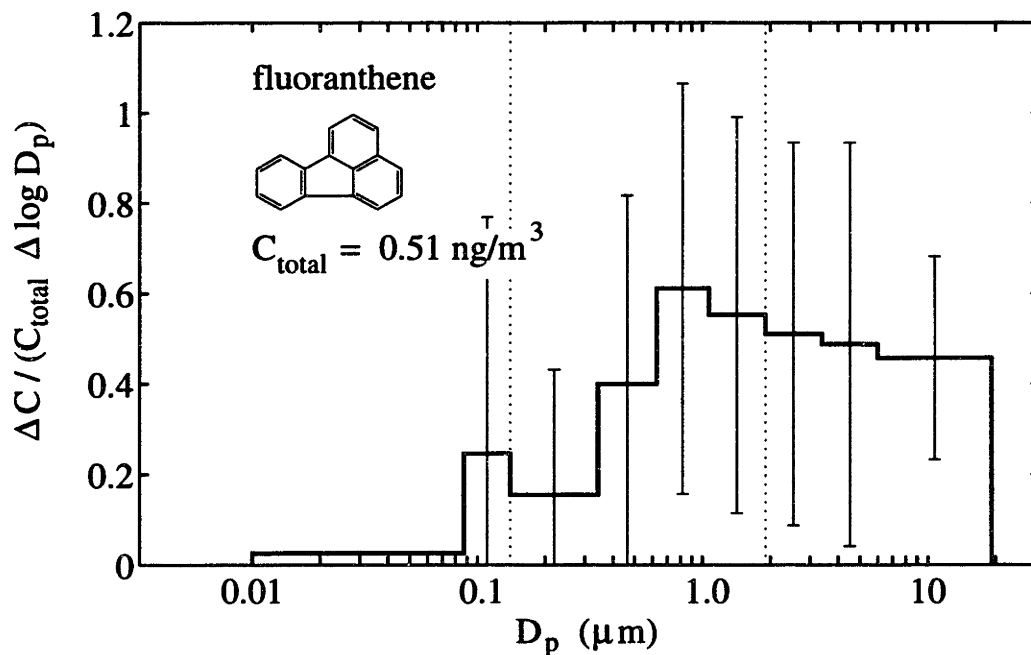


Figure 3-19: Fluoranthene distribution with particle size in Quabbin Summit aerosol.

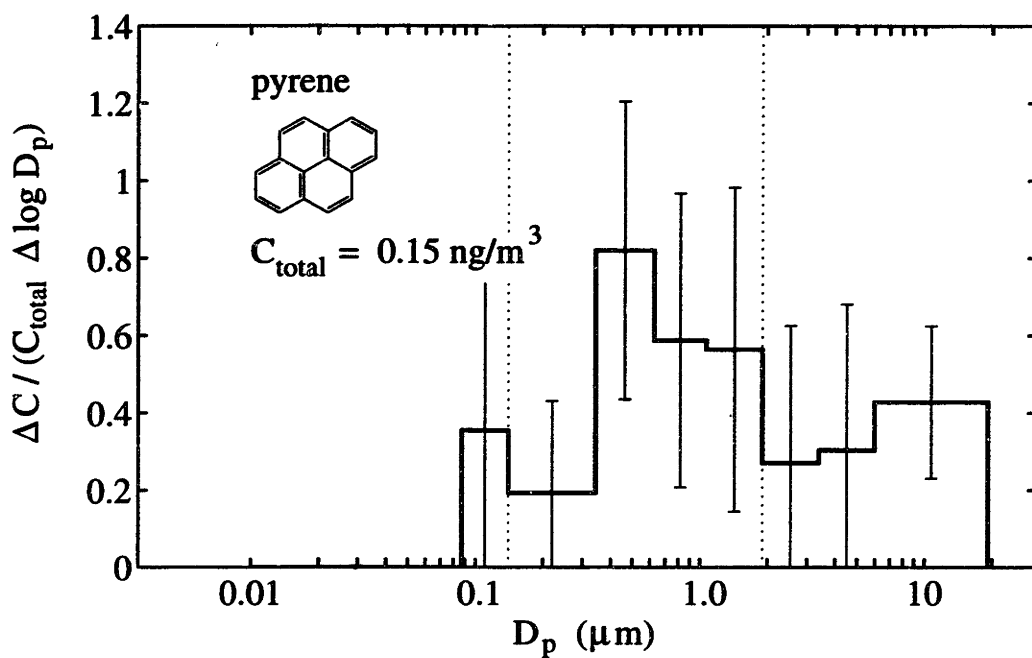


Figure 3-20: Pyrene distribution with particle size in Quabbin Summit aerosol.

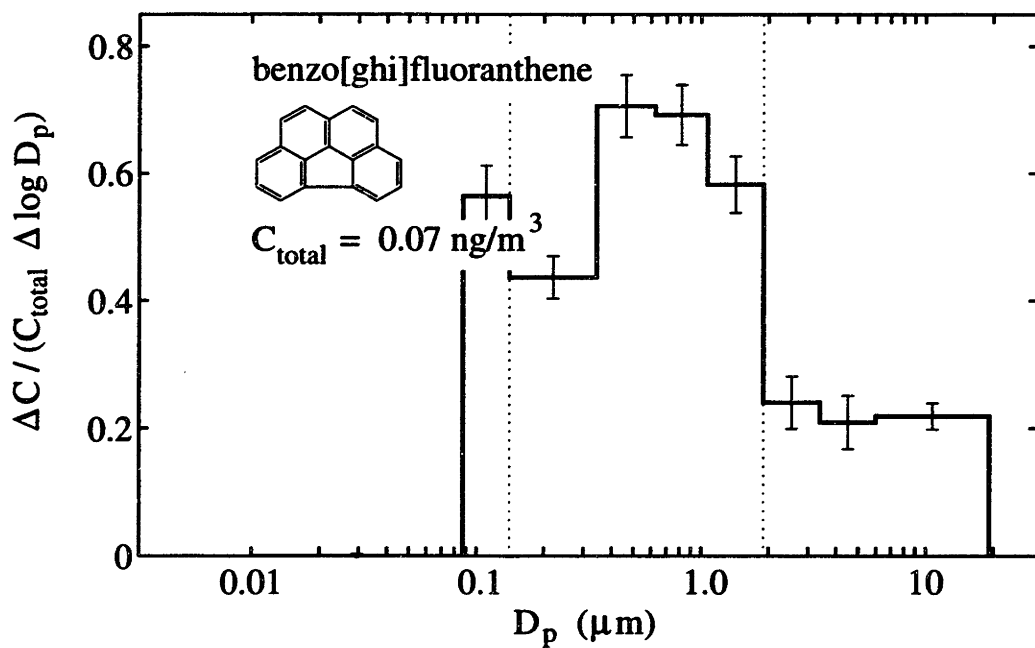


Figure 3-21: Benzo[ghi]fluoranthene distribution with particle size in Quabbin Summit aerosol.

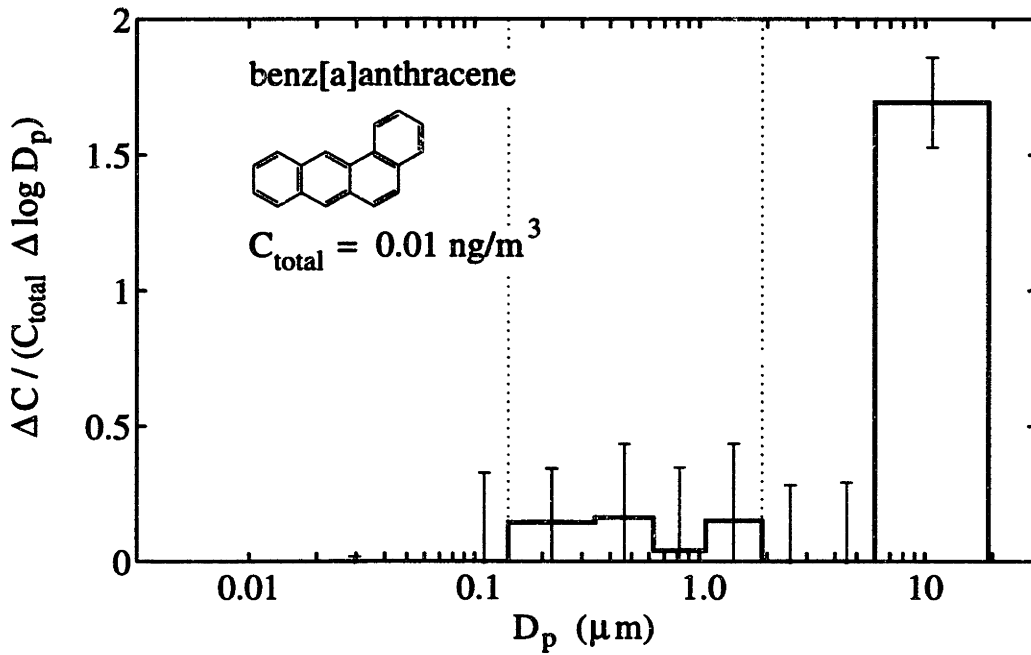


Figure 3-22: Benz[a]anthracene distribution with particle size in Quabbin Summit aerosol.

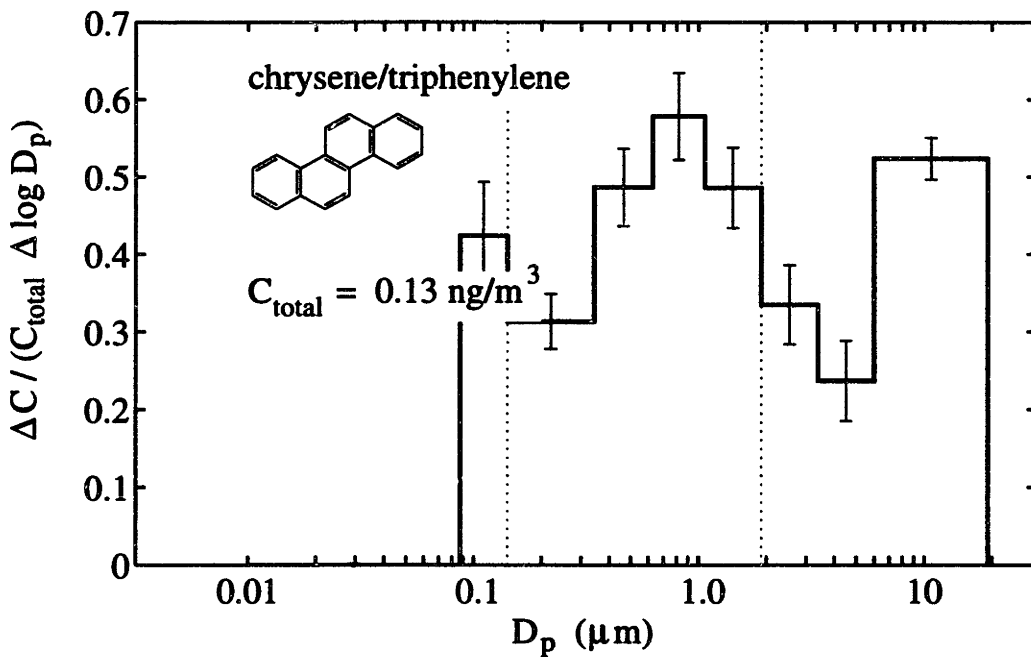


Figure 3-23: Chrysene/triphenylene distribution with particle size in Quabbin Summit aerosol.

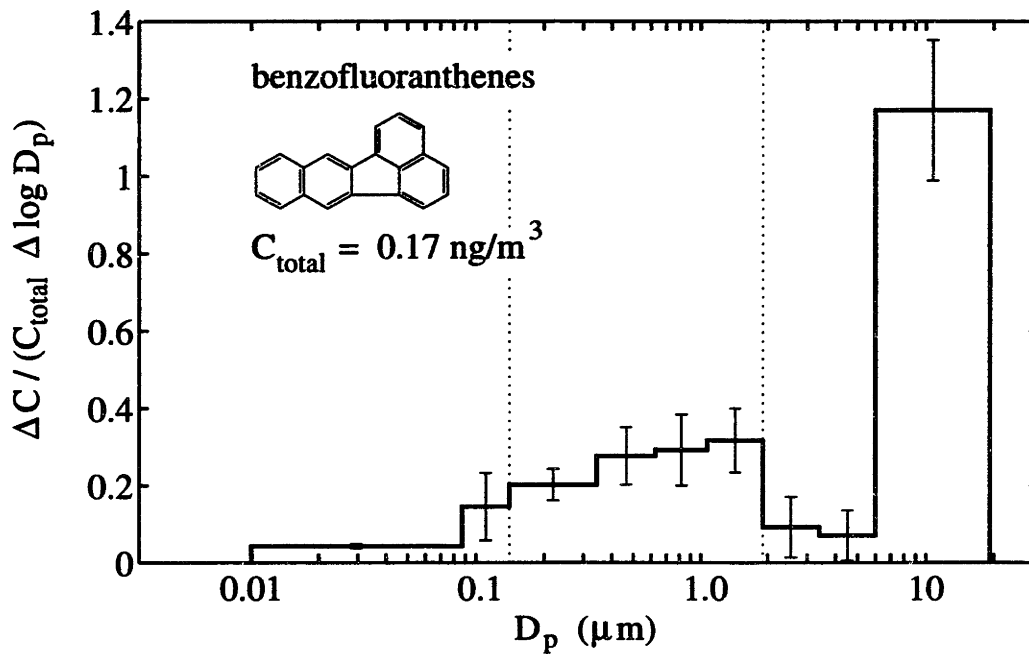


Figure 3-24: Benzofluoranthenes distribution with particle size in Quabbin Summit aerosol.

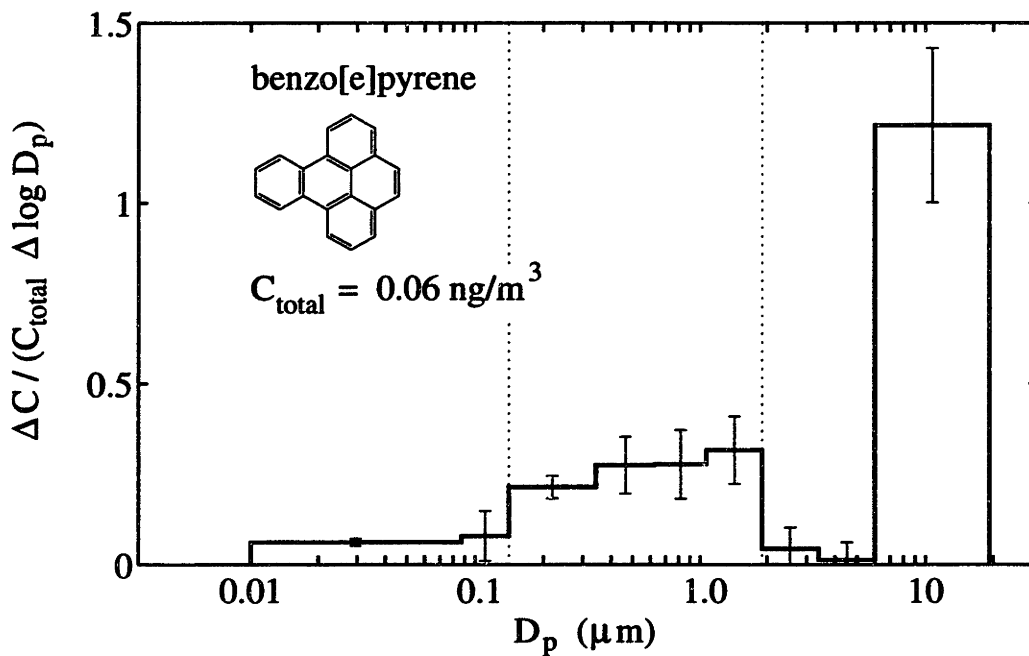


Figure 3-25: Benzo[e]pyrene distribution with particle size in Quabbin Summit aerosol.

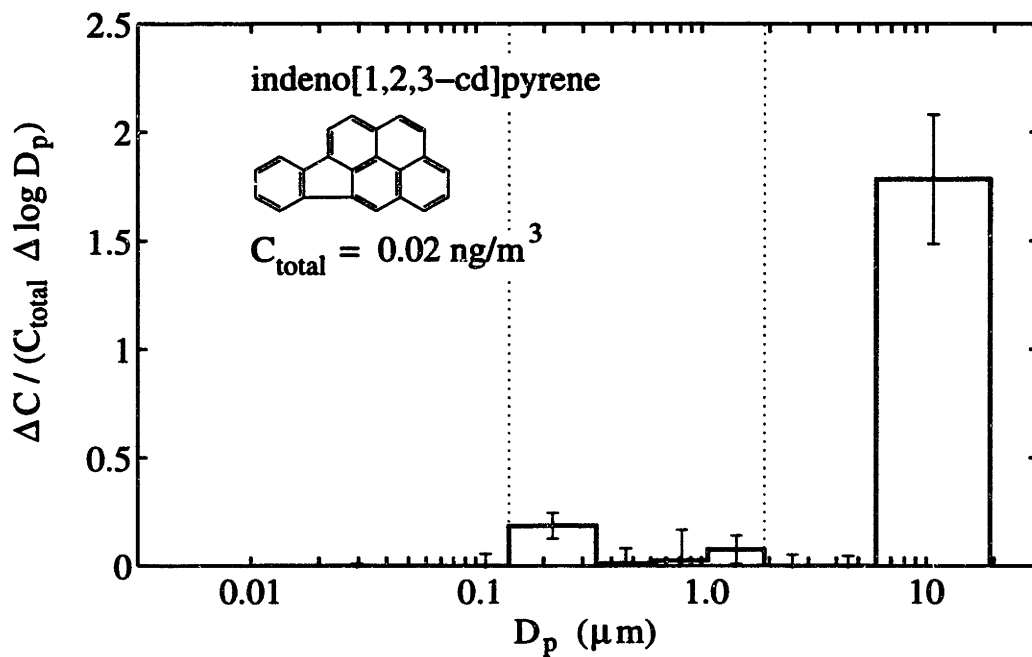


Figure 3-26: Indeno[1,2,3-*cd*]pyrene distribution with particle size in Quabbin Summit aerosol.

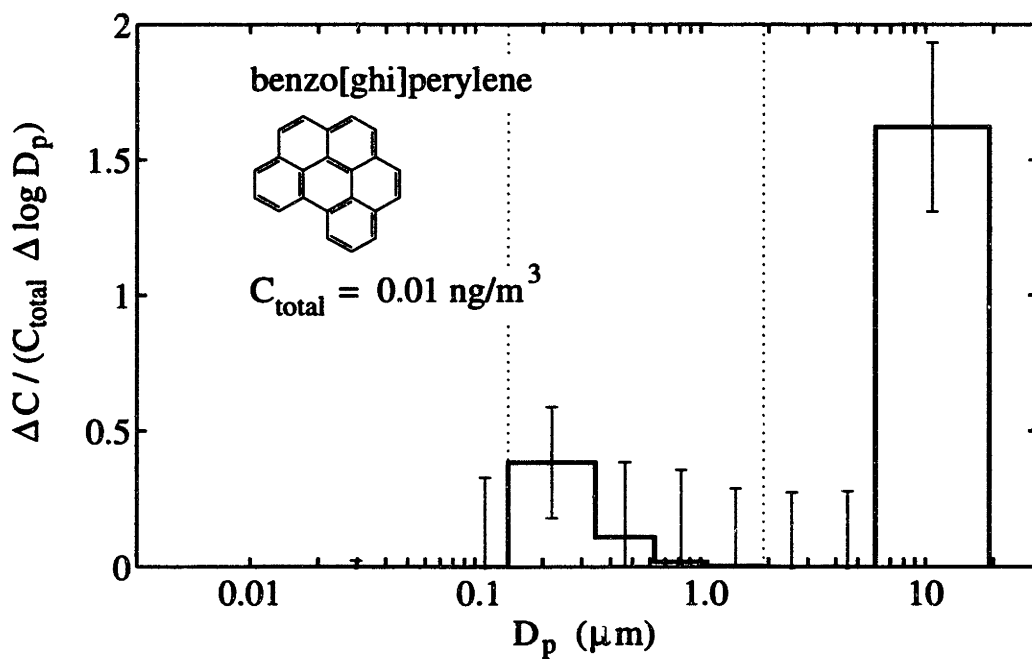


Figure 3-27: Benzo[*ghi*]perylene distribution with particle size in Quabbin Summit aerosol.

Table 3.3: OPAH Identified in Kenmore Square Samples.

OPAH	Molecular Weight	Concentration with Aerosol (ng/m ³)	Fraction with Aerosol Modes		
			Ultrafine	Accumulation	Coarse
1,4-naphthoquinone	158	Identified			
1-acenaphthenone	168	0.264 ± 0.017 ^a	0.043	0.383	0.574
9-fluorenone	180	2.072 ± 0.088	0.050	0.385	0.565
1,8-naphthalic anhydride	198	1.766 ± 0.081	0.084	0.487	0.429
OPAH-208a	208	0.379 ± 0.017	0.048	0.462	0.491
phenanthrenequinone	208	0.427 ± 0.035	0.000	0.343	0.657
OPAH-208b	208	0.041 ± 0.003	0.000	0.516	0.484
11 <i>H</i> -benzo[<i>a</i>]fluoren-11-one	230	1.026 ± 0.037	0.091	0.633	0.276
7 <i>H</i> -benzo[<i>c</i>]fluoren-7-one	230	0.372 ± 0.021	0.109	0.644	0.247
11 <i>H</i> -benzo[<i>b</i>]fluoren-11-one	230	0.852 ± 0.036	0.115	0.690	0.195
benzanthrone	230	1.176 ± 0.060	0.246	0.674	0.080
5,12-naphthacenequinone	258	0.323 ± 0.022	0.151	0.724	0.125
OPAH-248a	248	0.058 ± 0.004	0.351	0.649	0.000
OPAH-254a	254	0.059 ± 0.005	0.187	0.779	0.034
6 <i>H</i> -benzo[<i>cd</i>]pyrene-6-one	254	1.337 ± 0.070	0.362	0.600	0.038
OPAH-272a	272	0.049 ± 0.004	0.498	0.502	0.000
OPAH-280a	280	0.143 ± 0.013	0.194	0.776	0.030
benzo[<i>a</i>]pyrene-6,12-dione	282	0.096 ± 0.009	0.080	0.850	0.070
OPAH-280b	280	0.284 ± 0.018	0.161	0.837	0.002

^aOne standard deviation.

3.4 OPAH in Urban Boston Aerosol

OPAH found in the urban size-segregated aerosol samples are listed in Table 3.3. Compounds listed in Table 2.7 but not in Table 3.3 were not found in the samples. OPAH for which authentic reference standards were available are listed by their chemical name. GC/MS peaks which were tentatively identified as OPAH in the absence of reference standards are designated “OPAH-xy”, where “x” is the mass of the proposed molecular ion, and “y” is a letter to distinguish isomers. Because the MSD was operated in SIM mode, data are available on the abundance of only a few ions; this makes the identification less positive than if complete MS scan data were available. Table 3.4 lists all the tentatively identified OPAH found and the available GC/MS data.

Table 3.4: OPAH Tentatively Identified by GC/MS.

OPAH	Retention Index	Secondary Ion	Relative Abundance	Tentative Identification
OPAH-208a	351.7	180	0.087	dione of M 178 PAH
		152	0.151	
OPAH-208b	369.9	180	0.130	dione of M 178 PAH
		152	1.581	
OPAH-248a	435.8	204	1.280	dicarboxylic acid anhydride of M 178 PAH
		176	1.294	
OPAH-254a	440.3	226	0.183	ketone of M 240 PAH
OPAH-272a	488.2	228	1.272	dicarboxylic acid anhydride of M 202 PAH
		200	1.474	
OPAH-280a	488.6	252	0.155	ketone of dibenzofluorene
OPAH-280b	500.5	252	0.427	ketone of dibenzofluorene

3.4.1 PAH Ketones

Seven PAH ketones, 1-acenaphthenone, 9-fluorenone, 11*H*-benzo[*a*]fluoren-11-one, 7*H*-benzo[*c*]fluoren-7-one, 11*H*-benzo[*b*]fluoren-11-one, benzanthrone, and 6*H*-benzo[*cd*]pyrene-6-one, were identified by comparison with reference standards and quantified (see Table 3.3). In addition three compounds were tentatively identified as PAH ketones in the absence of reference standards. OPAH-254a may be an isomer of 6*H*-benzo[*cd*]pyrene-6-one. OPAH-280a and OPAH-280b were present as minor peaks in the 7*H*-dibenzo[*c,g*]fluoren-7-one reference standard, and are therefore assumed to be isomers of this PAH ketone.

Figures 3-28 through 3-37 show the normalized distributions of PAH ketones with particle size. Comparing OPAH of molecular weight 230, the benzofluorenones have nearly identical distributions, and the benzanthrone distribution is slightly shifted toward smaller particles (see Figures 3-30 through 3-33). PAH ketones tend to distribute to particle size fractions based on molecular weight, with lower molecular weight compounds associated with larger particles. The tentatively identified PAH

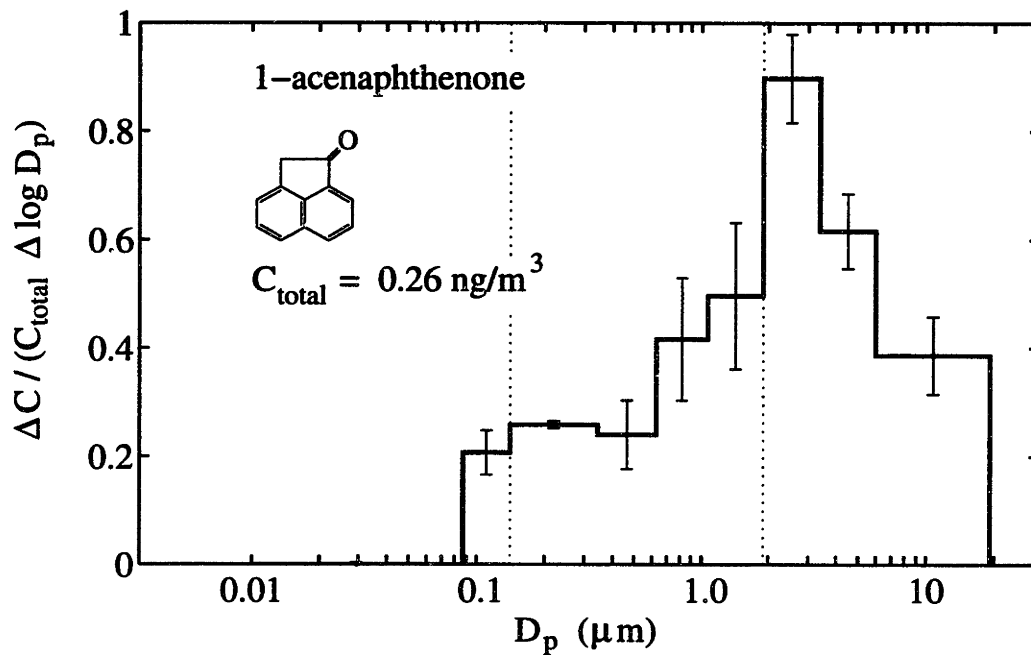


Figure 3-28: 1-Acenaphthenone distribution with particle size in Kenmore Square aerosol.

ketones have distributions with particle size similar to those for positively identified PAH ketones of similar molecular weight.

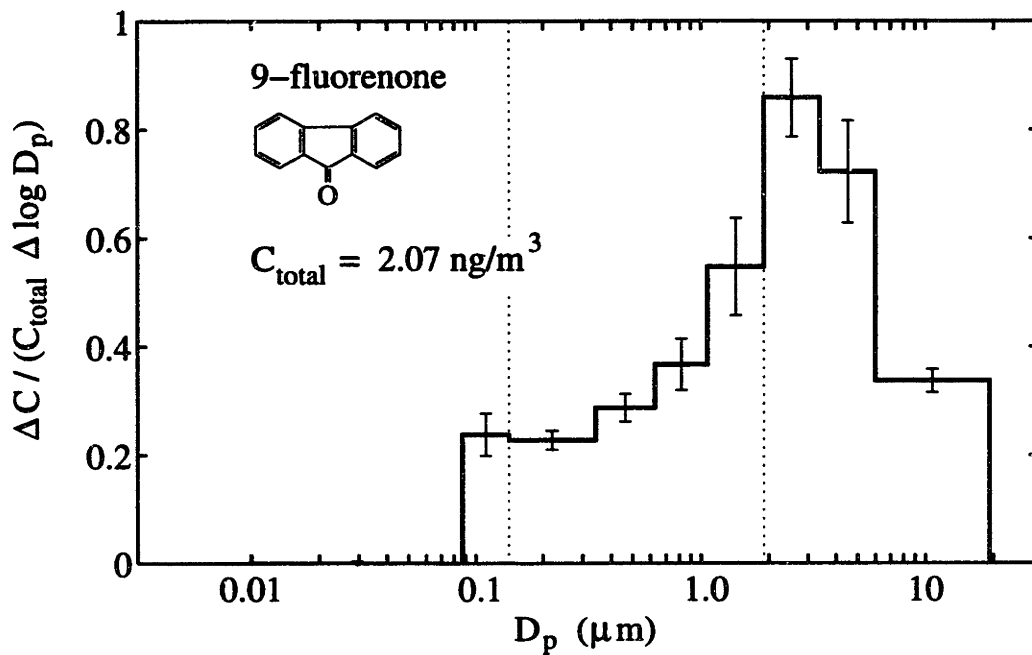


Figure 3-29: 9-Fluorenone distribution with particle size in Kenmore Square aerosol.

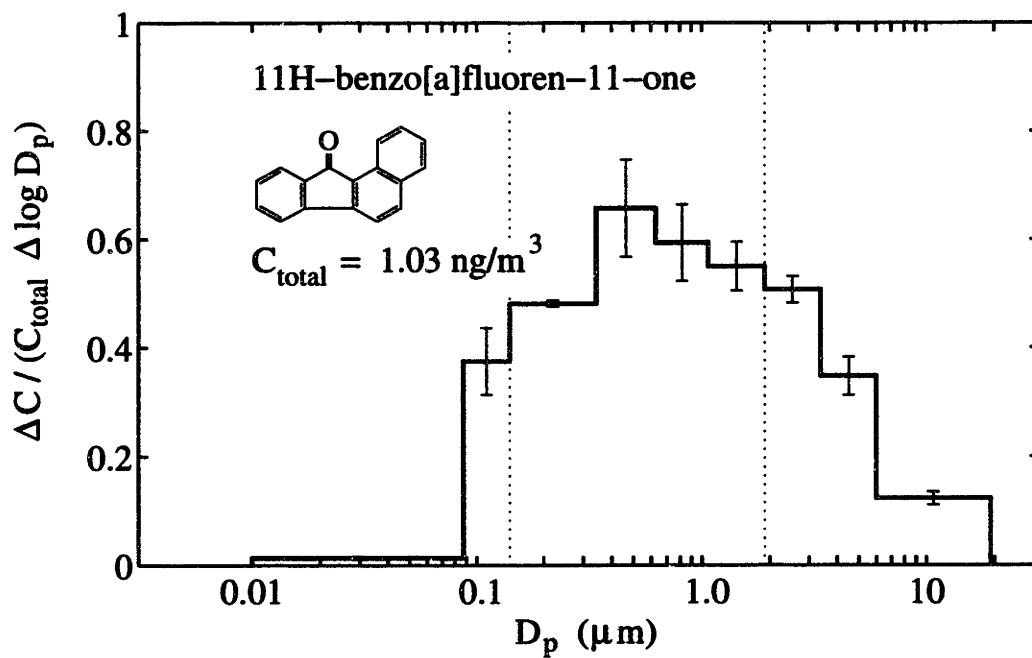


Figure 3-30: 11H-Benzo[a]fluoren-11-one distribution with particle size in Kenmore Square aerosol.

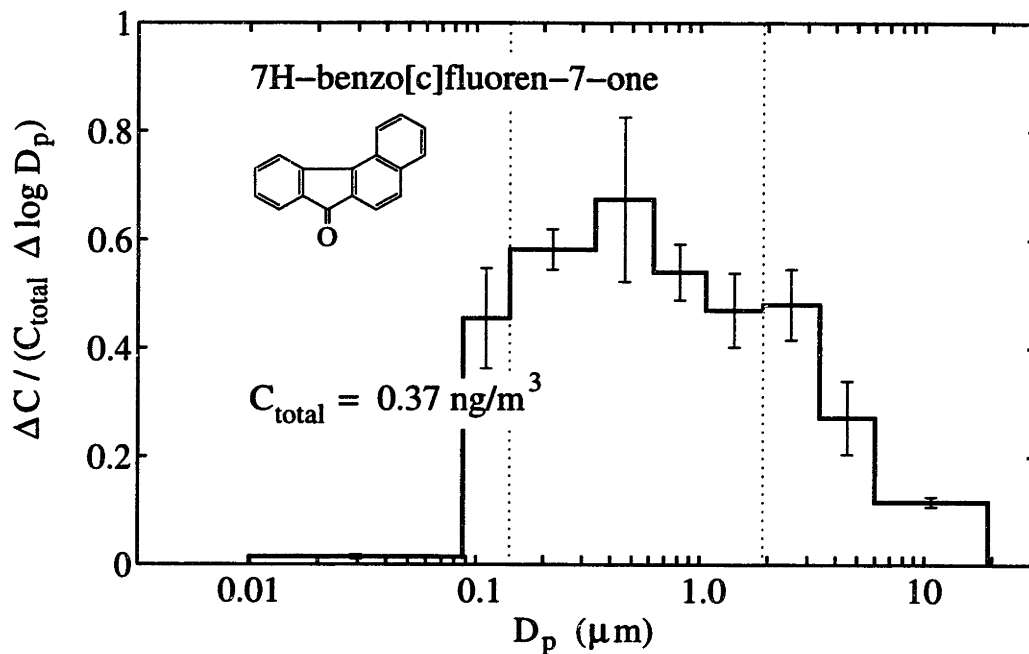


Figure 3-31: 7H-Benzo[c]fluoren-7-one distribution with particle size in Kenmore Square aerosol.

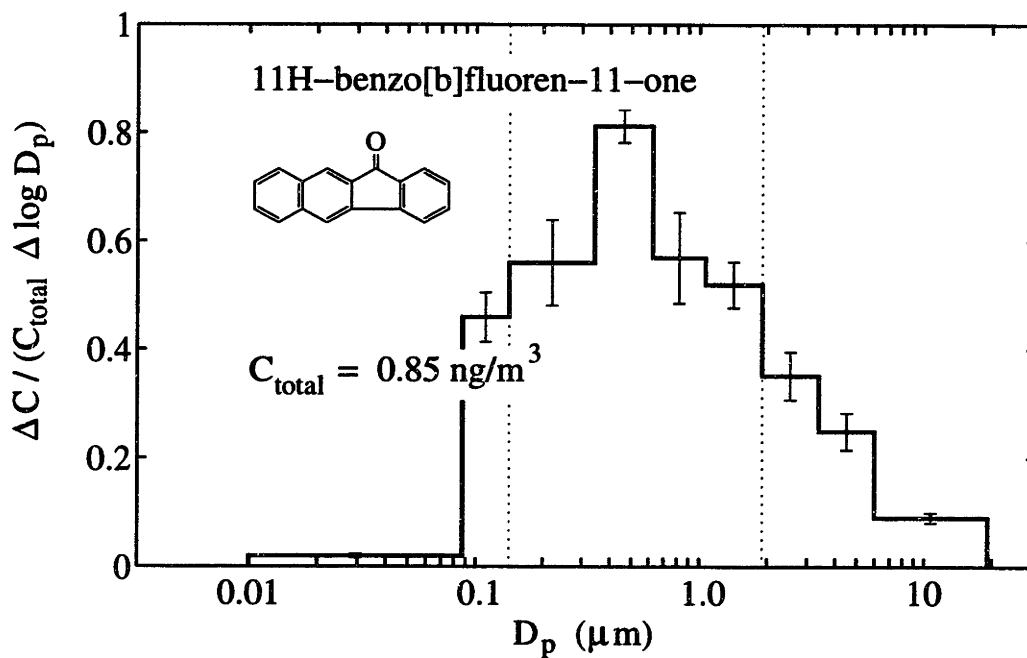


Figure 3-32: 11H-Benzo[b]fluoren-11-one distribution with particle size in Kenmore Square aerosol.

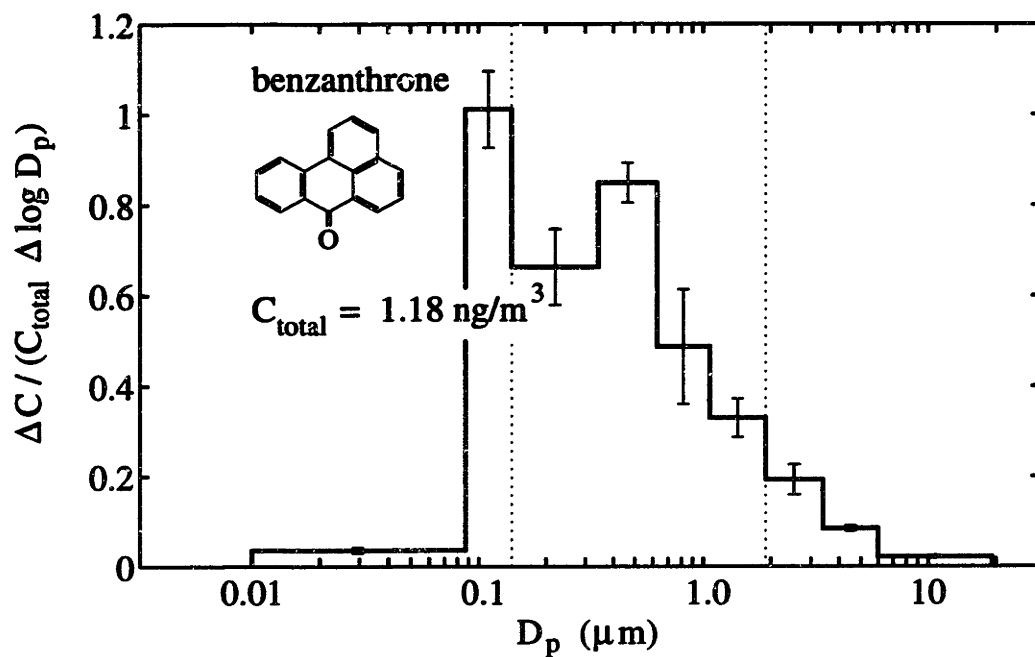


Figure 3-33: Benzanthrone distribution with particle size in Kenmore Square aerosol.

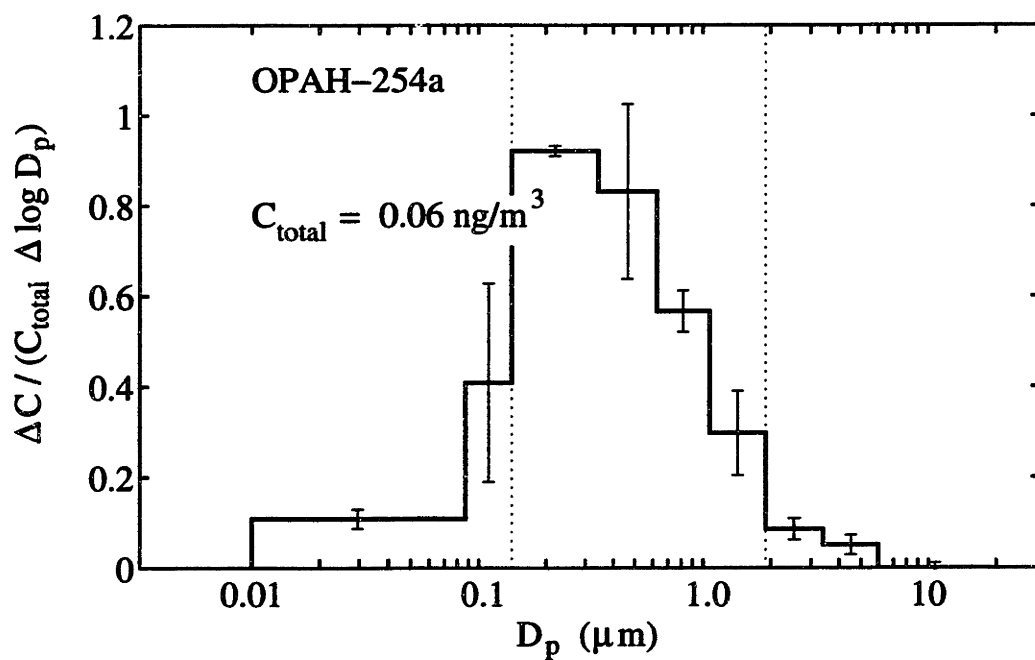


Figure 3-34: OPAH-254a distribution with particle size in Kenmore Square aerosol.

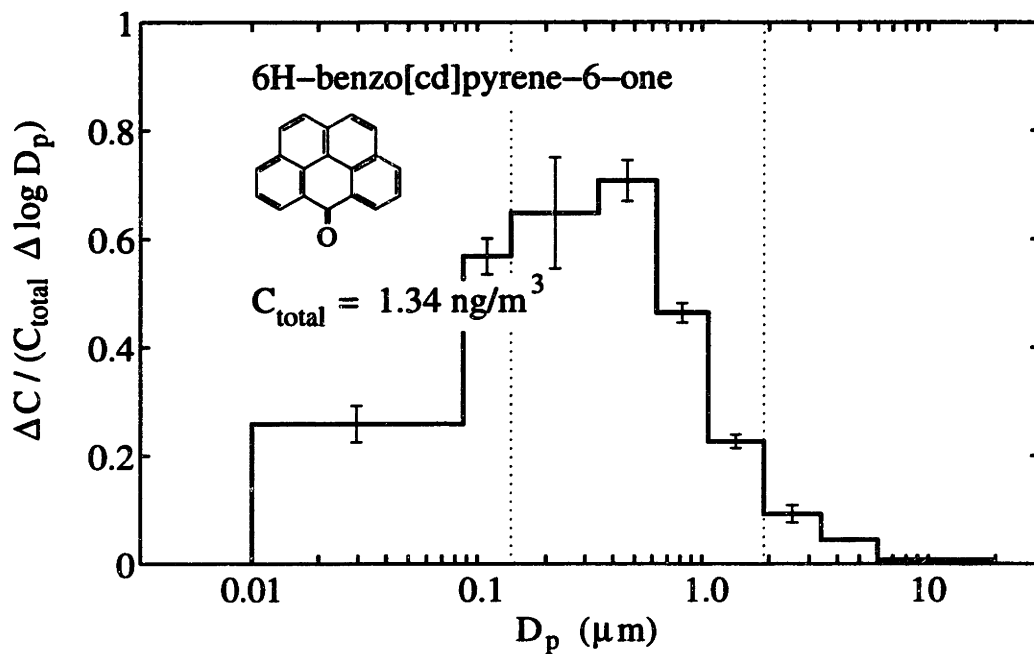


Figure 3-35: 6H-Benzo[cd]pyrene-6-one distribution with particle size in Kenmore Square aerosol.

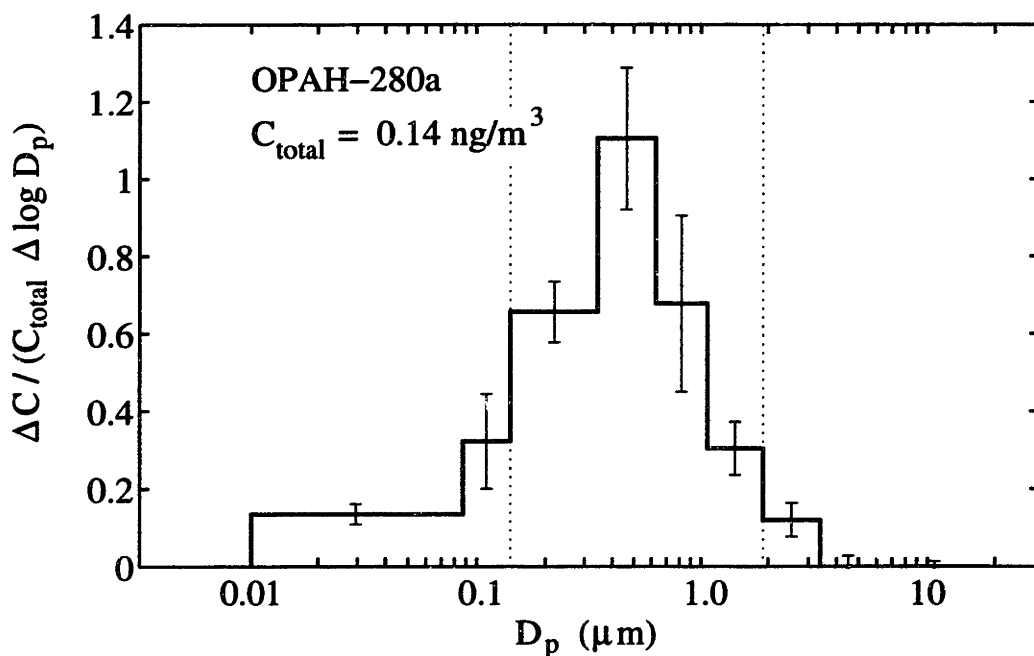


Figure 3-36: OPAH-280a distribution with particle size in Kenmore Square aerosol.

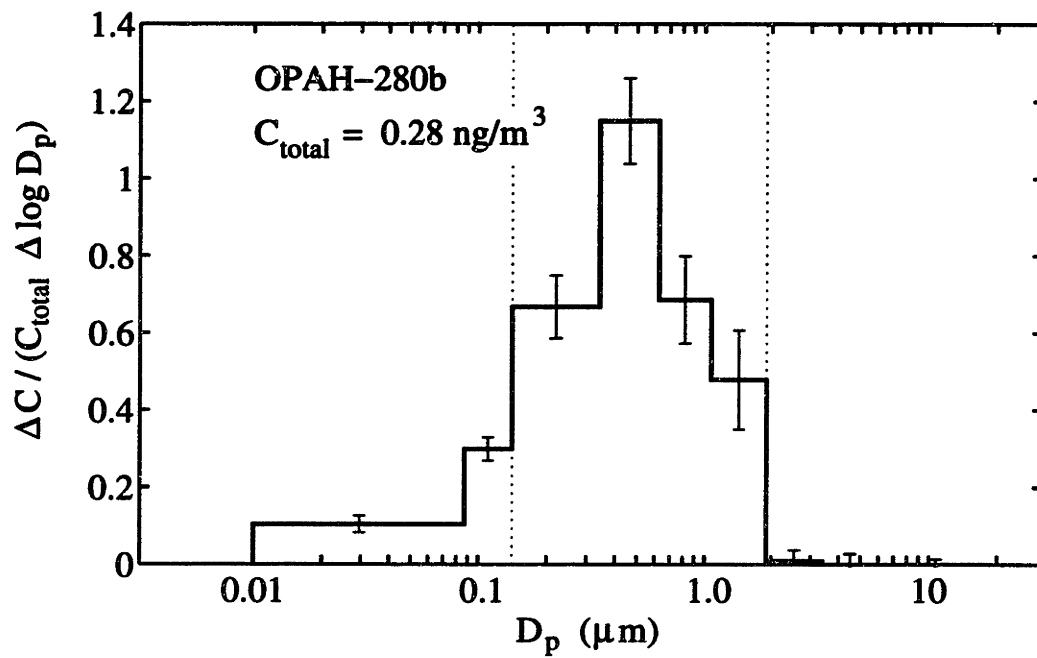


Figure 3-37: OPAH-280b distribution with particle size in Kenmore Square aerosol.

3.4.2 PAH Diones

Four PAH diones, 1,4-naphthoquinone, phenanthrenequinone, 5,12-naphthacenequinone, and benzo[*a*]pyrene-6,12-dione, were identified by comparison with reference standards. In addition, two compounds were tentatively identified as PAH diones in the absence of reference standards. OPAH-208a and OPAH-208b may be diones of phenanthrene or anthracene. Five of these six were quantifiable (see Table 3.3).

The normalized distributions of PAH diones with particle size are shown in Figures 3-38 through 3-42. Like other low molecular weight OPAH, OPAH-208a is distributed with approximately equal amounts in the coarse and fine aerosol fractions. This compound tended to be associated with larger particles than the higher molecular weight PAH diones, in keeping with the general trend that lower molecular weight compounds are associated with larger particles. Benzo[*a*]pyrene-6,12-dione has a unimodal distribution with a peak at $\approx 0.6 \mu\text{m}$. 5,12-Naphthacenequinone, which has a slightly higher molecular weight than benzo[*a*]pyrene-6,12-dione, tends to be associated with larger particles than benzo[*a*]pyrene-6,12-dione.

Phenanthrenequinone and OPAH-208b are distributed differently from other OPAH found in this study. Both compounds were found predominantly in two narrow size ranges centered at $D_p \approx 0.2 \mu\text{m}$ and $D_p \approx 2.5 \mu\text{m}$. Possible causes of these distributions are discussed below.

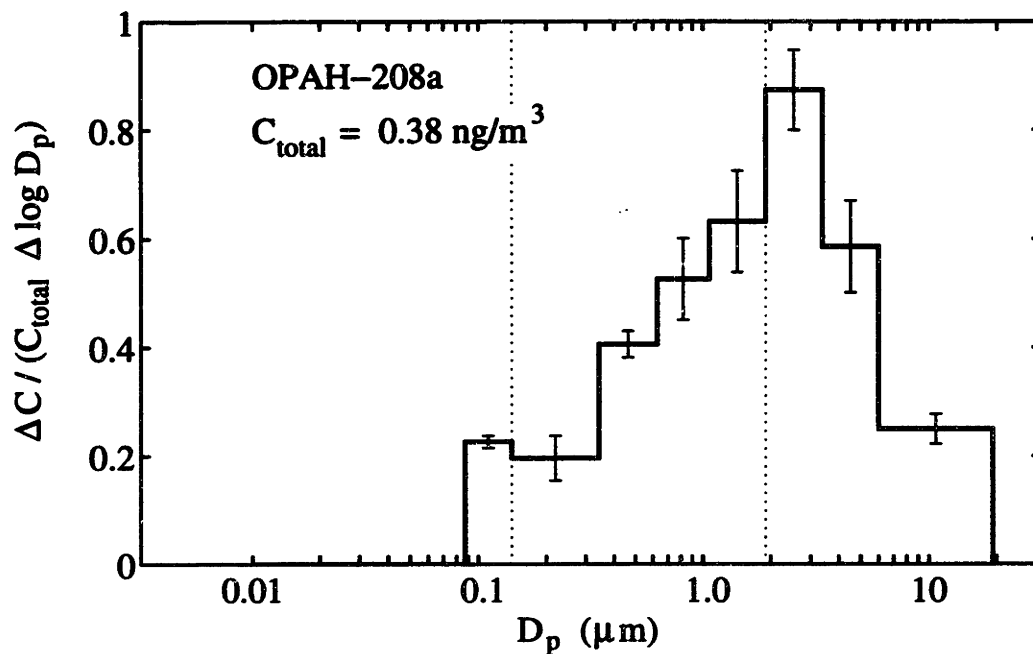


Figure 3-38: OPAH-208a distribution with particle size in Kenmore Square aerosol.

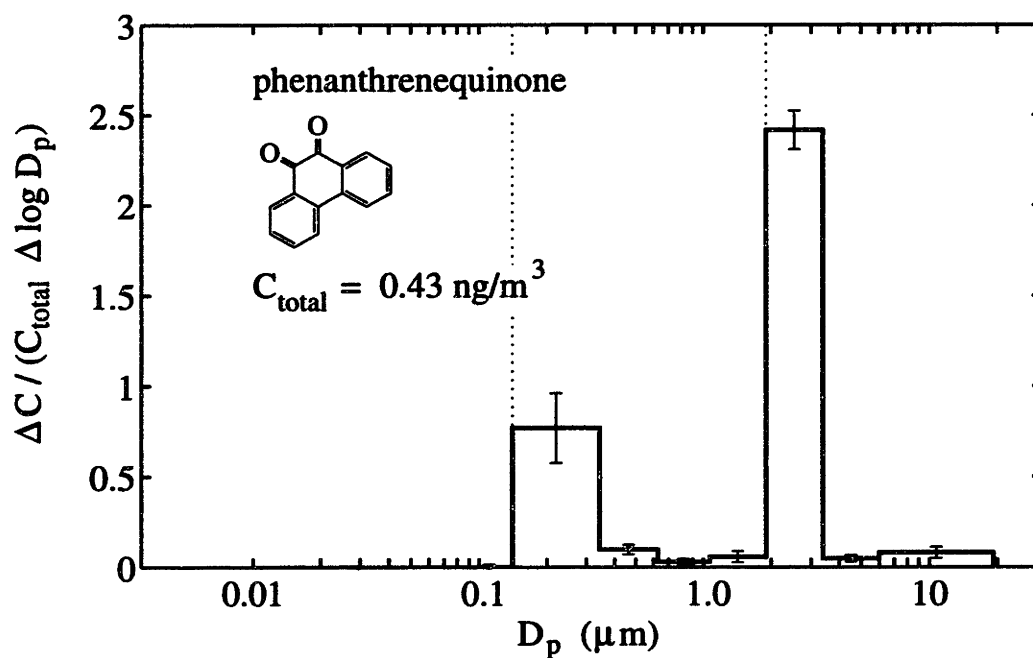


Figure 3-39: Phenanthrenequinone distribution with particle size in Kenmore Square aerosol.

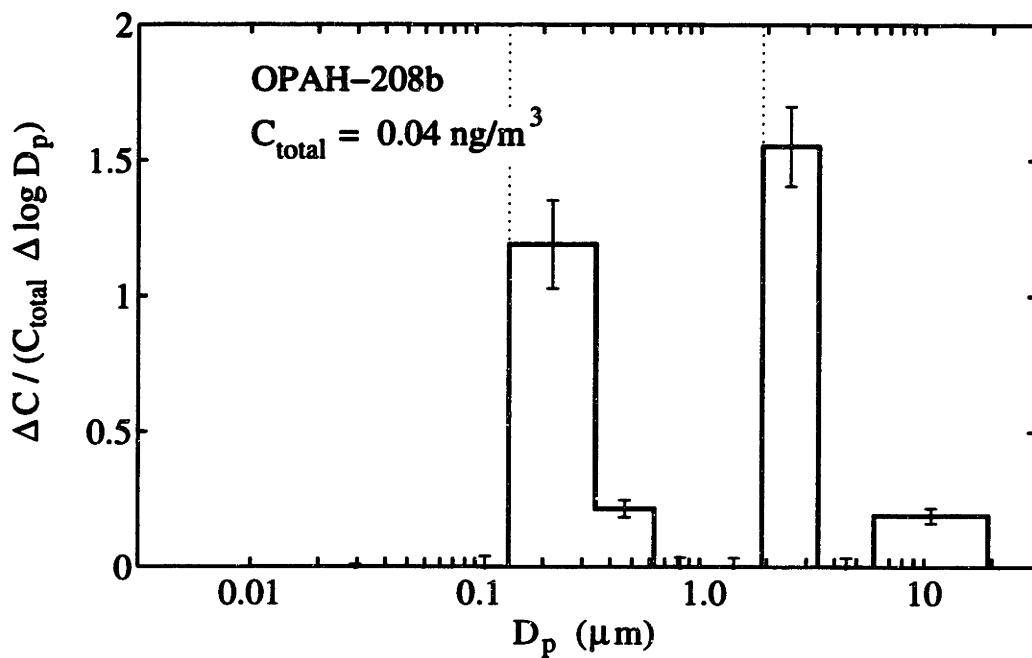


Figure 3-40: OPAH-208b distribution with particle size in Kenmore Square aerosol.

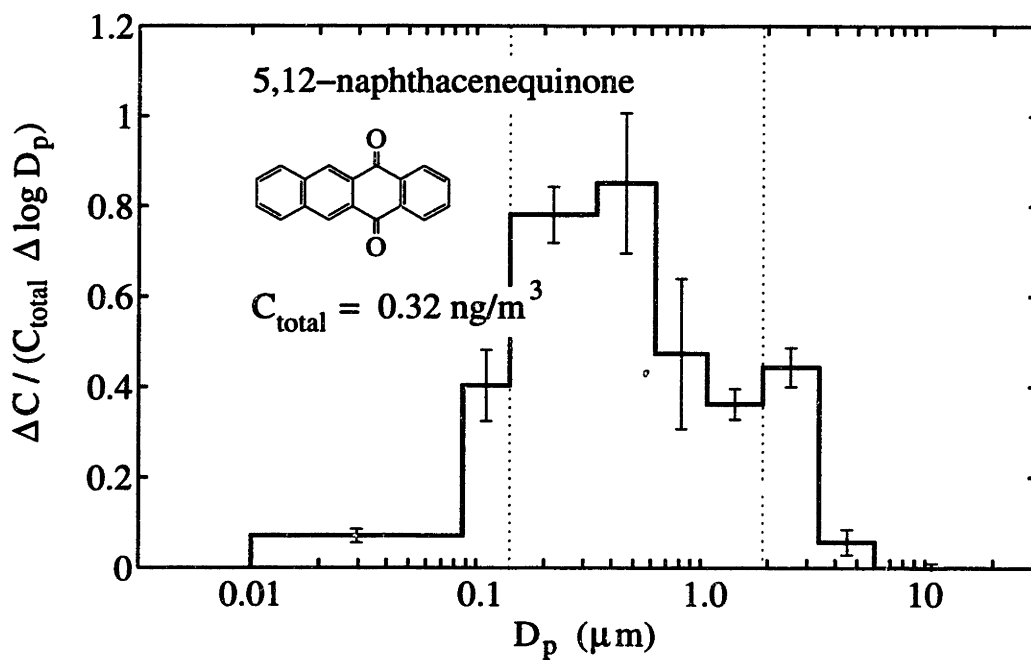


Figure 3-41: 5,12-Naphthacenequinone distribution with particle size in Kenmore Square aerosol.

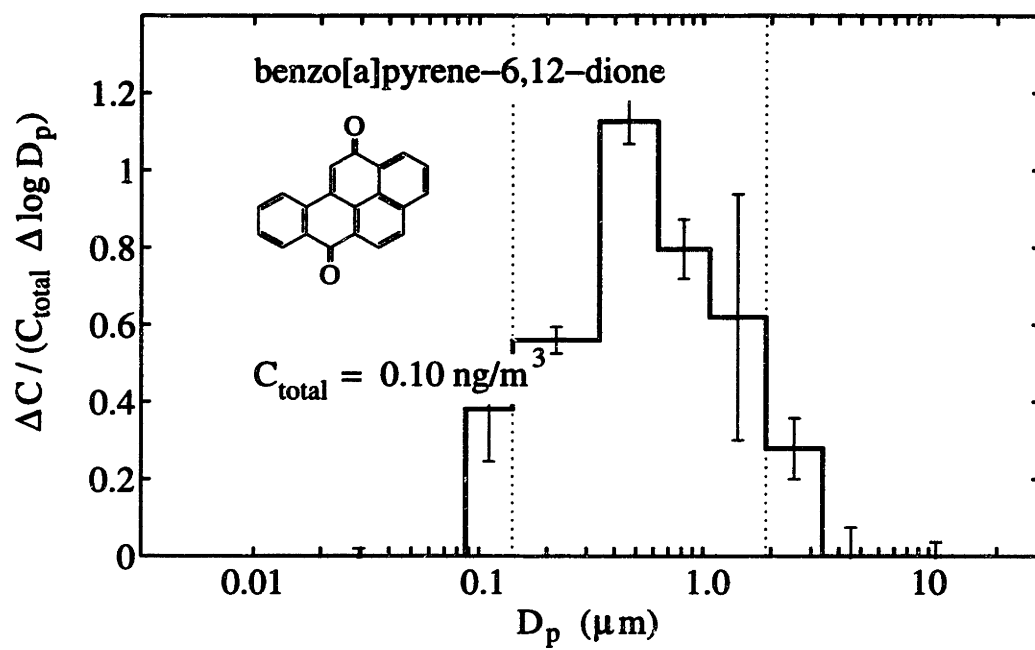


Figure 3-42: Benzo[a]pyrene-6,12-dione distribution with particle size in Kenmore Square aerosol.

3.4.3 PAH Dicarboxylic Acid Anhydrides

One PAH dicarboxylic acid anhydride (PAH DCAA), 1,8-naphthalic anhydride, was identified by comparison with a reference standard and quantified (see Table 3.3). In addition two compounds were tentatively identified as PAH DCAA in the absence of reference standards. Both tentatively identified PAH DCAA, OPAH-248a and OPAH-272a, matched compounds identified in an urban particulate matter reference material (NIST SRM 1649) by others in our laboratory using the same GC/MS system [15]. They operated the MSD in scan mode and obtained complete mass spectra for these compounds. The mass spectra were consistent with DCAA of PAH with 178 and 202 molecular weights, respectively. Therefore these compounds are less tentatively identified than others for which reference standards were not available.

The normalized distributions of the PAH DCAA with particle size are shown in Figures 3-43 through 3-45. Following the trend observed for other OPAH, lower molecular weight PAH DCAA were associated with larger particles. In contrast to most PAH ketones and diones, large fractions of the higher molecular weight PAH DCAA were found in the ultrafine fraction.

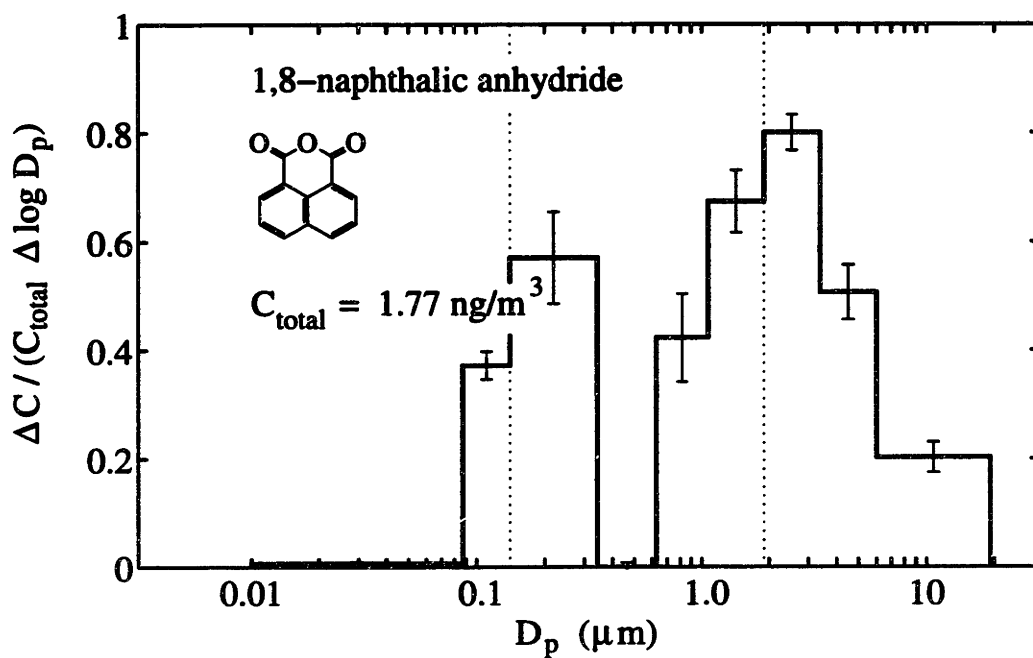


Figure 3-43: 1,8-Naphthalic anhydride distribution with particle size in Kenmore Square aerosol.

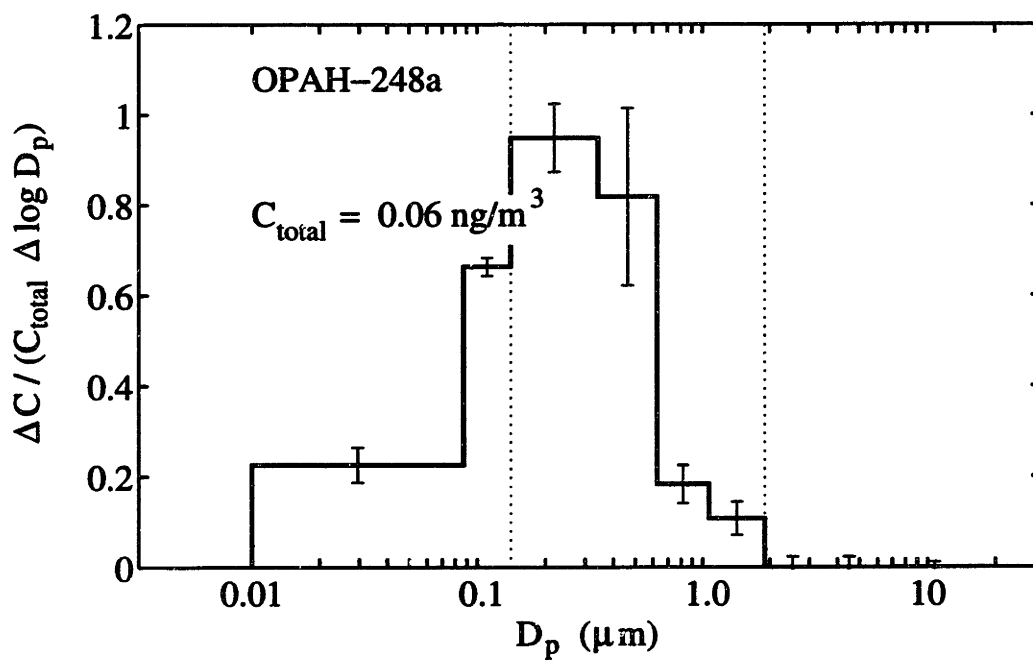


Figure 3-44: OPAH-248a distribution with particle size in Kenmore Square aerosol.

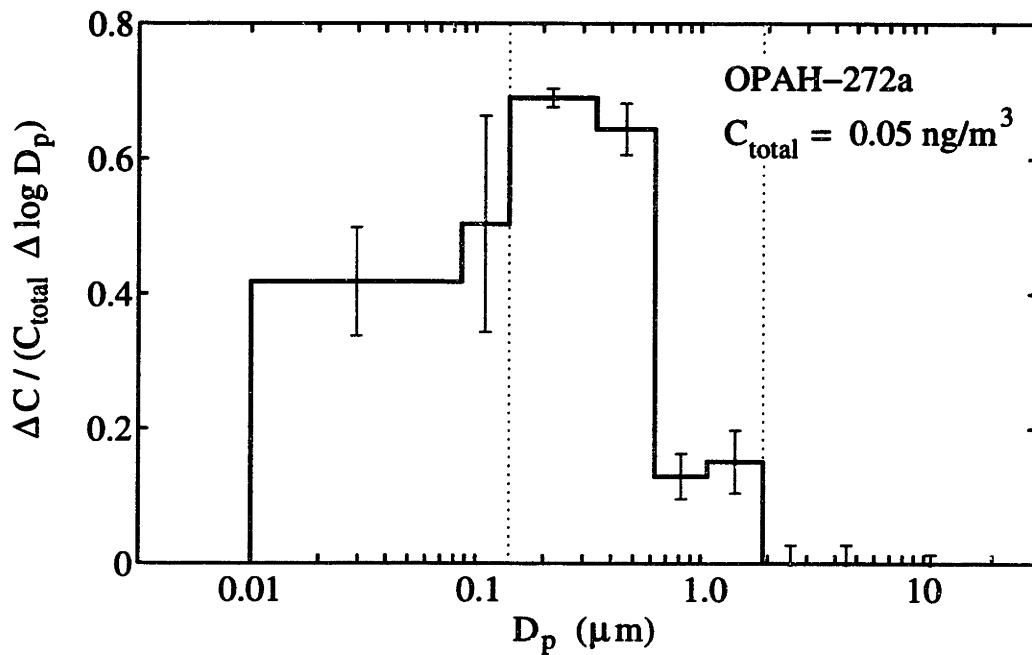


Figure 3-45: OPAH-272a distribution with particle size in Kenmore Square aerosol.

3.5 Qualitative Discussion of PAH Partitioning

PAH are mainly generated by combustion sources which also emit mainly fine particles [32, 34, 36]. Therefore PAH are emitted in the gas phase or associated with fine particles. PAH can become associated with coarse particles either by the growth of fine combustion generated particles, or by volatilization from fine particles followed by sorption onto coarse particles. If the main mechanism for PAH association with coarse particles were the growth of combustion generated particles, the mixture of PAH in fine and coarse particles would be similar. Figure 3-46 demonstrates that this is not observed. Instead, the fraction of PAH associated with coarse urban particles monotonically decreases from approximately 0.55 for PAH of molecular weight 178 to less than 0.1 for PAH of molecular weight greater than 252.

One explanation for the observed PAH partitioning is that PAH, especially higher molecular weight PAH, do not attain an equilibrium distribution in urban aerosols. The flux of PAH from fine combustion-generated particles to coarse particles by volatilization and sorption is directly related to the gas phase concentration of PAH. It has been shown that experimentally measured gas phase concentrations of PAH in urban samples correlate with their subcooled liquid vapor pressures [88]. PAH vapor pressures are strongly correlated with molecular weight. For example, the estimated sublimation pressures at 25°C for phenanthrene, pyrene, and coronene are 1.6×10^{-2} , 6.0×10^{-4} , and 1.9×10^{-10} Pa, respectively [113, 114]. Because high molecular weight PAH have much lower fluxes by volatilization and sorption, their time to partition to larger particles is much greater than that for the lower molecular weight PAH.

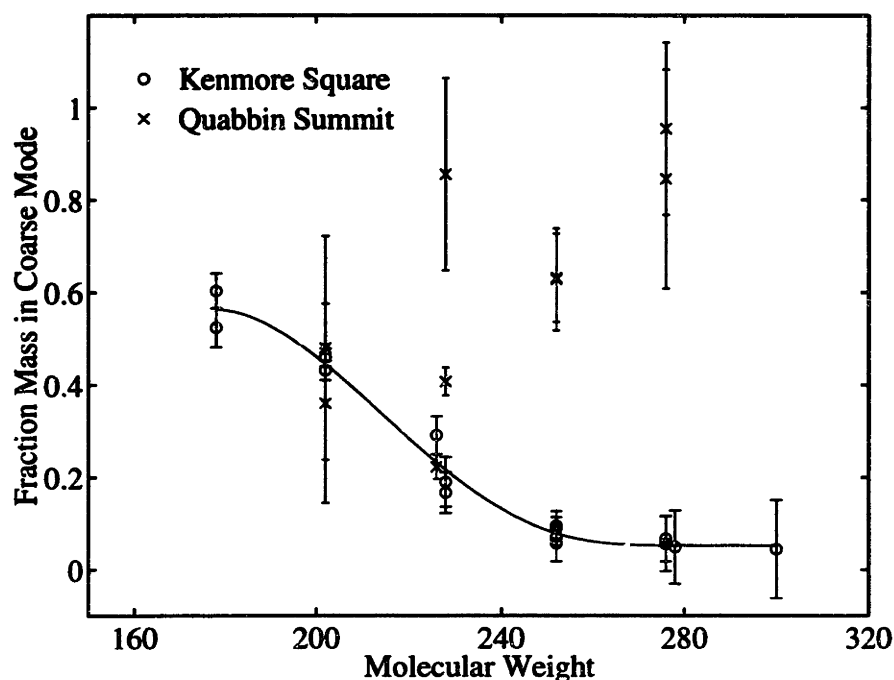


Figure 3-46: Fraction of PAH associated with coarse particles ($D_p > 1.9 \mu\text{m}$) in the Kenmore Square (○) and Quabbin Summit (×) samples.

Therefore they tend to remain on particles with which they were emitted.

Other studies of PAH associated with size-segregated aerosols have found that PAH tend to partition to larger aerosols to a greater degree in warmer periods [68, 93, 94, 95]. It has also been found that the fraction of PAH in the gas phase increases with temperature [40, 80]. An increase in the fraction of PAH in the gas phase would increase the flux of PAH by volatilization and sorption, leading to faster equilibration of PAH among aerosol size fractions, in agreement with these experimental observations.

It has been suggested that the observed partitioning of PAH as a function of molecular weight may be due to lower molecular weight PAH being co-emitted with larger particles, for example in meat cooking emissions. While some authors have

found that PAH emission profiles can be correlated with source types, the amount of PAH emitted has not been shown to vary monotonically with molecular weight for noncatalyst and catalyst-equipped automobiles, diesel trucks, or meat cooking [85, 33, 34]. Unless a correlation between source type and PAH molecular weight is established, this hypothesis can be put aside.

Individual PAH may be preferentially removed from the atmosphere by photooxidation. If PAH reactivity were correlated with molecular weight, higher molecular weight PAH might be rapidly removed by photooxidation soon after vaporizing from a particle. In this case little of the higher molecular weight PAH would be able to sorb from the gas phase to large particles. Condensed phase photooxidation might also explain the observed PAH partitioning behavior. If photooxidation of higher molecular weight PAH associated with large particles were rapid, then little of these compounds would remain with the large particles. Measurements of the rates of PAH disappearance in wood smoke and sorbed on fly ash, however, show that PAH reactivity is not correlated with molecular weight [115, 78]. Instead, Behymer and Hites found that PAH reactivity was correlated with the maximum net atomic charge which is independent of PAH molecular weight [78]. Because photooxidation is not correlated with molecular weight, the observed partitioning cannot be explained by photooxidation.

Differences in chemical affinities between PAH and particles of different size could also explain the observed PAH partitioning. As PAH molecular weight rises, PAH become more hydrophobic, as demonstrated by the *n*-octanol—water partition coefficient, which increases with PAH molecular weight [116]. If we hypothesize that coarse

particles contain a larger fraction of water, higher molecular weight PAH would tend to partition to the smaller particles. Similarly, if we hypothesize that high molecular weight PAH adsorb more strongly than lower molecular weight PAH, then high molecular weight PAH would tend to associate with the fine aerosol fraction which has a much higher surface area than the coarse fraction [22].

Figure 3-46 shows that the fraction of PAH associated with coarse particles in the rural samples is nearly constant at approximately 0.55, with the exception of benzo[ghi]fluoranthene. It should be noted that direct comparisons of partitioning between different aerosol samples cannot be made. This is because the nature (e.g. sources, chemical compositions and size distributions) and histories (e.g. temperature, humidity and photooxidation profiles) of the aerosols vary greatly with location, season, and weather. However, the observed differences in partitioning at urban and rural sites are consistent with the hypothesis that PAH mass transfer among urban particles is incomplete. On time scales relevant to urban aerosols, higher molecular weight PAH would remain with the particles with which they were emitted. But on time scales relevant to regional transport, all PAH would distribute more closely toward equilibrium. With this explanation, the rural data indicate that at equilibrium at least 50% of PAH will be associated with coarse particles in rural air.

3.6 Qualitative Discussion of OPAH Partitioning

Both direct emissions from combustors and photooxidation of PAH have been proposed as important sources of OPAH in the atmosphere [63, 66, 56, 67]. In the case of

combustion emissions, OPAH emitted would be initially released in the gas phase or associated with fine particles since combustors emit mainly fine particles [32]. Combustion generated OPAH would then be expected to have distributions with particle size similar to those of PAH, which are generated only by combustion.

Photooxidation reactions to produce OPAH may occur in the gas phase, on solid particles, or in liquid particles. For condensed phase reactions, the rates of PAH photooxidation have been shown to be highly dependent on the nature of the sorbent particle or the composition of the solution [78, 117]. Because detailed information on the nature of sorbent particles is not available, we focus on the partitioning of OPAH formed by gas phase photooxidation.

Once formed by gas phase photooxidation, the products undergo mass transfer from the gas phase to particles. These products are initially distributed among particle size fractions in proportion to the mass transfer rate. Mass transfer between spherical particles and a stagnant fluid is developed in Section 7.3. The rate of mass transfer in the continuum regime is proportional to D_p . The initial distribution of photooxidation products are therefore in proportion to the first moment of the particle number distribution with D_p . The first moment of Whitby's average aerosol distribution has a single peak at $\approx 0.1 \mu\text{m}$ [22]. This is similar to the size distribution of combustion particles [118]. Since the initial distributions of compounds generated by combustion and photooxidation are similar, the source of these compounds cannot be determined by measurements of their distribution with particle size.

Once associated with fine particles, OPAH formed by either combustion or photooxidation will migrate from the fine particles to coarse particles by volatilization

and sorption. The rate of this flux is directly related to the gas phase concentration of OPAH. Because higher molecular weight OPAH generally have much lower vapor pressures, the time needed for them to partition to large particles is much greater than that for lower molecular weight OPAH. Therefore, high molecular weight OPAH generated by combustion or photooxidation, tend to remain with the fine particles with which they were initially associated while lower molecular weight OPAH partition to other particles.

OPAH formed by photooxidation will undergo vaporization and sorption at a rate substantially slower than the PAH reactants since the equilibrium vapor pressure of the photooxidation products are expected to be much less than that for the PAH reactants. For example, the sublimation pressures of fluorene and 9-fluorenone at 298 K are 7.9×10^{-2} and 1.6×10^{-2} Pa, respectively [114, 119].

A useful measure of partitioning among aerosol size fractions is the mass fraction of a compound found with the coarse particles. Figure 3-47 shows the fraction of OPAH, by compound class and molecular weight, associated with coarse particles in the urban aerosol. The line shown is a curve fit to the PAH data (see Figure 3-46). Like PAH, lower molecular weight OPAH are observed to associate to a greater degree with coarse particles. The relation between molecular weight and fraction associated with the coarse particles for PAH ketones is remarkably similar to that for PAH. PAH diones seem to partition to coarse particles to a greater extent than PAH of the same molecular weight; PAH DCAA to a lesser extent.

The differences in partitioning with molecular weight among compound classes can be explained by noting that partial pressure in the atmosphere, not molecular weight,

will determine the rate of flux by evaporation and sorption. The fraction of PAH in the gas phase has been shown to correlate with its pure component vapor pressure [88]. Sublimation pressures at 298 K ($p_S(298\text{ K})$) for 9-fluorenone and benzanthrone are 1.6×10^{-2} and 2×10^{-5} Pa, respectively [119, 120]. These values are close to the extrapolated sublimation pressures of PAH of similar molecular weight. The vapor pressures of 9-fluorenone can be compared with phenanthrene, $p_S(298\text{ K}) = 1.6 \times 10^{-2}$ Pa, and anthracene, $p_S(298\text{ K}) = 7.9 \times 10^{-4}$ Pa; and that of benzanthrone with benz[*a*]anthracene, $p_S(298\text{ K}) = 2.7 \times 10^{-5}$ Pa, chrysene, $p_S(298\text{ K}) = 1.2 \times 10^{-6}$ Pa, and triphenylene $p_S(298\text{ K}) = 4.2 \times 10^{-6}$ Pa [114, 121]. The similar correlation of sublimation pressures with molecular weights for PAH and PAH ketones leads to an identical dependence with molecular weight of the fraction of the compounds associated with coarse particles. One can hypothesize that PAH diones have higher vapor pressures than PAH of the same molecular weight, therefore are associated to a greater degree with large particles. Similarly, PAH DCAA may tend to be associated with smaller particles because their vapor pressures are lower than those of PAH of the same molecular weight.

Two OPAH have size distribution profiles distinct from the PAH and most other OPAH. These compounds, 9,10-phenanthrenequinone and OPAH-208b, have distinct bimodal distributions with peaks at $D_p \approx 0.2\ \mu\text{m}$ and $D_p \approx 2.5\ \mu\text{m}$. An explanation for these distributions is that these OPAH have very different sorption behavior from PAH and other OPAH, and therefore partition to a different aerosol fraction. The existence of chemically distinct aerosol fractions has been recently observed by analyses of single atmospheric particles [24, 25]. The distributions of PAH and other OPAH

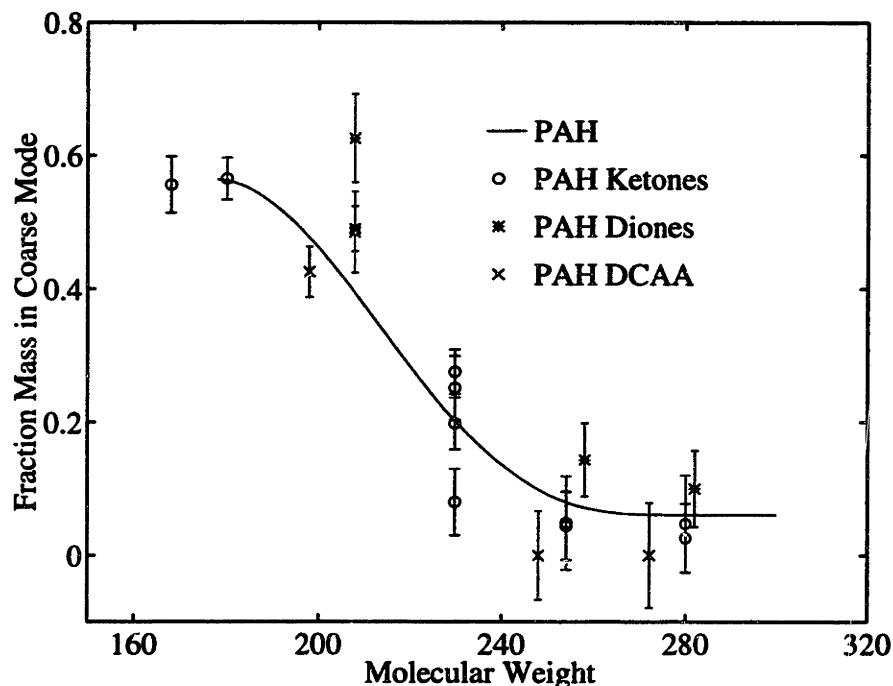


Figure 3-47: Fraction of PAH and OPAH associated with coarse particles ($D_p > 1.9 \mu\text{m}$) in an urban aerosol.

with particle size, in contrast, are approximately unimodal indicating that the aerosol fraction with which they associate also has a unimodal distribution. In contrast, the aerosol fraction with which 9,10-phenanthrenequinone and OPAH-208b associate has a bimodal distribution.

These results are consistent with the conclusion that most OPAH, like PAH, are primarily generated with small particles by combustors and partition to large particles by vaporization and sorption. For high molecular weight, low vapor pressure, compounds, mass transfer by vaporization and sorption will be slow and the compounds will not reach equilibrium partitioning in an urban aerosol. However the hypothesis that OPAH are generated mainly by photooxidation cannot be dismissed.

3.7 Conclusions

PAH are emitted with fine particle by combustion then partition to larger particles by vaporization and sorption. OPAH are emitted with fine particle by combustion or initially associate with fine particles after formation by gas phase photooxidation. Like PAH, they partition to larger particles by vaporization and sorption. On time scales relevant to urban aerosols, PAH and OPAH, especially high molecular weight species, do not attain equilibrium distribution among aerosol particles.

If PAH and OPAH do not attain equilibrium with urban aerosols due to slow mass transfer, there are important consequences for modeling the environmental fate of these compounds. Partitioning in the urban atmosphere cannot be assumed to be in equilibrium. Indeed the time scales to attain equilibrium partitioning may be on the order of time scales for photooxidation, deposition and coagulation, necessitating complex models which include these mechanisms.

The present conclusion, that organic compounds distribute very differently among aerosol size fractions based on their sorption behavior, implies that to predict the environmental fate of, and human exposure to, semi-volatile organics, one must understand the sorption behavior of these compounds to atmospheric particles. The simplistic assumption that all semi-volatile organics partition equally among atmospheric particles based on surface area or volume, must be revised to explain the complex, compound-dependent partitioning observed in these samples.

Chapter 4

Absorption Artifact Experiment

4.1 Introduction

The previous two chapters discussed the collection of size-segregated particles from the atmosphere by inertial impaction and the analysis of these samples for PAH and OPAH. Accurate size-segregation by impaction requires that all particles striking the impaction medium adhere to it. Particles which strike the impaction medium may rebound from it. Particles may also strike built-up deposits and re-entrain previously collected material. These sampling artifacts are indistinguishable from each other and are collectively called “particle bounce”. Particles which are not collected on the correct stage may be collected on lower stages, skewing the measured size distribution toward smaller particles. The collection efficiency of solid particles impacting on uncoated surfaces reaches a maximum near the designed aerodynamic cut-off diameter [122]. Particles which bounce off their designed collection stage will then be more likely to bounce off subsequent stages. This is of particular concern

when an after filter is used to collect particles which are not collected on the last impaction stage, as particles which bounce off the last stage will be collected there.

The use of oiled impaction media has been recommended to reduce particle bounce. Rao and Whitby found that the particle bounce artifact was eliminated by using oil-coated plates for low particle loadings [106]. Turner and Hering investigated the particle bounce artifact for high particle loadings [107]. They found that, even for high particle loadings, more than 90% of solid particles were collected on impaction media of 10 μm pore size PTFE membranes impregnated with moderate viscosity (30–300 centistokes) oil.

Oiled impaction media have been used recently for the collection of size-segregated atmospheric particles which were analyzed for PAH [94, 103]. A significant fraction of lower molecular weight PAH have been reported to partition to the gas phase in the atmosphere [40, 48, 80, 123, 64]. These compounds are readily soluble in oils and may absorb from the gas phase into the oiled impaction media during atmospheric sampling. Such absorption would artificially increase the amount of PAH attributed to the aerosol. The absorption artifact might also distort the measured distribution of PAH with particle size from that actually present in the aerosol.

We have reported on PAH analyses of size-segregated atmospheric aerosol samples collected in a micro-orifice impactor (MOI) on impaction media of PTFE membranes impregnated with dibutyl phthalate [103]. The objective of this chapter is to measure in the laboratory the absorption artifact for pyrene in this sampling system. An empirical description of the experimental results is then used to estimate the effect of the absorption artifact on measurements of PAH in size-segregated atmospheric

aerosols.

4.2 Experimental Method

4.2.1 Apparatus

The apparatus used in this work is shown schematically in Figure 4-1. Approximately 30 L/min of pressurized nitrogen was metered into the apparatus at the first valve. The gas flow was then split and approximately 30% of the flow passed through the pyrene saturator. The pyrene saturator was a column, 50 mm in diameter and 120 mm high, packed with 6 mm glass beads coated with pyrene. The saturator was immersed in a constant temperature water bath maintained at 32°C. The saturated N₂ stream was then mixed with the remainder of the flow. The main gas stream was then passed through a quartz filter to remove any suspended particles. The filter medium was a Pallflex (Putnam, CT) Tissuquartz 2500 QAT-UP quartz fiber filter which was baked by the manufacturer. Following the filter, the gas flow entered the impactor. The apparatus was controlled so that the pressure at the impactor inlet was 1.0 atm and the flow to the impactor was 30 L/min. Excess gas was vented to a hood. The vacuum pump used was a graphite vane Gast (Benton Harbor, MI) Model 523.

The cascade impactor used was a micro-orifice impactor (MOI) manufactured by MSP Corporation (Minneapolis, MN) [104]. The MOI has nine stages designed to collect particles from 18.0 to 0.08 μm (see Table 2.2). The impaction media were PTFE membranes with an underlay of aluminum foil. The PTFE membranes used

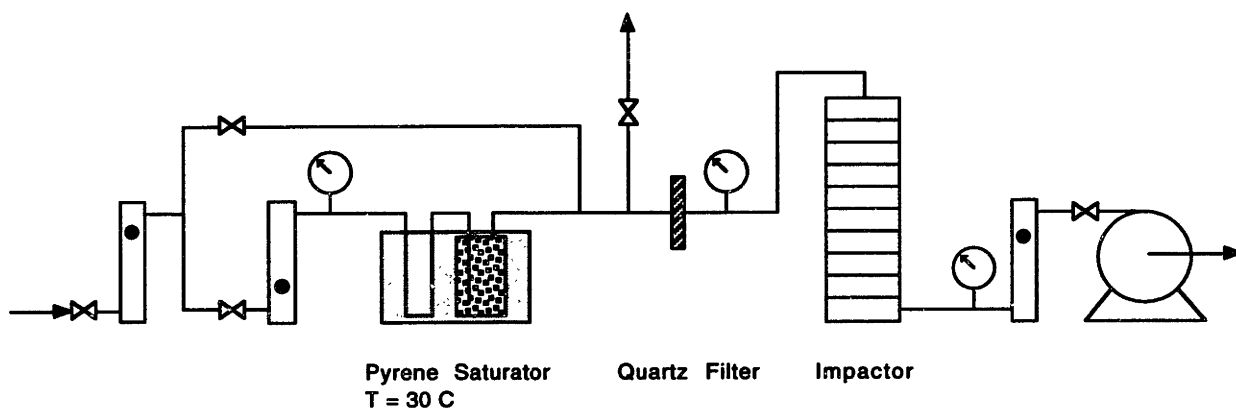


Figure 4-1: Experimental apparatus to measure absorption of pyrene in greased impaction media.

in this work were Millipore (Bedford, MA) Mitex 10 μm pore size membranes. PTFE membranes were cleaned by sonication in DCM for 5 minutes. The aluminum was cleaned with DCM in a Soxhlet extractor for 24 hours. Each impaction medium was coated with approximately 0.1 mL of a 20% by weight solution of dibutyl phthalate in cyclohexane. Media blanks were prepared in the same manner as the sampling media.

Pyrene was chosen as the PAH for this experiment because it fluoresces visible light and has an intermediate sublimation vapor pressure. Too high a sublimation pressure would have caused the experimental results to be affected by transient effects of starting and stopping the experiment. Too low a sublimation pressure would have resulted in the amount absorbed being below the detection limit of the HPLC system used.

4.2.2 Sample Analysis

The sampling media were removed from the impactor then covered with approximately 20 mL DCM and sonicated for 30 min. This solution and additional DCM used to rinse the jar were then filtered by syringe using a 0.2 μm pore size PTFE filter. The filtrate was evaporated to a volume of approximately 10 mL in a vacuum centrifuge and further evaporated to approximately 0.1 mL under clean dry N_2 at room temperature. Samples then were exchanged into 1.0 or 2.0 mL of dimethyl sulfoxide (DMSO).

Pyrene quantification was performed by high pressure liquid chromatography (HPLC) with spectrophotometric detection. The system used was an HP Model 1050 pumping system coupled to an HP Model 1040M, Series II, 190-600 nm diode array detector. Data acquisition and analysis were performed with HP ChemStation software running on a personal computer. A Vydac (Hesperia, CA) reverse phase C_{18} analytical column was used. The column was 25 cm in length, 0.46 cm in diameter, and packed with 5.0 μm (average particle size) C_{18} material. The mobile phase at the start of a run was a 60:40 solution of $\text{H}_2\text{O}:\text{CH}_3\text{CN}$ ramped to 100% CH_3CN in 35 minutes. The flow rate was 1.5 mL/min. Twenty μL aliquots of the samples were injected in triplicate. Pyrene was identified by comparing the retention time and observed uv spectra over the range 190–600 nm with those of an authentic pyrene standard. Pyrene was quantified by comparing the uv absorption at 368 nm with calibration standards injected at concentrations of 5–100 $\mu\text{g}/\text{mL}$. The limit of quantification for pyrene was 5 $\mu\text{g}/\text{mL}$.

With the set of samples from each experiment, a method blank, an extraction test sample, and a recovery test sample were prepared and analyzed. None of the method blanks had a measurable amount of pyrene. The extraction test samples were prepared by extracting the stage 4 or 6 samples a second time. None of the extraction test samples had a measurable amount of pyrene, indicating that 30 minute sonication in DCM completely extracted the absorbed pyrene. For the recovery tests, a known amount of pyrene was added in cyclohexane solution to an impaction medium. The results presented for impaction media analysis are corrected for the average recovery efficiency, 90%.

4.2.3 Saturator Performance

The pyrene saturator was tested by replacing the impactor with two solvent traps in series. The solvent traps were packed beds of 6 mm glass beads, 50 mm in diameter and 120 mm high, filled with approximately 125 mL of DCM. The apparatus was operated with the same flow rates as with the impactor, except that the flow to the solvent traps was limited to 1.6 L/min to prevent solvent entrainment. Approximately 30 L/min were vented to the hood. This experiment was run for 8 hours. DCM from each solvent trap was collected. The traps were rinsed three times with DCM and the rinsate was also collected. The samples were evaporated to 0.1 mL, exchanged into 1.0 mL of DMSO, and analyzed by HPLC as discussed above. A blank solvent trap sample was collected by refilling the first solvent trap with DCM after collection of the DCM exposed to gas phase pyrene. The amount of pyrene in the first solvent

trap corresponded to a partial pressure at the saturator exit of 3.89×10^{-4} Pa with a standard deviation of 0.47×10^{-4} Pa. Pyrene was not detected in the second solvent trap, indicating that the first trap absorbed all the pyrene from the gas stream. No pyrene was detected in the blank sample either. The limit of detection for these samples, which were exchanged into to 0.2 mL of DMSO, corresponds to a partial pressure of 0.5×10^{-4} Pa. It was subsequently determined that the saturated gas stream cooled to room temperature in the apparatus. The extrapolated sublimation pressure of pyrene at room temperature (22°C), 4.1×10^{-4} Pa, is nearly equal to the measured partial pressure [114].

4.3 Results

4.3.1 Saturation Concentration of PAH in Oil

To measure the equilibrium concentration of pyrene in dibutyl phthalate, an excess of pyrene crystals was added to 1.5 mL of dibutyl phthalate and the solution allowed to equilibrate for 2 weeks in a constant temperature bath maintained at 25°C. The solution was decanted and filtered through a 0.2 μm pore size PTFE syringe filter. A 20 μL aliquot of the filtered solution was added to 1.0 mL of DMSO. The solution was further diluted by a factor of 50 in DMSO to make a dilute solution for HPLC quantification. The concentration of pyrene in a saturated solution of dibutyl phthalate was 115 mg/mL as determined by triplicate injections of two duplicate solutions, with a standard deviation of 5 mg/mL.

From these results one can estimate the activity coefficient for pyrene in dibutyl phthalate. If the vapor is assumed to be an ideal gas, the fugacity of crystalline pyrene is equal to the sublimation vapor pressure of pure pyrene, p_S . Because the liquid and solid phases are in equilibrium, one can determine the activity coefficient in the solution by equating the solid and liquid phase fugacities. The activity coefficient is then

$$\gamma = \frac{p_S}{xp_L} \quad (4.1)$$

where x is the mole fraction of pyrene and p_L is the vapor pressure of subcooled liquid pyrene. The experimentally measured value of x is 0.146 with a standard deviation of 0.006. The sublimation vapor pressure, extrapolated to 25°C from literature data, is 5.94×10^{-4} Pa [114]. The subcooled liquid vapor pressure, estimated from literature values for enthalpy of fusion and heat capacity, is 4.15×10^{-3} Pa (see Section D.9). This yields $\gamma = 0.98$. Within experimental error, $\gamma = 1.0$, and the pyrene—dibutyl phthalate solution behaves ideally. In the absence of experimental data on the solution behavior of other PAH in dibutyl phthalate, we assume that all PAH behave ideally in solution with dibutyl phthalate.

4.3.2 Absorption Artifact Measurements

To measure the absorption of pyrene from the gas phase to the impaction media, three laboratory experiments were performed with different exposure times. The MOI impaction media were exposed to a gas stream with a known concentration of pyrene for 6, 24 and 73 h. The samples were extracted and analyzed for pyrene by

HPLC as discussed above.

Immediately after the 6 h absorption experiment, fluorescence images of absorbed pyrene were taken under a microscope. The samples were briefly irradiated with a 6 W uv lamp at a wavelength of 355 nm and pyrene fluorescence images were photographed at low magnification. Figures 4-2 and 4-3 are fluorescence images of stages 5 and 3, respectively. These absorption patterns are typical of the stage 0 through 5 samples in which a high concentration of pyrene is visible directly under the impaction jets and the concentration decreases away from the jet centers. The PTFE membranes have slight surface roughness; these features account for the uneven fluorescence on length scales of 0.1 mm. Some distortion of the absorption pattern from radial symmetry is observed. This is probably due to the interaction of adjacent jets. For stage 6 the fluorescence image appeared blotchy with features on the order of 0.1 mm. For stages 7 and 8, the fluorescence images were uniformly bright. The lack of distinct absorption patterns is due to the close packing of a large number of jets on these stages.

Figures 4-4 through 4-12 show the amounts of pyrene absorbed on each stage for the three exposure times studied. The points show mean quantification results with error bars corresponding to one standard deviation from the mean. The amount absorbed is expressed as a concentration in dibutyl phthalate. HPLC quantification results are also presented in tabular form in Appendix B.

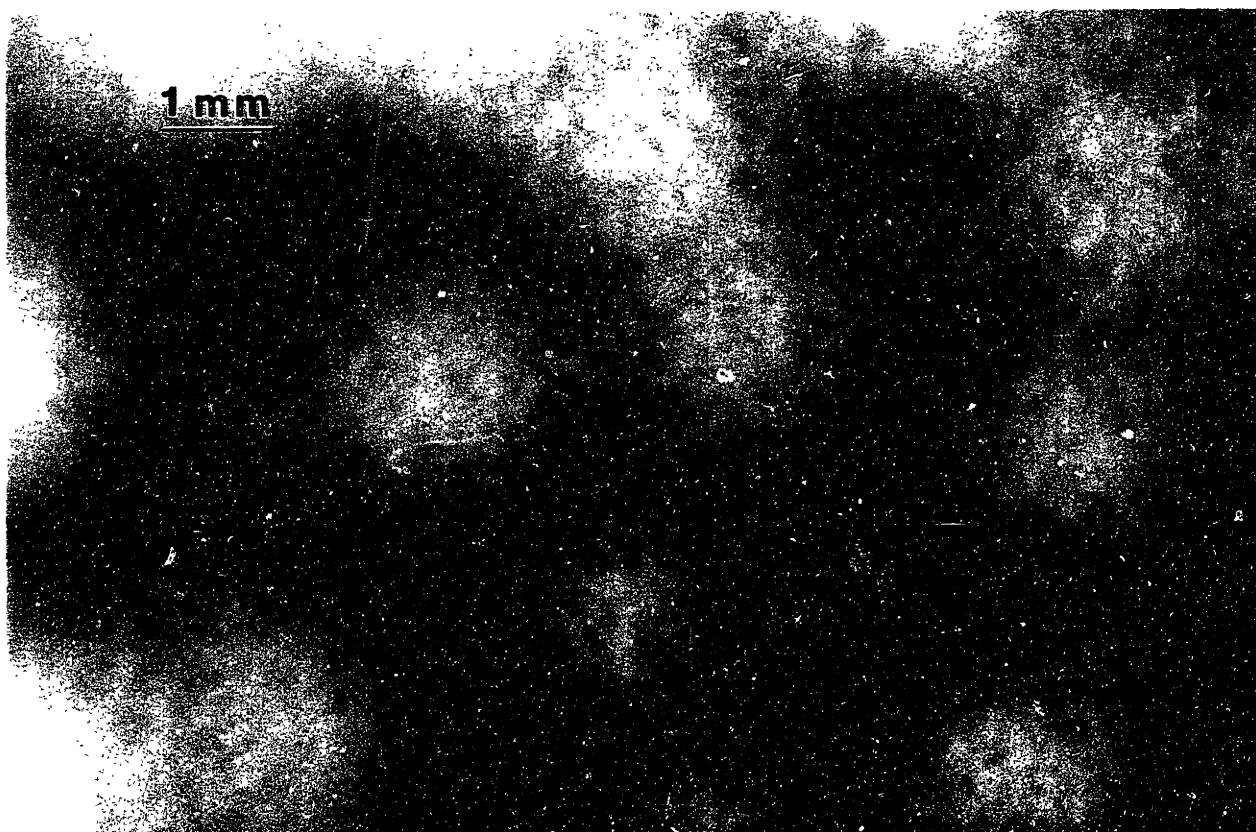


Figure 4-2: Fluorescence image of pyrene absorbed on stage 5 of the MOI after 6 hours.

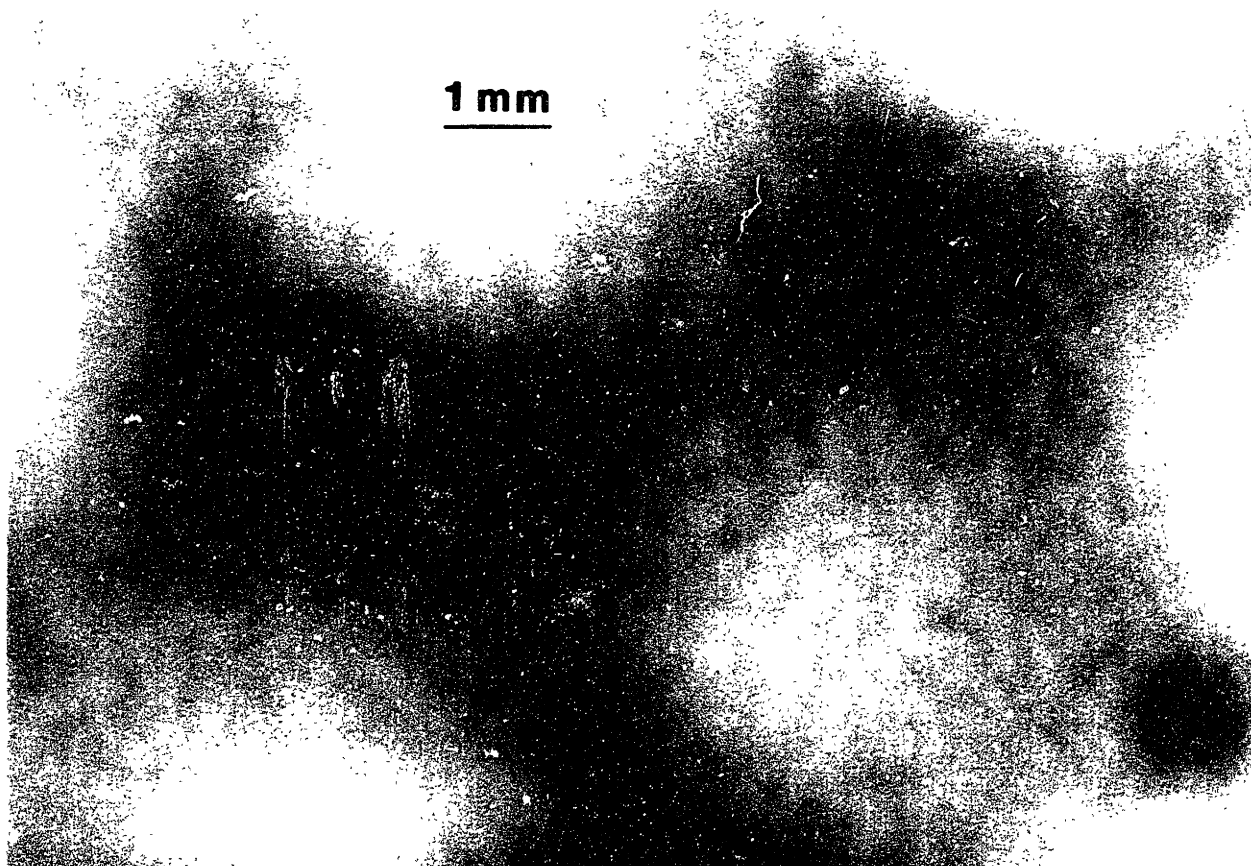


Figure 4-3: Fluorescence image of pyrene absorbed on stage 3 of the MOI after 6 hours.

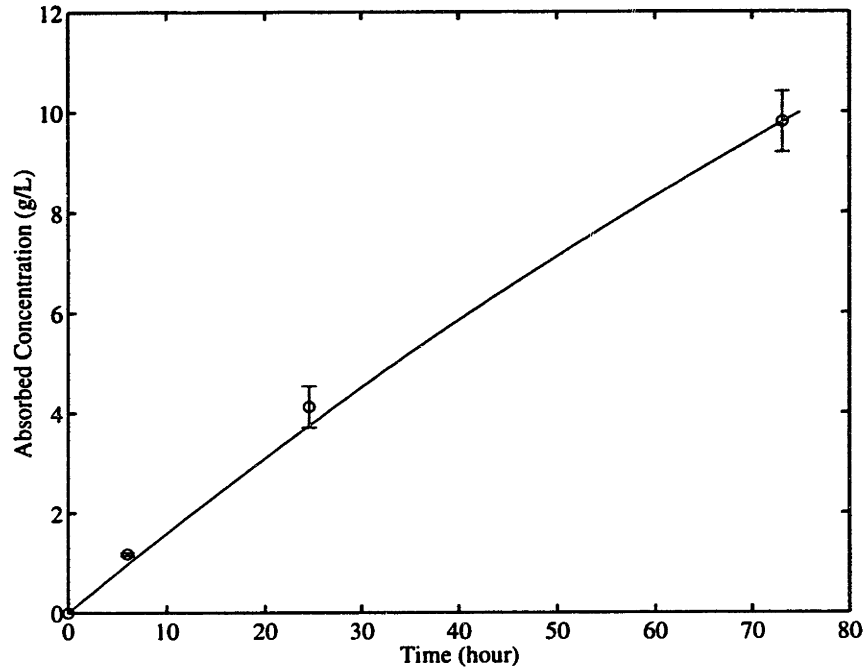


Figure 4-4: Experimental data and empirical model for pyrene absorption on stage 0 of the MOI.

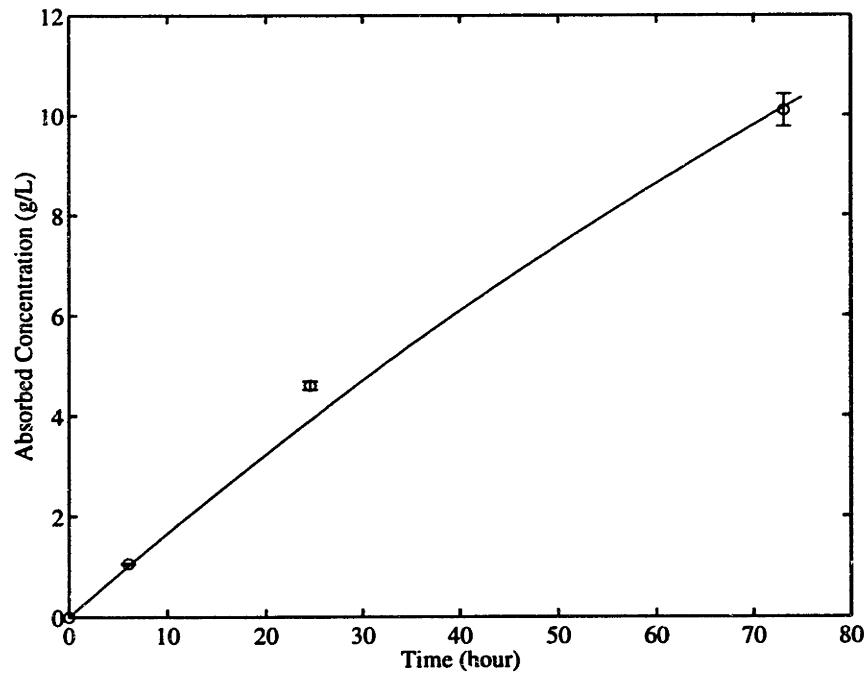


Figure 4-5: Experimental data and empirical model for pyrene absorption on stage 1 of the MOI.

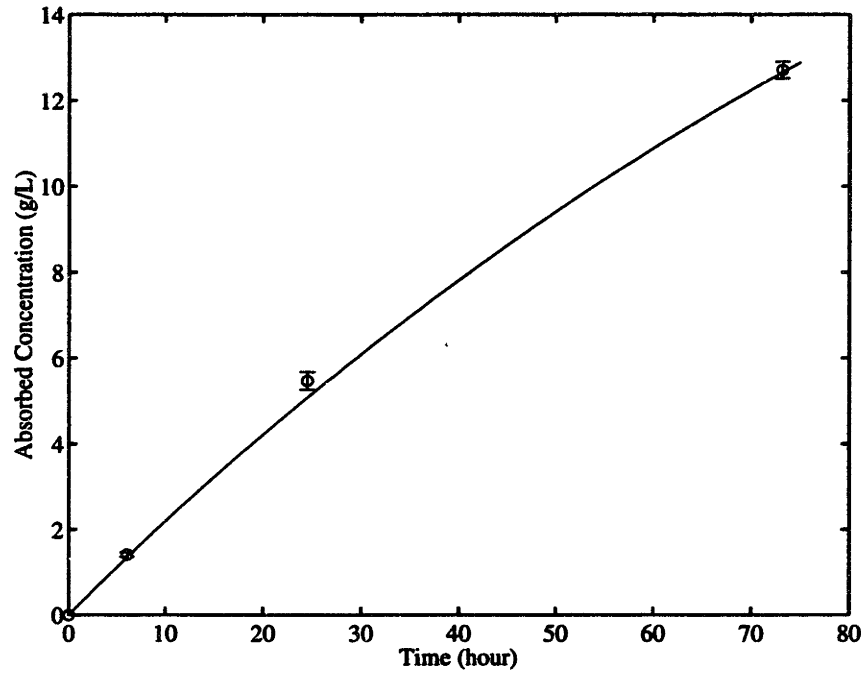


Figure 4-6: Experimental data and empirical model for pyrene absorption on stage 2 of the MOI.

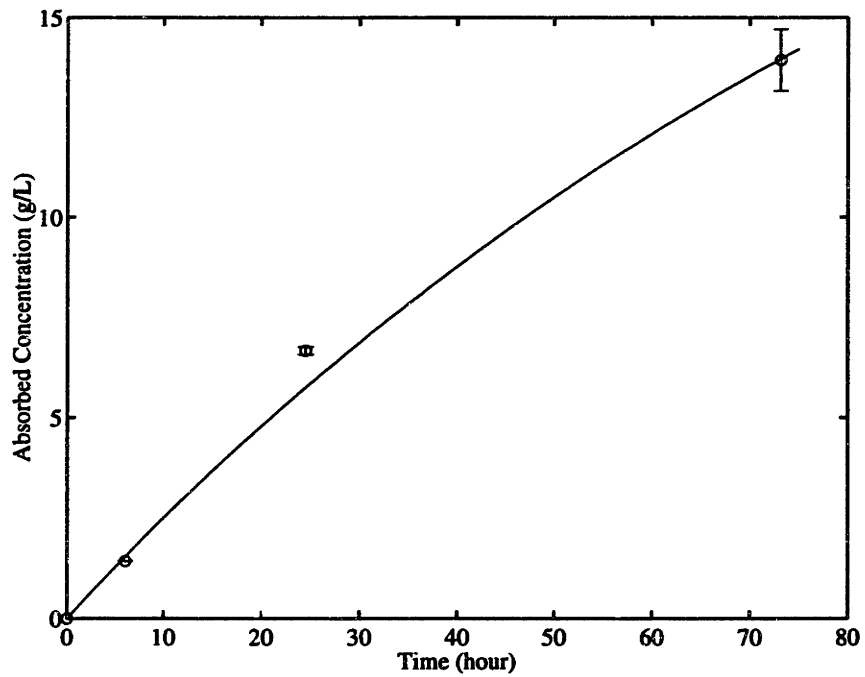


Figure 4-7: Experimental data and empirical model for pyrene absorption on stage 3 of the MOI.

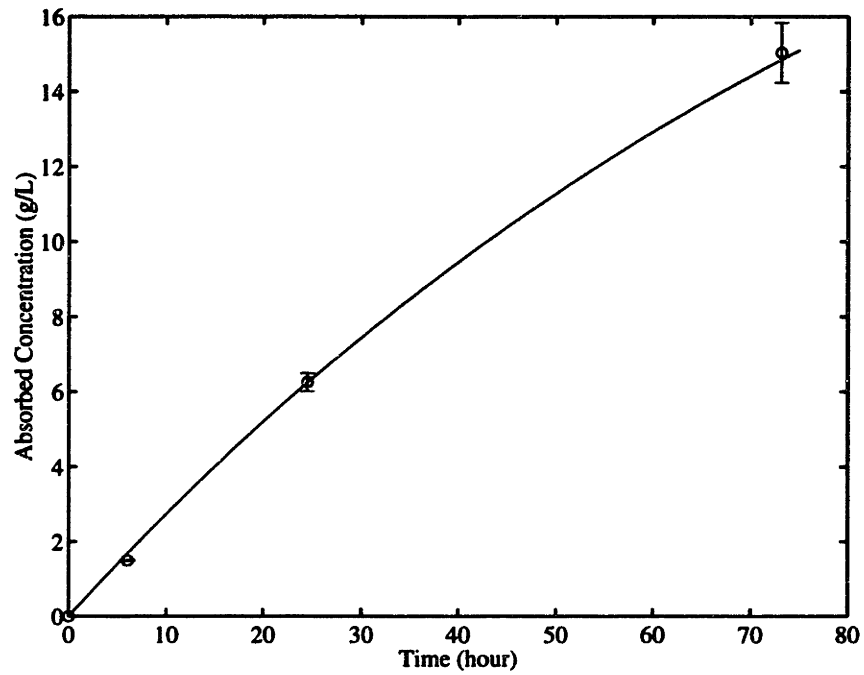


Figure 4-8: Experimental data and empirical model for pyrene absorption on stage 4 of the MOI.

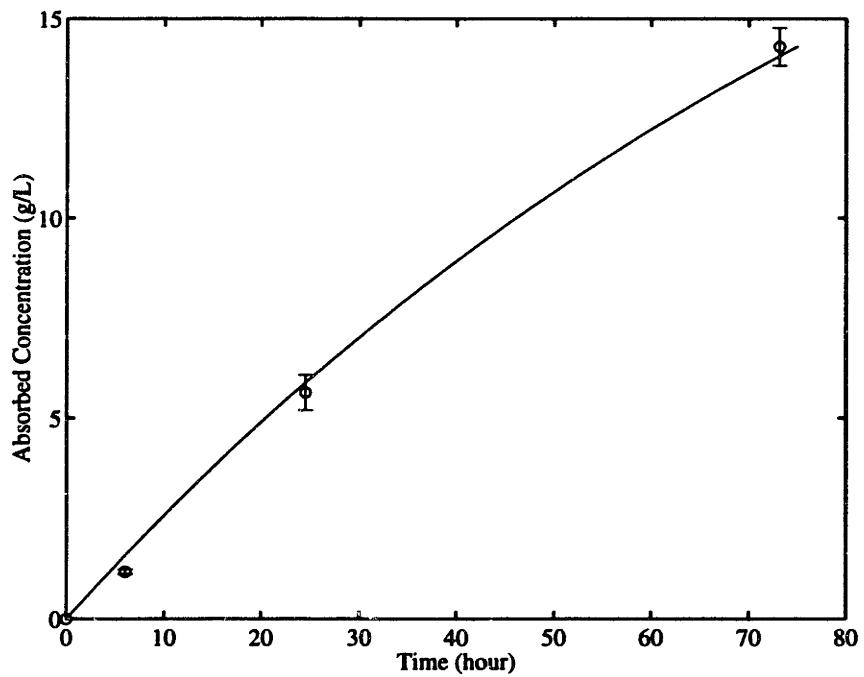


Figure 4-9: Experimental data and empirical model for pyrene absorption on stage 5 of the MOI.

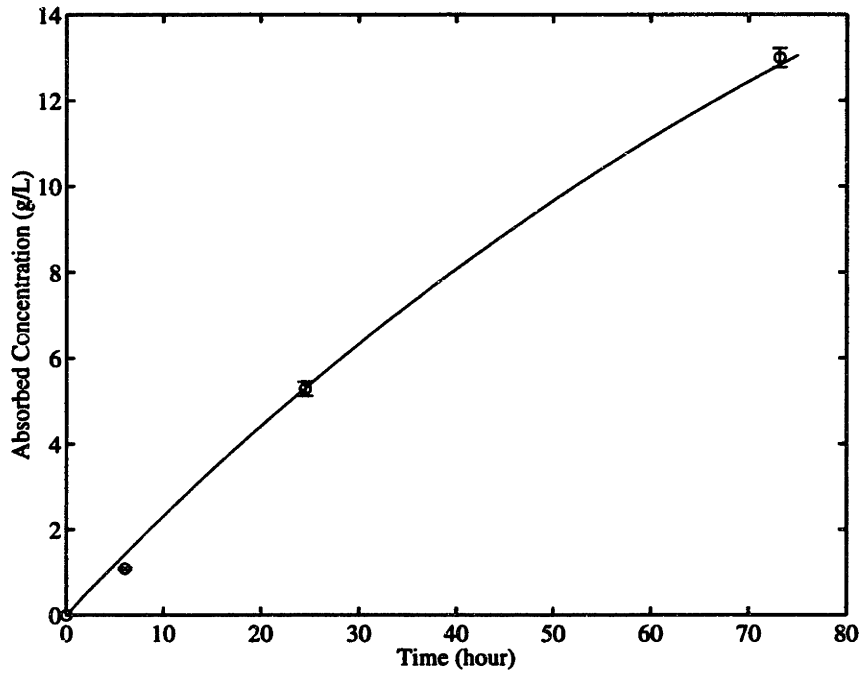


Figure 4-10: Experimental data and empirical model for pyrene absorption on stage 6 of the MOI.

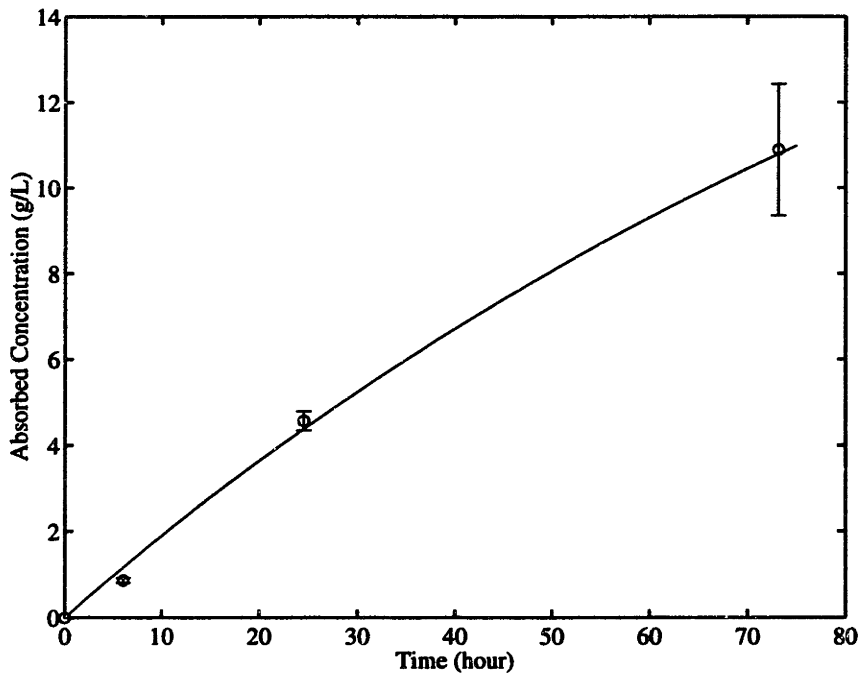


Figure 4-11: Experimental data and empirical model for pyrene absorption on stage 7 of the MOI.

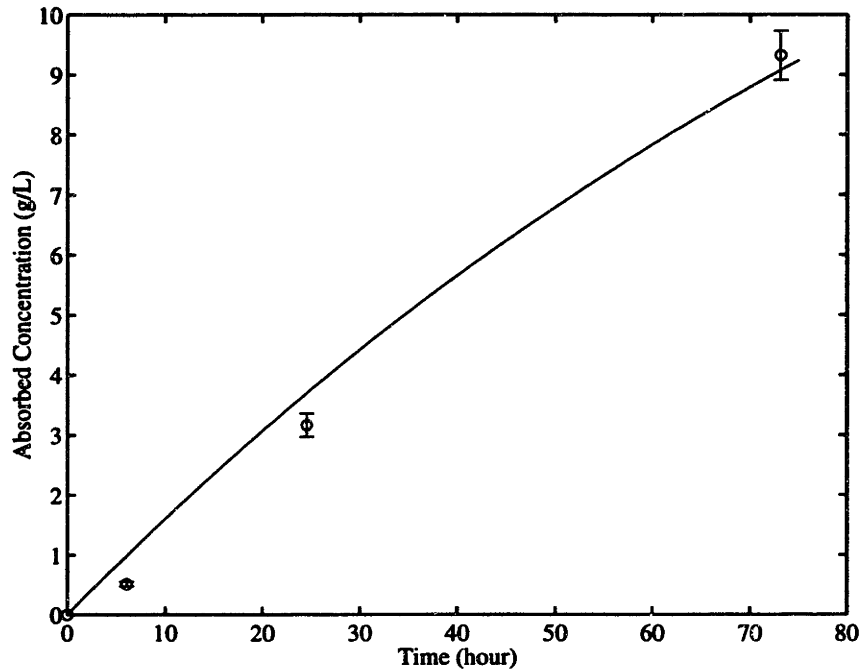


Figure 4-12: Experimental data and empirical model for pyrene absorption on stage 8 of the MOI.

4.3.3 Empirical Absorption Model

Drawn over the data points in Figures 4-4 through 4-12 are lines showing the predictions of a first order saturation model empirically fitted to the data. In this model, pyrene is assumed to have a uniform mass transfer coefficient over the impaction surface. The concentration of pyrene in the oil, C_L , asymptotically approaches its equilibrium concentration, $C_{L,eq}$, with a characteristic time, τ , as

$$C_L = C_{L,eq} \left[1 - \exp\left(\frac{-t}{\tau}\right) \right] \quad (4.2)$$

For low saturation concentrations of the absorbed compound, $C_{L,eq}$ can be expressed in terms of the bulk gas phase concentration, C_B , and an oil—air partition coefficient,

K_{oa} , as

$$C_{L,eq} = K_{oa}C_B \quad (4.3)$$

K_{oa} is

$$K_{oa} = \frac{RT\rho_{oil}}{\gamma p_L M_{oil}} \quad (4.4)$$

where

p_L	vapor pressure of subcooled liquid PAH
M_{oil}	molecular weight of oil
R	ideal gas constant
T	temperature
ρ_{oil}	density of oil

Values for K_{oa} are listed for a number of PAH in Table 7.1 under the heading “ideal solvent”. The bulk gas phase concentration is reduced by pressure drops in the MOI so that the bulk gas concentration on stage j is

$$C_B = \frac{P_j}{P_0} C_{B,0} \quad (4.5)$$

where P_j and P_0 are the pressures at stage j and the inlet, respectively; $C_{B,0}$ is the inlet bulk gas phase concentration. Substitution for $C_{L,eq}$ in Equation 4.2 yields

$$C_L = \frac{P_j K_{oa} C_{B,0}}{P_0} \left[1 - \exp\left(\frac{-t}{\tau}\right) \right] \quad (4.6)$$

Values of τ were calculated for each stage by a least squares fitting of $\ln(1 - C/C_{L,eq})$ versus time (see Table 4.1). The values of τ fell in the range 98—176 h.

To generalize the experimental results to other PAH, one can calculate an overall mass transfer coefficient for each stage, \bar{k} , defined as

$$\frac{dC_L}{dt} = \frac{\bar{k}}{\delta}(C_B - C_S) \quad (4.7)$$

where δ is the oil layer thickness and C_S is the gas phase concentration at surface. Note that δ is the thickness of a pure liquid layer. This expression ignores diffusive resistance to mass transfer within the oil and the effect of the membrane on mass transfer. The diffusivity of pyrene in oiled PTFE membrane was measured to be approximately 3×10^{-7} cm²/s. This is comparable to the diffusivity predicted for pyrene in pure liquid dibutyl phthalate by the method of Wilke and Chang, $\mathcal{D}_L = 8.9 \times 10^{-7}$ cm²/s [124]. The time scale for diffusion across the thickness of the membrane (125 μ m) is approximately 10 min, much less than τ . Therefore it is reasonable to neglect diffusion across the depth of the media.

At the surface the species will be in equilibrium between the gas and oil phases. Equation 4.7 can be expressed in terms of K_{oa} and $C_{B,0}$ as

$$\frac{dC_L}{dt} = \frac{-\bar{k}}{\delta K_{oa}} \left(C_L - \frac{P_j K_{oa} C_{B,0}}{P_0} \right) \quad (4.8)$$

Table 4.1: Characteristic Times, τ , and Overall Mass Transfer Coefficients, \bar{k} , for Absorption to Impaction Media in MOI.

Stage	Measured τ (h) at 295 K	\bar{k} (m/s)	Calculated τ (h) at 298 K			
			phenanthrene	pyrene	chrysene	benzo[a]pyrene
0	176	0.070	9.39	130	9390	149000
1	168	0.074	8.97	124	8970	142000
2	127	0.098	6.74	93.1	6740	107000
3	110	0.113	5.85	80.8	5850	92800
4	98	0.126	5.25	72.4	5250	83100
5	101	0.123	5.38	74.2	5380	85200
6	107	0.115	5.73	79.0	5730	90700
7	118	0.105	6.30	87.0	6300	99900
8	116	0.106	6.20	85.6	6200	98200

The solution of this equation, for the condition that initially there is no PAH in the oil, is

$$C_L = \frac{P_j K_{oa} C_{B,0}}{P_0} \left[1 - \exp\left(\frac{-\bar{k}t}{\delta K_{oa}}\right) \right] \quad (4.9)$$

Comparing Equations 4.6 and 4.9, it is apparent that

$$\bar{k} = \frac{\delta K_{oa}}{\tau} \quad (4.10)$$

Values of \bar{k} for each stage are listed in Table 4.1.

Although the experimental data fit reasonably well to this simple model, some known characteristics of the absorption process are not included in the model. The fluorescence images clearly show that the pyrene is not uniformly distributed in the medium, and therefore the mass transfer coefficients are not uniform. This is particularly relevant for the upper stages which have few jets and large variations in mass transfer with radial position. Immediately under the jets, the mass transfer coefficient is much larger than the average value. As a consequence, at intermediate

times, on the order of 72 h for pyrene, the oil under the centers of the jets will become saturated, slowing the rate of mass transfer. Fitting all the experimental data results in averaged \bar{k} values which are lower than the experimental values inferred from data taken at short times. This may be the reason that the model under predicts the amount of pyrene absorbed in the top four stages at 24 h.

In contrast, the model over predicts the amount of pyrene absorbed in stage 8 at short times. This may be because the model assumes a constant concentration of pyrene in the gas reaching this stage. In fact, the pyrene concentration entering stage 8 will be reduced by absorption in the prior stages. This concentration reduction will be greatest at the start of an experiment. A more general and detailed model to predict the absorption artifact is presented in the following chapter. It includes nonuniform mass transfer along the radial direction of the impinging jets and denuding of gas phase compounds in prior stages. At short times, denuding is found to reduce the gas phase concentration in stage 8 by an order of magnitude (see Figure 5-5).

Local mass transfer correlations for laminar jets impinging on surfaces are available in the literature [125, 126, 127]. The application of these mass transfer correlations to absorption in oiled impaction media is the topic of the next chapter. Briefly, local mass transfer coefficients, k , for pyrene absorption are in the range 5.0–0.03 m/s (see Figure 5-3). Values of k are highest near the center of the jet, and decrease, by up to an order of magnitude, away from the center of the jet. The values of \bar{k} determined here, are within the range of literature values of k . Values of \bar{k} , however, are generally lower than the literature values of k averaged over the area affected by the impinging jet. This is because local areas with high k values will saturate rapidly, slowing mass

transfer. This may also be due to overestimation of k by literature correlations for large values of nozzle to plate distance and tightly packed nozzle arrays, both features of the later stages of the MOI. These limitations are discussed at length in the next chapter.

The overall mass transfer coefficients measured for pyrene can be used for other PAH if the gas phase diffusivities of PAH are similar. The gas phase diffusivities of PAH can be estimated by the method of Fuller et al. [128]. Turpin and coworkers found PAH diffusivities equal to the values predicted by this method within the error of their measurements [129]. The predicted diffusivities are lower for high molecular weight PAH. Diffusivities are 0.060, 0.057 and 0.049 cm²/s for phenanthrene, pyrene, and coronene, respectively. Because PAH diffusivities vary from that for pyrene by at most 15%, the overall mass transfer coefficients measured for pyrene are reasonably applied for all PAH.

4.4 Apparent Distribution with Particle Size Due to Absorption

4.4.1 Absorption Artifact at Short and Long Times

The goal of this work is to estimate the amount of PAH absorbing from the gas phase into the impaction media during atmospheric sampling. Recall that, when data are reported for PAH associated with size-segregated particles, it is conventional practice to report the results as ng PAH per m³ of sampled air. Thus, for convenient

comparison, it is useful to express the absorption artifact on the same basis. The apparent concentration of a PAH in an aerosol size fraction due to absorption, C_{abs} , is then

$$C_{abs} = \frac{V_{oil}P_jK_{oa}C_{B,0}}{V_{air}P_0} \left[1 - \exp\left(\frac{-\bar{k}t}{\delta K_{oa}}\right) \right] \quad (4.11)$$

The only quantity in Equation 4.11 which has not been measured in this work is $C_{B,0}$.

The absorption artifact on each stage can be plotted versus the impactor cut-off diameters to show its effect on the measured size distribution. At short times, $t \ll \delta K_{oa}/\bar{k}$, Equation 4.11 reduces to

$$C_{abs} = \frac{V_{oil}P_jC_{B,0}}{V_{air}P_0} \left(\frac{\bar{k}t}{\delta}\right) \quad (4.12)$$

The only species dependent term in this equation is $C_{B,0}$. For pyrene with $t = 24$ h and $\bar{k} = 0.1$ m/s

$$\frac{\bar{k}t}{\delta K_{oa}} = 0.32 \quad (4.13)$$

so the short time condition holds for 24 h sampling of PAH with K_{oa} greater than that of pyrene. Figure 4-13 shows the absorption artifact versus the impactor cut-off diameters normalized by $C_{B,0}$. This figure shows that absorption is roughly equal across the stages with the maximum absorption on the middle stages.

At long times, $t \gg \delta K_{oa}/\bar{k}$, Equation 4.11 reduces to

$$C_{abs} = \frac{V_{oil}P_jK_{oa}C_{B,0}}{V_{air}P_0} \quad (4.14)$$

For phenanthrene with $t = 24$ h and $\bar{k} = 0.1$ m/s

$$\frac{\bar{k}t}{\delta K_{oa}} = 4.6 \quad (4.15)$$

so the long time condition holds for 24 h sampling of PAH with K_{oa} less than that of phenanthrene. Figure 4-14 shows the absorption artifact versus the impactor cut-off diameters normalized by $K_{oa}C_{B,0}$. The amount absorbed is proportional to the pressure on each stage. Because of variations in $\Delta \log D_p$, the step heights on the plot are not proportional to the pressures on each stage. At intermediate times the apparent size distribution due to the absorption artifact will be between the short and long time solutions. Therefore, the effect of the absorption artifact will be to increase the measured concentrations on all stages approximately uniformly since absorption at both short and long times is approximately equal for all stages.

4.4.2 Absorption Artifact Using Gas—Particle Distribution Ratios

The gas phase concentrations of PAH were not measured in the Massachusetts size-segregated sampling study. To estimate the $C_{B,0}$ we will use gas—particle distribution ratio, ϕ , which have been measured for PAH in the atmosphere by a number of investigators [40, 48, 80, 64]. Measured values of ϕ were determined as

$$\phi = \frac{C_{PUF}}{C_{filter}} \quad (4.16)$$

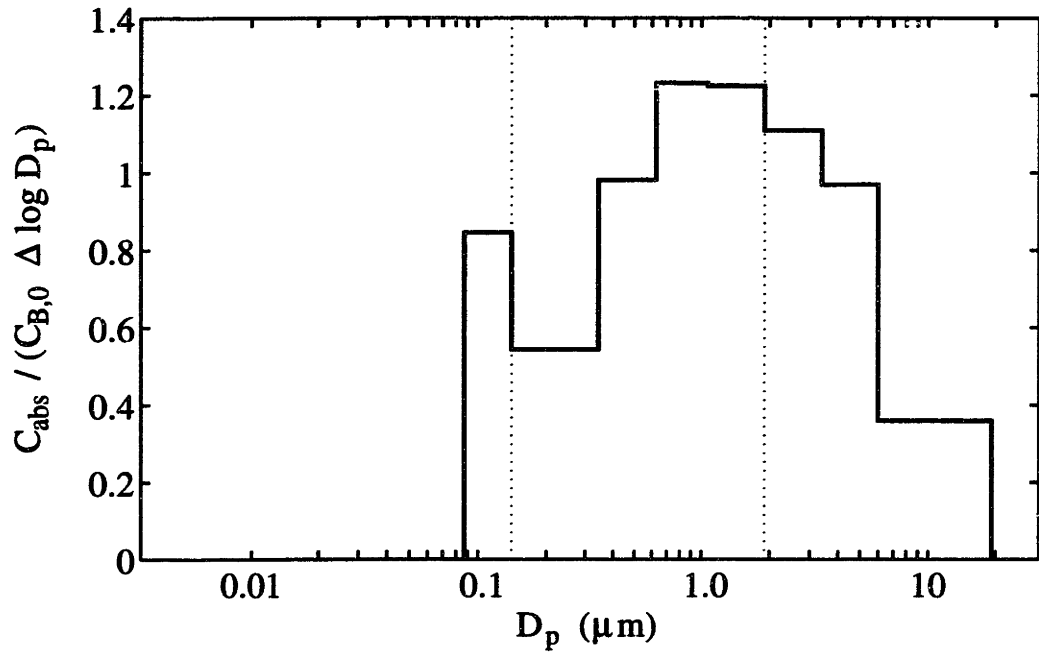


Figure 4-13: Apparent distribution with particle size of absorbed species at short times.

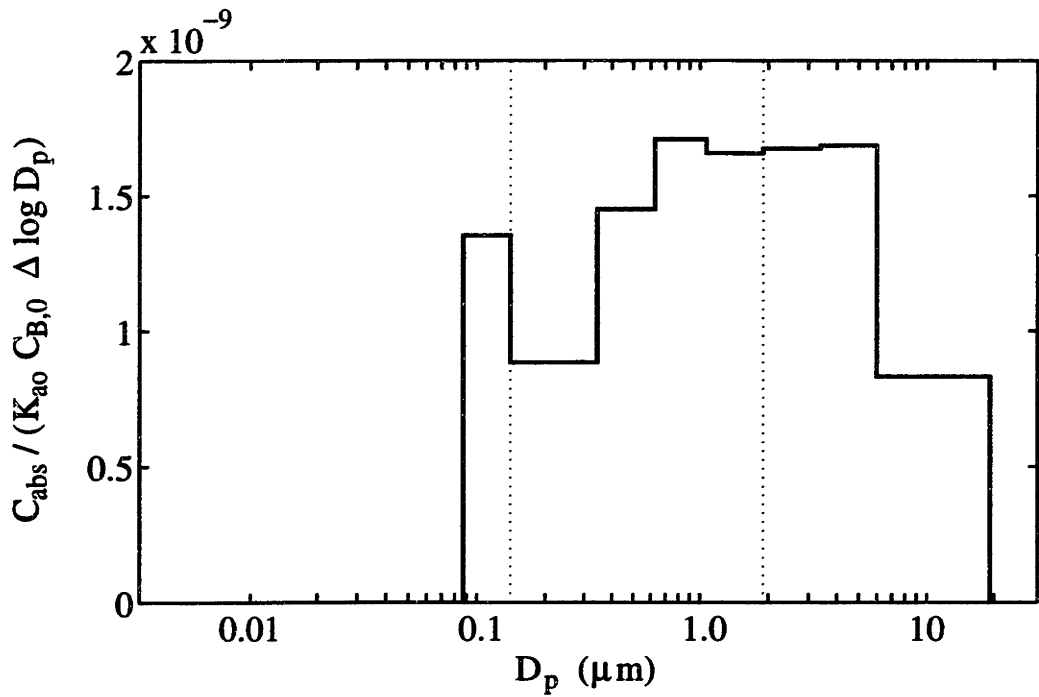


Figure 4-14: Apparent distribution with particle size of absorbed species at long times.

where C_{filter} is the the atmospheric concentration of PAH collected on the filter and C_{PUF} that collected in an absorbent (often polyurethane foam) downstream of the filter. Note that some authors designate this ratio K ; here we reserve K for equilibrium partition coefficients.

For the case that the collection of PAH by particle impaction and absorption are separable, the sum of the particulate PAH collected on all stages, $\sum C_{\text{part}}$, is equal to the measured concentration on all stages, $\sum C_{\text{meas}}$, less the absorption artifact on all stages, $\sum C_{\text{abs}}$,

$$\sum C_{\text{part}} = \sum C_{\text{meas}} - \sum C_{\text{abs}} \quad (4.17)$$

The condition of separability is met if collected particles do not occlude a significant fraction of the impaction surface, and if PAH do not diffuse to or from the particle deposits. For particle deposits twice the diameter of the nozzles, the fraction of the impaction surface covered by the deposits is less than 10% for all stages. The second condition depends on the nature of the PAH—particle association and the packing of PAH in the particle deposit. One extreme case is that PAH are associated with solid particles, either by adsorption or absorption in associated liquid, and that there is little the contact between these particles and the impaction media. In this case, PAH would not readily diffuse to the impaction medium. The other extreme is that atmospheric particles are liquid drops. In this case, the collected particles would form a liquid deposit from which PAH could diffuse into the impaction medium. Here we will assume that PAH collected with particles and by absorption are separable and discuss the implications of this assumption below.

Substitution of $C_{B,0} = \phi \sum C_{part}$ and C_{abs} in Equation 4.17 yields

$$\sum C_{part} = \frac{\sum C_{meas}}{1 + \frac{V_{oil}K_{oa}\phi}{V_{air}} \sum \left\{ \frac{P_j}{P_0} \left[1 - \exp\left(\frac{-\bar{k}t}{\delta K_{oa}}\right) \right] \right\}} \quad (4.18)$$

Substitution for $C_{B,0}$ in Equation 4.11 yields

$$C_{abs} = \frac{\frac{V_{oil}K_{oa}\phi}{V_{air}} \frac{P_j}{P_0} \left[1 - \exp\left(\frac{-\bar{k}t}{\delta K_{oa}}\right) \right] \sum C_{meas}}{1 + \frac{V_{oil}K_{oa}\phi}{V_{air}} \sum \left\{ \frac{P_j}{P_0} \left[1 - \exp\left(\frac{-\bar{k}t}{\delta K_{oa}}\right) \right] \right\}} \quad (4.19)$$

Yamasaki et al. collected an extensive set of ϕ data for a range of temperatures at an urban site in Japan [40]. The distribution ratios reported in this data set are comparable to later measurements [21]. A Clausius-Clapeyron type relation was assumed and the logarithm of measured ϕ values were plotted versus $1/T$ to obtain ϕ as a function of temperature. Values for ϕ thus determined at 298 K are listed in Table 4.2 and designated ϕ_Y . Note that Yamasaki et al. fitted $\log(C_{PUF}TSP/C_{filter})$ versus $1/T$ to determine the temperature dependence of the distribution, where TSP is the concentration of total suspended particulate matter in air. This formulation assumes that PAH interact with the total aerosol mass. This is clearly not the case if PAH interact with particle surfaces by adsorption or with an organic aerosol fraction by absorption. In fact, as has been noted by others, no more than 10% of the observed variation in the gas—particle distribution is explained by the variation in TSP [80]. Therefore, we use the dimensionless form of the distribution ratio.

Figures 4-15 through 4-18 show the measured distributions of representative PAH with particle size and the absorption artifact as predicted from Equation 4.19. The

Table 4.2: Gas—Particle Distribution Ratios.

PAH	Measured by	Maximum consistent with
	Yamasaki et al. (1982)	Allen et al. (1996)
	ϕ_Y	ϕ_{lim}
phenanthrene ^a	275	1.4
anthracene ^a	275	1.9
fluoranthene	37	1.2
pyrene	29	1.2
benz[<i>a</i>]anthracene ^b	1.8	0.34
chrysene/triphenylene ^b	1.8	0.43
benzo[<i>e</i>]pyrene ^c	0.038	0.11
benzo[<i>a</i>]pyrene ^c	0.038	0.058
perylene	—	0.020
benzo[<i>ghi</i>]perylene	—	0.047

^aPhenanthrene and anthracene quantified together by Yamasaki et al. (1982).

^bBenz[*a*]anthracene and chrysene/triphenylene quantified together by Yamasaki et al. (1982).

^cBenzo[*e*]pyrene and benzo[*a*]pyrene quantified together by Yamasaki et al. (1982).

dotted lines show the predicted absorption artifact using ϕ_Y values. For phenanthrene, pyrene, and chrysene/triphenylene the absorption artifact predicted using ϕ_Y is greater than the total measured amount of PAH in some particle size ranges. These predictions are therefore inconsistent with the atmospheric sampling data. Hypotheses to explain this inconsistency are presented below.

4.4.3 Upper Limit for Absorption Artifact

The upper limit for the absorption artifact consistent with amounts of PAH measured in size-segregated atmospheric aerosols will be that for which C_{abs} is equal to the measured concentration, C_{meas} , on one stage and less than C_{meas} on all other stages. Adjusting ϕ so that these conditions are met yields an upper limit on the gas—particle distribution, ϕ_{lim} . In Figures 4-15 through 4-18 the upper limit for the absorption

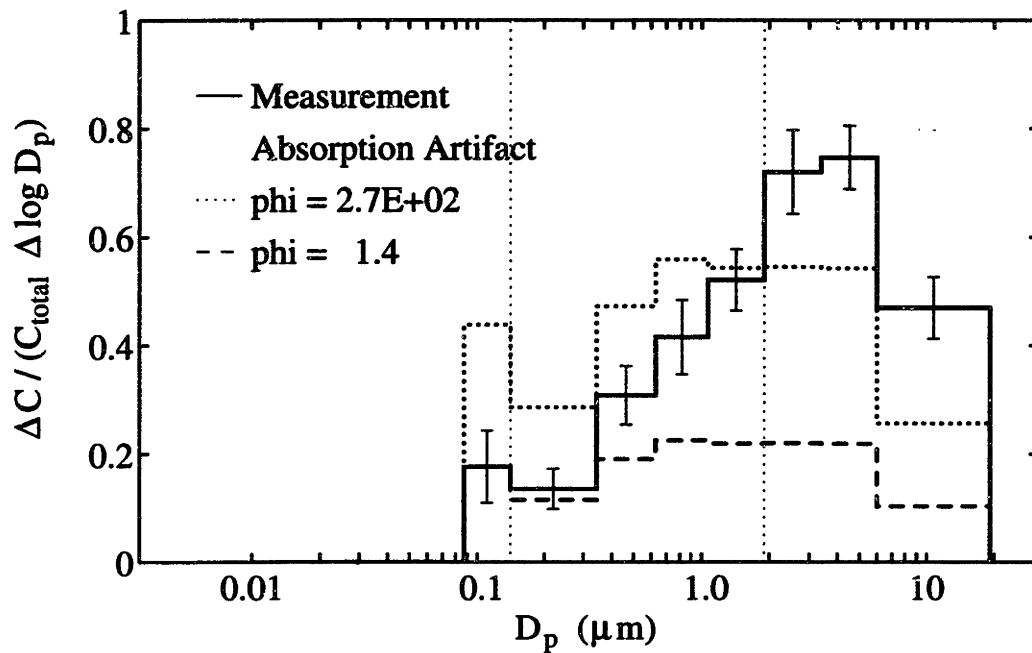


Figure 4-15: Measured distribution of phenanthrene with particle size in Kenmore Square aerosol and predicted absorption artifact.

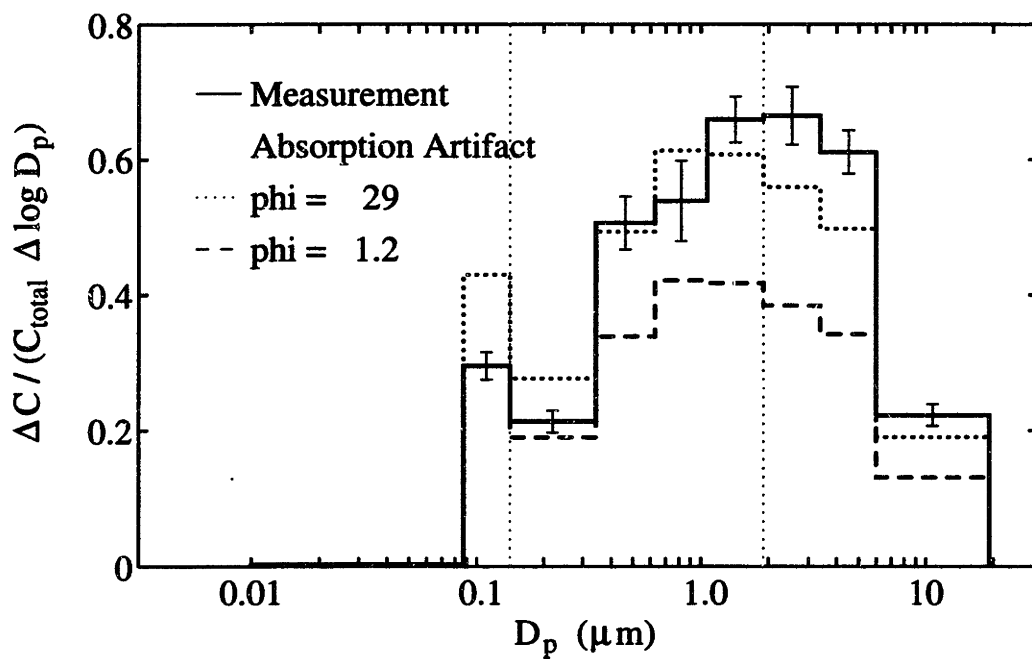


Figure 4-16: Measured distribution of pyrene with particle size in Kenmore Square aerosol and predicted absorption artifact.

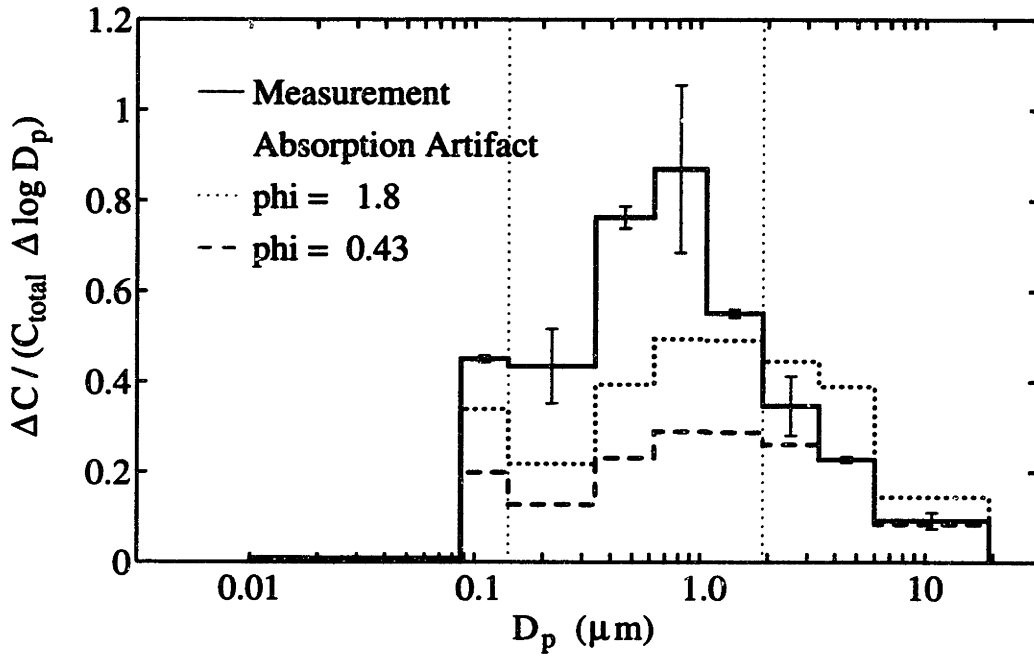


Figure 4-17: Measured distribution of chrysene/triphenylene with particle size in Kenmore Square aerosol and predicted absorption artifact.

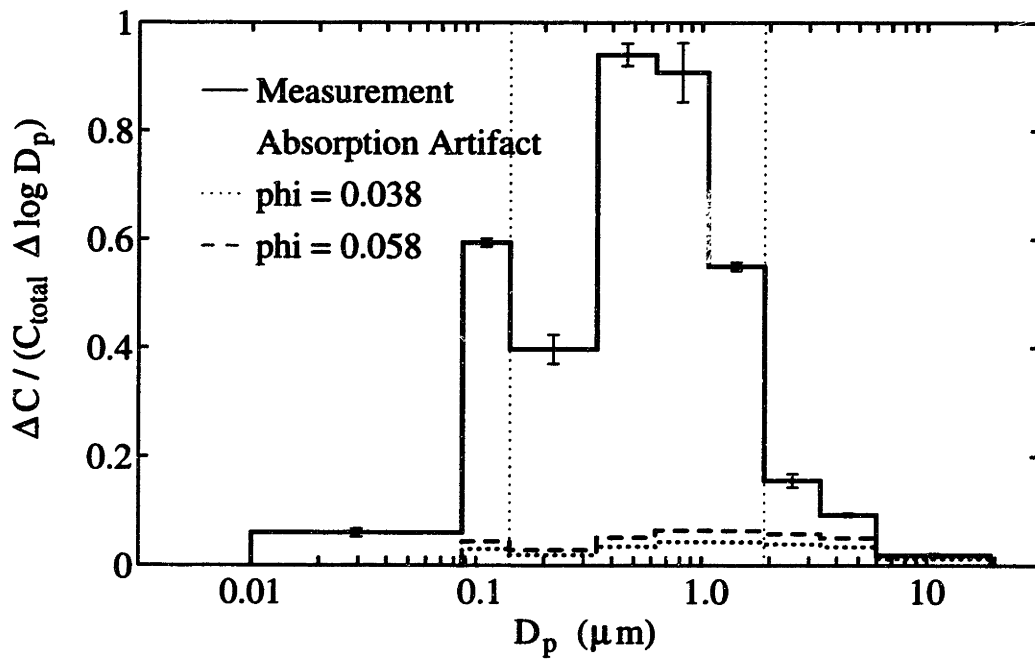


Figure 4-18: Measured distribution of benzo[a]pyrene with particle size in Kenmore Square aerosol and predicted absorption artifact.

artifact is shown as a dashed line. Values of ϕ_{lim} are listed in Table 4.2.

Since the measured distributions of PAH with particle size are similar for PAH of similar molecular weight, so too the maximum absorption artifacts will be similar. For low molecular weight PAH ($M < 202$), low concentrations on stages 7 and 8 suggest a relatively small absorption artifacts. Similarly, the low concentrations of high molecular weight PAH ($M > 228$) on stage 1, suggest a small absorption artifact. The upper limit on the absorption artifact is greatest for PAH of intermediate molecular weight ($202 \leq M \leq 228$) since, for these PAH, C_{meas} varies least with particle size.

Within a given particle size range, the amount of associated PAH must be between the measured amount and the measured amount less the upper limit of absorption. Even assuming that the absorption artifact is at its upper limit, the conclusion that PAH associate with particle size fractions based on their molecular weight is not qualitatively changed. Indeed, low molecular weight PAH are still approximately evenly distributed between the fine and coarse aerosols; high molecular weight PAH are still associated primarily with the fine aerosol fraction.

4.4.4 Comparison of Gas—Particle Distribution Ratios

For PAH of molecular weight less than 252, ϕ_Y is greater than ϕ_{lim} , in some cases by more than two orders of magnitude. A number of physical processes, singly or a combination, could lead to these large differences. The measured value, ϕ_Y , might be artificially high due to blow-off of collected material from the filter to the sorbent. This artifact has been investigated experimentally [130, 131] and theoretically [132].

For high vapor pressure (10^{-2} – 10^{-1} Pa) species, the predicted collection efficiencies are on the order of 10%; this could lead to order of magnitude errors in the ϕ_V values.

The urban sampling site at which the size-segregated particles were sampled was located 4 m above street level on a traffic island in a busy intersection. PAH are co-emitted with combustion aerosols and may not have had time to establish a gas—particle equilibrium between emission and sampling. In this case, the actual value of ϕ will be lower near emission sources than at sampling sites further removed from emission sources.

A third explanation is that, for species with short characteristic times for absorption, the gas phase concentration relevant to absorption will be that at the end of the sampling period. Table 4.1 shows τ calculated for some representative PAH at 298 K. Because τ for phenanthrene is less than the sampling time, the relevant gas phase concentration for the absorption is that at the end of the sampling period. The atmospheric samples were collected from midnight to midnight so absorption of phenanthrene is affected by its evening gas phase concentration. Gas phase concentrations in the evening are expected to be lower due to lower temperatures and lower emissions. Therefore, estimating ϕ by comparing evening averaged gas phase concentrations to daily averaged particulate concentrations will lead to artificially low values for ϕ_{lim} .

The assumption that PAH collected with particles and by absorption can be treated separately may not be valid. If PAH are able to diffuse from particle deposits to the impaction media on time scales less than, or comparable, to sampling times, absorption of PAH in the impaction media will be reduced. In fact, for rapid

diffusion, the net effect may be mass transfer from the particle deposit to the gas phase. This is analogous to the impactor blow-off artifact studied by Zhang and McMurry who considered mass transfer only from the particle deposit to the gas phase [133].

Finally we must consider the effect of exhaust plumes on the sampling results. Because the sampler was positioned within meters of emission sources, large variations in concentration of gas and particulate phase PAH on time scales on the order of seconds are likely as unmixed plumes from combustors are sampled. This is shown in Figure 4-19, the response from a photoionization detector positioned at the same sampling location. The photoionization detector is designed to have a linear response to four and five ring PAH associated with fine particles [134, 135, 136]. These data show that transient peaks which last tens of seconds and have PAH concentrations an order of magnitude greater than the time averaged values.

Within such plumes both the gas and particulate phase concentrations of PAH will be higher than average. However, due to the increase in sites available for adsorption or organic material available for absorption, the increase in concentration of particle-associated PAH is expected to be greater than the increase in the gas phase concentration. This could increase ϕ by an order of magnitude over the average value. Temporarily high values of ϕ will result in a larger fraction of PAH collected with particles than on average. As sampling continues, cleaner air drawn through the impactor will preferentially remove PAH absorbed from the gas phase because of the large surface area available for mass transfer and resistance to mass transfer within the particle deposit.

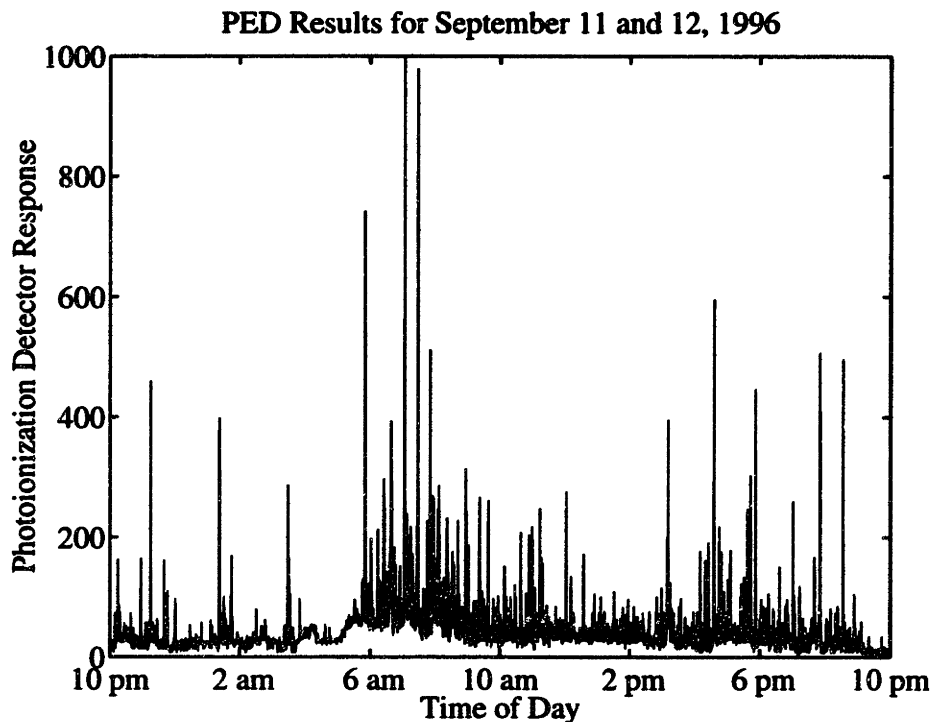


Figure 4-19: Photoionization detector response at Kenmore Square, September 11 and 12, 1996.

4.5 Conclusions

The absorption of pyrene from the gas phase into oiled impaction media in the MOI was measured in the laboratory. The results fit well to a simple overall mass transfer coefficient model. The measured overall mass transfer coefficients were within the range of literature values for impinging jet mass transfer.

The mass transfer model was applied to determine the amount of PAH absorption during atmospheric sampling. Even for the case that the absorbed amounts were equal to the upper limit of the predictions, PAH distributions with particle size remained qualitatively unchanged. The original conclusion of the size-segregated sampling work, that PAH associate with particle size fractions based on their molecular weight, stands. If the upper limit of the absorption artifact is subtracted from

the measured PAH concentrations, low molecular weight PAH are still approximately evenly distributed between the fine and coarse aerosols; high molecular weight PAH are still associated primarily with the fine aerosol fraction.

The gas—particle distributions from literature data and consistent with the size-segregated data differ by as much as two orders of magnitude. We are unable to resolve these differences. Likely explanations indicate that the assumption that concentrations of PAH are constant during sampling must be revisited. Preliminary data show that PAH concentrations vary on time scales on the order of seconds due to emission plumes, and on the order of hours due to diurnal weather and emission patterns.

Chapter 5

Absorption Artifact Model

5.1 Introduction

In the previous chapter laboratory measurements of the absorption of pyrene from the gas phase into impaction media of PTFE membranes impregnated with dibutyl phthalate in a MOI were reported. An empirical description of the experimental results adequately predicted the effect of this artifact on atmospheric aerosol measurements for this sampling system. However, these experimental results cannot be used directly to predict the absorption artifact for other impactor designs or impaction media, for example, in the case of a Hering low pressure impactor with aluminum impaction media coated with Vaseline which was recently used to collect size-segregated atmospheric particles in Los Angeles for PAH analysis [94].

The objective of this chapter is to develop a general model to describe the absorption of gas phase species to oiled impaction plates based on existing models of mass transfer from impinging laminar jets. Model predictions will be compared to exper-

imental measurements of the absorption of pyrene in a MOI. The model may then be used to predict the absorption artifact for different impactor designs, impaction media, and semi-volatile compounds.

5.2 Cascade Impactors

Cascade impactors collect size-segregated particles by inertial impaction on a series of stages. The sampled aerosol is drawn through an orifice or array of orifices on each stage. The resulting jets are directed toward an impaction plate. On each stage the gas stream flows around the impaction plate and particles with an aerodynamic diameter (D_p) larger than the designed cut-off D_p ideally impact and are collected on the plate. Impaction is not ideal and the cut-off size is designated by D_{p50} , the aerodynamic diameter for which 50% of the particles are collected. Particles with $D_p < D_{p50}$ ideally flow with the gas stream to the next impaction stage. Subsequent stages are designed to collect smaller particles so that each stage ideally collects particles with D_p between its D_{p50} and the previous stage's D_{p50} .

The micro-orifice impactor (MOI) used in this work was manufactured by MSP Corporation (Minneapolis, MN) and is designed to collect particles on 8 stages [104]. Orifice diameters as small as 50 μm allow collection of particles with aerodynamic diameters as small as 0.080 μm . The impactor is designed to sample at a moderate flow rate (30 L/min) with low pressure drops (< 0.5 atm). Figure 5-1 is a schematic drawing of two MOI stages. Table 5.1 lists the characteristics of the MOI used for atmospheric sampling in this work (see Chapter 2).

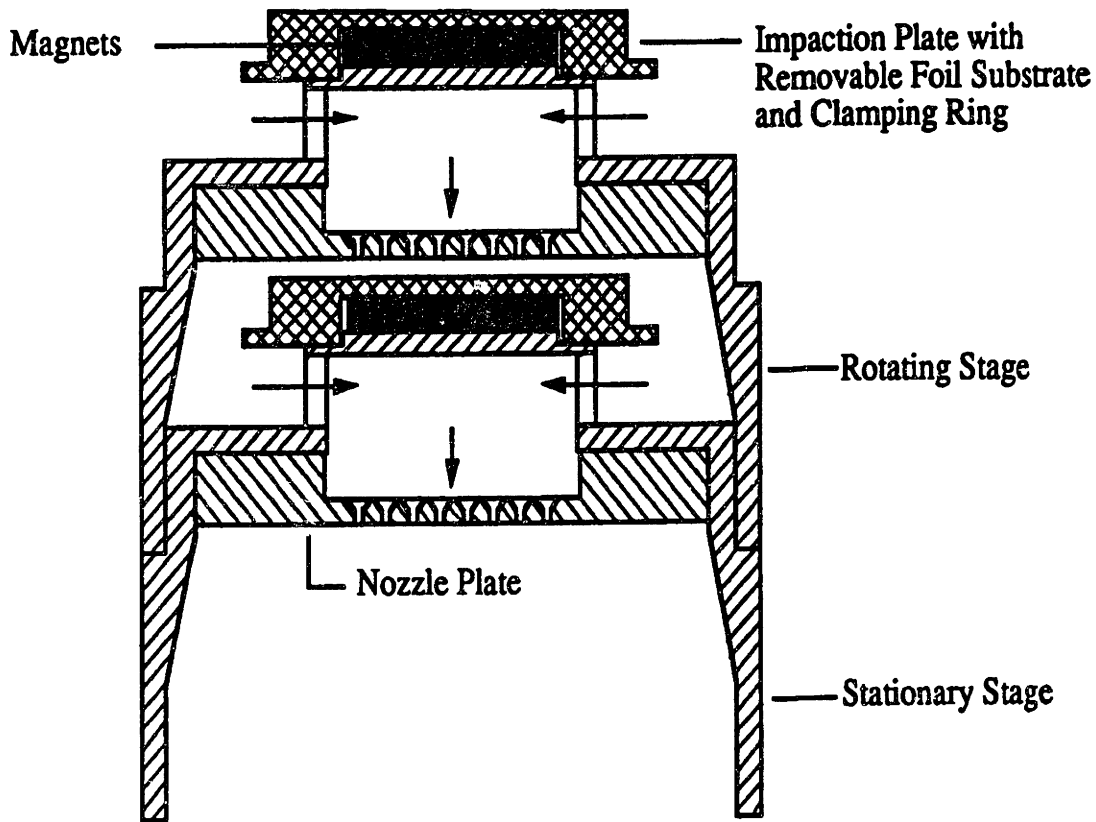


Figure 5-1: MOI impactor stage design [104].

5.3 Impinging Jet Mass Transfer

5.3.1 Impinging Jet Flow

All practical impactor designs use round orifices to generate subsonic laminar impinging jets. Therefore, we will consider round axisymmetric impinging jets of incompressible fluid. Figure 5-2 shows schematically the flow pattern of a single impinging jet. The impinging jet flow near the surface can be divided into three regions. Flow in the region directly under the nozzle is described as a stagnation flow. Flow far from the stagnation region is laminar wall jet flow which exhibits a semi-parabolic velocity profile. Between these regions the flow is in transition between stagnation and wall

Table 5.1: Characteristics of MOI Stages.

Stage	Cut-off D_p (μm)	Pressure (atm)	Number of Jets	Jet Diameter (μm)	Jet Velocity (m/s)	Jet Re	Nozzle to Plate Length (H/D)	Maximum r
0	18.000	1.000	1	10000.0	6.37	4120	0.75	3.22
1	5.620	1.000	10	3800.0	4.41	1080	1.00	2.68
2	3.160	1.000	10	2470.0	10.40	1670	1.00	4.12
3	1.780	0.997	20	1370.0	17.00	1500	1.00	5.25
4	1.000	0.983	40	720.0	31.20	1430	1.00	7.06
5	0.585	0.947	80	438.0	43.80	1180	1.50	8.21
6	0.320	0.901	900	136.0	42.40	336	6.40	7.88
7	0.131	0.812	2000	59.4	111.00	347	10.60	12.10
8	0.080	0.675	2000	51.4	179.00	401	11.10	14.00

jet flow. It is convenient to express the distance from the center of the jet, x , in dimensionless form, r , as

$$r = \frac{x}{R} \quad (5.1)$$

where R is the nozzle radius. Following Scholtz and Trass, the flow region divisions are: stagnation flow for $0 < r < 1.5$, transition flow for $1.5 < r < 3.0$, and wall jet flow for $r > 3.0$ [127].

At each stage air is drawn from a relatively quiescent volume through the jet nozzles. The entrance length, L_e required for a fully developed laminar velocity profile to form is [138]

$$L_e = 0.0575 Re D \quad (5.2)$$

For nozzle lengths, L , much less than L_e , the flow exiting the orifice will be approximately uniform. Marple et al. studied the impaction of particles from laminar jets [139]. The fraction of particles of a given D_p which impacted was calculated for a

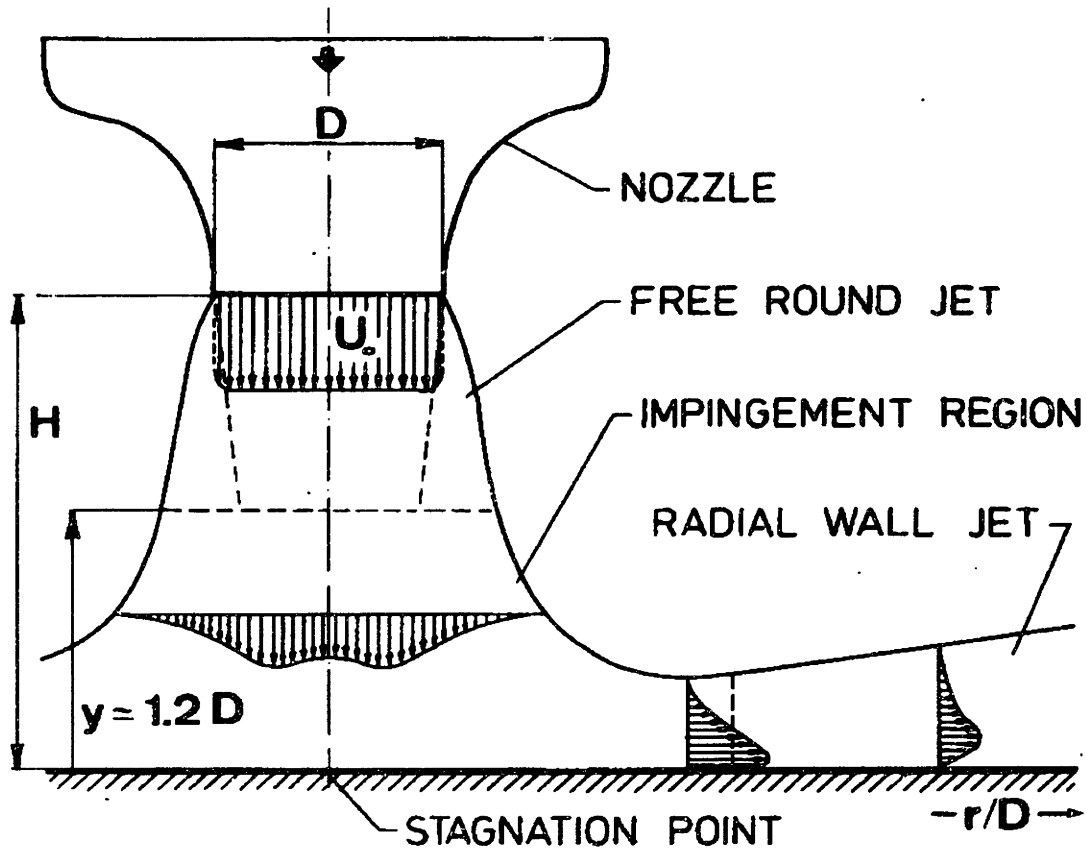


Figure 5-2: Schematic of flow for a round impinging jet [137].

number of geometries. Ideally, the collection efficiency of particles smaller than D_{p50} will be zero, and unity for those larger than D_{p50} . Marple et al. found sharp collection efficiency curves for approximately uniform velocity laminar jets. Therefore, impactors are designed to generate nearly uniform velocity jets, for example in the MOI $L/D \approx 1$.

The velocity profile of flow at the nozzle exit will affect the mass transfer coefficient in the stagnation and transition regions. Uniform velocity profiles at the nozzle exit are assumed for all stages of the MOI, except stage 0. In the atmospheric sampling part of this work, the aerosol was drawn through a 0.95 cm diameter 0.6 m long tube.

For this stage

$$\frac{L}{L_e} = 0.25 \quad (5.3)$$

In the absorption experiments described above, the tubing upstream of the MOI was many meters long. In both these cases, the velocity profile is expected to be significantly non-uniform and fully developed laminar flow is assumed.

5.3.2 Stagnation Region

The local mass transfer coefficient, k , is defined as

$$n_A = k(C_B - C_S) \quad (5.4)$$

where n_A is flux of species from the jet to the surface, C_B is the bulk gas phase concentration, and C_S is the gas phase concentration at the surface. Values of k for each of the flow regions will be taken from theoretical or semi-empirical results in the literature. Scholtz and Trass calculated the hydrodynamics and mass transfer for inviscid laminar impinging jets [126, 127]. Dimensionless mass transfer coefficients in terms of the Sherwood number, Sh , were expressed as polynomials of the Reynolds, Re , and Schmidt, Sc , numbers for the three flow regions. Experimental measurements of the rate of mass loss from a large crystal of naphthalene under an impinging jet agreed well with their calculations.

The inviscid solutions describe reasonably well the flow field for relatively high Reynolds numbers and small nozzle to plate distances. For larger nozzle heights,

however, viscous entrainment of the surrounding fluid results in an increase in jet diameter, a decrease in jet velocity, and a change in the velocity profile [140]. For small nozzle to plate distances, $H/D < 5$, the inviscid assumption is accurate [126]. Here the nozzle to plate distance, H , is made dimensionless by division by the jet diameter, D . Since Scholtz and Trass assumed inviscid jets, the k values derived from the work of are applicable to stages 0–5 of the MOI. In the absence of correlations applicable to large values of H/D , we will also use the Scholtz and Trass correlations for stages 6–8 even though these are expected to be inaccurate. The later work by this group included the effect of viscous entrainment of jets [140, 141]. These modifications are not included here.

For a jet with a uniform velocity profile at the nozzle exit, the mass transfer in the stagnation region is estimated as

$$\frac{Sh}{Re^{0.5}} = aSc^{0.361} + bSc^{0.368} r^2 + cSc^{0.408} r^4 + dSc^{0.424} r^6 \quad (5.5)$$

Here a, b, c, d are functions of H/D . For $H/D > 0.5$, the values of these constants are $a = 0.3634, b = 0.0344, c = -2.551 \times 10^{-3}, d = 1.741 \times 10^{-3}$. For a jet with a parabolic velocity profile at the nozzle exit, the mass transfer correlation for the stagnation region is

$$\frac{Sh}{Re^{0.5}} = aSc^{0.361} + bSc^{0.368} r^2 + cSc^{0.408} r^4 + dSc^{0.424} r^6 \quad (5.6)$$

For $H/D > 0.5$, the values of these constants are $a = 0.8242, b = -1.351 \times 10^{-1}, c =$

$$-9.850 \times 10^{-3}, d = -1.171 \times 10^{-3}.$$

5.3.3 Wall Jet Region

For mass transfer in the wall jet region Scholtz and Trass recommend the correlation

$$Sh = 0.2429 Re^{0.75} r^{-1.25} \quad (5.7)$$

The wall jet region extends from $r = 3$ to the maximum value of r , r_{max} . Values for r_{max} are calculated by dividing the impaction area among the jets

$$r_{max} = \sqrt{\frac{4A}{\pi N_{jet} D^2}} \quad (5.8)$$

where A is the impaction plate area and N_{jet} is the number of jets. For some MOI stages $r_{max} < 3$, for these stages the wall jet region is neglected.

5.3.4 Transition Region

For the transition region, Scholtz and Trass fit empirical data to the following correlation

$$\frac{Sh}{Re^{0.5}} = 0.95 r^{-0.86} \quad (5.9)$$

Figure 5-3 is a plot of k versus r for stages 0–8. Discontinuities are apparent at $r = 1.5$ and $r = 3.0$, the locations of flow region transitions. The values of k in the stagnation region are approximately an order of magnitude greater than those for the wall jet region of the same stage. There are significant stage-to-stage differences

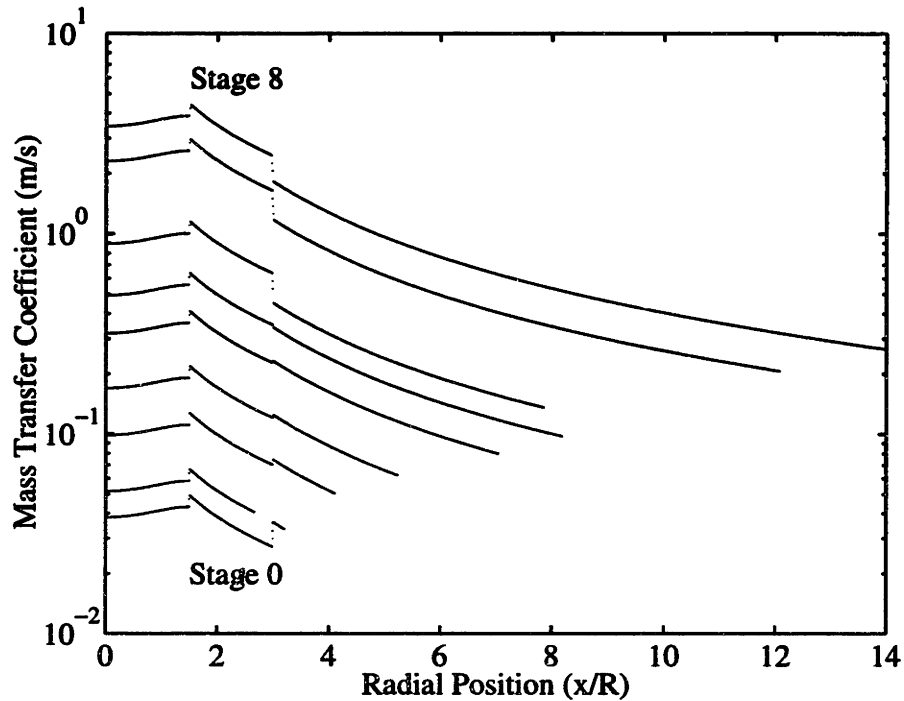


Figure 5-3: Mass transfer coefficient (k) versus radial position (r) for pyrene in MOI stages 0–8.

among the stages, with higher k values for those stages which have smaller jet diameters. The gas phase diffusivities of pyrene were used to calculate k for this plot. Diffusivities were estimated from the method of Fuller et al. at a temperature of 298 K (see Appendix D.5) [128].

5.3.5 Correction for Arrays of Impinging Jets

The mass transfer from an array of jets is less than that for the same number of independent jets due to interference by neighboring jets [142]. In the MOI impactor design, such arrays of jets issue from perforated plates on each stage. Martin derived a correlation to estimate the overall mass transfer coefficient for an array of jets formed by nozzles. This overall correction was applied uniformly to k values to calculate

corrected local mass transfer coefficients, k' , as

$$k' = \left[1 + \left(\frac{H/D}{0.6/\sqrt{r_{max}}} \right)^6 \right]^{0.5} k \quad (5.10)$$

5.4 Absorption without Gas Phase Denuding

Assuming that the concentration of absorbed compounds is small, Equation 5.4 can be written in terms of concentration in the oil, C_L , as

$$\frac{\partial C_L}{\partial t} = \frac{k'}{\delta} (C_B - C_S) \quad (5.11)$$

where δ is the oil layer thickness. Note that δ is the thickness of a pure liquid layer. This expression ignores diffusive resistance to mass transfer within the thickness of the oil. This is a reasonable assumption for the present case where $\delta \approx 10^{-5}$ m.

At the surface the species will be in equilibrium in the gas and oil phases. C_S can then be expressed in terms of C_L and an oil—air partition coefficient, K_{oa} , as

$$C_S = \frac{C_L}{K_{oa}} \quad (5.12)$$

K_{oa} is

$$K_{oa} = \frac{RT\rho_{oil}}{\gamma p_L M_{oil}} \quad (5.13)$$

where

p_L vapor pressure of subcooled liquid PAH

M_{oil}	molecular weight of oil
R	ideal gas constant
T	temperature
ρ_{oil}	density of oil

Values for K_{oa} for PAH in an ideal solvent, e.g. dibutyl phthalate, are listed in Table 7.1. The bulk gas phase concentration is reduced by pressure drops in impactors so that, in the absence of solute removal from the gas phase, the bulk gas concentration on stage j is

$$C_B = \frac{P_j}{P_0} C_{B,0} \quad (5.14)$$

where P_j and P_0 are the pressures at stage j and the inlet, respectively; $C_{B,0}$ is the bulk gas phase concentration at the inlet. The bulk gas concentration is also reduced by mass transfer on earlier stages, this effect, “denuding”, is ignored here but will be discussed in the next section. Substitution for C_S and C_B in Equation 5.11 yields

$$\frac{\partial C_L}{\partial t} = \frac{-k'}{\delta K_{oa}} (C_L - K_{oa} \Pi C_{B,0}) \quad (5.15)$$

where Π is P_j/P_0 .

It is convenient to define dimensionless variables for concentration, time, and the mass transfer coefficient, θ , τ , and κ , respectively, as

$$\theta = \frac{C_L}{K_{oa} C_{B,0}} \quad (5.16)$$

$$\tau = \frac{k'_0 t}{\delta K_{oa}} \quad (5.17)$$

$$\kappa = \frac{k'}{k'_0} \quad (5.18)$$

where k'_0 is the mass transfer coefficient at $r = 0$. Equation 5.15 now can be expressed in dimensionless form as

$$\frac{\partial \theta}{\partial \tau} = -\kappa(\theta - \Pi) \quad (5.19)$$

Initially there is no the absorbate in the oil. For this initial condition, the solution of Equation 5.19 is

$$\theta = \Pi (1 - e^{-\kappa \tau}) \quad (5.20)$$

The dimensionless concentration averaged over the impaction media, $\bar{\theta}$, is convenient for comparing the model results to experimental data. This is calculated as

$$\bar{\theta} = \frac{2}{r_{max}^2} \int_0^{r_{max}} \theta r dr \quad (5.21)$$

Figure 5-4 shows the evolution of $\bar{\theta}$ from the analytic solution for absorption without denuding in the MOI. As expected $\bar{\theta}$ approaches its saturation value, Π , with a characteristic time which reflects k' averaged over the impaction surface. The bottom stages saturate most quickly, because these stages have the highest k' values. The program which generates these results is listed in Appendix E.

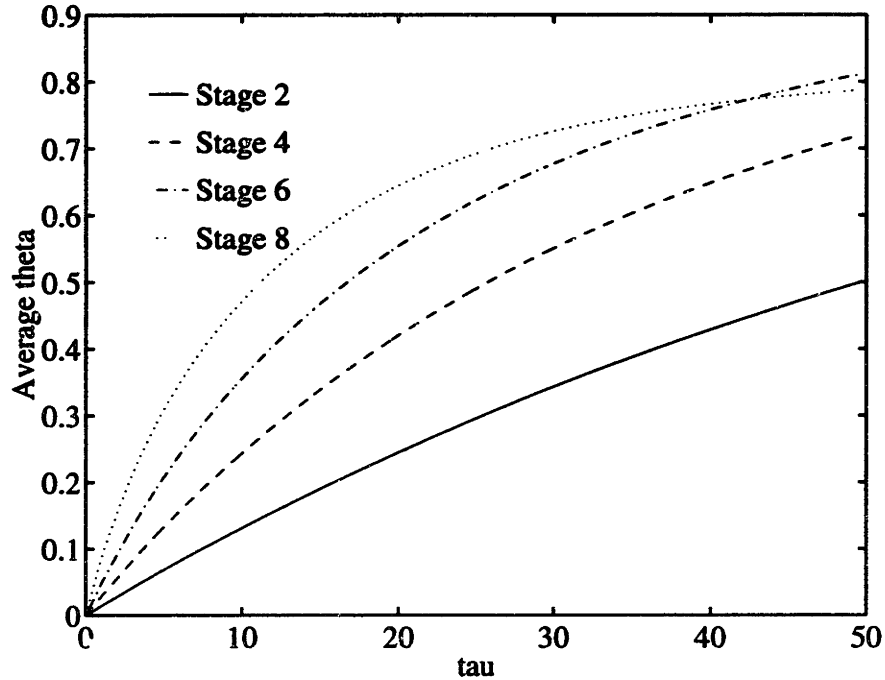


Figure 5-4: Prediction of absorption in MOI versus time for stages 2, 4, 6, and 8 without denuding.

5.5 Absorption with Gas Phase Denuding

The removal of PAH from the gas phase will be important if the characteristic time for mass transfer is comparable to, or shorter than, the characteristic time for mass input through the impactor. The characteristic time for mass transfer, τ_k , is

$$\tau_k = \frac{\delta K_{oa}}{k_0} \quad (5.22)$$

The characteristic time for mass input, τ_i , is the time for an amount of PAH sufficient to saturate the oil on all impactor stages to flow through the impactor

$$\tau_i = \frac{N_{st} A \delta K_{oa}}{Q} \quad (5.23)$$

where Q is the volumetric flow rate through the impactor and N_{st} is the number of stages. The ratio of these characteristic times is

$$\frac{\tau_k}{\tau_i} = \frac{Q}{k'_0 AN_{st}} \quad (5.24)$$

For the MOI, taking $k'_0 = 0.3$ m/s, $\tau_k/\tau_i = 0.2$. Since the condition $\tau_k \ll \tau_i$ is not met, the change in the gas phase concentration due to mass transfer to previous stages cannot be neglected.

A dimensionless measure of denuding, ζ , can be defined as

$$\zeta = 1 - \frac{C_B}{C_{B0}} \quad (5.25)$$

This definition is convenient because, in the case of no denuding, $\zeta = 0$, and in the case of complete denuding $\zeta = 1$. With the inclusion of denuding, Equation 5.19 becomes

$$\frac{\partial \theta}{\partial \tau} = -\kappa(\theta + \zeta - 1) \quad (5.26)$$

Because ζ depends on the integrated absorption of the previous stages, Equation 5.26 can not be integrated analytically. This equation was evaluated by Eulerian integration over radial position and time. The integration method was verified by comparing the results for $\zeta = 0$ to the analytical result obtained above. The program which integrates this equation is listed in Appendix E.

Figure 5-5 shows the evolution of ζ for pyrene in the MOI with time. At short times denuding significantly reduces the gas phase concentration in the lower stages.

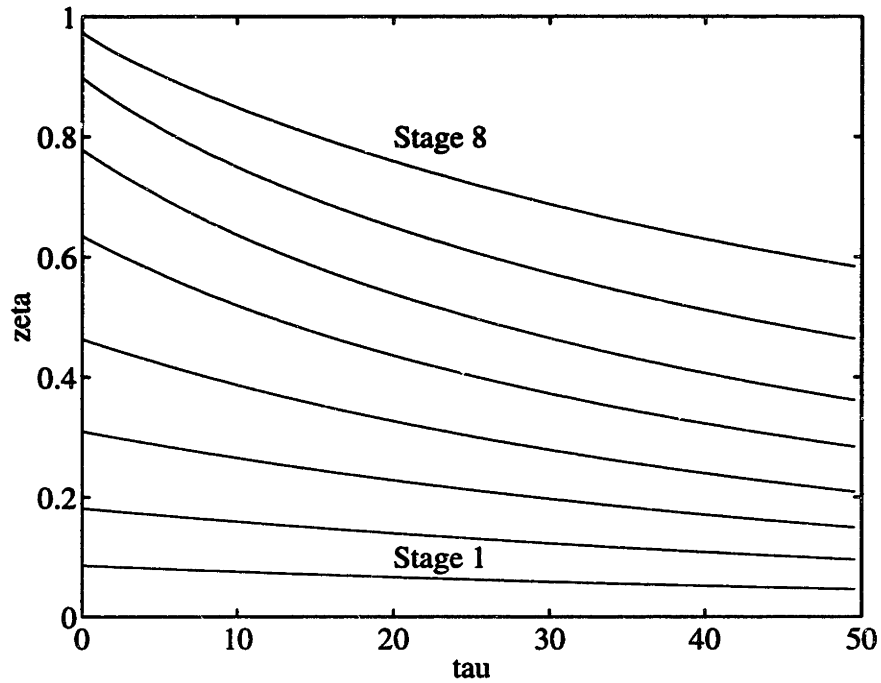


Figure 5-5: Dimensionless denuding, ζ , versus dimensionless time, τ , in the MOI.

Figure 5-6 shows the evolution of $\bar{\theta}$ calculated by numerical integration of Equation 5.26. In comparison with the analytical solution which ignores denuding, (see Figure 5-4), the results for stage 2 are nearly identical. For lower stages, there is a noticeable decrease in $\bar{\theta}$ as a result of denuding.

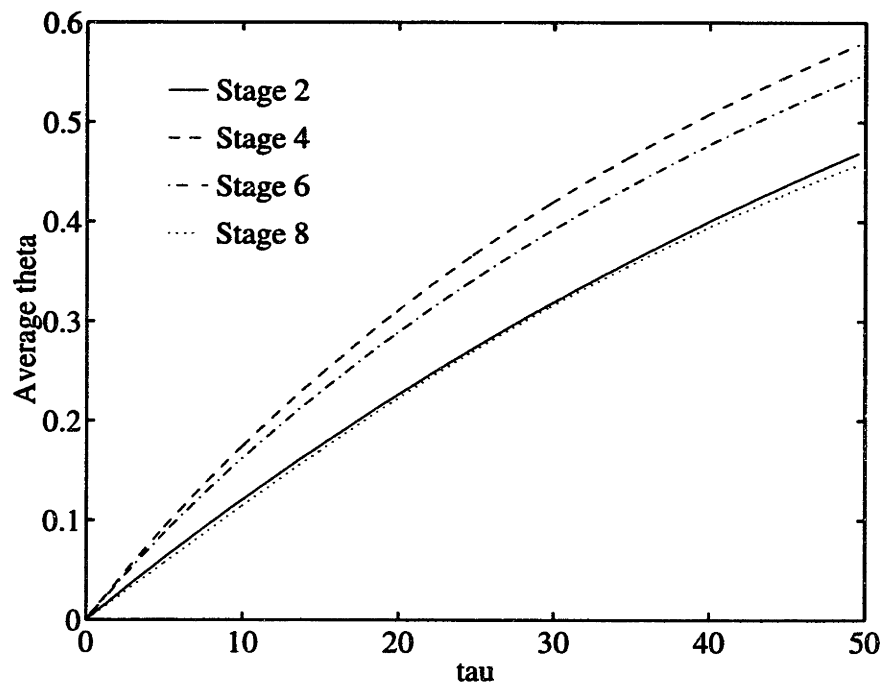


Figure 5-6: Prediction of absorption in MOI versus time for stages 2, 4, 6, and 8 with denuding.

5.6 Comparison with Experimental Results

In the previous chapter the absorption of pyrene in oiled impaction media in the MOI was measured for exposure times of 6, 24 and 73 h. The results from the numerical integration of Equation 5.26 can be compared with these results by using available physical property data for pyrene and dibutyl phthalate. Figures 5-7, 5-8, and 5-9 show these comparisons.

The model predictions compare well with the experimental results for stages 1 through 4 for all exposure times. The model generally under predicts the mass transfer, but under predicts by at most 30%. A possible explanation for the under prediction of mass transfer on these stages is that the PTFE membrane is not a smooth surface. Surface roughness could increase k' above that which was predicted for a flat surface.

For stages 5 through 8 the model systematically over predicts the amount absorbed. These lower stages all have a large number of jets issuing from closely packed perforations made in a 25 mm plate. Scholtz and Trass, and Martin considered jets issuing from nozzles which project below the upper plate. In an array of nozzles design, the head space permits flow from the inner jets to leave the vicinity of the plate without interfering with the outer jets. In the perforated plate design, the exhaust from the inner jets is more likely to disturb the flow patterns of neighboring jets. In fact, particle deposits collected on the lower stages of the MOI are not round, instead the deposits near the outer edge of the impaction plate resemble short arc segments. Stages 6 through 8 also depart from the H/D conditions studied in the literature.

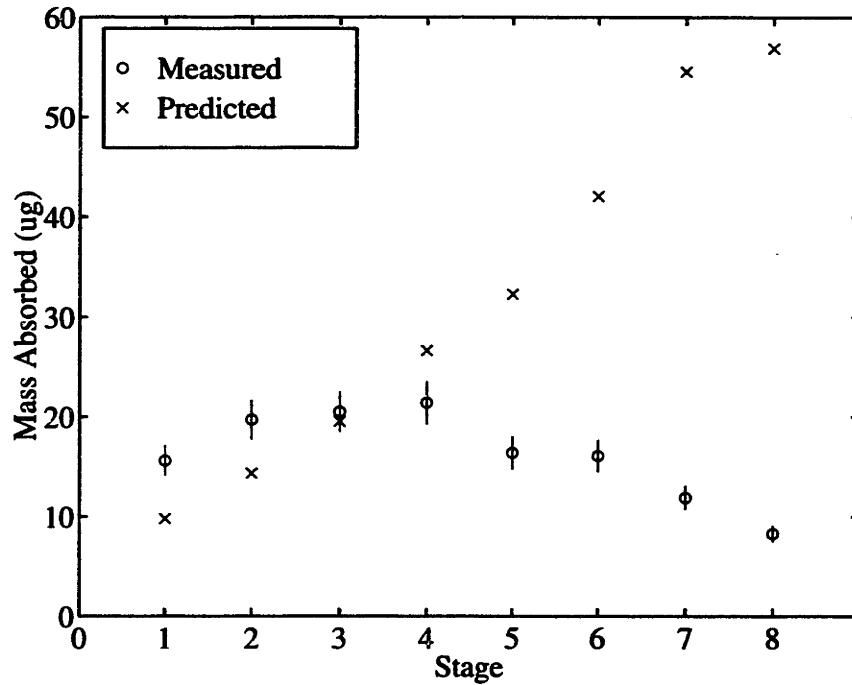


Figure 5-7: Measured and predicted pyrene absorption in MOI after 6 hours.

For these stages $H/D > 5$ and jet spreading due to viscous entrainment is expected to further reduce mass transfer.

The model predictions for stages 5 through 8 establish an upper bound on mass transfer to the impaction media. A lower bound of the mass transfer could be estimated by substituting a single orifice for the array of perforations; this represents the extreme case that the jets mixing completely before encountering the impaction surface. Stage 0 has a single 10 mm nozzle. Using an average mass transfer coefficient from stage 0 for these stages would result in predicted absorption less than that for stage 0 because C_B is lower on these stages due to pressure drops and denuding.

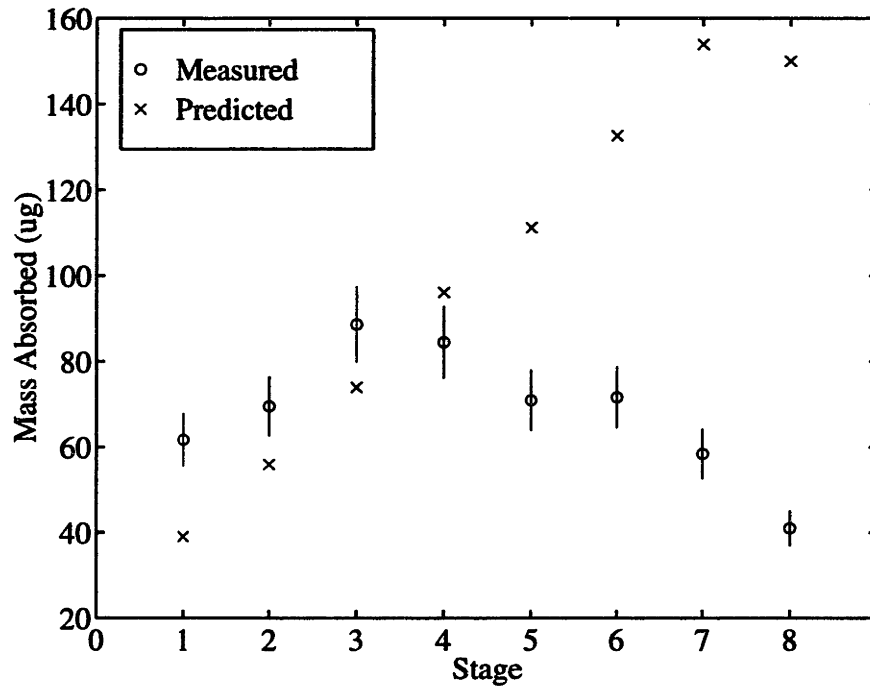


Figure 5-8: Measured and predicted pyrene absorption in MOI after 24 hours.

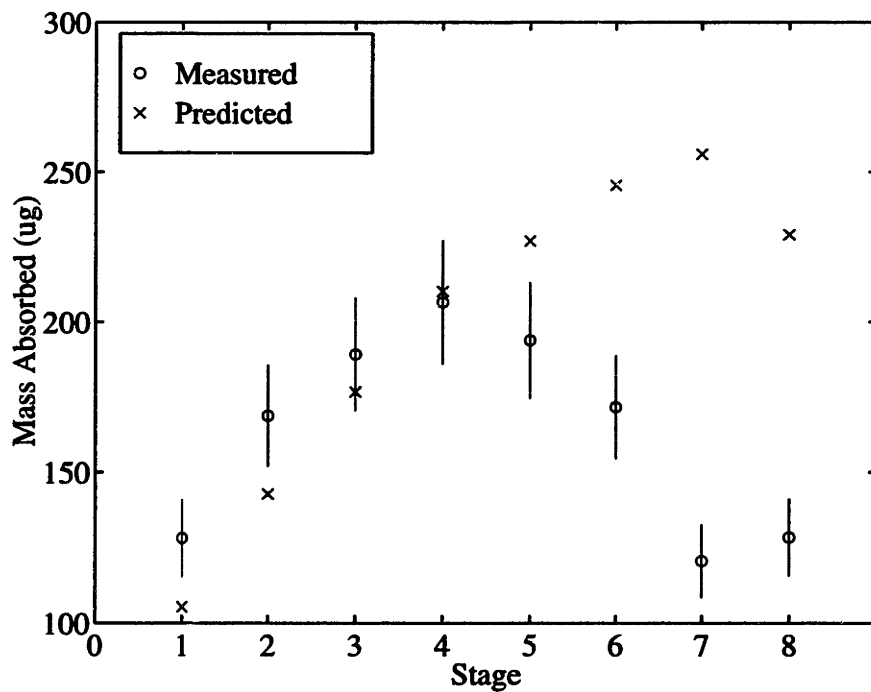


Figure 5-9: Measured and predicted pyrene absorption in MOI after 73 hours.

5.7 Conclusions

A model of mass transfer to oiled impaction media was developed using literature correlations for impinging jet mass transfer. Model predictions were compared to experimental measurements for pyrene absorbing in the MOI. The predictions compared well with measurements for the first four stages. For the lower four stages, predictions were systematically higher than the measured values, by as much as 6 times. This discrepancy was attributed to closely packed jets issuing from a perforated plate and large values of H/D , configurations not studied in the literature. The predicted mass transfer for these stages can be bounded by the present model and one using a single large jet.

The results of this analysis can be extended to cascade impactors other than the MOI. These designs include the Micro-Orifice Uniform Deposit Impactor (MOUDI), Hering Low Pressure Impactor, Berner Impactor, and Andersen Impactor. For the MOI and MOUDI, which have closely packed jets issuing from perforated plates of the same design, empirical corrections to k' for the lower stages may be made. None of the other impactor designs mentioned here have closely packed jets issuing from a perforated plate. For these, the uncorrected literature correlations should yield reasonable predictions of the absorption artifact. Such predictions would take the form of dimensionless plots of $\bar{\theta}$ versus τ .

Chapter 6

Adsorptive Partitioning

6.1 Introduction

Adsorptive association of PAH with particles has been proposed to explain the atmospheric partitioning of PAH and semi-volatile atmospheric pollutants in general [87, 40, 88]. These explanations have assumed that the pollutants are uniformly distributed among the airborne particles, and that equilibrium partitioning is attained in the atmosphere. Further, the adsorption is proposed to be “liquid-like” and non-competitive.

The objective of this chapter is to describe the partitioning of PAH between a single particle and the atmosphere by adsorption, then to test this description for agreement with the available atmospheric data. The approach will be to examine the equilibrium and transient predictions of partitioning by adsorption. The equilibrium gas—particle partitioning, enthalpy of association and characteristic times for mass transfer will be estimated. Comparisons of these estimates with atmospheric data will

be used to evaluate this proposed mechanism of PAH partitioning in the atmosphere.

6.2 Equilibrium Adsorptive Partitioning

As discussed in Chapter 1, BET and Langmuir models of adsorption have been proposed to explain the observed PAH partitioning in the atmosphere [40, 88]. For submonolayer physical adsorption at atmospheric conditions these descriptions can be shown to be equivalent [88]. Equilibrium partitioning between the gas and particulate phases is then

$$\frac{C_{part}}{C_G} = \frac{bRT\theta_J N_s}{p_L} \quad (6.1)$$

where

C_{part} concentration in particulate phase per volume of air

C_G concentration in gas phase

b BET parameter, $b \approx e^{\frac{\Delta H_{ads} - \Delta H_{vap}}{RT}}$

ΔH_{ads} enthalpy of sorbent—sorbate association

θ_J surface area of particles per volume air

N_s mole sorbed per surface area for monolayer coverage

p_L pure component vapor pressure

6.3 Single Particle Mass Transfer

The approach to equilibrium partitioning in the atmosphere depends on the rate of mass transfer between the particles and gas. Here we consider a spherical particle

with adsorption sites on its exterior surface in stagnant fluid.

The characteristic time for a molecule to adsorb has been shown to be less than 10^{-11} s [88]. Since the adsorption processes is rapid, the gas phase concentration at the surface can be assumed to be in equilibrium with the adsorbed species.

More relevant to atmospheric partitioning is diffusive resistance to mass transfer in the gas phase. The characteristic time for gas phase diffusion, τ_G , is

$$\tau_G = \frac{D_p^2}{4D_G} \quad (6.2)$$

This characteristic time is, for 1 μm particles, on the order 10^{-5} s. Since the gas phase diffusion process is rapid with respect to the residence time of air in an urban environment, the gas phase concentrations can be assumed to be in quasi-steady state.

The characteristic time for a particle to adsorb material to come into equilibrium with a constant gas phase concentration can be found by considering a solid spherical particle introduced into a gas with a specified constant concentration of PAH. The change in adsorbed PAH on the particle due to flux of PAH across the gas-particle interface is

$$\frac{\partial n}{\partial t} = Ak[C_G(\infty) - C_G(R_p)] \quad (6.3)$$

where n is the number of moles adsorbed, A the particle surface area, k the mass transfer coefficient, and $C_G(\infty)$ and $C_G(R_p)$ are the gas phase concentrations far from the particle and at the particle surface. This expression is valid for constant physical properties, and low mass transfer rates [143].

The gas phase concentration near the surface can be assumed to be in equilibrium with the surface. Application of Equation 6.1, and the ideal gas law gives

$$C_G(R_p) = n \frac{p_L}{bRTN_s\pi D_p^2} \quad (6.4)$$

At long times, the amount adsorbed will reach its equilibrium value, n_{eq} . Equation 7.11 then becomes

$$\frac{\partial n}{\partial t} = \frac{-Akp_L}{bRTN_s\pi D_p^2} (n - n_{eq}) \quad (6.5)$$

The characteristic time for equilibration to a spherical particle, τ_{eq} , is then

$$\tau_{eq} = \frac{bRTN_s}{kp_L} \quad (6.6)$$

Since the Reynolds number of particles in the atmosphere is less than 1, the expression for k in a stagnant fluid can be used [143]

$$k = \frac{2D_G}{D_p} \quad (6.7)$$

Equation 6.6 becomes

$$\tau_{eq} = \frac{bRTN_s D_p}{2p_L D_G} \quad (6.8)$$

Expressions for mass transfer in the continuum regime are inaccurate when applied to small particles which have D_p comparable to the mean free path of gas molecules. We use the Sitarski-Nowakowski equation for transition regime mass transfer as modified by Davis et al. [144]. This equation has been found to be in agreement with the

measured rate evaporation for single particles [144, 145]. The accommodation coefficient is taken to be 1. This expression for the transition regime is used to calculate τ_{eq} for all particles since the predictions match those for the continuum regime for large particles. Transition regime τ_{eq} are greater, by up to an order of magnitude, than those calculated for the continuum regime.

Figure 6-1 shows τ_{eq} for some PAH adsorbing to spherical particles over a range of sizes. The values of τ_{eq} vary over 12 orders of magnitude among PAH because of large variations in p_L and D_p . The curves deviate from straight lines for $D_p < 1 \mu\text{m}$ due to the Kelvin effect and transition regime mass transfer. The characteristic time for an urban aerosol is ≈ 1 h. For high molecular weight PAH $\tau_{eq} > 1$ h. Therefore, equilibrium partitioning can only be assumed for PAH with equilibrium adsorbate-gas partitioning ratios equal to or less than that of pyrene.

6.4 Comparison with Atmospheric Data

6.4.1 Surface Coverage

For energetic adsorption, sites on the surface of particles must be available. Whether sub-monolayer or multi-layer absorption is relevant for atmospheric partitioning may be addressed by comparing estimates from atmospheric data of the total surface area available for adsorption with the surface area required to adsorb a monolayer of the associated condensed species.

The surface area required to accommodate a monolayer of molecules that make up

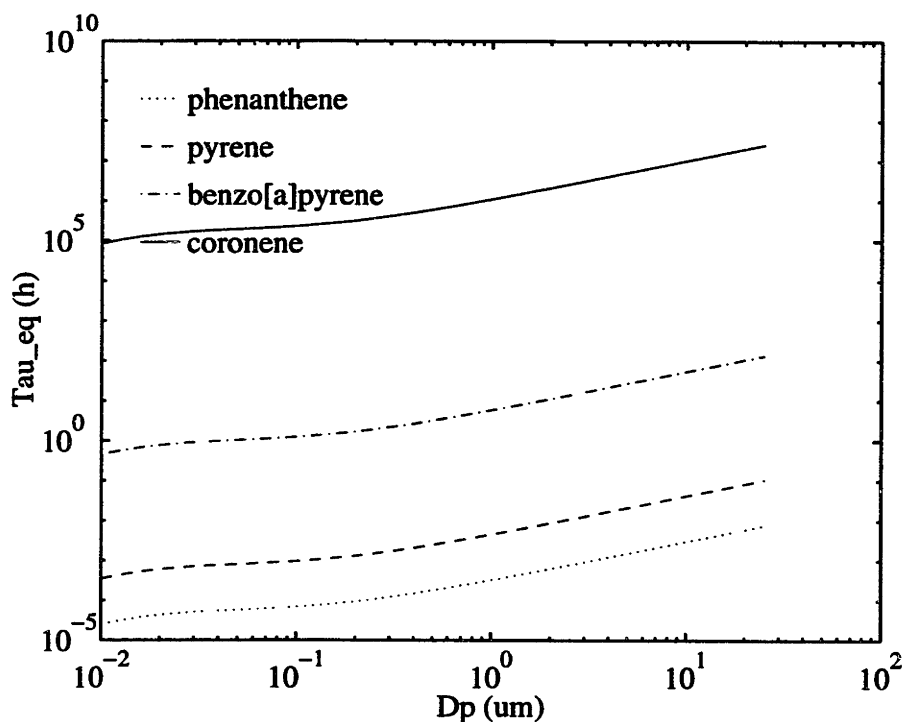


Figure 6-1: Characteristic time for equilibration between the gas phase and spherical adsorbate particles for some PAH at 25°C.

organic carbon, σ_{OC} , can be expressed as the monolayer area divided by the carbon mass. A lower estimate of σ_{OC} can be made from the surface area of a single layer of graphite, where the surface area per carbon atom is 2.55 \AA^2 or $1300 \text{ m}^2/\text{g}$ carbon. The surface areas required to accommodate a monolayer of some atmospherically relevant organic molecules which have been experimentally measured can be compared to this lower estimate. Expressed in m^2/g carbon, σ_{OC} for benzene, *n*-decane, fluoranthene, and pyrene are 3600, 4300, 2000, and 2200, respectively. This demonstrates that the lower estimate for σ_{OC} is a factor of 2–3 lower than that for typical organic pollutants [146, 31].

The surface area available for adsorption in an atmospheric aerosol can be estimated by summing the external surface area of the aerosol and the internal surface

area due to porous elemental carbon. NIST DPM was thermally desorbed at 450°C for 1 hour in an inert atmosphere (see Chapter 8). The surface area of the desorbed DPM was subsequently measured by N₂ adsorption and determined to be 224 m² per g of desorbed soot by BET analysis. This is taken to be the surface area of elemental carbon, σ_{EC} . The BET area of the DPM is approximately twice the external surface area, typical of soots where both the internal and external surface areas are of importance. For $\sigma_{OC} = 2000 \text{ m}^2/\text{g}$, a monolayer coverage of organic compounds would correspond to 0.112 g of organic material per gram of carbon, or about one third of the observed organic content. DPM therefore has multilayer coverage of organic compounds on the soot.

The total external surface area of the fine fraction of an average urban aerosol, $\sum_{ext} A$, estimated from the work of Whitby is approximately 10 cm²/m³ [22]. The sum of the external and internal surface areas is $EC \sigma_{EC} + \sum_{ext} A$, where EC is the mass of elemental carbon in a volume of air. This should be regarded as an upper estimate on the total aerosol surface area available for adsorption because the external surface area of elemental carbon particles is counted twice and the surface area of liquid particles is also included.

The average number of layers of adsorbed organic carbon, θ , is

$$\theta = \frac{OC \sigma_{OC}}{EC \sigma_{EC} + \sum_{ext} A} \quad (6.9)$$

Where OC is the mass of condensed phase organic carbon in a volume of air. Using the OC and EC measurements for fine particles in the Los Angeles area, θ is in the

range 3.8–5.1 [147]. For DPM thermally desorbed at 450°C, θ is 2.24 (see Chapter 8).

The above analysis assumes equal distribution of OC among adsorption sites and neglects pores which limit adsorption. It demonstrates that adsorption can only affect a modest fraction of organic molecules which will be tightly bound to surface. Such adsorbed molecules will not readily participate in partitioning because the enthalpy of adsorption is greater than the enthalpy of association for molecules in either a liquid or solid solution.

To date, there has been no comprehensive treatment of competitive adsorption on atmospheric particles. Treatments of atmospheric partitioning have assumed that PAH are the only species adsorbing on the particle surface. In fact, PAH are a small fraction of the particle-associated organic compounds in the atmosphere and estimates of the surface available for adsorption should acknowledge that competitive adsorption may occur. For surface coverages greater than a monolayer, the adsorbate and adsorbent do not interact in the Langmuir adsorption model. In this case the equilibrium partial pressure of the adsorbent is equal to that of the pure material. In the case of surface coverages greater than a monolayer, the partitioning could be described as either a solid or liquid solution. This paper will not address the problem of partitioning to a solid solution. The absorption model presented in the next chapter can describe partitioning to a liquid film condensed on an adsorbent.

6.4.2 Observed Enthalpies of Gas—Particle Association

Gas—particle distribution ratios for PAH in the atmosphere have been measured by a number of investigators [40, 48, 80, 64]. The measured distribution, ϕ is

$$\phi = \frac{C_{\text{PUF}}}{C_{\text{filter}}} \quad (6.10)$$

where C_{filter} is the atmospheric concentration of PAH collected on the filter and C_{PUF} that collected in an absorbent (often polyurethane foam) downstream of the filter. Note that some authors designate this ratio K ; here we reserve K for equilibrium partition coefficients. Yamasaki et al. collected an extensive set of ϕ values for a range of temperatures at an urban site in Japan [40]. The distribution ratios reported in this data set are comparable to later measurements [21].

For the case of equilibrium partitioning, a Clausius-Clapeyron type relation can be used to determine b as the slope of the line fitted to $\ln \phi$ versus $1/T$ data. These data yield information on the energy of PAH—particle association

$$\ln b = \frac{\Delta H_{\text{ads}}}{RT} \quad (6.11)$$

From Yamasaki's data set, enthalpies of adsorption are 8–16 kJ/gmol above the enthalpy of vaporization, ΔH_{vap} , for all PAH measured. The coincidence that $\Delta H_{\text{ads}} - \Delta H_{\text{vap}}$ is typical of that for physical adsorption of species which are liquids at the temperature of adsorption, has led some authors to suggest that PAH undergo "liquid-like adsorption" in the atmosphere.

Recently Neue and Rudolph measured the adsorption of pyrene and fluoranthene on carbon black [31]. Carbon black was used as a surrogate for the nonvolatile carbonaceous particles emitted from combustors, soot. Soot is expected to be an important adsorbent because it has a high specific surface area (see Chapter 8) and PAH are emitted with soot from combustors [118, 34]. Soot is roughly equivalent to elemental carbon (EC) emitted by combustors. Both pyrene and fluoranthene exhibited Type I adsorption isotherms, characterized by energetic association between the adsorbate and adsorbent up to monolayer coverages [148]. There was no apparent interaction between the adsorbent and adsorbate for coverages above a monolayer. Type I adsorption isotherm data are amenable to description by the simple Langmuir adsorption model.

Neue and Rudolph found that ΔH_{ads} , for pyrene ranged from 4 to 28 kJ/gmol above the enthalpy of sublimation, ΔH_{sub} , for submonolayer coverages. For coverages greater than a monolayer $\Delta H_{ads} \approx \Delta H_{sub}$. These results are consistent with Langmuir-type physical adsorption. Other PAH may have different heats of adsorption, but, in the absence of further experimental evidence, it seems reasonable to suppose that all PAH undergo Langmuir-type physical adsorption. The enthalpies of adsorption for PAH can reasonably be assumed to be in the range 0–30 kJ/gmol above ΔH_{sub} .

To further test the mechanism for PAH—particle association, one can compare the enthalpies of partitioning observed in the atmosphere with estimated enthalpies of adsorption, vaporization and sublimation. As shown above, the data set of Yamasaki

et al., when interpreted assuming adsorptive partitioning, yield

$$\Delta H_{ads} = \Delta H_{vap} + 8-16 \text{ kJ/gmol} \quad (6.12)$$

However, measurements of PAH adsorption on carbon black found [31]

$$\Delta H_{ads} = \Delta H_{sub} + 0-30 \text{ kJ/gmol} \quad (6.13)$$

These data contradict the hypothesis of “liquid-like adsorption” of PAH in the atmosphere. This hypothesis supposes that PAH attain a liquid-like state upon adsorption though in pure form all PAH are crystalline at atmospheric temperatures. There is no evidence to support this supposition. If this were the case, the crystalline state of PAH would be energetically favored over the adsorbed state and PAH adsorption isotherms would be of Type III [148]. In fact, adsorption isotherms of pyrene and fluoranthene on carbon black are of Type I, and $\Delta H_{ads} > \Delta H_{sub}$ [31].

6.4.3 Distribution of PAH with Particle Size

From the adsorptive partitioning hypothesis, PAH with molecular weights less than or equal to that of pyrene should be at equilibrium distribution among the particles in the atmosphere. Recent data on the distribution of polycyclic aromatic hydrocarbons (PAH) with particle size have found that low molecular weight PAH were not uniformly distributed among aerosol size fractions [94, 103]. To account for the variations in PAH distributions with particle size, one must hypothesize different types

of adsorption sites which preferentially adsorb lower molecular weight PAH on larger particles and higher molecular weight PAH on smaller particles. This seems unlikely.

6.5 Conclusions

The hypothesis that PAH partitioning in the atmosphere can be explained as non-competitive, “liquid-like” adsorption has been examined and compared to available atmospheric and thermodynamic data. An examination of the amount of condensed organic material associated with emitted and atmospheric particles shows that the assumption of non-competitive adsorption is unreasonable. In fact, the condensed organic compounds occupy multiple layers, therefore the condensed organic compounds, not the surface of the solid particle, is the surface with which condensing PAH interact.

The enthalpy of adsorption for PAH on carbonaceous particles has been measured to be 0–30 kJ/mol greater than the sublimation enthalpy. The observed enthalpy of gas—particle association for PAH is in all cases less than the enthalpy of sublimation. These data demonstrate that the adsorption of PAH on carbonaceous particles is not “liquid-like”, as is assumed in the adsorptive partitioning hypothesis.

Analysis of characteristic times for the equilibration of PAH between the gas phase and spherical adsorbate particles, shows that, on time scales relevant to urban aerosols, some PAH can be considered to have reached equilibrium partitioning. These lower molecular weight PAH ($M \leq 202$) should have identical distributions with particle size. Data presented here (see Chapter 3) shows that the distributions

of PAH with $M = 178$ and $M = 202$ are substantially different. In sum, the adsorptive partitioning hypothesis does not agree with the available atmospheric and thermodynamic data on PAH and must be substantially revised or discarded.

Chapter 7

Absorptive Partitioning

7.1 Introduction

In the previous chapter the widely circulated hypothesis that atmospheric partitioning of PAH can be described as adsorption was examined and found to be incompatible with available atmospheric data. If gas—solid interactions cannot explain atmospheric partitioning, one must turn to gas—liquid interactions, specifically absorption of PAH in a liquid fraction of the aerosol. This mechanism of association has been suggested in the literature, but not compared to atmospheric sampling data [102].

A number of recent experimental observations suggest that within atmospheric aerosols there exists a distinct fraction of particles which are composed, at least in part, of liquid organic compounds. A selection of these observations are listed here.

1. A large fraction of aerosol mass in source emissions is composed of organic species as determined by solvent extraction and organic carbon analyses. For

example, the extractable fraction of NIST DPM is 17.5% [149] and the organic carbon content of combustion emission sources is in the range 38–50% [34].

2. Macroscopic examinations of collected wood smoke and diesel emission particles show that these aerosols contain a viscous liquid component [150].
3. Microscopic examination of atmospheric particles shows liquid particles and liquid coated soot particles (see Figure 1-3).
4. Atmospheric particles of uniform size were conditioned in a high humidity environment. After conditioning, the particle size distribution was bimodal, indicating that a significant fraction of atmospheric particles are non-hygroscopic [151]. These non-hygroscopic particles may be composed of organic species.
5. Single particle mass spectrometry of atmospheric particles indicates that there is a great variety of particle types in the atmosphere [25, 24]. The particles do not have uniform composition, a number of the prominent particle types contain mass spectra characteristic of organic compounds [25].

The objective of this chapter is to describe absorptive partitioning of PAH in an atmospheric aerosol and to test whether this explanation is consistent with available atmospheric data. The approach will be to first describe equilibrium partitioning of PAH absorbing into the organic fraction. Rates of mass transfer for single particles and within the aerosol will then be analyzed. A simple non-equilibrium model of absorptive partitioning will be developed to combine the results of the equilibrium and mass transfer analyses. Because the chemical composition of the organic fraction

is unknown, parameters necessary for the model, including activity coefficients and the distribution of the organic fraction with particle size, are not available. These parameters will be estimated from literature data and size-segregated atmospheric sampling data for some PAH. The results of this model will be compared with the size-segregated atmospheric sampling results for other PAH to test whether the proposed mechanism is consistent with the size-segregated data and PAH physical properties.

7.2 Equilibrium Absorptive Partitioning

Absorption is the uptake of an absorbate (e.g. PAH) by a liquid solvent. The fugacity of a species in solution can be described in terms of an activity coefficient, γ [152]. For ideal behavior in the gas phase, the gas—solution equilibrium is

$$p = x\gamma p_L \quad (7.1)$$

Where p is the partial pressure of the PAH in the gas phase, x is the mole fraction in the absorbent, and p_L is the vapor pressure of the pure absorbate in its liquid state.

Estimation of subcooled vapor pressures, p_L , for PAH is discussed in Section D.9 and a table of values for atmospheric temperatures given there. Due to surface curvature, p_L for a small drop will be greater than that for a flat interface; this is the well known Kelvin effect [153]. This effect is incorporated in Equation 7.2 as, ψ , the ratio of p_L over a drop to p_L over a flat surface

$$p = x\gamma\psi p_L \quad (7.2)$$

The expression for ψ is

$$\psi = \exp \frac{4\sigma M}{D_p RT \rho} \quad (7.3)$$

where σ is surface tension.

Individual PAH species make up a small fraction of organic compounds in both the emission sources and atmospheric aerosols. For example, in exhaust from autos not equipped with catalysts, x for phenanthrene, pyrene, benzo[*a*]pyrene are 7.50×10^{-4} , 1.18×10^{-3} , and 1.33×10^{-3} , respectively [34]. For the calculation of these values, organic carbon is assumed to be an organic sorbent with an average molecular weight of 300 g/gmol. Mole fractions in organic carbon of these PAH, measured in the same study, in exhaust from catalyst-equipped autos and heavy-duty diesels were less than those from non-catalyst-equipped autos. These combustion sources are believed to be the main contributors to PAH in the atmosphere, so atmospheric mole fractions will be smaller than in the exhaust [34].

Because $x \ll 1$ in the atmosphere, x can be expressed in terms of mass concentration in the liquid organic phase, C_L ,

$$x = \frac{C_L M_o}{\rho_o M} \quad (7.4)$$

where M_o is the average molecular weight of the organic sorbent, M is the molecular weight of the absorbate, and ρ_o is the density of the sorbent.

The nature of the organic sorbent in atmospheric aerosols is unknown. Extensive studies of the chemical composition of major contributors to organic particulate

matter reveal that large fractions of it are unidentifiable and that the identifiable fractions are complex mixtures [33, 34, 35, 36]. Mixed with emissions from additional untested sources and products of partial photooxidation, the composition of the organic fraction in atmospheric aerosols can be expected to be even more complex than that from emission sources. Therefore, γ for PAH in the atmospheric aerosol sorbent cannot be determined and must be estimated.

The activity coefficients of PAH in the organic sorbent can be estimated by two approaches. In the first, the behavior of the atmospheric aerosol is assumed and values for γ are determined from comparisons of the model predictions and atmospheric sampling results. In this work we develop a non-equilibrium absorptive partitioning model and compare the results to distributions of PAH with particle size measured in an urban aerosol. In the second approach, the sorbent is supposed to behave like a solvent or mixture of solvents for which γ data are available or can be estimated. In this work we examine three prototypical solvents for which γ data are available, water, *n*-octanol, and an ideal solvent. These model compounds are typical of species found in the atmosphere. Semi-polar organic compounds like *n*-octanol are emitted by combustors and formed by photooxidation. Approximately ideal solution behavior has been found for PAH in complex organic mixtures like gasoline, diesel, and coal tar [90, 91]. These mixtures are representative of hydrocarbons emitted by combustors. The results from both these methods will be compared to test whether the model is consistent with atmospheric data and PAH physical properties.

The temperature dependence of γ is

$$\left(\frac{\partial \ln \gamma}{\partial T}\right)_{P,x} = \frac{\Delta H_{mix}}{RT^2} \quad (7.5)$$

where ΔH_{mix} is the enthalpy of mixing [152]. The range of relevant temperatures is narrow, -5–35°C, and ΔH_{mix} is generally small, therefore γ will be assumed constant with temperature. Because $x \ll 1$ in atmospheric aerosols, γ will also be independent of absorbate concentration.

7.3 Single Particle Mass Transfer

7.3.1 Gas Phase Diffusion

In this section we consider a liquid particle in which the PAH concentration is not in equilibrium with the gas phase. The evolution of gas phase concentration, C_G , in the continuum regime can be expressed as

$$\frac{\partial C_G}{\partial t} = \mathcal{D}_G \nabla^2 C_G \quad (7.6)$$

where \mathcal{D}_G is the diffusivity of PAH in air, since the vapor pressures of PAH are low.

The characteristic time for gas phase diffusion, τ_G , is then

$$\tau_G = \frac{D_p^2}{4\mathcal{D}_G} \quad (7.7)$$

7.3.2 Liquid Phase Diffusion

For low concentrations of PAH in the particle, typical of combustion emissions and atmospheric aerosols, the concentration of PAH within the liquid particle, C_L , can be expressed as

$$\frac{\partial C_L}{\partial t} = \mathcal{D}_L \nabla^2 C_L \quad (7.8)$$

where \mathcal{D}_L is the diffusivity of PAH in the sorbent. The characteristic time for liquid phase diffusion, τ_L , is then

$$\tau_L = \frac{D_p^2}{4\mathcal{D}_L} \quad (7.9)$$

The ratio of characteristic times for gas and liquid phase diffusion is

$$\frac{\tau_L}{\tau_G} = \frac{\mathcal{D}_G}{\mathcal{D}_L} \quad (7.10)$$

Values for \mathcal{D}_L are in the range 10^{-9} – 10^{-11} m²/s [124]. For PAH, \mathcal{D}_G are in the range 4 – 7×10^{-6} m²/s (see Section D.5). Because $\tau_G \ll \tau_L$, the spatial variation C_G can be considered in quasi-steady state with respect to C_L .

7.3.3 Gas—Liquid Equilibration

The characteristic time for a particle to come into equilibrium with a constant gas phase concentration can be found by considering a liquid particle introduced into a gas with a specified constant concentration of PAH. The particle is assumed to be a spherical liquid particle in stagnant air. This idealized situation is representative of particles emitted with high concentrations of PAH, e.g. diesel and auto exhaust, as

well as particles emitted with low PAH concentrations, e.g. meat cooking aerosol, into a polluted urban atmosphere. This analysis is also applicable to particles in rapidly rarefied gas, for example in an instrument with large pressure drops.

The change of PAH concentration in the particle due to flux of PAH across the gas-particle interface is

$$V \frac{\partial C_L}{\partial t} = Ak[C_G(\infty) - C_G(R_p)] \quad (7.11)$$

where V is the particle volume, A the particle surface area, k the mass transfer coefficient, and $C_G(\infty)$ and $C_G(R_p)$ are the gas phase concentrations far from the particle and at the particle surface. This expression is valid for negligible radial variation in C_L , constant physical properties, and low mass transfer rates [143]. The first assumption will be tested below by comparing the characteristic times for liquid diffusion and gas—liquid equilibration.

The gas phase concentration near the surface can be assumed to be in equilibrium with the liquid. Application of Equations 7.2, 7.4, and the ideal gas law gives

$$C_G(R_p) = \frac{C_L M_o \gamma \psi p_L}{\rho_o RT} \quad (7.12)$$

At long times, the liquid concentration will reach its equilibrium value, $C_{L,eq}$, which can be expressed in terms of the equilibrium partition coefficient, K ,

$$\frac{K}{\psi} = \frac{C_{L,eq}}{C_G} \quad (7.13)$$

Note that $C_{L,eq}$ is for a flat surface. The expression for K , the ratio of PAH concentration in the sorbent to that in the air, is

$$K = \frac{\rho_o RT}{M_o \gamma p_L} \quad (7.14)$$

Equation 7.11 then becomes

$$\frac{\partial C_L}{\partial t} = \frac{-Ak\psi(C_L - C_{L,eq})}{VK} \quad (7.15)$$

The characteristic time for gas—particle equilibration, τ_{eq} , is then

$$\tau_{eq} = \frac{VK}{Ak\psi} \quad (7.16)$$

Since the Reynolds number of particles in the atmosphere is less than 1, the expression for k in a stagnant fluid can be used [143]

$$k = \frac{2D_G}{D_p} \quad (7.17)$$

For a spherical particle Equation 7.16 becomes

$$\tau_{eq} = \frac{D_p^2 K}{12D_G \psi} \quad (7.18)$$

The ratio of characteristic times for gas—liquid equilibration to liquid phase dif-

fusion is

$$\frac{\tau_{eq}}{\tau_L} = \frac{D_L K}{3D_G \psi} \quad (7.19)$$

If $\tau_L \ll \tau_{eq}$, the liquid phase concentration can be considered in quasi-steady state and radial variation of C_L neglected. This will be the case if

$$\frac{K}{\psi} \gg \frac{3D_G}{D_L} \quad (7.20)$$

At atmospheric conditions, for $D_G/D_L = 10^5$, this inequality becomes

$$\frac{K}{\psi} \gg 3 \times 10^5 \quad (7.21)$$

For phenanthrene in a 0.01 μm drop of an ideal solvent at 25°C, $K/\psi = 2.13 \times 10^7$.

For an aqueous drop, $K/\psi = 190$. Therefore this approach is not valid for aqueous drops and we consider only cases for which $\log K \geq 7.5$ and $D_p > 0.01 \mu\text{m}$.

Expressions for mass transfer in the continuum regime are inaccurate when applied to small particles which have D_p comparable to the mean free path of gas molecules. We use the Sitarski-Nowakowski equation for transition regime mass transfer as modified by Davis et al. [144]. This equation has been found to be in agreement with the measured rate evaporation for single particles [144, 145]. The accommodation coefficient is taken to be 1. This expression for the transition regime is used to calculate τ_{eq} for all particles since the predictions match those for the continuum regime for large particles. Transition regime τ_{eq} are greater, by up to an order of magnitude, that those calculated for the continuum regime.

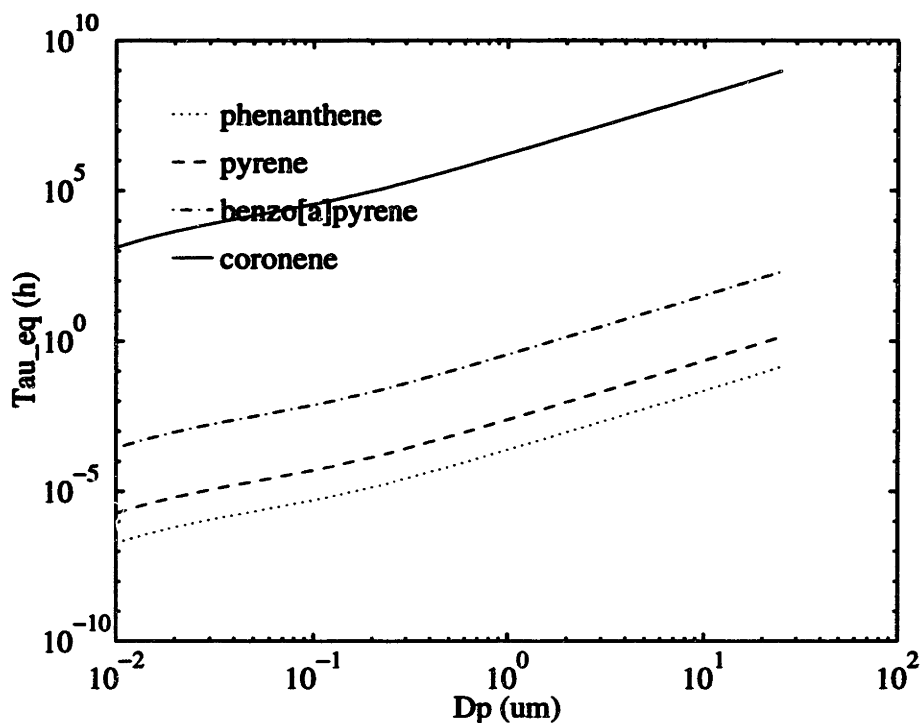


Figure 7-1: Characteristic time for equilibration between the gas phase and *n*-octanol particles for some PAH at 25°C.

Figure 7-1 shows τ_{eq} for some PAH in *n*-octanol at 25°C for a range of particle sizes. The values of τ_{eq} vary over 16 orders of magnitude among PAH because of large variations in K and D_p . The curves deviate from straight lines for $D_p < 1 \mu\text{m}$ due to the Kelvin effect and transition regime mass transfer. The characteristic time for an urban aerosol is ≈ 1 h. For high molecular weight PAH and large particles, $\tau_{eq} > 1$ h. Therefore, an accurate description of atmospheric partitioning cannot assume equilibrium partitioning.

7.4 Aerosol Partitioning Model

7.4.1 Model Description

To test the hypothesis that atmospheric partitioning can be explained as non-equilibrium absorption to an organic aerosol fraction, a model which incorporates transient atmospheric processes is required. These transient processes include emissions, deposition, coagulation, vaporization, sorption, and photooxidation. Each of these processes are examined for their significance on urban aerosol time scales, and, if important, included in a Lagrangian model. Some processes which may be significant, but for which no data are available, cannot be included; the qualitative effect of these processes is discussed with the model results. The results of the model are then compared to size-segregated sampling data.

The model follows a parcel of air which initially contains organic sorbent and gas phase PAH at background conditions. Emissions of both PAH and sorbent are added uniformly to the parcel for a residence time, t_{res} . This is representative of an air parcel traveling over an urban area with well distributed sources. A reasonable value for t_{res} is 100 min, this is the time for an air parcel to travel the 15 km from Route 128 to Kenmore Square at 2.5 m/s. Because the model results will be compared to impactor sampling data, the aerosol is divided into 9 bins each with the same cut-off D_p as the MOI. The particle size in each bin is assumed to be uniform and equal to the volumetric average of the upper and lower cut-off aerodynamic diameters.

7.4.2 Sorbent Evolution

The organic aerosol fraction has not been studied in size-segregated aerosol samples and has not been analyzed completely in whole aerosol samples. Because the nature and distribution with particle size of the sorbent is unknown, the chemical nature of the sorbent will be assumed to be uniform for all particle sizes, and its distribution with particle size will be inferred from the observed distributions of some PAH.

At equilibrium PAH will distribute among the aerosol size fractions based on the amount of sorbent in each size fraction. For each size bin, i , in equilibrium with the gas phase

$$C_G = \frac{\psi C_{L,i}}{K} \quad (7.22)$$

where $C_{L,i}$ is the concentration of PAH in sorbent in bin i . Expressed in terms of the concentration of PAH on a volume of air basis, C_i , associated with size bin i , at equilibrium

$$C_G = \frac{\psi C_i \rho_o}{K C_{o,i}} \quad (7.23)$$

where $C_{o,i}$ is the concentration of sorbent in bin i on a volume of air basis.

We assume that all PAH are in equilibrium in the rural aerosol. In the case of partitioning to *n*-octanol, τ_{eq} for benzo[*e*]pyrene partitioning to a 10 μm particle is 4.7 h. The physical constants used in this and subsequent calculations are tabulated in Appendix D. For regional transport, for which time scales are on the order of one day, it is therefore reasonable to assume that benzo[*e*]pyrene has attained an equilibrium distribution with the rural aerosol. Good rural size distribution data were obtained

for this PAH and those data are used to estimate the distribution of $C_{o,i}$ in the rural aerosol.

We also assume that the highest vapor pressure PAH are in equilibrium with the urban aerosol. For phenanthrene partitioning to a 10 μm particle of *n*-octanol, τ_{eq} is 10 s. Because $\tau_{eq} \ll t_{res}$, it is reasonable to assume that phenanthrene has attained an equilibrium distribution with the urban aerosol. Because $\tau_{eq} \propto K$, the approach to equilibrium will be faster for other sorbents in which PAH are less soluble. A reasonable upper estimate τ_{eq} can be made by considering an ideal solvent. For an ideal solvent with physical constant values $\sigma = 30 \text{ mN/m}$, $M_o = 300 \text{ g/gmol}$, and $\rho_o = 0.9 \text{ g/cm}^3$, τ_{eq} for 10 μm particles are 30 s for phenanthrene and 173 h for benzo[*e*]pyrene. Clearly the assumption that phenanthrene has reached equilibrium with urban aerosols is reasonable, while that for benzo[*e*]pyrene equilibration with rural aerosols depends on the sorbent.

The distributions of PAH can be used to estimate the relative distribution of sorbent with particle size. However, they cannot be used to determine the amount of sorbent in each size fraction. We will use Whitby's average aerosols to estimate the sorbent amounts [22]. The procedure will be first to estimate the mass of ultrafine combustion-generated particles in an aerosol, then to estimate the amount of sorbent in the ultrafine mode from the organic fraction of particulate combustion emissions, and lastly to calculate the amount of sorbent in the other bins from the sorbent distributions.

In Whitby's paradigm, ultra-fine particles are generated by combustors and homogeneous nucleation. In a polluted urban atmosphere, homogeneous nucleation can

usually be neglected because of the large number of particles available for sorption [154]. The organic fraction of whole combustion particulate emissions has been measured. For NIST DPM the fraction of the mass extractable with DCM is 17.5% [149]. For auto and diesel exhaust, the amount of organic carbon is in the range 38–50% [34]. We will estimate the amount of sorbent associated with the smallest sized particles to be one third of their total mass. The volume of particles in a bin containing particles in the size range $D_{p,1}$ – $D_{p,2}$ is

$$V_i = \frac{\pi}{6} \int_{D_{p,1}}^{D_{p,2}} D_p^3 n(D_p) d \log D_p \quad (7.24)$$

where $n(D_p)$ is Whitby's trimodal log-normal distribution of particle number concentration [22]. The mass of particles on a volume of air basis in size bin i is M_i . This was determined by assuming unit density for the particles and scaling the mass by the ratio of PM10 mass measured during sampling to that calculated for an average aerosol, as

$$M_i = \frac{\rho_{\text{PM10}}}{V_{\text{PM10}}} \frac{\pi}{6} \int_{D_{p,1}}^{D_{p,2}} D_p^3 n(D_p) d \log D_p \quad (7.25)$$

where V_{PM10} , is V_i from Equation 7.24 integrated from $-\infty$ to $10 \mu\text{m}$. For size bins in the ultrafine mode, which contain mainly combustion particles,

$$C_{o,i} = \text{OF } M_i \quad (7.26)$$

where OF is the fraction of the mass which is organic material in combustion particles.

Figures 7-2 and 7-3 show the distributions of Whitby's average aerosol and the

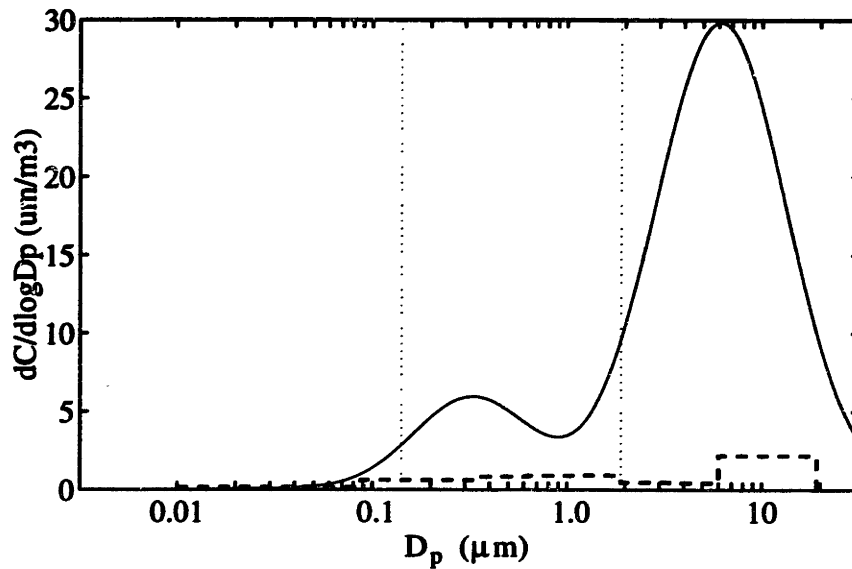


Figure 7-2: Distributions of total and sorbent mass with particle size in rural aerosol [22].

sorbent estimated by this method for the rural and urban aerosols. Note that, unlike Whitby's aerosol, the urban sorbent mass distribution is unimodal with a peak at $D_p = 2.5 \mu\text{m}$, near the minimum of the average urban aerosol volume. These sorbent amounts are distributions scaled by $C_{o,i}$ for the second size bin, $0.141 < D_p < 0.343 \mu\text{m}$, since scaling by the first size bin, $0.01 < D_p < 0.141 \mu\text{m}$, resulted in the sorbent mass exceeding the total mass for some particle sizes.

The aerosol sorbent will evolve by addition from sources, removal by deposition, and changes in particle size due to coagulation and condensation. Wexler et al. have shown that the shortest time scales for coagulation in an urban aerosol are on the order of 1 h [154]. This was for the case of $0.01 \mu\text{m}$ particles colliding with $0.3 \mu\text{m}$ particles; for particles with $D_p \geq 0.1 \mu\text{m}$, the characteristic time will be ≈ 100 h

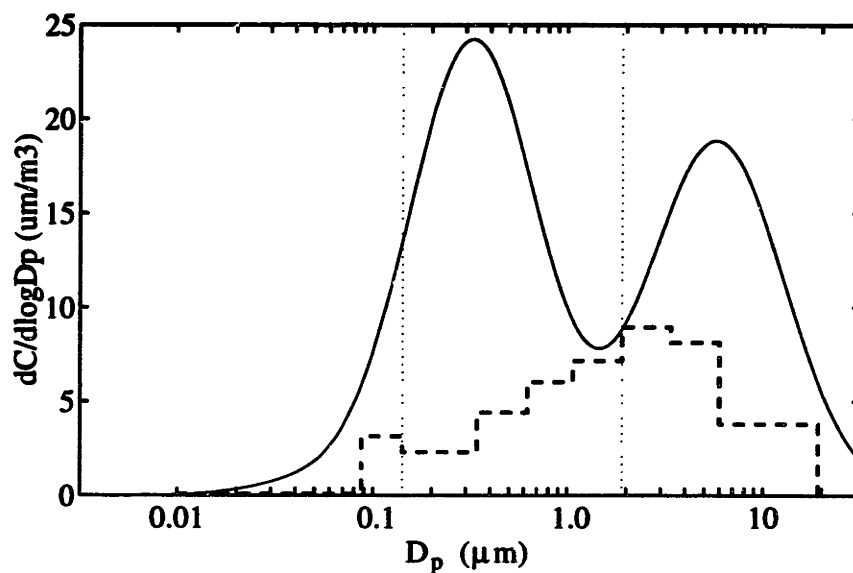


Figure 7-3: Distributions of total and sorbent mass with particle size in urban aerosol [22].

[23]. Since the characteristic time for coagulation is much greater than t_{res} , changes in particle size by coagulation are neglected.

Redistribution of the sorbent by vaporization and sorption cannot be included here, as its composition is unknown. High molecular weight alkanes and alkanolic acids make up a large fraction of the organic emissions from combustors [34]. For these low vapor pressure species it is reasonable to assume that redistribution is negligible since $\tau_{eq} \gg t_{res}$.

Because coagulation of particles and redistribution of the sorbent are neglected, the aerosol sorbent is affected only by additions to each size bin representative of urban emissions of sorbent and by deposition. Emissions are assumed to be uniform,

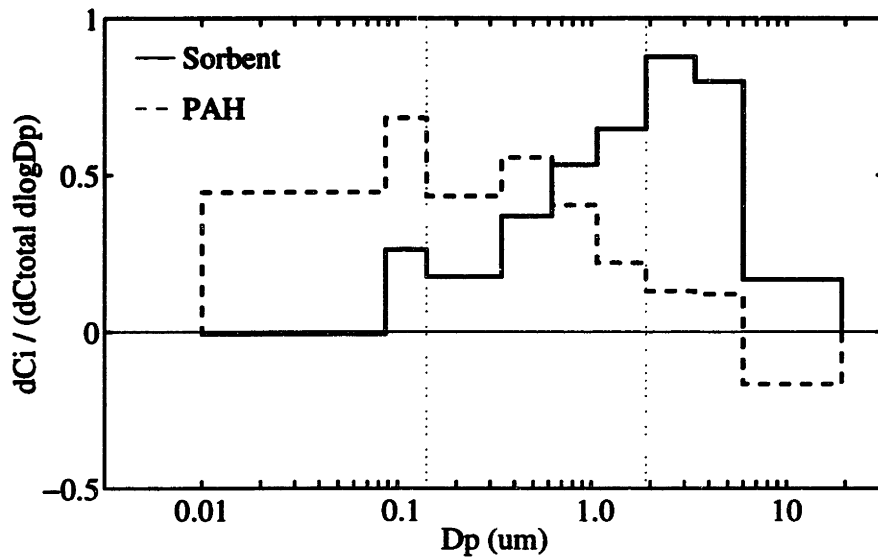


Figure 7-4: Net addition of aerosol sorbent and PAH by emissions and deposition.

therefore the change in sorbent in bin i is

$$\frac{dC_{o,i}}{dt} = \frac{C_{o,i}(t_{res}) - C_{o,i}(0)}{t_{res}} \quad (7.27)$$

The rural and urban distributions of $C_{o,i}$ are used for the initial and final distributions, respectively. Figure 7-4 shows the rate of sorbent addition to each size bin normalized by sum of sorbent addition for all bins. Note the small net removal of material from the smallest size bin. This may be indicative of particle coagulation or sorbent redistribution by vaporization and sorption which is not included in this model.

7.4.3 PAH Evolution

PAH in the air parcel are assumed to have achieved an equilibrium distribution in the rural aerosol. PAH distributions with particle size will evolve as a result of emissions, changes in particle size, photooxidation, vaporization, and absorption. As discussed above, changes in particle size due to coagulation and condensation will be neglected here.

From smog chamber studies, Atkinson et al. concluded that the primary reaction of gas phase PAH is with OH· [76]. Using $[\text{OH}\cdot] \approx 10^6$ molecules/cm³, a typical value for polluted urban atmospheres [23], the half-lives for PAH in the gas phase on the order of 4 h. These half-lives apply only to that fraction of PAH in the gas phase. Measurements of photooxidation reactions of PAH associated with particles found that PAH associated with carbon-containing fly ash had half-lives on the order of 1000 h [78]. Because the photooxidation half-lives for both gas and particulate phase reactions are much greater than t_{res} , photooxidation of PAH can be neglected.

PAH concentration in bin i therefore evolves due to emissions, and mass transfer by vaporization and sorption

$$\frac{dC_i}{dt} = \left(\frac{dC_i}{dt}\right)_{\text{emissions}} + \left(\frac{dC_i}{dt}\right)_{\text{mass transfer}} \quad (7.28)$$

Since all PAH are mainly emitted by combustors [34], the distributions of all PAH with particle size at the emission source are expected to be equal. High molecular weight PAH, for which $\tau_{eq} \gg t_{res}$ will not significantly redistribute from the particles with which they were emitted by volatilization and sorption on time scales relevant

for urban aerosols. For coronene $\tau_{eq} = 19$ h for a $0.01 \mu\text{m}$ particle of *n*-octanol. Therefore, the distribution of PAH in emissions is inferred from that of coronene.

Like emissions of sorbent, PAH emissions were assumed to be uniform; the addition of PAH to bin *i* is

$$\left(\frac{dC_i}{dt}\right)_{\text{emissions}} = \frac{(1 - \alpha) \sum C_i(t_{res})}{t_{res}} \left[\frac{C_i(\text{coronene})}{\sum C_i(\text{coronene})} - \frac{C_i(\text{rural})}{\sum C_i(\text{rural})} \right] \quad (7.29)$$

where α is the ratio of the rural to final urban concentration of PAH. The value of α was set to 0.05, this is was typical of the ratio of urban to rural concentrations found in the size-segregated sampling study. The distribution of PAH emissions is shown in Figure 7-4. Note that there is net removal of PAH from the largest size bin. This may be the result of deposition of large particles of rural origin.

Combustion emissions will be rich in particles at the tail pipe and be rapidly diluted by mixing in the atmosphere. Due to the rapid dilution, on the order of 10 s, equilibration of PAH between the gas and particles may not be attained. An upper limit for the gas phase concentration is that in equilibrium with particles in the smallest bin. This upper limit is assumed in the model. The gas phase emissions were

$$\left(\frac{dC_G}{dt}\right)_{\text{emissions}} = \frac{\psi \rho_o}{KC_{o,n}} \frac{dC_{i,n}}{dt} \quad (7.30)$$

where *n* is the smallest size bin. The model results were relatively insensitive to this assumption, so that running the model with no gas phase emissions gave results similar to those based on the assumption that C_G was in equilibrium with the smallest

particles.

The partitioning of PAH to differently sized particles by vaporization and sorption is included in this model. PAH in the gas phase and sorbent are assumed to be well mixed as justified above. The concentration change due to mass transfer is

$$\left(\frac{dC_i}{dt}\right)_{\text{mass transfer}} = \frac{-1}{\tau_{eq}} \left(C_i - \frac{C_G C_{o,i} K}{\psi \rho}\right) \quad (7.31)$$

The evolution of gas phase PAH is determined by the mass balance of PAH in the air parcel

$$\frac{\partial C_G}{\partial t} = \left(\frac{dC_G}{dt}\right)_{\text{emissions}} = - \sum \left(\frac{\partial C_i}{\partial t}\right)_{\text{mass transfer}} \quad (7.32)$$

7.4.4 Model Implementation

The equations describing the evolution of the sorbent aerosol and PAH were numerically integrated in time using an Eulerian procedure. The time step, Δt , was less than $0.3 \tau_{eq}$ for the minimum τ_{eq} . Integration using smaller Δt gave the same results, indicating that time step was sufficiently small for accurate numerical integration. At each time step, sorbent and PAH emissions were first added to the particle bins and gas phase, then mass transfer between the particle bins and the gas phase was calculated, and finally a new C_G was calculated from the PAH mass balance. Physical constants for the sorbent were $\sigma = 30 \text{ mN/m}$, $M_o = 300 \text{ g/gmol}$, and $\rho_o = 0.9 \text{ g/cm}^3$. This code is listed in Appendix E.

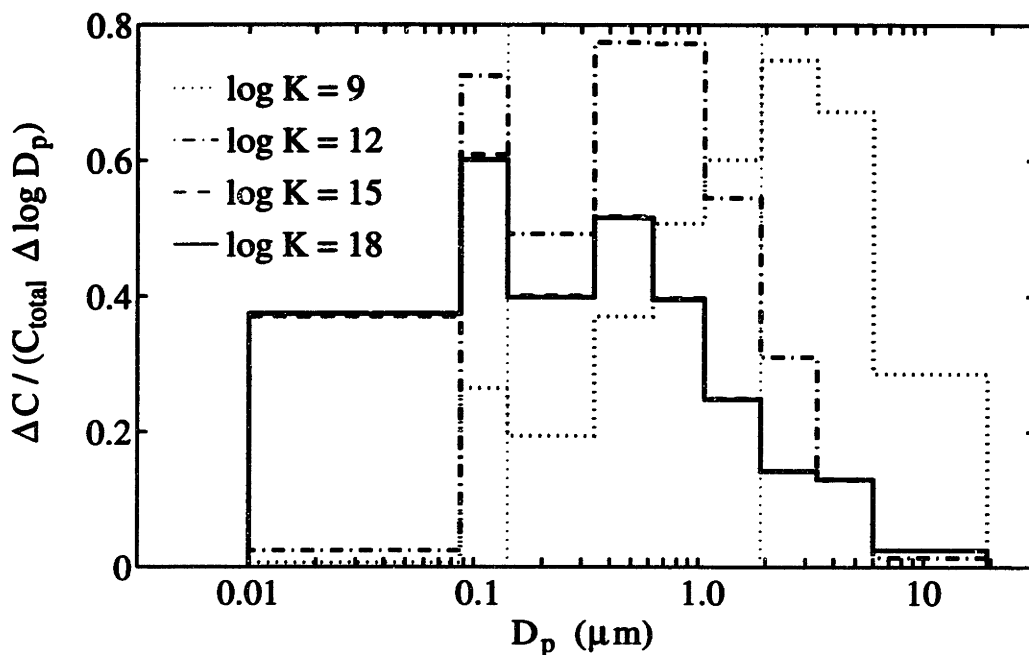


Figure 7-5: Predicted distributions of PAH with particle size for $\log K = 9-18$.

7.5 Predictions for Combustion Products in Urban Air

7.5.1 Distributions with Particle Size

Figure 7-5 shows the distributions of PAH with particle size for $\log K = 9-18$. For $\log K = 9$, the model results closely match the distributions of phenanthrene and anthracene with particle size measured in the urban aerosol (see Figures 3-3 and 3-4). This is a result of forcing the sorbent size distribution to match that of phenanthrene. For the other extreme value, $\log K = 18$, the model results match the distribution of coronene with particle size measured in the urban aerosol (see Figure 3-18). This is a result of forcing the distribution of emitted PAH to match that of coronene.

Table 7.1: Equilibrium Gas—Sorbent Partition Coefficients (K).

PAH	log K			
	water	<i>n</i> -octanol	ideal solvent	best-fit
Phenanthrene	3.06	7.63	8.11	9.00
Anthracene	3.11	7.65	8.16	9.00
Fluoranthene	3.42	8.65	9.12	9.40
Pyrene	3.45	8.63	9.26	9.60
Benz[<i>a</i>]anthracene	3.75	9.66	10.51	11.80
Chrysene	4.35	10.21	11.19	11.80
Benzo[<i>e</i>]pyrene	4.77	—	12.31	12.00
Benzo[<i>a</i>]pyrene	4.76	10.80	12.37	12.00
Perylene	6.01	12.26	13.25	11.80
Dibenz[<i>a,h</i>]anthracene	6.51	13.26	13.96	12.00
Benzo[<i>ghi</i>]perylene	10.32	16.82	18.84	13.40
Coronene	12.07	17.47	17.64	18.00

The results for extreme values of K are trivial; of interest is the predicted distribution of PAH with intermediate values of K . Comparing distributions in Figure 7-5 with those of PAH, near matches between some of the plots are apparent. For example, the plots for benzo[*a*]pyrene (Figure 3-12) and $\log K = 12$, and for benzo[*ghi*]perylene (Figure 3-17) and $\log K = 15$ match closely. The best fit matches of $\log K$ to PAH were determined by first calculating the predicted distributions with particle size for $\log K = 9$ –18 in 0.2 increments. These distributions were then normalized and compared with those of PAH in the urban aerosol. The best-fit value of $\log K$ for a PAH was that for which the sum of the squared errors was a minimum. Table 7.1 shows the best-fit values for $\log K$ and $\log K$ values for water, *n*-octanol, and an ideal solvent. Note that the best-fit values of $\log K$ for phenanthrene, anthracene, and coronene are the extreme values of $\log K$ for which the model was run and are not useful for comparisons.

Figures 7-6 through 7-14 show the comparison between the best-fit model results and the atmospheric data for some of the PAH listed in Table 7.1. Agreement be-

tween the ideal solvent and best-fit values of K are good for fluoranthene, pyrene, benz[*a*]anthracene, chrysene, benzo[*e*]pyrene, and benzo[*a*]pyrene. For these PAH, the model of non-equilibrium absorptive partitioning to an ideal sorbent presented here approximately matches the atmospheric data.

For PAH with vapor pressures lower than benzo[*a*]pyrene, the best-fit values of $\log K$ are up to 5 orders of magnitude below that for the ideal solvent. It seems unlikely that γ for PAH in the same sorbent would differ greatly, especially between benzo[*a*]pyrene and perylene. The PAH for which there is poor correspondence between the ideal solution and best-fit K s all have very low subcooled liquid vapor pressures, with $\log p_L$ (Pa) < -6 . If the sorbent also partitions by vaporization and condensation at a rate comparable to, or faster than, these PAH, an assumption of the model is violated. As sorbent vaporizes from particles, the concentration and thus equilibrium partial pressure of PAH in these particles will be increased. This would lead to a more rapid repartitioning, and smaller best-fit K s, than for the case of a non-volatile sorbent.

The simple assumption of homogeneous sorbent particles may explain some of the systematic variations between model predictions and atmospheric data. The model seems to under predict the amount of PAH associated with smallest particles. This may be due to slow mass transfer within the smallest atmospheric particles, for example diffusion through pores in a soot particle. The model also seems to under predict the amount of PAH associated with the largest particles. If these are solid particles coated with organic material, the surface area to volume ratio will be greater than for a pure liquid particle. Thus τ_{eq} will be lower than for wholly liquid particles.

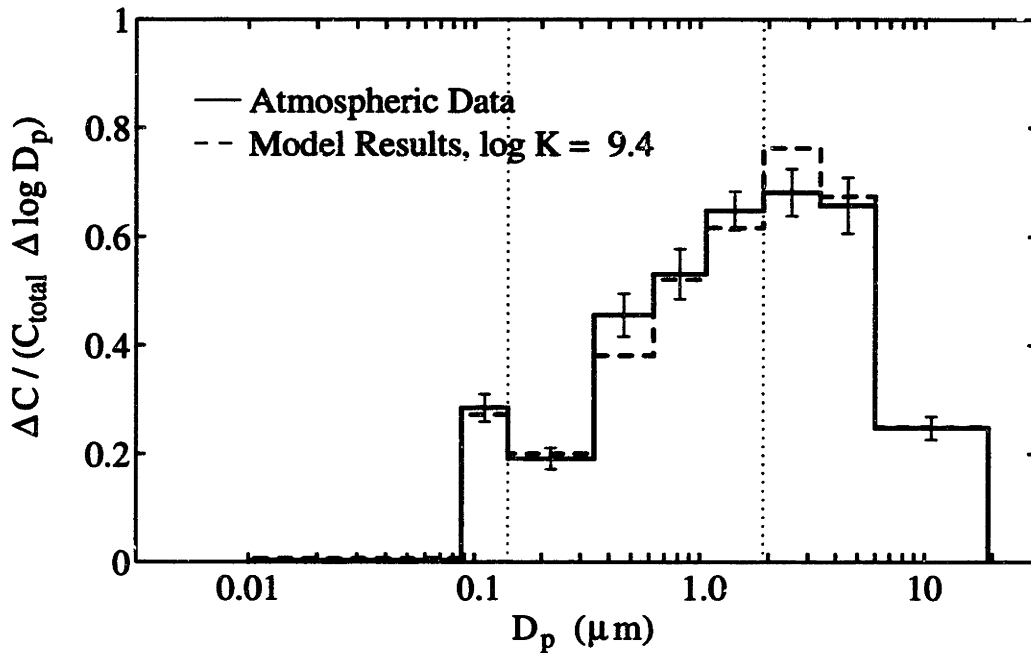


Figure 7-6: Comparison of the distributions of fluoranthene with particle size as measured in an urban aerosol and predicted by the absorptive partitioning model.

The model predictions for the largest and smallest particles could be improved by making empirical adjustments to τ_{eq} for different particle size bins. However, without data on the morphologies of these particles in the atmosphere, such adjustments seem arbitrary.

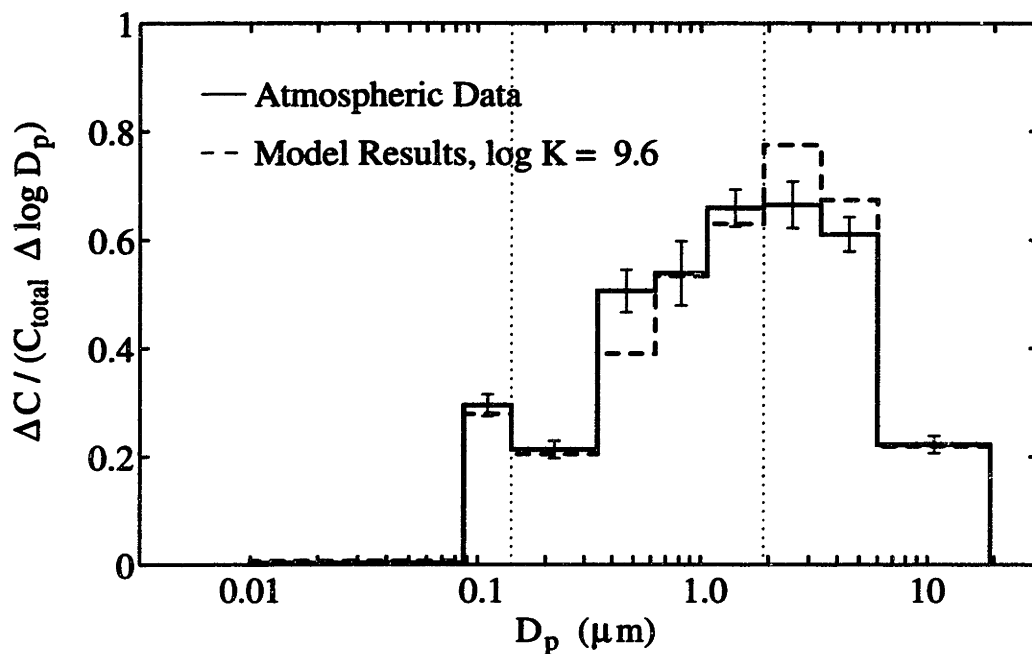


Figure 7-7: Comparison of the distributions of pyrene with particle size as measured in an urban aerosol and predicted by the absorptive partitioning model.

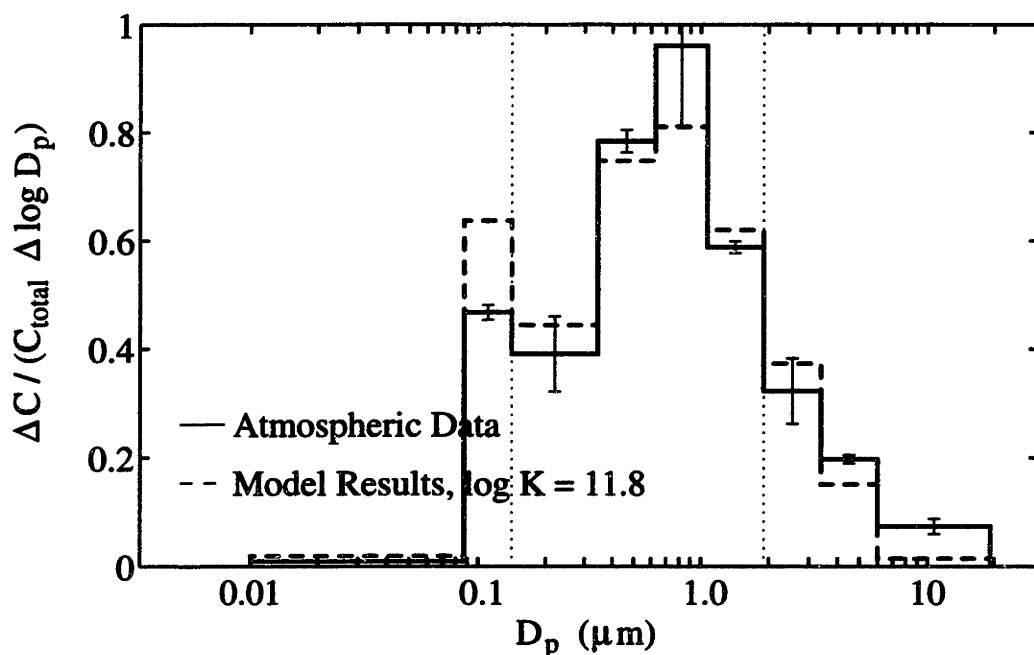


Figure 7-8: Comparison of the distributions of benz[a]anthracene with particle size as measured in an urban aerosol and predicted by the absorptive partitioning model.

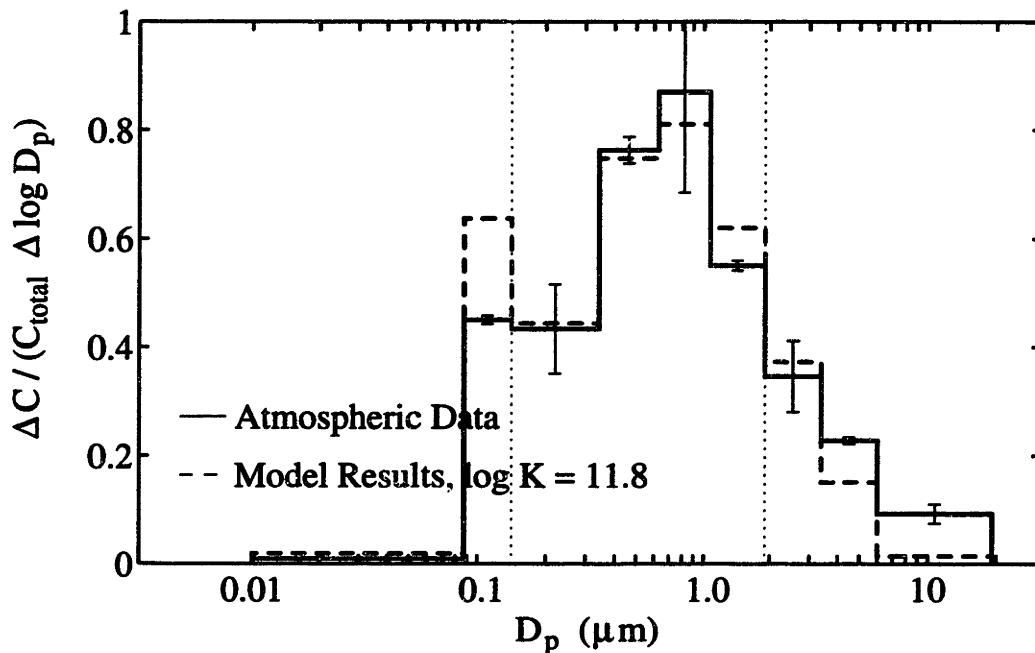


Figure 7-9: Comparison of the distributions of chrysene/triphenylene with particle size as measured in an urban aerosol and predicted by the absorptive partitioning model.

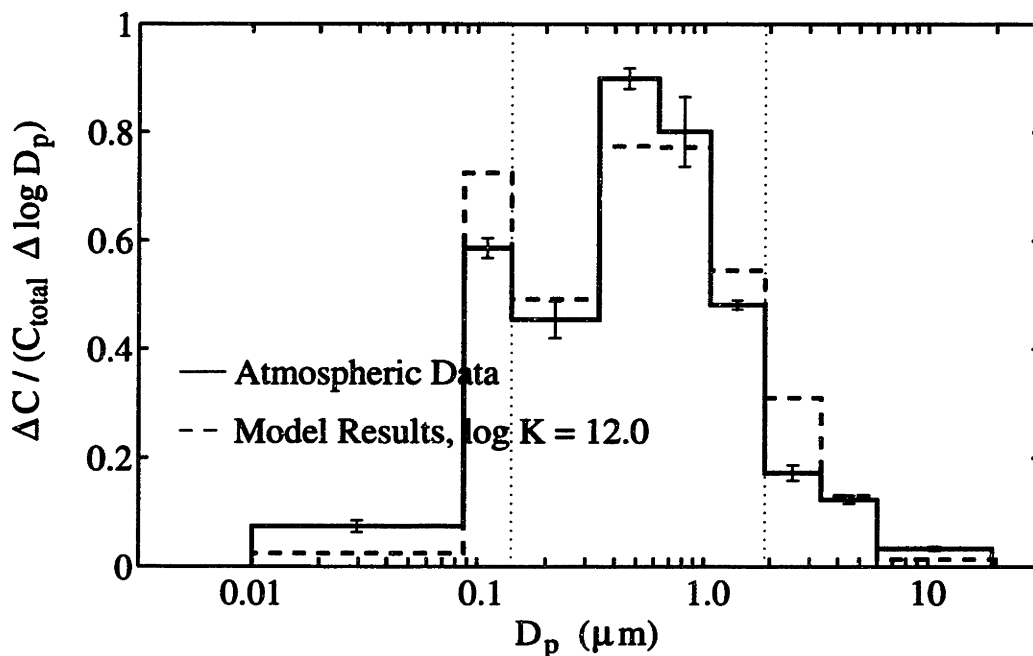


Figure 7-10: Comparison of the distributions of benzo[e]pyrene with particle size as measured in an urban aerosol and predicted by the absorptive partitioning model.

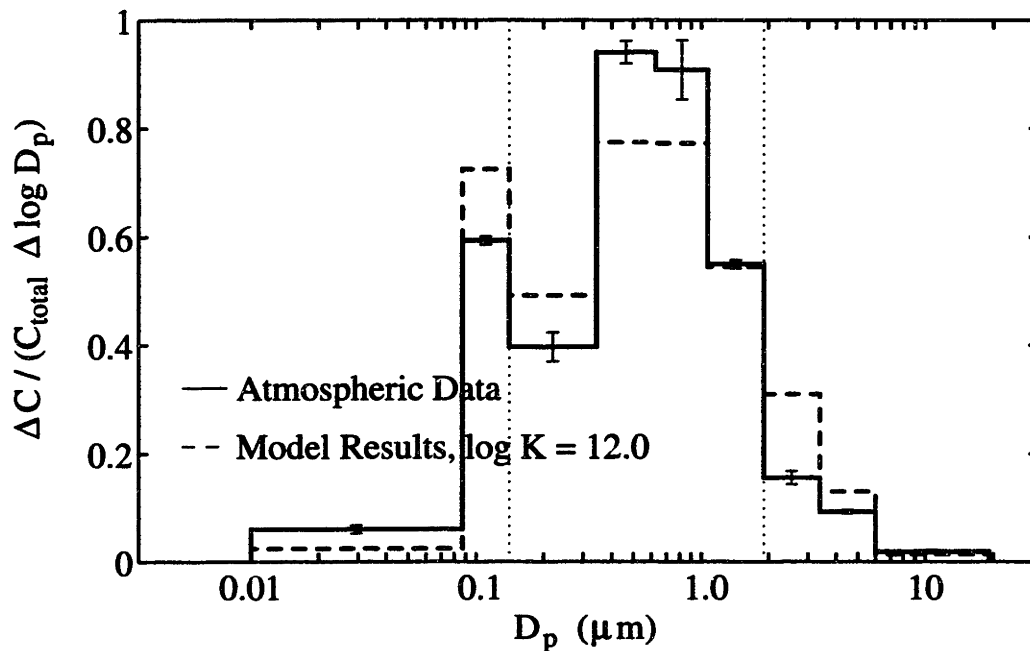


Figure 7-11: Comparison of the distributions of benzo[a]pyrene with particle size as measured in an urban aerosol and predicted by the absorptive partitioning model.

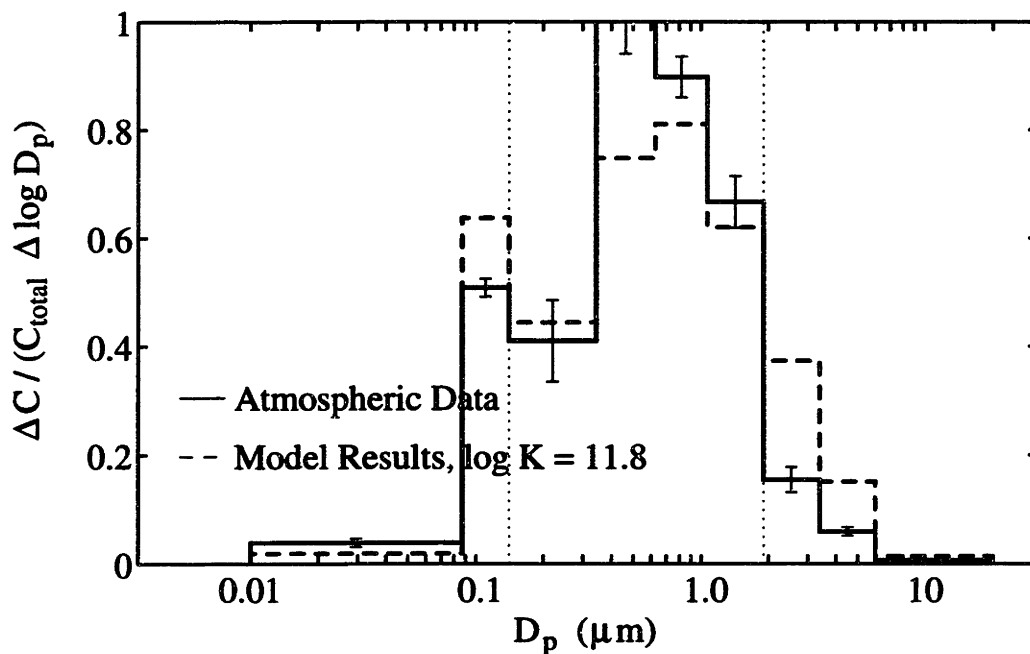


Figure 7-12: Comparison of the distributions of perylene with particle size as measured in an urban aerosol and predicted by the absorptive partitioning model.

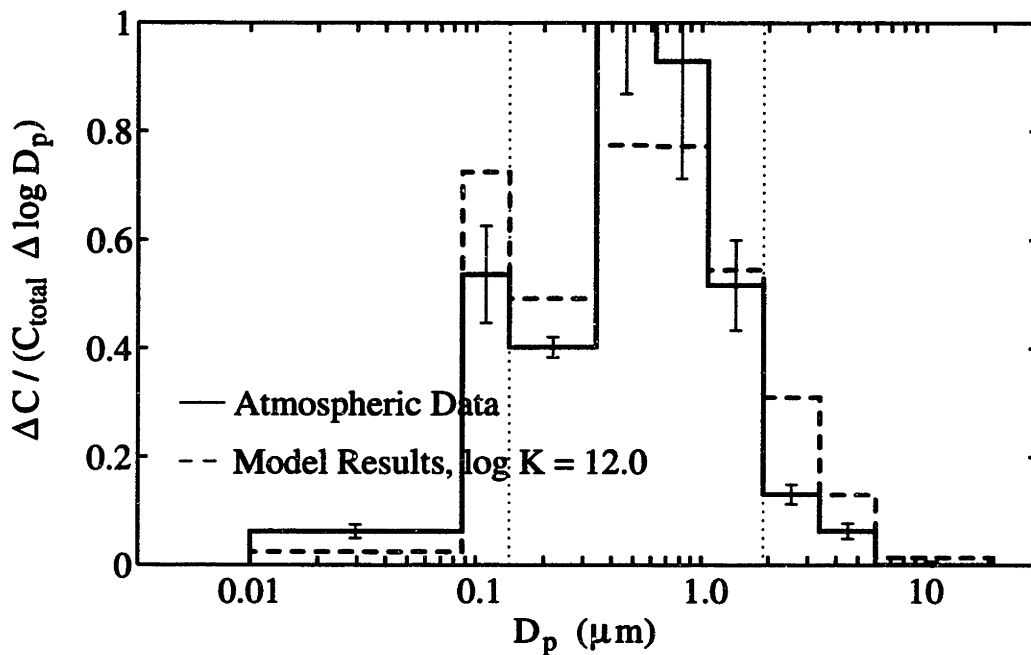


Figure 7-13: Comparison of the distributions of dibenzanthracenes with particle size as measured in an urban aerosol and predicted by the absorptive partitioning model.

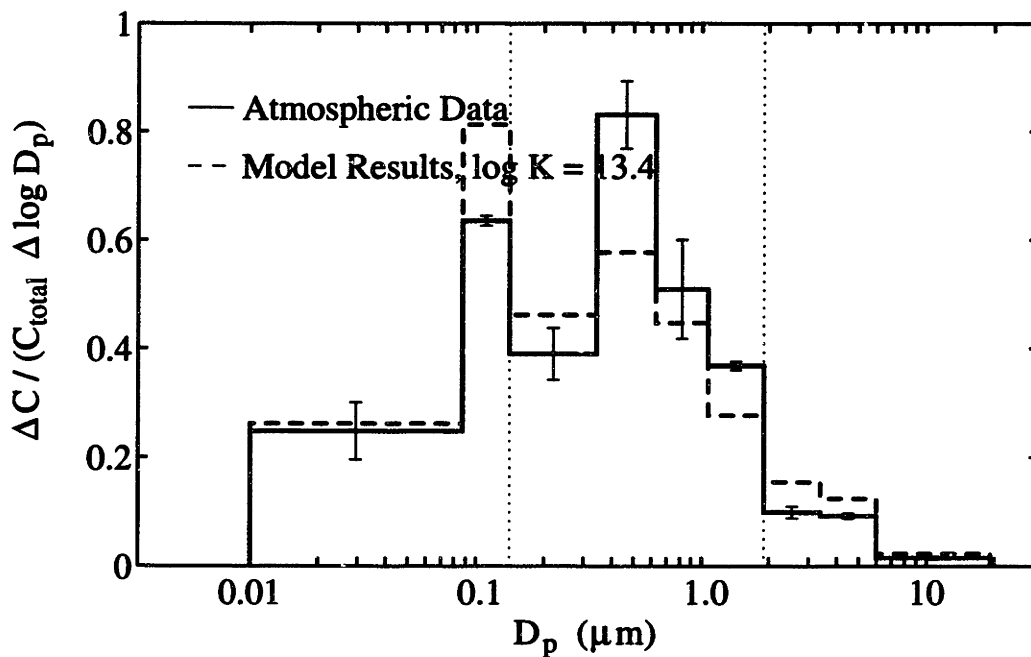


Figure 7-14: Comparison of the distributions of benzo[ghi]perylene with particle size as measured in an urban aerosol and predicted by the absorptive partitioning model.

7.5.2 Gas Phase Concentration

The model also predicts the evolution of the gas phase concentrations of PAH. Figure 7-15 shows the evolution of C_G and the gas—particle partitioning ratio, ϕ , with time for $\log K = 12$. In this case, C_G in emissions is assumed to be in equilibrium with the smallest particles. The qualitative features of C_G evolution are independent of $\log K$. At short times C_G rises due to the importance of PAH emitted in the gas phase and with small particles. At longer times, PAH initially in the gas phase and associated with small particles collect in the larger particles. This has the effect of lowering the average value of C_i and therefore C_G . Because of the lag in mass transfer from the gas phase and smallest particles to the larger particles, ϕ reaches a maximum then asymptotically approaches a value corresponding to the gas—particle equilibrium, 0.074 in this case. In the case of $\log K = 12$, typical of higher molecular weight PAH like benzo[*a*]pyrene, the gas—particle partition is clearly not at equilibrium; ϕ can be an order of magnitude greater than its equilibrium value.

Figure 7-16 shows the evolution of C_G using the assumption that no PAH is emitted in the gas phase. Like the previous case, ϕ reaches a maximum at short times and asymptotically approaches its equilibrium value. The deviation from equilibrium gas—particle distribution is less than in the case of partial gas phase emissions.

7.6 Conclusions

The hypothesis that PAH partitioning to urban aerosols can be described as non-equilibrium absorptive partitioning was tested against atmospheric data. A simple

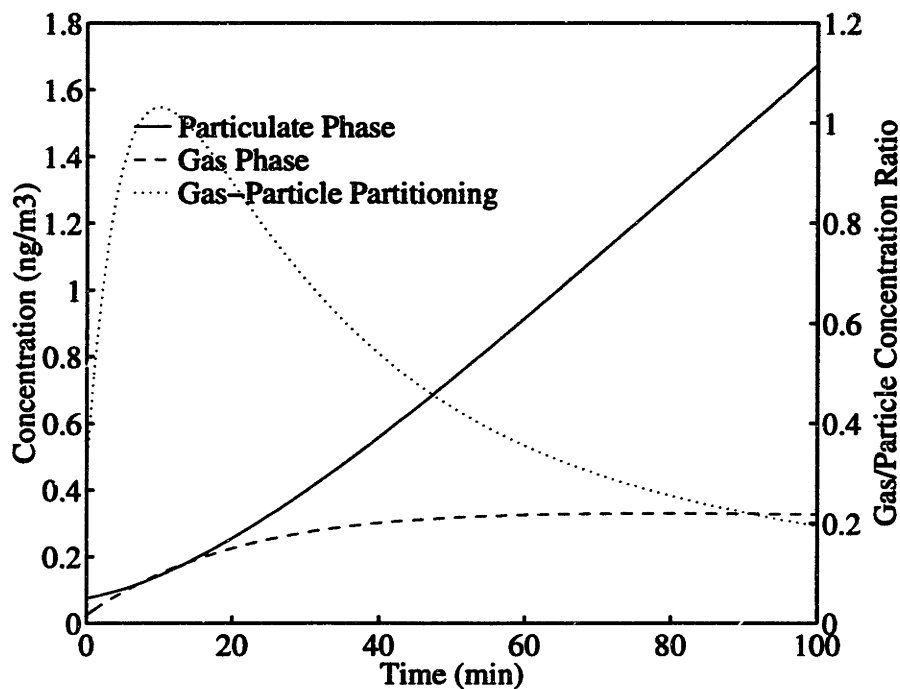


Figure 7-15: Evolution of gas phase and total particulate phase concentrations with time for $\log K = 12$ and partial gas phase emissions.

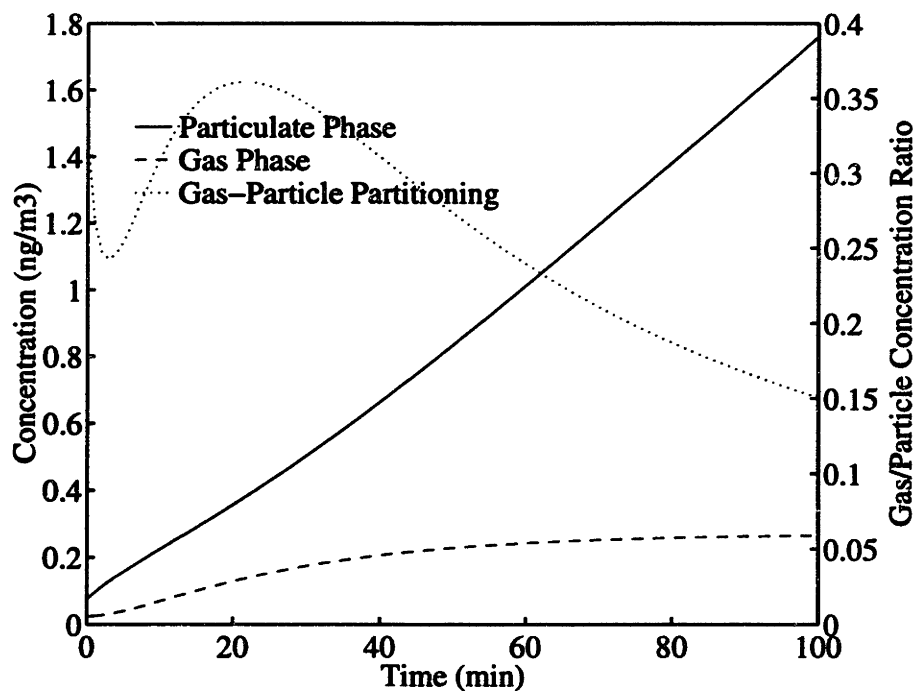


Figure 7-16: Evolution of gas phase and total particulate phase concentrations with time for $\log K = 12$ and no gas phase emissions.

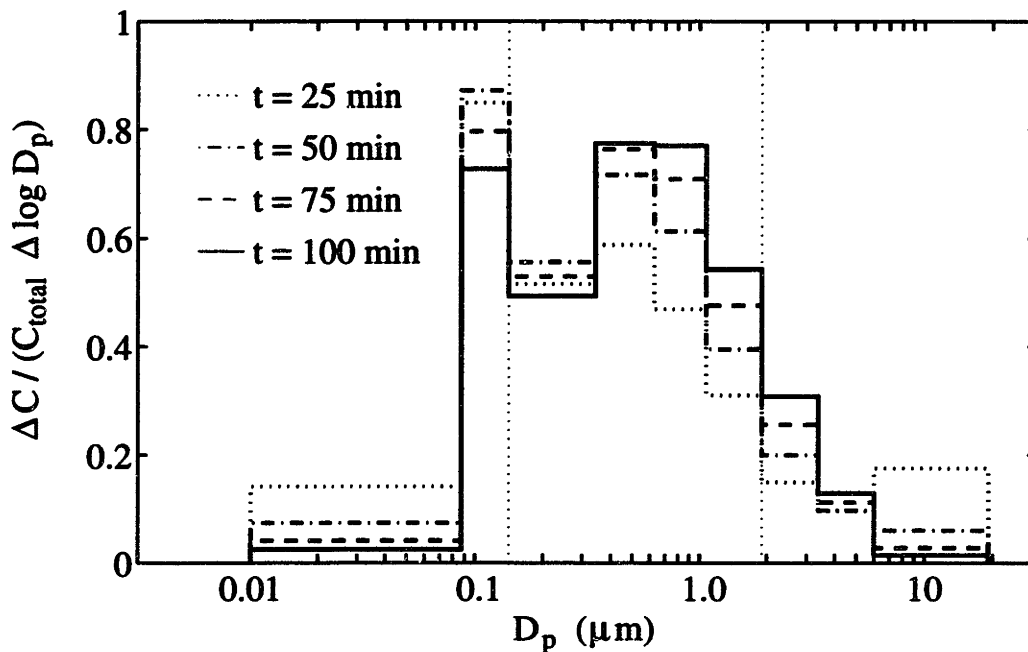


Figure 7-17: Predicted distributions of PAH with particle size for $\log K = 12$ at various times.

Lagrangian model for an urban aerosol was developed and the results compared with measured distributions of PAH with particle size. For PAH with $\log p_L(\text{Pa}) > -6$, the model results for sorption into an ideal solvent agreed well with the atmospheric data. For PAH with $\log p_L(\text{Pa}) < -6$, the model results for sorption to an ideal solvent did not agree with the atmospheric data. This may be because the sorbent was assumed to be non-volatile, but may be repartition on time scales comparable to or faster than these low vapor pressure PAH. This explanation suggests that $\log p_L(\text{Pa}) \approx -6$ for the sorbent.

Figure 7-17 shows the evolution with time of the distribution of a PAH with $\log K = 12$. This plot shows the sensitivity of the model results to the value of t_{res} . An important, and somewhat arbitrary, assumption, that $t_{res} = 100$ min, was made.

If local emissions dominated the PAH and sorbent collected at Kenmore Square, the average residence time could be much less than 100 min. If a lower t_{res} is used, the distributions with particle size will be shifted toward smaller particles for the same values of $\log K$. This would result in smaller values of best-fit K for PAH.

Subsequent studies of the distribution of PAH with particle size should measure the gas phase concentration. With this additional data, one could more directly determine the absolute values of $C_{o,i}$. In addition one could directly determine $\log K$ for species in equilibrium with the aerosol. The distribution of sorbent with particle size could also be measured directly, by analyzing size-segregated aerosol samples for organic carbon or solvent-extractable mass.

This model may be used to predict the size distributions for compounds and environments beyond PAH in urban air. These conditions might include

1. combustion generated pollutants in urban air (e.g. some OPAH),
2. combustion generated pollutants downwind of urban sources,
3. photochemically generated compounds in urban air,
4. photochemically generated compounds downwind of urban sources, and
5. compounds in smog chamber studies.

Chapter 8

Other Experiments

8.1 Atmospheric Particle Imaging

8.1.1 Introduction

Electron microscopic analyses of atmospheric particles has been widely used to identify particle morphologies and attribute particles to emission sources. A compendium of particle morphologies has been published [26]. Recent studies of this kind have been made by Buseck and coworkers [27, 28]. Electron microscopy studies of soots sampled from combustors have identified characteristic features of these particles [155, 156].

The work described in this section was a background study to analyze submicron particles from Boston air by electron microscopy. The objectives of the study were to design collection and microscopy techniques for the analysis of an unbiased sample of atmospheric particles. The results of this work were used to construct a qualitative description of an urban aerosol which was used throughout this work.

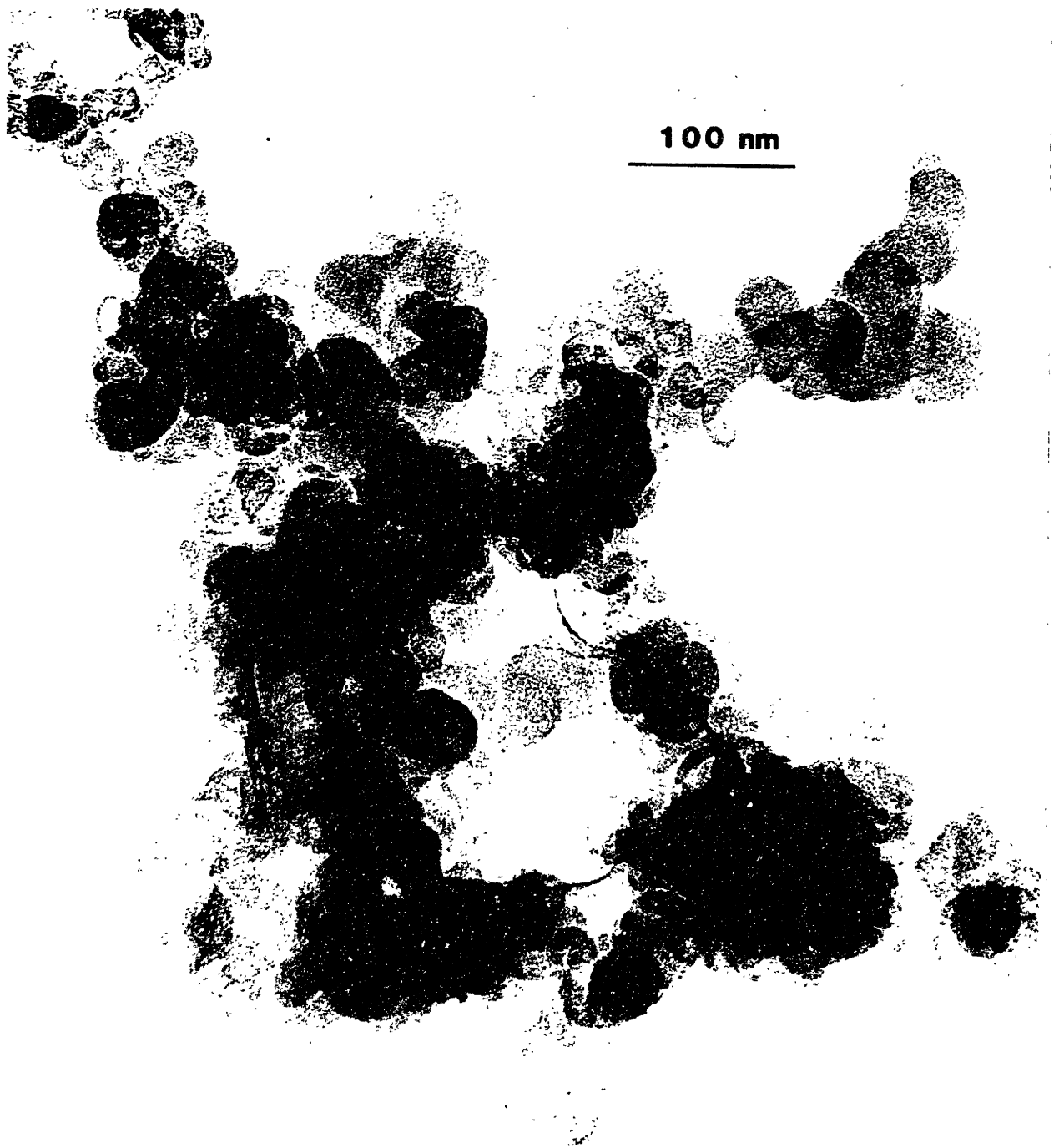


Figure 8-1: Intermediate magnification TEM image of a carbonaceous aggregate particle collected on a carbon grid.

8.1.2 Sample Collection

Samples were collected from a port in a second level window of a six level building. The window faced the rear of the building. Below the window was a one-lane service road. Four feet of 0.375 in. i.d. tubing connected the sampling port to the first five stages of a micro-orifice impactor (MOI). The impactor was used to remove particles larger than 1 μm from the incoming air. The design specifications of MOI stages 0 through 4 are listed in Table 2.2. The impactor plates were coated with a few drops of 5% by weight solution of Dow Corning silicone grease in cyclohexane to prevent particle bounce. Following the MOI, was a Model 3100 electrostatic precipitator (ESP) manufactured by TSI Inc. (St. Paul, MN). The precipitating electric field of the ESP was pulsed on and off to collect particles uniformly on the sampling surface. A diaphragm vacuum pump, Gast (Benton Harbor, MI) model DOL-101-AH, was the last unit in the sampling train.

Post-itTM adhesive strips were affixed to the center of the ESP sample collection area with the adhesive side up. Three electron microscopy grids were placed on the adhesive strips in a line perpendicular to the flow. The samples were collected continuously for approximately 60 hours. This sampling time was calculated to collect particles to cover approximately 10% of the the sampling surface. This time was calculated from the first moment of Whitby's urban aerosol size distribution [22]. Samples were collected over weekends to minimize the impact of local emissions from vehicles on the service road. The first aerosol sample was collected on carbon film grids for 63.5 hours starting at 4:00 pm on September 25, 1992. The second sample

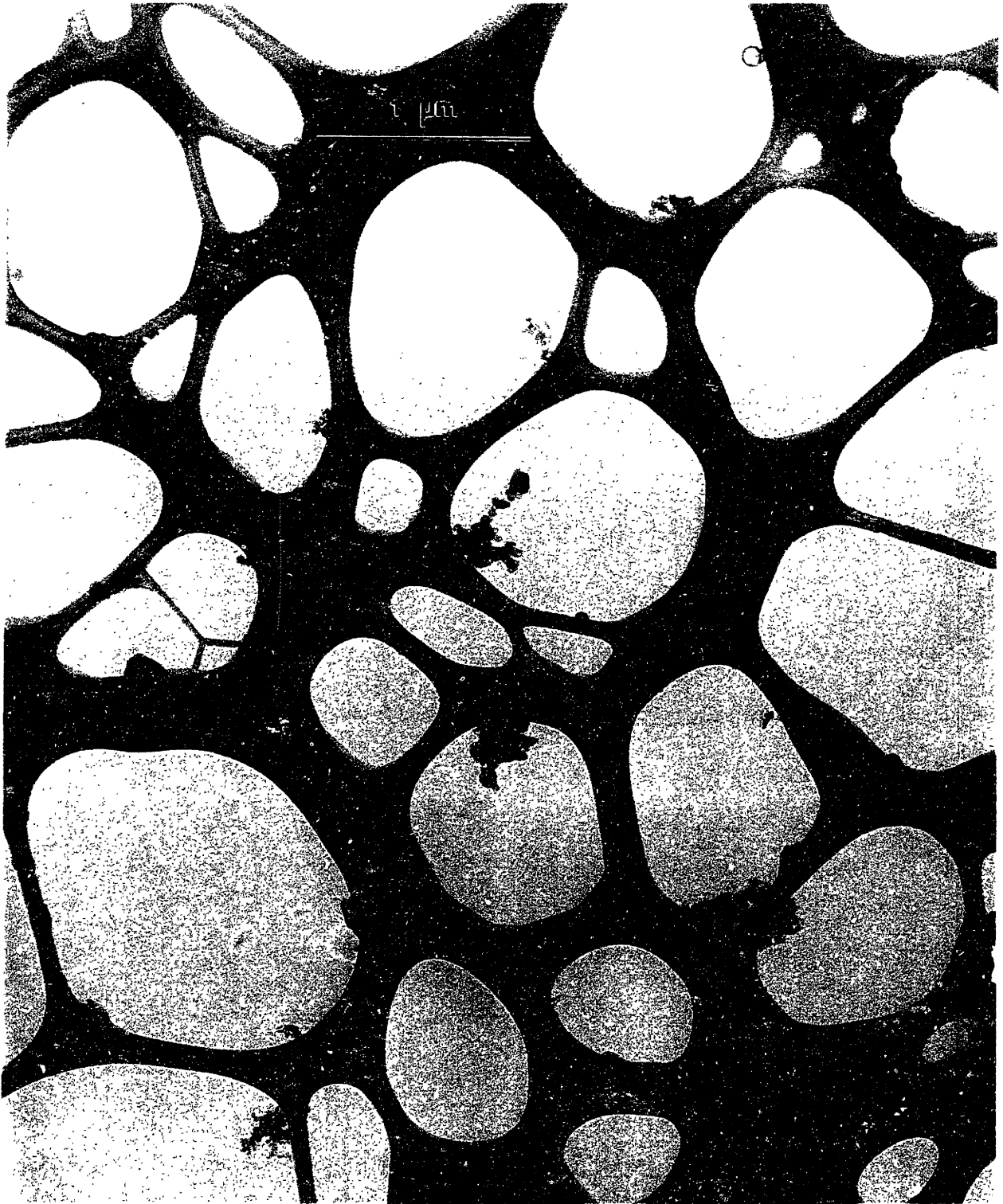


Figure 8-2: Low magnification TEM image of atmospheric particles collected on a lacey grid.

was collected on lacey carbon grids for 64.75 hours starting at 2:45 pm on January 22, 1993. All grids were obtained from Ted Pella, Inc. (Redding, CA): the carbon grids were catalog number 01810, the lacey grids catalog number 01882. The grids were stored for approximately two weeks in a desiccator prior to electron microscopic analysis.

8.1.3 Electron Microscopy

The transmission electron microscope used in this work was a Akashi/Topcon 002B unit operated at 200 keV. Figure 1-3 is a low magnification image of atmospheric particles collected on a carbon grid. As discussed in the Chapter 1, these particles are believed to be carbonaceous aggregates (particles A, B, and C), liquid droplets of low vapor pressure organics (D, E, and F), evaporated aqueous droplets (G and H), and mixtures of these types (I and J). Figure 8-1 is a higher resolution image of a carbonaceous aggregate collected on a carbon grid. The graphitic carbon microstructure of this particle is visible.

As seen in Figure 8-1, the amorphous carbon of the grid interfered with the imaging of lattice fringes at the edges of carbonaceous particles. Therefore lacey grids were used in the second experiment. Lacey grids consist of a carbon coated film with holes $\approx 1 \mu\text{m}$ in diameter. The microstructure of particles which are collected on the edge of the grid material can be examined without interference from the substrate.

Figure 8-2 is a low magnification image of particles collected on a lacey grid. As with the carbon grid sample, different particle types are apparent, including liquid

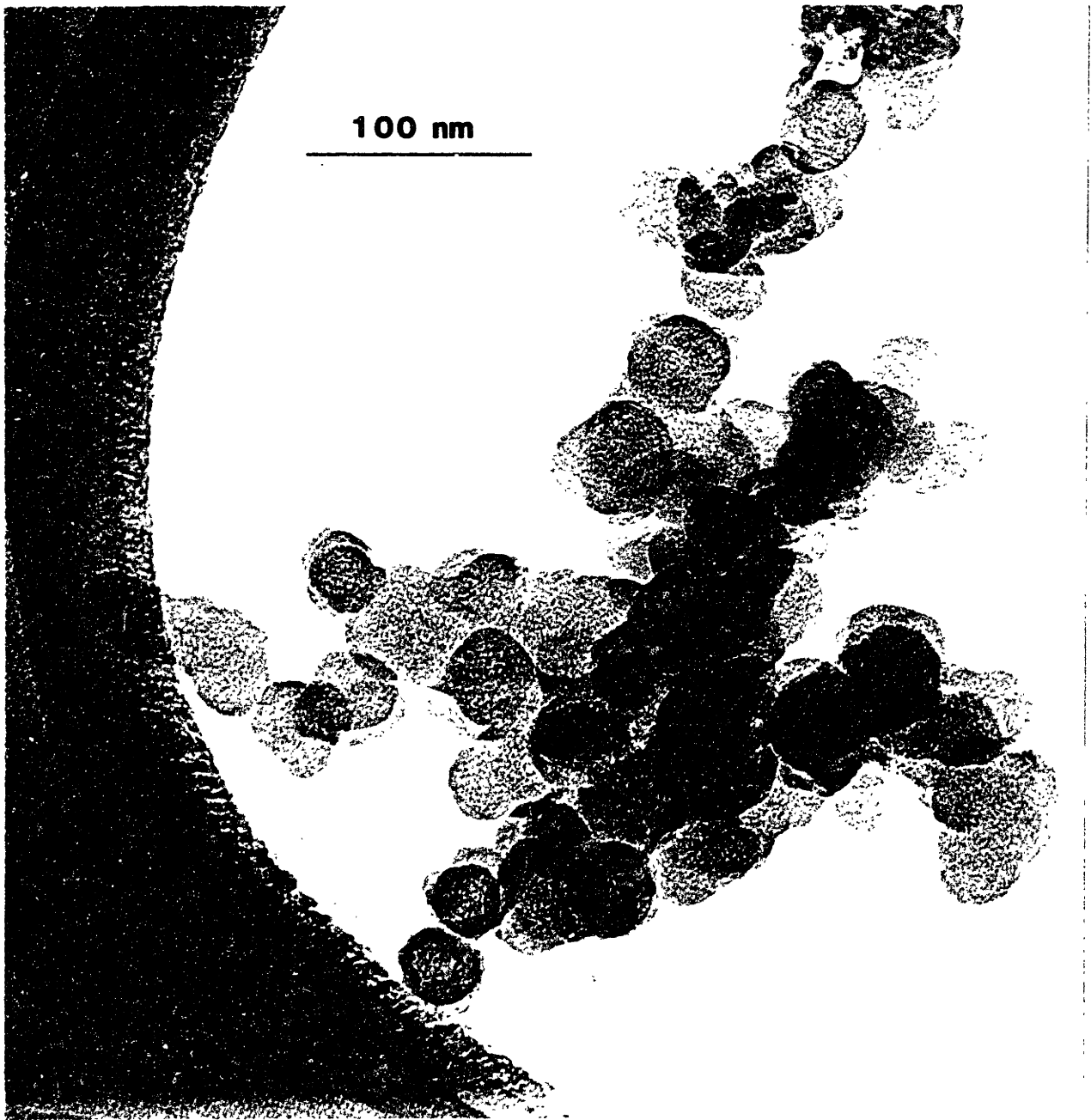


Figure 8-3: Intermediate magnification TEM image of a carbonaceous aggregate particle collected on a lacey grid.

droplets and carbonaceous aggregates. Figure 8-3 is an intermediate magnification of a carbonaceous particle, shown in the center of Figure 8-2. The microstructure of this particle is visible and the edges of the particle image are clear. Figure 1-4 is a high magnification image of a lattice fringe of this particle. The turbostratic lattice fringes characteristic of soots are visible [155, 156].

Figure 8-4 is a low magnification image of a large aggregate particle collected on a lacey grid. The particle is larger than 1 μm in some dimensions and did not satisfy the Bragg condition necessary to bring the entire particle into focus [157]. Note the association of what appear to be liquid droplets with the particle. It is unknown whether this large aggregate was formed at its source, by coagulation in the atmosphere, or during sampling.

Scanning transmission electron microscope (STEM) images were made of some carbonaceous aggregates to determine the distribution of elements in the particles. The STEM used in this work was a Vacuum Generator Microscopes (East Grinstead, UK) model HB603 unit operated at 250 keV. Most aggregates were found to contain primarily carbon. Figure 8-5 shows an exceptional aggregate particle at intermediate magnification. Unlike the rest of the aggregate, a spherical primary particle shown in the box had significant concentrations of oxygen, sulfur, and silicon. Further magnification of this region (see Figure 8-6) found detectable amounts of metals. This primary particle may have been formed as the residue of a fuel oil droplet and subsequently aggregated with soot particles formed in the same combustor.



Figure 8-1: Low magnification TEM image of mixed aggregate particle collected on a lacey grid

8.1.4 Conclusions

Submicron particles were successfully collected from the atmosphere and the particles analyzed by TEM and STEM. These images show that particles with the same size can have very different morphologies. Three main particle morphologies were observed: soot particles, organic droplets and aqueous particles. Particles of mixed morphologies, most commonly soot—organic mixtures, were also observed. These observations indicate that the organic fraction of the atmospheric aerosol forms a distinct phase. It is therefore reasonable to consider the partitioning of PAH and OPAH to liquid organic droplets.

The microstructure of soot particles was imaged by high resolution TEM. These data may be used to identify the sources of the soots by comparative image analysis of the microstructure [155, 156]. STEM analysis of soot particles found some with non-carbonaceous primary particles embedded in the agglomerate. These data may also be used to identify soot formation mechanisms and sources.

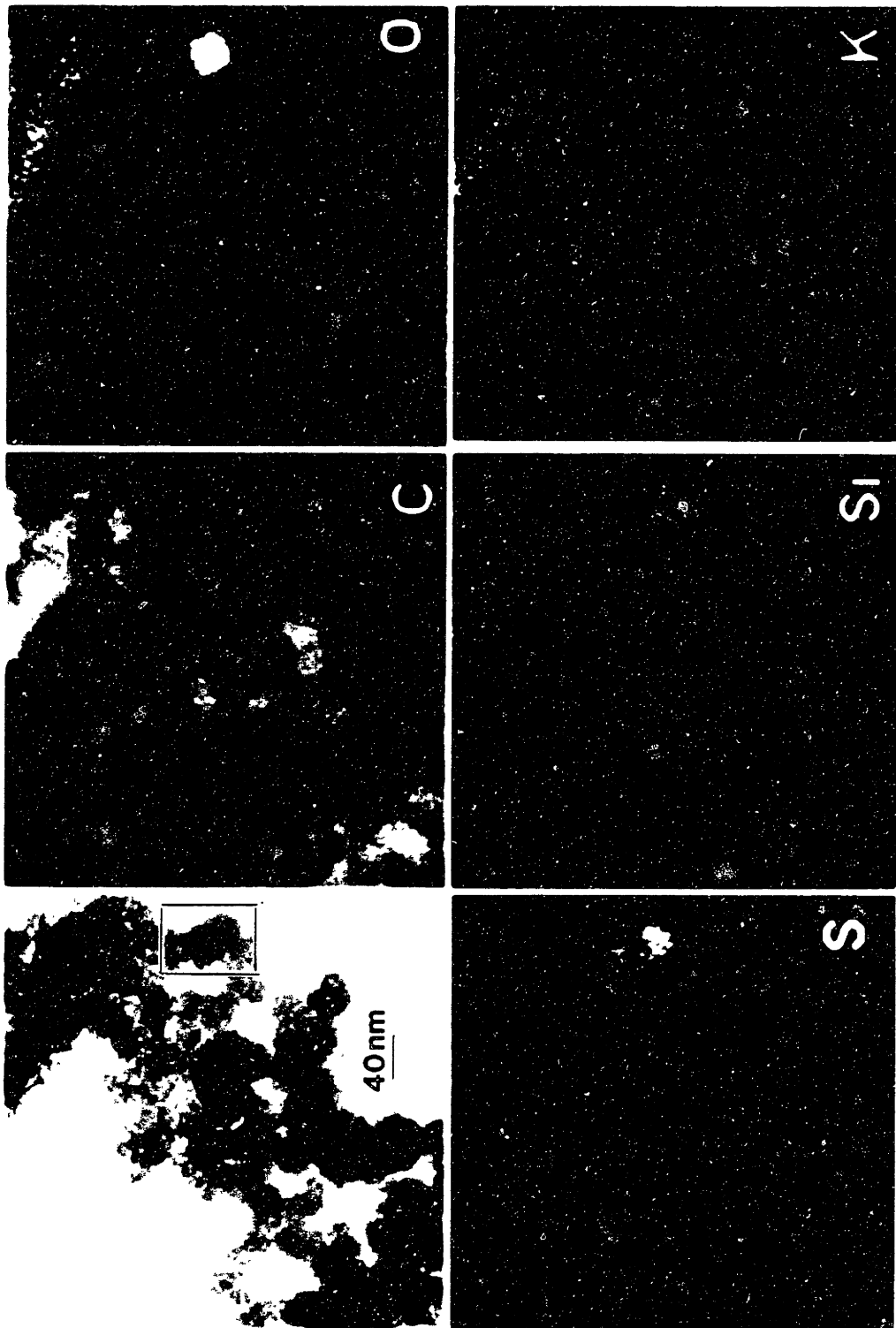


Figure 8-5: Intermediate magnification STEM image of aggregate particle collected on a lacey grid. Symbols on the images designate chemical elements with the exception of “BF” which is the bright field image.

8.2 Surface Study of Thermally Desorbed Soot

8.2.1 Introduction

The partitioning of PAH in atmospheric aerosols has been explained as adsorption of PAH on the surface of atmospheric particles [87, 40, 88]. The models of adsorption presented in the literature, Langmuir and BET adsorption, hypothesize energetic interactions between the adsorbate and adsorbent for molecules adsorbed in the monolayer adjacent to the solid sorbent. Therefore it is useful to estimate the surface area available for adsorption in an atmospheric aerosol. The external surface area can be estimated from Whitby's average urban aerosol [22]. However the surface area internal to the aerosol particles has not been estimated. Soot has been proposed as an important contributor to the total aerosol surface area, and measurements of PAH adsorption on its analog, carbon black, have been made [31].

In contrast to carbon blacks, gasoline and diesel engine emissions contain carbonaceous aggregates associated with a large fraction of extractable organic compounds, typically 10–30% [149, 85, 86]. These particles are referred to as “soot”. Whether the association of PAH with soots can be described as adsorptive or absorptive will depend on the location of PAH in relation to the soot surface. The associated organics also makes analysis of the surface area and pore structures of untreated soots impossible.

Therefore, we investigated the surface area of an environmentally relevant soot. Standard reference material (SRM) diesel particulate matter (DPM) was thermally desorbed at a range of temperatures. The surface area and pore structures of the

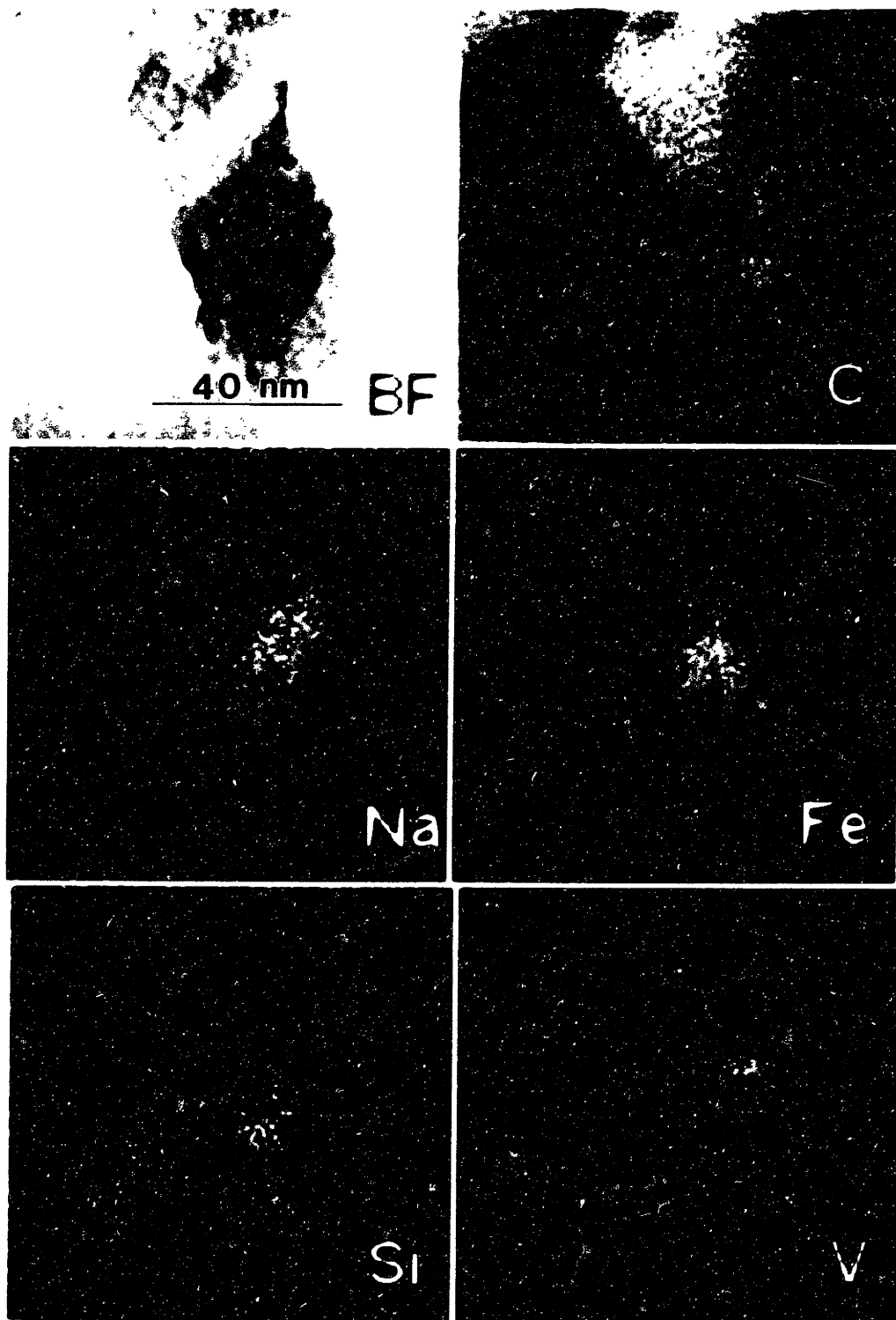


Figure 8-6: High magnification STEM image of aggregate particle collected on a lacey grid. Symbols on the images designate chemical elements with the exception of “BF” which is the bright field image.

desorbed soots were measured. These results are used in Chapter 6 to estimate the extent of surface coverage of emitted soots and atmospheric particles.

8.2.2 Soot Desorption

The soot analyzed here was the NIST diesel particulate matter reference material (NIST SRM 1650) [149]. This material was collected on filters from diluted, cooled diesel exhaust. It contains 17.5% extractable organics as measured by 24 h Soxhlet extraction in DCM. Certified analyses for some PAH are available for this material.

Thermal desorption was performed in a Cahn System 113 Thermogravimetric Analyzer (TGA) manufactured by Cahn Instruments (Cerritos, CA). Data signals were processed by a Cahn 2000 data system and collected on a personal computer running Labtech Notebook. The system is shown schematically in Figure 8-7. The system was assembled without the sample and zeroed electronically. The zero adjustments were set so that the weight signal had a small positive value. These data were recorded and the average later subtracted from weight data recorded during the run.

The sample pan was then removed and filled with approximately 15 mg of soot. The weight data recording range was set to 0–10 mg. The zero suppression setting was adjusted so that the initial sample weight signal was approximately 9 mg, to give maximum sensitivity and range for the weight loss measurement. The sample pan was positioned in the center of the furnace and the thermocouple was positioned approximately 5 mm below the pan. The TGA was reassembled and ultrahigh purity N₂ was passed through the system at a rate of approximately 60 mL/min. The system

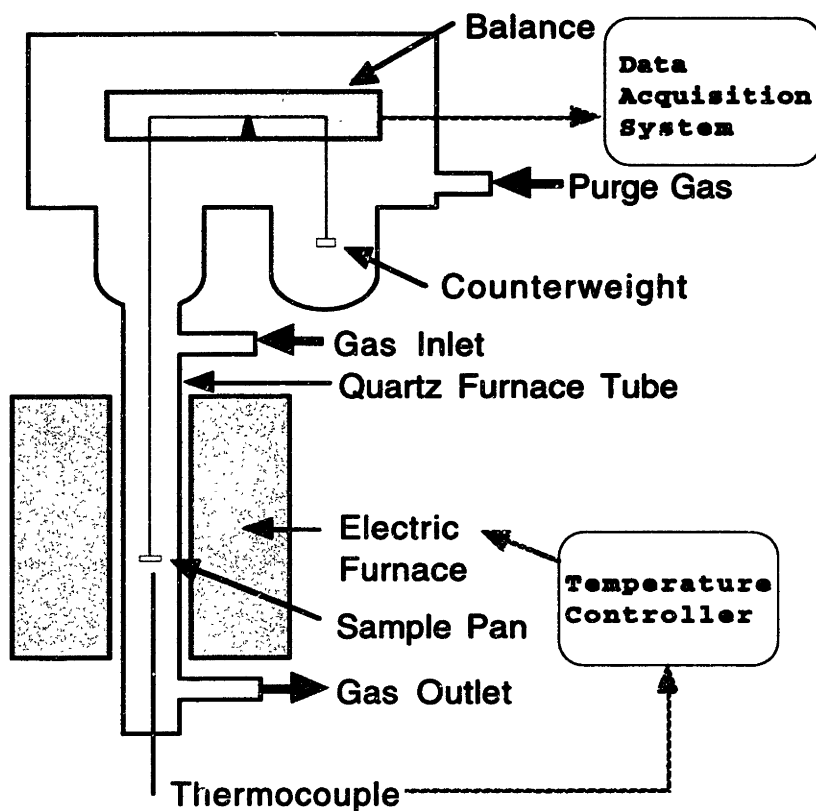


Figure 8-7: Schematic of Cahn System 113 thermogravimetric analyzer.

was kept at slight positive pressure; it was checked for leaks at this time.

Before each run the system was purged for one hour with ultrahigh purity N_2 to remove oxygen. After purging, the furnace was turned on and the temperature program started. The temperature was held at 20°C for five minutes, then increased to the final temperature at $20^\circ\text{C}/\text{min}$. The final temperature was maintained for one hour. The system was rapidly cooled at the end of the run and the desorbed soot collected. The sample weight and temperature were recorded at a rate of 1 Hz during the run.

Three final desorption temperatures were chosen. The lowest temperature, 150°C ,

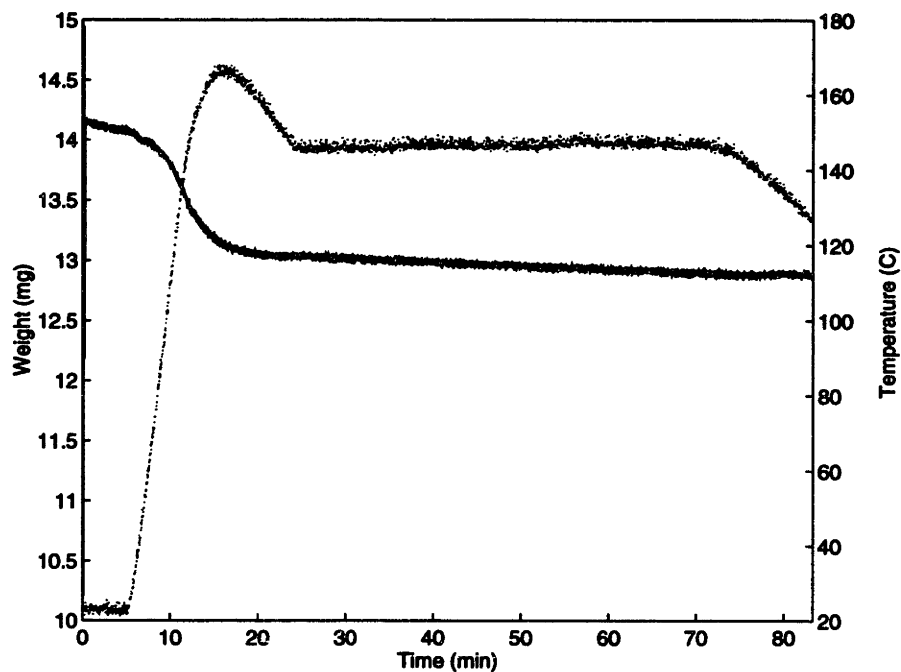


Figure 8-8: Temperature programmed desorption of diesel particulate matter, 150°C final temperature. Heavy line is weight, light line is temperature.

was the minimum temperature required to devolatilize the sample sufficiently for surface area analysis (see below). The highest temperature, 450°C, was chosen to be less than the pyrolysis temperature of PAH with only 6-membered rings [158]. An intermediate desorption temperature, 300°C, was also chosen.

Figures 8-8, 8-9, and 8-10 show the temperature and weight loss profiles during desorption. In all cases the initial mass loss is rapid. For the 450°C desorption, the rate of mass loss slows when the temperature reaches approximately 250°C. Once the final temperature was reached, the mass loss rate was low ($< 0.1 \mu\text{g/s}$). The sample cannot reach equilibrium with the clean inlet gas, but the low rate of mass loss indicates that the desorption method is relatively insensitive to the duration for which the final temperature is maintained.

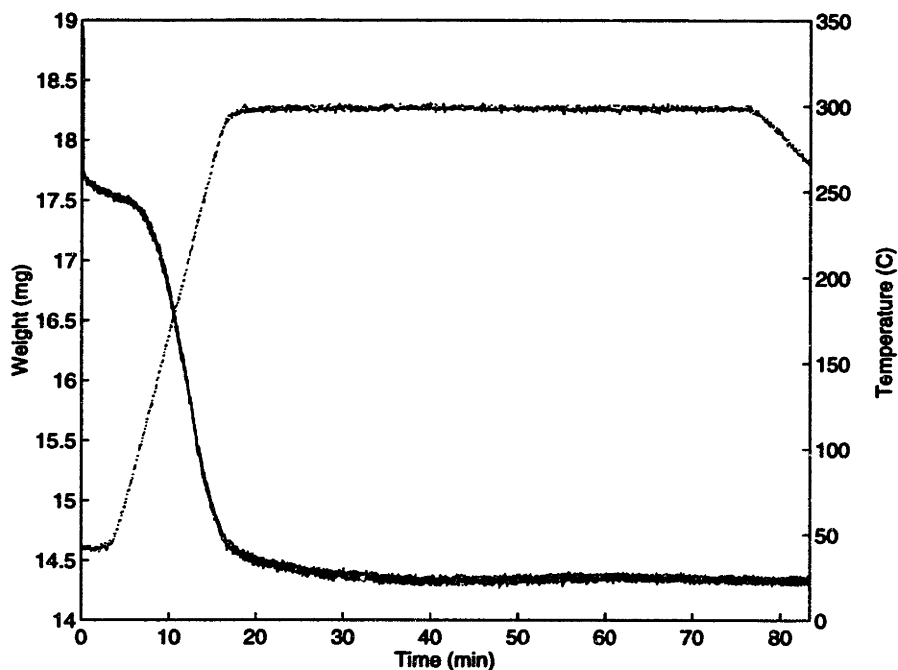


Figure 8-9: Temperature programmed desorption of diesel particulate matter, 300°C final temperature. Heavy line is weight, light line is temperature.

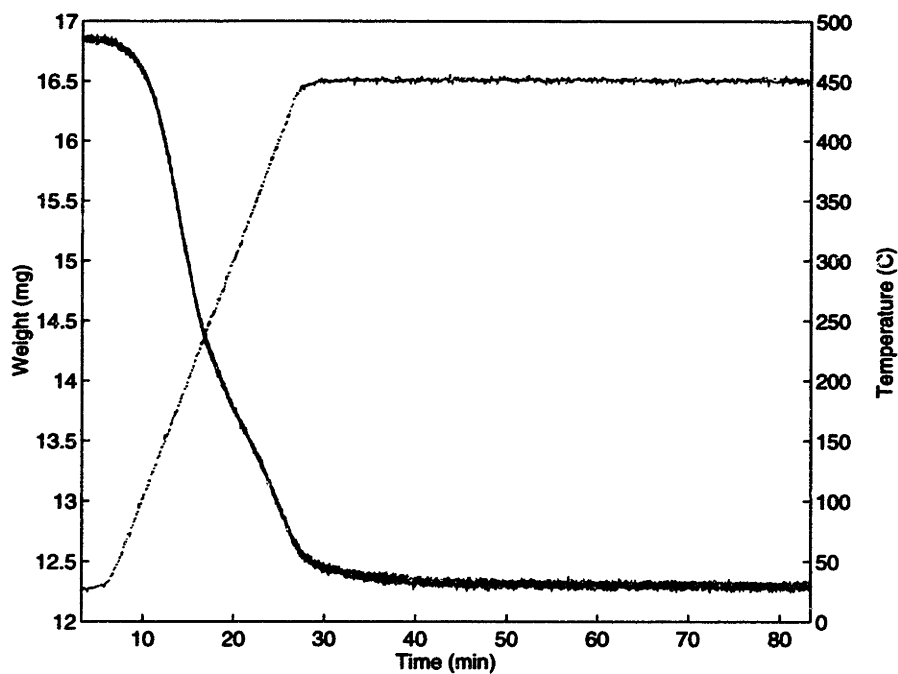


Figure 8-10: Temperature programmed desorption of diesel particulate matter, 450°C final temperature. Heavy line is weight, light line is temperature.

Table 8.1: Summary of Soot Desorption Experiments.

Desorption Temperature (°C)	Mass Loss (g/g)	Total BET Surface Area (m²/g)	Micropore Surface Area (m²/g)	Total Pore Volume (cm³/g)	Micropore Volume (cm³/g)
150	0.090	52.5	-16.3	0.137	-0.010
300	0.186	89.9	-9.1	0.185	-0.007
450	0.212	224.1	94.6	0.249	0.046

8.2.3 Surface Area Measurements

Soot samples desorbed using the same temperature program were composited to collect a total sample mass of approximately 100 mg. The composited samples were then analyzed by N₂ adsorption in a Model ASAP 2000 instrument from Micromeritics (Norcross, GA). The N₂ adsorption data were used to estimate surface areas and pore size distributions from the method of Barrett, Joyner and Halenda [159]. These calculations were performed by the Micromeritics software.

The samples were first degassed at either 100°C, for the sample desorbed at 150°C, or 250°C, for the samples desorbed at 300°C and 450°C. The samples were degassed until the pressure over the sample was less than 5 μm Hg. Degassing was necessary for accurate N₂ adsorption measurements. Soot which had not been thermally desorbed in the TGA could not be sufficiently degassed.

Table 8.1 shows the results of the surface analyses of the desorbed samples. Note that 24 h Soxhlet extraction of this material recovered 17.5% of the initial mass; this is comparable to the mass lost by thermal desorption at 300°C. The BET surface areas found for the sample desorbed at 450°C are comparable to similar measurements of carbon black [160].

Figures 8-11, 8-12, and 8-13 show the distribution of pore volume with pore size as

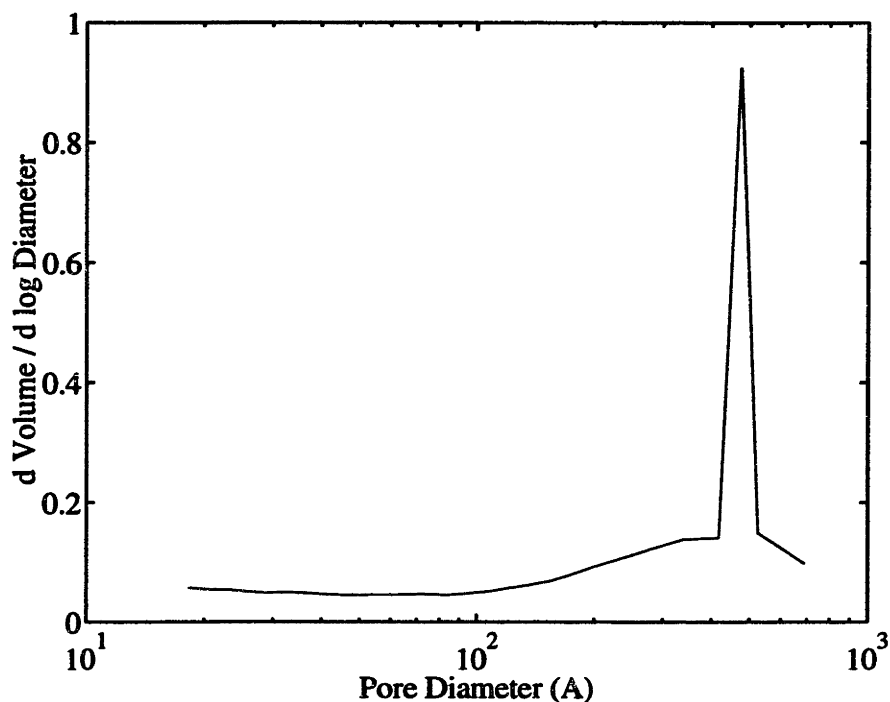


Figure 8-11: Distribution of pore volume with pore size for diesel particulate matter thermally desorbed at 150°C.

determined from N₂ adsorption. The sample desorbed at 150°C shows a large fraction of the pore volume for pores of 400-500 Å diameter. This is the length scale of soot primary particles and may represent void space between soot primary particles, either in the same aggregate particle or in adjacent soot particles. The sample desorbed at 300°C shows additional peaks in pore volume for 200-300 Å diameter pores. Only in the 450°C desorbed sample is a peak characteristic of micropores apparent at 30-40 Å pore diameter. This suggests that for samples desorbed at lower temperatures, much of the microporous volume is filled with sorbed organic compounds.

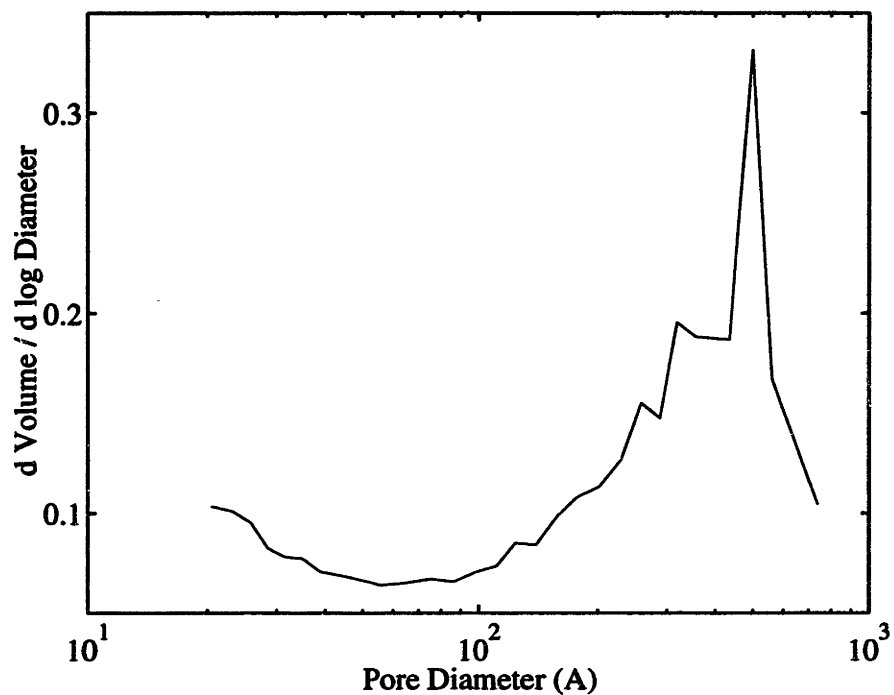


Figure 8-12: Distribution of pore volume with pore size for diesel particulate matter thermally desorbed at 300°C.

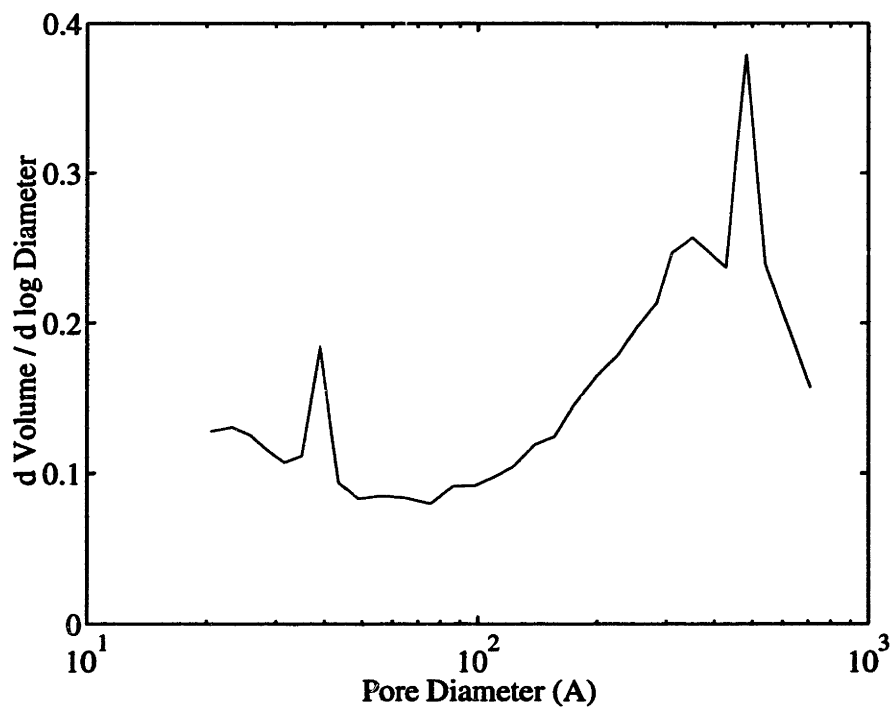


Figure 8-13: Distribution of pore volume with pore size for diesel particulate matter thermally desorbed at 450°C.

8.2.4 Conclusions

Diesel particulate matter was thermally desorbed to final temperatures of 150, 300 and 450°C. The surface areas and pore volumes of these samples were determined by BET analysis of N₂ adsorption. For the most complete desorption the total surface area was 224 m²/g. This value can be used to estimate the contribution of soot particles to the total aerosol surface area.

The results suggest that for samples desorbed at 150 and 300°C, much of the porous volume remains occupied by sorbed organic compounds. Because the mass loss for the 300°C desorbed sample and the same material extracted by 24 h Soxhlet extraction in DCM are comparable, a significant fraction of organic compounds may remain with the soot after normal extraction procedures. The remaining material may be energetically bound to the surface of the soot.

Bibliography

- [1] Douglas W. Dockery, Joel Schwartz, and John D. Spengler. Air pollution and daily mortality: Associations with particulates and acid aerosols. *Environmental Research*, 59:362–373, 1992.
- [2] Jonathan M. Samet, Scott I. Zeger, and Kiros Berhane. The association of mortality and particulate air pollution. In *Particulate Air Pollution and Daily Mortality*. Health Effects Institute, Cambridge, MA, 1995.
- [3] J. L. Mumford, X. Z. He, R. S. Chapman, S. R. Cao, D. B. Harris, X. M. Li, Y. L. Xian, W. Z. Jiang, C. W. Xu, J. C. Chuang, W. E. Wilson, and M. Cooke. Lung cancer and indoor air pollution in Xuan Wei, China. *Science*, 235:217–220, 1987.
- [4] Roger O. McClellan. Health effects of exposure to diesel exhaust particles. *Annual Review of Pharmacology and Toxicology*, 27:279–300, 1987.
- [5] Aaron J. Cohen and Millicent W. P. Higgins. Health effects of diesel exhaust: Epidemiology. In *Diesel Exhaust: A Critical Analysis of Emissions, Exposure, and Health Effects*. Health Effects Institute, Cambridge, MA, 1995.
- [6] William F. Busby, Jr. and Paul M. Newberne. Diesel emissions and other substances associated with animal carcinogenicity. In *Diesel Exhaust: A Critical Analysis of Emissions, Exposure, and Health Effects*. Health Effects Institute, Cambridge, MA, 1995.
- [7] IARC Working Group on the Evaluation of the Carcinogenic Risk of Chemicals to Humans. *Polynuclear Aromatic Compounds, Part 1: Chemical, Environmental and Experimental Data*, volume 32 of *IARC Monographs on the Evaluation of the Carcinogenic Risk of Chemicals to Humans*. International Agency for Research on Cancer, Lyon, France, 1983.
- [8] IARC Working Group on the Evaluation of the Carcinogenic Risk of Chemicals to Humans. *Polynuclear Aromatic Compounds, Part 2: Carbon Blacks, Mineral Oils (Lubricant Base Oils and Derived Products) and Some Nitroarenes*, volume 33 of *IARC Monographs on the Evaluation of the Carcinogenic Risk of Chemicals to Humans*. International Agency for Research on Cancer, Lyon, France, 1984.

- [9] IARC Working Group on the Evaluation of the Carcinogenic Risk of Chemicals to Humans. *Polynuclear Aromatic Compounds, Part 3: Industrial Exposures in Aluminum Production, Coal Gasification, Coke Production and Iron and Steel Founding*, volume 34 of *IARC Monographs on the Evaluation of the Carcinogenic Risk of Chemicals to Humans*. International Agency for Research on Cancer, Lyon, France, 1984.
- [10] IARC Working Group on the Evaluation of the Carcinogenic Risk of Chemicals to Humans. *Polynuclear Aromatic Compounds, Part 4: Bitumens, Coal-tars and Derived Products, Shale-oils and Soots*, volume 35 of *IARC Monographs on the Evaluation of the Carcinogenic Risk of Chemicals to Humans*. International Agency for Research on Cancer, Lyon, France, 1985.
- [11] IARC Working Group on the Evaluation of the Carcinogenic Risk of Chemicals to Humans. *Overall Evaluations of Carcinogenicity: An Updating of IARC Monographs Volumes 1 to 42*, volume Supplement 7 of *IARC Monographs on the Evaluation of the Carcinogenic Risk of Chemicals to Humans*. International Agency for Research on Cancer, Lyon, France, 1987.
- [12] Lata Shirnamé-Moré. Genotoxicity of diesel emissions. Part I: Mutagenicity and other genetic effects. In *Diesel Exhaust: A Critical Analysis of Emissions, Exposure, and Health Effects*. Health Effects Institute, Cambridge, MA, 1995.
- [13] Janet Arey, William P. Harger, Detlev Helmig, and Roger Atkinson. Bioassay-directed fractionation of mutagenic PAH atmospheric photooxidation products and ambient particulate extracts. *Mutation Research*, 281:67–76, 1992.
- [14] John L. Durant, William G. Thilly, Harold F. Hemond, and Arthur L. Lafleur. Identification of the principal human cell mutagen in an organic extract of a mutagenic sediment. *Environmental Science and Technology*, 28:2033–2044, 1994.
- [15] John L. Durant, Arthur L. Lafleur, Elaine F. Plummer, Koli Taghizadeh, and William G. Thilly. Identification of human mutagens in urban atmospheric particulate material. In preparation.
- [16] John L. Durant, William F. Busby, Arthur L. Lafleur, and Bruce M. Penman. Human cell mutagenicity of nitrated, oxygenated, and unsubstituted polycyclic aromatic hydrocarbons associated with urban aerosol. *Mutation Research*. Submitted.
- [17] Milton L. Lee, Milos Novotny, and Keith D. Bartle. *Analytical Chemistry of Polycyclic Aromatic Compounds*. Academic Press, New York, 1981.
- [18] Tuan Vo-Dinh, editor. *Chemical Analysis of Polycyclic Aromatic Compounds*. John Wiley & Sons, New York, 1989.

- [19] A. Bjorseth and T. Ramdahl. *Handbook of Polycyclic Aromatic Hydrocarbons*, chapter Sources and emissions of PAH, pages 1–20. Marcel Dekker, New York, 1985.
- [20] Donald Mackay, Wan Ying Shiu, and Kuo Ching Ma. *Illustrated Handbook of Physical-chemical Properties and Environmental Fate for Organic Chemicals*, volume II. Lewis Publishers, Chelsea, MI, 1992.
- [21] James F. Pankow and Terry F. Bidleman. Interdependence of the slopes and intercepts from log—log correlations of measured gas—particle partitioning and vapor pressure: I. Theory and analysis of available data. *Atmospheric Environment*, 26A(6):1071–1080, 1992.
- [22] Kenneth T. Whitby. The physical characteristics of sulfur aerosols. *Atmospheric Environment*, 12:135–159, 1978.
- [23] John H. Seinfeld. *Atmospheric Chemistry and Physics of Air Pollution*. John Wiley & Sons, New York, 1986.
- [24] D. M. Murphy and D. S. Thomson. Laser ionization mass spectroscopy of single aerosol particles. *Aerosol Science and Technology*, 22:237–249, 1995.
- [25] Christopher A. Noble and Kimberly A. Prather. Real-time measurement of correlated size and composition profiles of individual atmospheric aerosol particles. *Environmental Science and Technology*, 30(9):2667–2680, 1996.
- [26] Walter C. McCrone. *The Particle Atlas: An Encyclopedia of Techniques for Small Particle Identification*, volume 1–6. Ann Arbor Science Publishers, Ann Arbor, MI, second edition, 1973.
- [27] Peter R. Buseck and John P. Bradley. Electron beam studies of individual natural and anthropogenic microparticles: Compositions, structures and surface reactions. In David R. Schryer, editor, *Heterogeneous Atmospheric Chemistry*, pages 57–77. American Geophysical Union, Washington, D. C., 1982.
- [28] Karen A. Katrinak, James R. Anderson, and Peter R. Buseck. Individual particle types in the aerosol of Phoenix, Arizona. *Environmental Science and Technology*, 29:321–329, 1995.
- [29] Terence H. Risby, Shelley S. Sehnert, Long Jiang, and Bhim S. Dhingra. A model for the release of adsorbed molecules from the surfaces of airborne particulate matter based on liquid-phase desorption from amorphous carbon blacks. *Environmental Health Perspectives*, 77:141–149, 1988.
- [30] Terence H. Risby and Shelley S. Sehnert. A model for the formation of airborne particulate matter based on the gas-phase adsorption on amorphous carbon blacks. *Environmental Health Perspectives*, 77:131–140, 1988.

- [31] G. Neue and F. Rudolph. A method for measuring the vapour pressures of PAH's adsorbed on the surface of soot. *International Journal of Analytical Chemistry*, 52:229–236, 1993.
- [32] Lynn M. Hildemann, Gregory R. Markowski, Michael C. Jones, and Glen R. Cass. Submicrometer aerosol mass distributions of emissions from boilers, fireplaces, automobiles, diesel trucks, and meat-cooking operations. *Aerosol Science and Technology*, 14:138–152, 1991.
- [33] Wolfgang F. Rogge, Lynn M. Hildemann, Monica A. Mazurek, Glen R. Cass, and Bernd R. T. Simoneit. Sources of fine organic aerosol: 1. Charbroilers and meat cooking operations. *Environmental Science and Technology*, 25(6):1112–1125, 1991.
- [34] Wolfgang F. Rogge, Lynn M. Hildemann, Monica A. Mazurek, Glen R. Cass, and Bernd R. T. Simoneit. Sources of fine organic aerosol: 2. Noncatalyst and catalyst-equipped automobiles and heavy-duty diesel trucks. *Environmental Science and Technology*, 27(4):636–651, 1993.
- [35] Wolfgang F. Rogge, Lynn M. Hildemann, Monica A. Mazurek, Glen R. Cass, and Bernd R. T. Simoneit. Sources of fine organic aerosol: 4. Particulate abrasion products from leaf surfaces of urban plants. *Environmental Science and Technology*, 27(4):2700–2711, 1993.
- [36] Wolfgang F. Rogge, Lynn M. Hildemann, Monica A. Mazurek, Glen R. Cass, and Bernd R. T. Simoneit. Sources of fine organic aerosol: 5. Natural gas home appliances. *Environmental Science and Technology*, 27(4):636–651, 1993.
- [37] R. J. Gordon. Distribution of airborne polycyclic aromatic hydrocarbons throughout Los Angeles. *Environmental Science and Technology*, 10:370–373, 1976.
- [38] G. Lunde and A. Bjorseth. Polycyclic aromatic hydrocarbons in long-range transported aerosols. *Nature*, 286:518–519, 1977.
- [39] W. Cautreels and K. Van Cauwenberghe. Experiments on the distribution of organic pollutants between airborne particulate matter and the corresponding gas phase. *Atmospheric Environment*, 12:1133–1141, 1978.
- [40] Hiroyasu Yamasaki, Kazuhiro Kuwata, and Hiroko Miyamoto. Effects of ambient temperature on aspects of airborne polycyclic aromatic hydrocarbons. *Environmental Science and Technology*, 16(4):189–194, 1982.
- [41] Daniel Grosjean, Kochy Fung, and Jeffrey Harrison. Interactions of polycyclic aromatic hydrocarbons with atmospheric pollutants. *Environmental Science and Technology*, 17(11):673–679, 1983.

- [42] H. C. Steinmetzer, W. Baumeister, and O. Vierle. Analytical investigation on the contents of polycyclic aromatic hydrocarbons in airborne particulate matter from two Bavarian cities. *Sci. Total Environ.*, 36:91–96, 1984.
- [43] C. Muel and S. Saguem. Determination of 23 polycyclic aromatic hydrocarbons in atmospheric particulate matter of the Paris area and photolysis by sunlight. *International Journal of Environmental Analytical Chemistry*, 19:111–131, 1985.
- [44] J. R. Cretney, H. K. Lee, G. J. Wright, W. H. Swallow, and M. C. Taylor. Analysis of polycyclic aromatic hydrocarbons in air particulate matter from a lightly industrialized urban area. *Environmental Science and Technology*, 19:397–404, 1985.
- [45] J. Jaklin and P. Krenmayr. A routine method for the quantitative determination of polycyclic aromatic hydrocarbons (PAHs) in urban air. *International Journal of Environmental Analytical Chemistry*, 21:33–42, 1985.
- [46] R. Guicherit and F. L. Schulting. The occurrence of organic chemicals in the atmosphere of the Netherlands. *Sci. Total Environ.*, 43:193–219, 1985.
- [47] Anders L. Colmsjö, Yngve U. Zebühr, and Conny E. Östman. Polynuclear aromatic compounds in flue gases and ambient air in the vicinity of a municipal incineration plant. *Atmospheric Environment*, 20(11):2279–2282, 1986.
- [48] Heikki Pyysalo, Jari Tuominen, Kim Wickström, Eija Skyttä, Leena Tikkanen, Sisko Salomaa, Marja Sorsa, Tuomo Nurmela, Tiina Mattila, and Viejo Pohjola. Polycyclic organic material (POM) in urban air: Fractionation, chemical analysis and genotoxicity of particulate and vapor phases in an industrial town in Finland. *Atmospheric Environment*, 21(5):1167–1180, 1987.
- [49] A. Rosell, J. O. Grimalt, M. G. Rosell, X. Guardino, and J. Albaigés. The composition of volatile and particulate hydrocarbons in urban air. *Fresenius' Journal of Analytical Chemistry*, 339:639–698, 1991.
- [50] R. Barale, L. Giromini, G. Ghelardini, C. Scapoli, N. Loprieno, M. Pala, F. Valerio, and I. Barrai. Correlations between 15 polycyclic aromatic hydrocarbons (PAH) and the mutagenicity of the total PAH fraction in ambient air particles in La Spezia (Italy). *Mutation Research*, 249:227–241, 1991.
- [51] Danuta Bodzek, Krystyna Luks-Betlej, and Lidia Warzecha. Determination of particle-associated polycyclic aromatic hydrocarbons in ambient air samples from the Upper Silesia region of Poland. *Atmospheric Environment*, 27A(5):759–764, 1993.
- [52] Debra A. Kaden, Ronald A. Hites, and William G. Thilly. Mutagenicity of soot and associated polycyclic aromatic hydrocarbons to *Salmonella typhimurium*. *Cancer Research*, 39:4152–4159, 1979.

- [53] M. F. Salamone, J. A. Heddle, and M. Katz. The mutagenic activity of thirty polycyclic aromatic hydrocarbons (PAH) and oxides in urban airborne particulates. *Environment International*, 2:37–43, 1979.
- [54] Mona Møller, Inger Hagen, and Thomas Ramdahl. Mutagenicity of polycyclic aromatic compounds (PAC) identified in source emissions and ambient air. *Mutation Research*, 157:149–156, 1985.
- [55] M. Sakai, D. Yoshina, and S. Mizusaki. Mutagenicity of polycyclic aromatic hydrocarbons and quinones on *salmonella typhimurium* TA97. *Mutation Research*, 156:61–67, 1985.
- [56] Michael Strandell, Susanne Zakrisson, Tomas Alsberg, Roger Westerholm, Lars Winquist, and Ulf Rannug. Chemical analysis and biological testing of a polar fraction of ambient air, Diesel engine, and gasoline engine particulate extracts. *Environmental Health Perspectives*, 102:85–92, 1994.
- [57] Torsten Spitzer and Toyohide Takeuchi. Determination of benzanthrone in environmental samples. *Journal of Chromatography A*, 710:109–116, 1995.
- [58] M. P. Hannigan, G. R. Cass, B. M. Penman, C. L. Crespi, A. L. Lafleur, W. F. Busby, Jr., and W. G. Thilly. Human cell mutagens in Los Angeles air. *Environmental Science and Technology*. Submitted.
- [59] Tomas Alsberg and Ulf Stenberg. Capillary GC-MS analysis of PAH emissions from combustion of peat and wood in a hot water boiler. *Chemosphere*, 7:487–496, 1979.
- [60] Dilip R. Choudhury. Characterization of polycyclic ketones and quinones in Diesel emission particulates by gas chromatography/mass spectrometry. *Environmental Science and Technology*, 16:102–106, 1982.
- [61] Thomas Ramdahl. Polycyclic aromatic ketones in environmental samples. *Environmental Science and Technology*, 17:666–670, 1983.
- [62] John T. Barbas, Michael E. Sigman, and Reza Dabestani. Photochemical oxidation of phenanthrene sorbed on silica gel. *Environmental Science and Technology*, 30(5):1776–1780, 1996.
- [63] Johann König, Eckhard Balfanz, Werner Funcke, and Thomas Romanowski. Determination of oxygenated polycyclic aromatic hydrocarbons in airborne particulate matter by capillary gas chromatography and gas chromatography/mass spectrometry. *Analytical Chemistry*, 55:599–603, 1983.
- [64] Mary P. Ligocki and James F. Pankow. Measurements of the gas/particle distributions of atmospheric organic compounds. *Environmental Science and Technology*, 23(1):75–83, 1989.

- [65] Steven B. Hawthorne, David J. Miller, John J. Langenfeld, and Mark S. Krieger. PM-10 high-volume collection and quantitation of semi- and nonvolatile phenols, methoxylated phenols, alkanes, and polycyclic aromatic hydrocarbons from winter urban air and their relationship to wood smoke emissions. *Environmental Science and Technology*, 26(11):2251–2262, 1992.
- [66] D. Bodzek, K. Tyrpien, and L. Warzecha. Identification of oxygen derivatives of polycyclic aromatic hydrocarbons in airborne particulate matter of Upper Silesia (Poland). *International Journal of Environmental Analytical Chemistry*, 52:75–85, 1993.
- [67] Alastair C. Lewis, Robert E. Robinson, Keith D. Bartle, and Michael J. Pilling. On-line coupled LC-GC-ITD/MS for the identification of alkylated, oxygenated, and nitrated polycyclic aromatic compounds in urban air particulate extracts. *Environmental Science and Technology*, 29(8):1977–1981, 1995.
- [68] Ronald C. Pierce and Morris Katz. Dependency of polynuclear aromatic hydrocarbon content on size distribution of atmospheric aerosols. *Environmental Science and Technology*, 9(4):347–353, 1975.
- [69] Barbara J. Finlayson-Pitts and James N. Pitts, Jr. *Atmospheric Chemistry: Fundamentals and Experimental Techniques*. John Wiley & Sons, New York, 1986.
- [70] Roger Atkinson. Gas-phase tropospheric chemistry of organic compounds: A review. *Atmospheric Environment*, 24A(1):1–41, 1990.
- [71] James N. Pitts, Jr., Karel A. Van Cauwenberghe, Daniel Grosjean, Joachim P. Schmid, Dennis R. Fitz, William L. Belser, Jr., Gregory B. Knudson, and Paul M. Hynds. Atmospheric reactions of polycyclic aromatic hydrocarbons: Facile formation of mutagenic nitro derivatives. *Science*, 202:515–519, 1978.
- [72] James N. Pitts, Jr., David M. Lokensgard, Paul S. Ripley, Karel A. Van Cauwenberghe, Luk Van Vaeck, Steven D. Shaffer, Alan J. Thill, and William L. Belser, Jr. “Atmospheric” epoxidation of benzo[a]pyrene by ozone: Formation of the metabolite benzo[a]pyrene-4,5-oxide. *Science*, 210:1347–1349, 1980.
- [73] Detlev Helmig, Janet Arey, William P. Harger, Roger Atkinson, and José López-Cancio. Formation of mutagenic nitrodibenzopyranones and their occurrence in ambient air. *Environmental Science and Technology*, 26(3):622–624, 1992.
- [74] Richard Kamens, Douglas Bell, Andrea Dietrich, Jean Perry, Randall Goodman, Larry Claxton, and Sylvestre Tejada. Mutagenic transformations of dilute wood smoke systems in the presence of O₃ and NO₂. In Marcus Cooke and Anthony J. Dennis, editors, *Polycyclic Aromatic Hydrocarbons: Mechanisms, Methods and Metabolism*, pages 663–683. Battelle Press, Columbus, OH, 1985.

- [75] Janet Arey, Barbara Zielinska, Roger Atkinson, Arthur M. Winer, Thomas Ramdahl, and James N. Pitts, Jr. The formation of nitro-PAH from the gas-phase reactions of fluoranthene and pyrene with the OH radical in the presence of NO_x . *Atmospheric Environment*, 20(12):2339–2345, 1986.
- [76] Roger Atkinson, Janet Arey, Barbara Zielinska, and Sara M. Aschmann. Kinetics and nitro-products of the gas-phase OH and NO_3 radical-initiated reactions of naphthalene- d_8 , fluoranthene- d_{10} , and pyrene. *International Journal of Chemical Kinetics*, 22:999–1014, 1990.
- [77] Roger Atkinson and Sara M. Aschmann. Kinetics of the reactions of acenaphthene and acenaphthylene and structurally-related aromatic compounds with OH and NO_3 radicals, N_2O_5 and O_3 at 296 ± 2 K. *International Journal of Chemical Kinetics*, 20:513–539, 1988.
- [78] Thomas D. Behymer and Ronald A. Hites. Photolysis of polycyclic aromatic hydrocarbons adsorbed on fly ash. *Environmental Science and Technology*, 22:1311–1319, 1988.
- [79] Thomas D. Behymer and Ronald A. Hites. Photolysis of polycyclic aromatic hydrocarbons adsorbed on simulated atmospheric particulates. *Environmental Science and Technology*, 19(10):1004–1006, 1985.
- [80] Bruce D. McVeety and Ronald A. Hites. Atmospheric deposition of polycyclic aromatic hydrocarbons to water surfaces: A mass balance approach. *Atmospheric Environment*, 22(3):511–536, 1988.
- [81] Hilary Hafner Main and Sheldon K. Friedlander. Dry deposition of atmospheric aerosols by dual tracer method: I. Area source. *Atmospheric Environment*, 24A:103–108, 1990.
- [82] W. G. N. Slinn. Precipitation scavenging. In *Atmospheric Sciences and Power Production — 1979*, chapter 11. U. S. Department of Energy, 1983.
- [83] U. S. Environmental Protection Agency. Air quality criterion for particulate matter and sulfur oxides. Technical Report EPA-600/8-82-029, 1982.
- [84] James. D. Sun, Ronald. K. Wolff, and George. M. Kanapilly. Deposition, retention and biological fate of inhaled benzo[a]pyrene adsorbed onto ultrafine particles and as a pure aerosol. *Toxicology and Applied Pharmacology*, 65:231–244, 1982.
- [85] Roger N. Westerholm, Thomas E. Alsberg, Åke B. Frommelin, Michael E. Strandell, Ulf Rannug, Lars Winquist, Vassilios Grigoriadis, and Karl-Erik Egeback. Effect of fuel polycyclic aromatic hydrocarbon content on the emissions of polycyclic aromatic hydrocarbons and other mutagenic substances from a gasoline-fueled automobile. *Environmental Science and Technology*, 22(8):925–930, 1988.

- [86] Roger N. Westerholm, Jacob Almén, Hang Li, J. Ulf Rannug, Karl-Erik Egebäck, and Kerstin Grägg. Chemical and biological characterization of particulate-, semivolatile-, and gas-phase-associated compounds in diluted heavy-duty diesel exhausts: A comparison of three different semivolatile-phase samplers. *Environmental Science and Technology*, 25(2):332–338, 1991.
- [87] C. E. Junge. Basic considerations about trace constituents in the atmosphere as related to the fate of global pollutants. In I. H. Suffet, editor, *Fate of Pollutants in the Air and Water Environments*, pages 7–26. J. Wiley & Sons, New York, 1977.
- [88] James F. Pankow. Review and comparative analysis of the theories on partitioning between the gas and aerosol particulate phases in the atmosphere. *Atmospheric Environment*, 21(11):2275–2283, 1987.
- [89] James F. Pankow, Lorne M. Isabelle, Donald A. Buchholz, Wentai Luo, and B. Douglas Reeves. Gas/particle partitioning of polycyclic aromatic hydrocarbons and alkanes to environmental tobacco smoke. *Environmental Science and Technology*, 28:363–365, 1994.
- [90] Linda S. Lee, Mats Hagwall, Joseph J. Deifino, and P. Suresh C. Rao. Partitioning of polycyclic aromatic hydrocarbons from diesel fuel into water. *Environmental Science and Technology*, 26(11):2104–2110, 1992.
- [91] Linda S. Lee, P. Suresh C. Rao, and Itaru Okuda. Equilibrium partitioning of polycyclic aromatic hydrocarbons from coal tar into water. *Environmental Science and Technology*, 26(11):2110–2115, 1992.
- [92] Morris Katz and Cecilia Chan. Comparative distribution of eight polycyclic aromatic hydrocarbons in airborne particulates collected by conventional high-volume sampling and by size fractionation. *Environmental Science and Technology*, 14(7):838–843, 1980.
- [93] Antonio H. Miguel and Sheldon K. Friedlander. Distribution of benzo[a]pyrene and coronene with respect to particle size in Pasadena aerosols in the submicron range. *Atmospheric Environment*, 12:2407–2413, 1978.
- [94] Chandra Venkataraman and Sheldon K. Friedlander. Size distributions of polycyclic aromatic hydrocarbons and elemental carbon: 2. Ambient measurements and effects of atmospheric processes. *Environmental Science and Technology*, 28(4):563–572, 1994.
- [95] L. Van Vaeck and K. Van Cauwenberghe. Cascade impactor measurements of the size distribution of the major classes of organic pollutants in atmospheric particulate matter. *Atmospheric Environment*, 12:2229–2239, 1978.
- [96] L. Van Vaeck, G. Broddin, and K. Van Cauwenberghe. Differences in particle size distributions of major organic pollutants in ambient aerosols in urban, rural

- and seashore areas. *Environmental Science and Technology*, 13(12):1494–1502, 1979.
- [97] Luc Van Vaeck and Karel A. Van Cauwenberghe. Characteristic parameters of particle size distributions of primary organic constituents of ambient aerosols. *Environmental Science and Technology*, 19(8):707–716, 1985.
- [98] Merce Aceves and Joan O. Grimalt. Seasonally dependent size distributions of aliphatic and polycyclic aromatic hydrocarbons in urban aerosols from densely populated areas. *Environmental Science and Technology*, 27(13):2896–2908, 1993.
- [99] M. A. Sicre, J. C. Marty, A. Saliot, X. Aparicio, J. Grimalt, and J. Albaigés. Aliphatic and aromatic hydrocarbons in different sized aerosols over the Mediterranean Sea: Occurrence and origin. *Atmospheric Environment*, 21(10):2247–2259, 1987.
- [100] P. Pistikopoulos, H. M. Wortham, L. Gomes, S. Masclet-Beyne, E. Bon Nguyen, P. A. Masclet, and G. Mouvier. Mechanisms of formation of particulate polycyclic aromatic hydrocarbons in relation to the particle size distribution; effects of meso-scale transport. *Atmospheric Environment*, 24A(10):2573–2584, 1990.
- [101] Chandra Venkataraman, James M. Lyons, and Sheldon K. Friedlander. Size distributions of polycyclic aromatic hydrocarbons and elemental carbon: 1. Sampling, measurement methods, and source characterization. *Environmental Science and Technology*, 28(4):555–562, 1994.
- [102] James F. Pankow. An absorption model of gas/particle partitioning of organic compounds in the atmosphere. *Atmospheric Environment*, 28:185–188, 1994.
- [103] Jonathan O. Allen, Nameeta M. Dookeran, Kenneth A. Smith, Adel F. Sarofim, Koli Taghizadeh, and Arthur L. Lafleur. Measurement of polycyclic aromatic hydrocarbons associated with size-segregated atmospheric aerosols in Massachusetts. *Environmental Science and Technology*, 30:1023–1031, 1996.
- [104] Virgil A. Marple, Kenneth L. Rubow, and Stephen M. Behm. A microorifice uniform deposit impactor (MOUDI): Description, calibration and use. *Aerosol Science and Technology*, 14:434–446, 1991.
- [105] Jonathan O. Allen, Nameeta M. Dookeran, Kenneth A. Smith, Adel F. Sarofim, Koli Taghizadeh, and Arthur L. Lafleur. Measurement of oxygenated polycyclic aromatic hydrocarbons associated with a size-segregated urban aerosol. *Environmental Science and Technology*. Submitted.
- [106] A. K. Rao and K. T. Whitby. Non-ideal collection characteristics of inertial impactors: I. Single-stage impactors and solid particles. *Journal of Aerosol Science*, 9:77–86, 1978.

- [107] Jay R. Turner and Susanne V. Hering. Greased and oiled substrates as bounce-free impaction surfaces. *Journal of Aerosol Science*, 18(2):215–224, 1987.
- [108] Mark D. Burford, Steven B. Hawthorne, and David J. Miller. Extraction rates of spiked versus native PAHs from heterogeneous environmental samples using supercritical fluid extraction and sonication in methylene chloride. *Analytical Chemistry*, 65:1497–1505, 1993.
- [109] Arthur L. Lafleur and Mary J. Wornat. Multimode separation of polycyclic aromatic compounds by size exclusion chromatography with poly(divinylbenzene). *Analytical Chemistry*, 60(11):1096–1102, 1988.
- [110] Milton L. Lee, Daniel L. Vassilaros, Curt M. White, and Milos Novotny. Retention indices for programmed-temperature capillary-column gas chromatography of polycyclic aromatic hydrocarbons. *Analytical Chemistry*, 51(6):768–774, 1979.
- [111] Ronald A. Hites. Mass spectrometry of polycyclic aromatic compounds. In Tuan Vo-Dinh, editor, *Chemical Analysis of Polycyclic Aromatic Compounds*, chapter 8. John Wiley & Sons, 1989.
- [112] P.-J. Tsai and J. H. Vincent. Impaction model for the aspiration efficiencies of aerosol samplers at large angles with respect to the wind. *Journal of Aerosol Science*, 24(7):919–928, 1993.
- [113] John James Murray, Roswell Francis Pottie, and Christian Pupp. The vapor pressures and enthalpies of sublimation of five polycyclic aromatic hydrocarbons. *Canadian Journal of Chemistry*, 52:557–563, 1974.
- [114] W. J. Sonnefeld, W. H. Zoller, and W. E. May. Dynamic coupled-column liquid chromatographic determination of ambient temperature vapor pressures of polynuclear aromatic hydrocarbons. *Analytical Chemistry*, 55:275–280, 1983.
- [115] Richard M. Kamens, Zhishi Guo, James N. Flucher, and Douglas A. Bell. Influence of humidity, sunlight, and temperature on the daytime decay of polycyclic aromatic hydrocarbons on atmospheric soot particles. *Environmental Science and Technology*, 22(1):103–108, 1988.
- [116] Rene P. Schwarzenbach, Philip M. Gschwend, and Dieter M. Imboden. *Environmental Organic Chemistry*. John Wiley & Sons, New York, 1993.
- [117] Myoseon Jang and Stephen R. McDow. Benz[*a*]anthracene photodegradation in the presence of known organic constituents of atmospheric aerosols. *Environmental Science and Technology*, 29:2654–2660, 1995.
- [118] Lynn M. Hildemann, Gregory R. Markowski, and Glen R. Cass. Chemical composition of emissions from urban sources of fine organic aerosol. *Environmental Science and Technology*, 25(4):744–759, 1991.

- [119] Philip C. Hansen and Charles A. Eckert. An improved transpiration method for the measurement of very low vapor pressures. *Journal of Chemical and Engineering Data*, 31:1–3, 1986.
- [120] Hiroo Inokuchi, Sukekuni Shiba, Takashi Handa, and Hideo Akamatu. Heats of sublimation of condensed polynuclear aromatic hydrocarbons. *Bull. Chem. Soc.*, 25:299–302, 1952.
- [121] C. G. De Kruif. Enthalpies of sublimation and vapour pressures of 11 polycyclic hydrocarbons. *Journal of Chemical Thermodynamics*, 12:243–248, 1980.
- [122] A. K. Rao and K. T. Whitby. Non-ideal collection characteristics of inertial impactors: II. Cascade impactors. *Journal of Aerosol Science*, 9:87–100, 1978.
- [123] Jari Tuominen, Sisko Salomaa, Heikki Pyysalo, Eija Skyttä, Leena Tikkanen, Tuomo Nurmela, Marja Sorsa, Veijo Pohjola, Marketta Sauri, and Kimmo Himberg. Polynuclear aromatic compounds and genotoxicity in particulate and vapor phases of ambient air: Effect of traffic, season, and meteorological conditions. *Environmental Science and Technology*, 22(10):1228–1234, 1988.
- [124] Robert H. Perry and Cecil H. Chilton. *Chemical Engineers' Handbook*. McGraw-Hill Book Company, fifth edition, 1973.
- [125] T. Strand. On the theory of normal ground impingement of axi-symmetric jets in inviscid incompressible flow. In *First AIAA Annual Meeting*, Washington, DC, 1964. American Institute of Aeronautics and Astronautics. AIAA Paper No. 64-424.
- [126] M. T. Scholtz and Olev Trass. Mass transfer in a nonuniform impinging jet: Part I. Stagnation flow-velocity and pressure distribution. *American Institute of Chemical Engineering Journal*, 16(1):82–90, 1970.
- [127] M. T. Scholtz and Olev Trass. Mass transfer in a nonuniform impinging jet: Part II. Boundary layer flow-mass transfer. *American Institute of Chemical Engineering Journal*, 16(1):90–96, 1970.
- [128] Robert C. Reid, John M. Prausnitz, and Bruce E. Poling. *The Properties of Gases & Liquids*. McGraw-Hill, Inc., New York, fourth edition, 1987.
- [129] Barbara J. Turpin, Shi-Ping Liu, Kathryn S. Podolske, Marcos S. P. Gomes, Steve J. Eisenreich, and Peter H. McMurry. Design and evaluation of a novel diffusion separator for measuring gas/particle distributions of semivolatile organic compounds. *Environmental Science and Technology*, 27:2441–2449, 1993.
- [130] Hwa-Chi Wang and Walter John. Characteristics of the Berner impactor for sampling inorganic ions. *Aerosol Science and Technology*, 8:157–172, 1988.

- [131] Xinqiu Zhang. *Measurements of size resolved atmospheric aerosol chemical composition with impactors: Data integrity and applications*. PhD thesis, University of Minnesota, 1990.
- [132] X. Q. Zhang and P. H. McMurry. Theoretical analysis of evaporative losses from impactor and filter deposits. *Atmospheric Environment*, 21(8):1779–1789, 1987.
- [133] Xinqiu Zhang and Peter H. McMurry. Theoretical analysis of evaporative losses of adsorbed or absorbed species during atmospheric aerosol sampling. *Environmental Science and Technology*, 25(3):456–459, 1991.
- [134] H. Burtscher. Measurement and characteristics of combustion aerosols with special consideration of photoelectric charging and charging by flame ions. *Journal of Aerosol Science*, 23:549–595, 1992.
- [135] H. Burtscher, L. Scherrer, H. C. Siegmann, A. Schmidt-Ott, and B. Federer. *Journal of Applied Physics*, 53:3787, 1982.
- [136] H. Burtscher and A. Schmidt-Ott. *In situ* measurement of adsorption and condensation of a polyaromatic hydrocarbon on ultrafine C particles by means of photoemission. *Journal of Aerosol Science*, 17:699–703, 1986.
- [137] Czeslaw O. Popiel and Olev Trass. Visualization of a free and impinging round jet. *Experimental Thermal and Fluid Science*, 4:253–264, 1991.
- [138] H. L. Langhaar. *Transactions of the ASME*, 64:A–55, 1942.
- [139] Virgil A. Marple and Benjamin Y. H. Liu. Characteristics of laminar jet impactors. *Environmental Science and Technology*, 8(7):648–654, 1974.
- [140] Francesc Giralt, Chu-Jen Chia, and Olev Trass. Characterization of the impingement region in an axisymmetric turbulent jet. *Industrial and Engineering Chemistry, Fundamentals*, 16:21–28, 1977.
- [141] Chu-Jen Chia, Francesc Giralt, and Olev Trass. Mass transfer in axisymmetric turbulent impinging jets. *Industrial and Engineering Chemistry, Fundamentals*, 16:28–35, 1977.
- [142] Holger Martin. Heat and mass transfer between impinging gas jets and solid surfaces. volume 13 of *Advances in Heat Transfer*, chapter 1, pages 1–60. Academic Press, 1977.
- [143] R. Byron Bird, Warren E. Stewart, and Edwin N. Lightfoot. *Transport Phenomena*. John Wiley & Sons, New York, 1960.
- [144] E. J. Davis, P. Ravindran, and A. K. Ray. A review of the theory and experiments on diffusion from submicron particles. *Chemical Engineering Communications*, 5:251–268, 1980.

- [145] D. J. Rader, P. H. McMurray, and S. Smith. Evaporation rates of monodisperse organic aerosols in the 0.02 to 0.2 μm diameter range. *Aerosol Science and Technology*, 6:247–260, 1987.
- [146] A. L. McClellan and H. F. Harnsberger. Cross-sectional area of molecules adsorbed on solid surfaces. *Journal of Colloid and Interface Science*, 23:577–599, 1967.
- [147] H. Andrew Gray, Glen R. Cass, James J. Huntzicker, Emily K. Heyerdahl, and John A. Rau. Characteristics of atmospheric organic and elemental carbon particle concentrations in Los Angeles. *Environmental Science and Technology*, 20:580–589, 1986.
- [148] Arthur W. Adamson. *Physical Chemistry of Surfaces*. John Wiley & Sons, Inc., New York, fifth edition, 1990.
- [149] William P. Reed. Certificate of analysis for standard reference material 1650: Diesel particulate matter. Technical report, National Institute of Standards and Technology, Gaithersburg, MD, 1991.
- [150] Jay R. Odum, Jianzhen Yu, and Richard M. Kamens. Modeling the mass transfer of semivolatile organics in combustion aerosols. *Environmental Science and Technology*, 28:2278–2285, 1994.
- [151] Peter H. McMurry and Mark R. Stolzenburg. On the sensitivity of particle size to relative humidity for Los Angeles aerosols. *Atmospheric Environment*, 23(2):497–507, 1989.
- [152] Michael Modell and Robert C. Reid. *Thermodynamics and Its Applications*. Prentice-Hall, Englewood Cliffs, NJ, second edition, 1983.
- [153] S. K. Friedlander. *Smoke, Dust and Haze: Fundamentals of Aerosol Behavior*. John Wiley & Sons, 1977.
- [154] Anthony S. Wexler, Frederick W. Lurmann, and John H. Seinfeld. Modelling urban and regional aerosols: I. Model development. *Atmospheric Environment*, 28:531–546, 1994.
- [155] L. Rainey, Á. Palotás, J. B. Vander Sande, and A. F. Sarofim. Application of high resolution electron microscopy for the characterization and source assignment of diesel particulates. *Appl. Occup. Environ. Hyg.*, 11:777–781, 1996.
- [156] Árpád B. Palotás, Lenore C. Rainey, Christian J. Feldermann, Adel F. Sarofim, and John B. Vander Sande. Soot morphology: An application of image analysis in high-resolution transmission electron microscopy. *Microscopy Research and Technique*, 33:266–278, 1996.
- [157] J. W. Edington. Fundamentals of electron diffraction. In *Electron Diffraction in the Electron Microscope*, volume 2, pages 5–6. Macmillan, 1975.

- [158] I. C. Lewis. Thermal polymerization of aromatic hydrocarbons. *Carbon*, 18:191–196, 1980.
- [159] Elliott Barrett, Leslie G. Joyner, and Paul P. Halenda. The determination of pore volume and area distributions in porous substances: I. Computations from nitrogen isotherms. *Journal of the American Chemical Society*, 73:373–380, 1951.
- [160] Jean-Baptiste Donnet and Andries Voet. *Carbon Black: Physics, Chemistry and Elastomer Reinforcement*. Marcel Dekker, New York, first edition, 1976.
- [161] Curt M. White. Prediction of the boiling point, heat of vaporization, and vapor pressure at various temperatures for polycyclic aromatic hydrocarbons. *Journal of Chemical and Engineering Data*, 31(2):198–203, 1986.
- [162] Edward N. Fuller, Keith Ensley, and J. Calvin Giddings. Diffusion of halogenated hydrocarbons in helium: The effect of structure on collision cross sections. *Journal of Physical Chemistry*, 73(11):3679–3685, 1969.
- [163] Lloyd Caldwell. Diffusion coefficient of naphthalene in air and hydrogen. *Journal of Chemical and Engineering Data*, 29(1):60–62, 1984.
- [164] Edward Mack, Jr. Average cross-sectional areas of molecules by gaseous diffusion methods. *Journal of the American Chemical Society*, 47:2468–2482, 1925.
- [165] J. P. McCullough, H. L. Finke, J. F. Messerly, S. S. Todd, T. C. Kinchloe, and Guy Waddington. The low-temperature thermodynamic properties of naphthalene, 1-methylnaphthalene, 2-methylnaphthalene, 1,2,3,4-tetrahydronaphthalene, *trans*-decahydronaphthalene and *cis*-decahydronaphthalene. *Journal of Physical Chemistry*, 61:1105–1116, 1957.
- [166] P. Goursot, H. L. Girdhar, and Edgar F. Westrum, Jr. Thermodynamics of polynuclear aromatic molecules: III. Heat capacities and enthalpies of fusion of anthracene. *Journal of Physical Chemistry*, 74:2538–2541, 1970.
- [167] Wen-Kuei Wong and Edgar F. Westrum, Jr. Thermodynamics of polynuclear aromatic molecules: I. Heat capacities and enthalpies of fusion of pyrene, fluoranthene, and triphenylene. *Journal of Chemical Thermodynamics*, 3:105–124, 1971.
- [168] H. L. Finke, J. F. Messerly, S. H. Lee, A. G. Osborn, and D. R. Douslin. Comprehensive thermodynamic studies of seven aromatic hydrocarbons. *Journal of Chemical Thermodynamics*, 9:937–956, 1977.
- [169] Wen-Kuei Wong and Edgar F. Westrum, Jr. Thermodynamics of polynuclear aromatic molecules: II. Low-temperature thermal properties of perylene, coronene, and naphthacene. *Mol. Cryst. Liq. Cryst.*, 61:207–228, 1980.

- [170] David R. Lide, editor. *Handbook of Chemistry and Physics*. CRC Press, Boca Raton, 73rd edition, 1992.
- [171] Shanti A. Kudchadker, Arvind P. Kudchadker, and Bruno J. Zwolinski. Chemical thermodynamic properties of anthracene and phenanthrene. *Journal of Chemical Thermodynamics*, 11:1051–1059, 1979.
- [172] N. Durupt, A. Aoulmi, M. Bouroukba, and M. Rogalski. Heat capacities of liquid polycyclic aromatic hydrocarbons. *Thermochimica Acta*, 260:87–94, 1995.
- [173] Rosario Gigli, Leopoldo Malaspina, and Giampiero Bardi. Tensione de vapor ed entalpia di sublimazione del perilene. *Annali di Chimica*, 63:627–633, 1973.
- [174] Terry F. Bidleman and William T. Foreman. Vapor–particle partitioning of semivolatile organic compounds. In Ronald A. Hites and S. J. Eisenreich, editors, *Sources and Fates of Aquatic Pollutants*, pages 27–56. American Chemical Society, 1987.
- [175] Donald Mackay and Wan Ying Shiu. Aqueous solubility of polynuclear aromatic hydrocarbons. *Journal of Chemical and Engineering Data*, 22(4):399–402, 1977.

Appendix A

Tabulated GC/MS Data for Size-segregated Aerosol Samples

The data generated from GC/MS analysis of the size-segregated aerosol samples are presented here in tabular form. Data are presented in the form $\mu \pm \sigma(n)$; where μ is the mean amount of analyte in the whole sample in ng, σ is one standard deviation of the amount of analyte in the whole sample in ng, and n is the number data points. Samples in which the analyte was not present in quantifiable amounts in any of the GC/MS injections are indicated by “—”. The Quabbin Summit stage 3 sample from one of the sampling days was lost. For comparison with other samples, the amounts of analytes found in this sample have been multiplied by 1.25.

Table A.1: Amounts of naphthalene, acenaphthylene, and acenaphthene in Kenmore Square aerosol samples.

Sample	naphthalene			acenaphthylene			acenaphthene		
Stage 0	61.46	± 9.02	(2)	4.32	± 0.27	(2)	28.60	± 1.85	(3)
Stage 1	48.69	± 1.90	(3)	3.03	± 0.66	(2)	26.70	± 0.58	(3)
Stage 2	—			—			23.13	± 1.51	(2)
Stage 3	69.10	± 2.68	(3)	3.97	± 0.45	(3)	22.37	± 0.69	(3)
Stage 4	100.85	± 2.18	(3)	3.81	± 0.20	(3)	17.86	± 0.17	(3)
Stage 5	36.33	± 2.24	(3)	1.72	± 0.30	(2)	13.11	± 0.51	(3)
Stage 6	110.53	± 3.16	(3)	3.24	± 0.20	(3)	14.36	± 0.31	(3)
Stage 7	27.26	± 1.90	(2)	—			8.45	± 0.10	(3)
Stage 8	74.92	± 4.19	(3)	1.61	± 0.14	(2)	7.13	± 0.21	(3)
After Filter	23.68		(1)	—			—		
Field Blank	41.42	± 1.53	(3)	—			5.17	± 0.27	(3)
Method Blank 0	21.91	± 3.11	(2)	—			2.98	± 0.67	(2)
Method Blank 1	93.30	± 3.47	(2)	3.10		(1)	7.71	± 0.55	(2)
Method Blank 2	—			—			—		
Filter Blank	21.41		(1)	—			—		
Extraction Test	22.03	± 1.14	(2)	—			—		
Aging Test (Stage 2)	—			—			—		
Aging Test (Stage 7)	—			—			—		

Table A.2: Amounts of fluorene, phenanthrene, and anthracene in Kenmore Square aerosol samples.

Sample	fluorene			phenanthrene			anthracene		
Stage 0	124.30	± 38.35	(3)	653.88	± 57.00	(3)	55.73	± 1.07	(2)
Stage 1	81.60	± 2.61	(2)	647.57		(1)	41.51		(1)
Stage 2	243.82	± 25.06	(3)	515.60	± 9.84	(3)	43.87	± 1.93	(3)
Stage 3	75.64	± 4.10	(3)	500.12	± 34.23	(2)	48.27	± 5.10	(2)
Stage 4	71.61	± 7.10	(3)	370.85	± 5.05	(3)	38.85	± 3.06	(3)
Stage 5	35.81	± 6.38	(3)	285.51	± 19.87	(2)	30.92	± 0.16	(2)
Stage 6	67.31	± 11.70	(3)	243.69	± 5.31	(3)	25.63	± 1.70	(3)
Stage 7	23.15	± 1.18	(3)	170.74	± 7.60	(3)	20.23	± 0.28	(3)
Stage 8	28.60	± 2.27	(3)	131.71	± 2.67	(3)	15.41	± 1.09	(3)
After Filter	6.54	± 3.27	(2)	13.22	± 0.05	(3)	1.51	± 0.31	(2)
Field Blank	11.65	± 0.88	(3)	26.82	± 0.60	(2)	6.76	± 0.05	(2)
Method Blank 0	8.46		(1)	32.27	± 1.31	(2)	—		
Method Blank 1	11.95	± 1.90	(2)	20.63	± 0.99	(3)	—		
Method Blank 2	12.85	± 1.99	(3)	19.12	± 0.37	(3)	—		
Filter Blank	—			13.54	± 0.56	(3)	—		
Extraction Test	4.17	± 0.71	(2)	9.61	± 0.25	(3)	0.96	± 0.03	(2)
Aging Test (Stage 2)	—			543.53		(1)	40.97		(1)
Aging Test (Stage 7)	—			163.31		(1)	16.72		(1)

Table A.3: Amounts of fluoranthene, pyrene, and benzo[ghi]fluoranthene in Kenmore Square aerosol samples.

Sample	fluoranthene			pyrene			benzo[ghi]fluoranthene		
Stage 0	388.64	± 54.49	(3)	182.73	± 24.95	(3)	12.80	± 0.24	(3)
Stage 1	357.25	± 27.55	(3)	175.58	± 11.99	(3)	13.31	± 2.27	(3)
Stage 2	464.63	± 33.89	(3)	236.23	± 11.88	(3)	15.11	± 0.58	(3)
Stage 3	482.76	± 28.05	(3)	257.63	± 16.13	(3)	21.54	± 3.47	(3)
Stage 4	458.21	± 22.13	(3)	254.67	± 12.64	(3)	22.19	± 0.37	(3)
Stage 5	353.63	± 27.93	(3)	195.34	± 20.85	(3)	27.79	± 4.41	(3)
Stage 6	340.72	± 26.66	(3)	205.69	± 15.41	(3)	26.93	± 0.69	(3)
Stage 7	215.54	± 18.22	(3)	129.68	± 9.25	(3)	26.33	± 5.08	(3)
Stage 8	176.69	± 10.53	(3)	98.48	± 5.96	(3)	15.43	± 0.57	(3)
After Filter	8.21	± 0.86	(3)	5.29	± 0.59	(3)	1.97	± 0.11	(3)
Field Blank	10.32	± 0.72	(3)	4.12	± 0.23	(3)	0.48		(1)
Method Blank 0	7.84	± 1.49	(2)	6.88	± 1.25	(2)	—		
Method Blank 1	6.44	± 0.85	(2)	2.77	± 0.20	(3)	—		
Method Blank 2	6.16	± 0.63	(3)	2.73	± 0.18	(3)	—		
Filter Blank	—			1.15		(1)	—		
Extraction Test	5.33	± 0.42	(3)	3.53	± 0.21	(3)	—		
Aging Test (Stage 2)	397.12		(1)	191.03		(1)	15.97		(1)
Aging Test (Stage 7)	235.56		(1)	133.57		(1)	22.08		(1)

Table A.4: Amounts of benz[a]anthracene, chrysene/triphenylene, and benzofluoranthenes in Kenmore Square aerosol samples.

Sample	benz[a]anthracene			chrysene/triphenylene			benzofluoranthenes		
Stage 0	12.14	± 0.21	(3)	15.00	± 0.33	(3)	13.98	± 1.62	(3)
Stage 1	12.12	± 2.16	(3)	16.45	± 2.95	(3)	11.43	± 1.17	(3)
Stage 2	15.82	± 0.54	(3)	19.81	± 0.40	(3)	20.61	± 1.45	(3)
Stage 3	25.51	± 4.63	(3)	29.73	± 5.44	(3)	29.04	± 1.91	(3)
Stage 4	45.80	± 0.82	(3)	46.56	± 0.66	(3)	81.15	± 0.32	(3)
Stage 5	69.48	± 10.60	(3)	68.21	± 14.29	(3)	122.85	± 15.42	(3)
Stage 6	63.71	± 1.67	(3)	67.17	± 2.09	(3)	146.00	± 3.55	(3)
Stage 7	47.13	± 8.23	(3)	56.59	± 10.51	(3)	100.50	± 8.92	(3)
Stage 8	30.87	± 0.86	(3)	32.32	± 0.42	(3)	72.33	± 2.68	(3)
After Filter	2.96	± 0.20	(3)	3.17	± 0.10	(3)	28.17	± 4.30	(3)
Field Blank	0.69	± 0.17	(2)	1.13	± 0.22	(3)	1.50	± 0.12	(3)
Method Blank 0	—			0.42		(1)	0.89		(1)
Method Blank 1	—			—			1.50	± 0.42	(2)
Method Blank 2	—			0.47	± 0.01	(2)	0.72		(1)
Filter Blank	—			—			—		
Extraction Test	0.81	± 0.05	(3)	1.04	± 0.02	(3)	2.76	± 0.51	(3)
Aging Test (Stage 2)	15.68		(1)	20.60		(1)	20.93		(1)
Aging Test (Stage 7)	39.75		(1)	47.31		(1)	105.45		(1)

Table A.5: Amounts of benzo[e]pyrene, benzo[a]pyrene, and perylene in Kenmore Square aerosol samples.

Sample	benzo[e]pyrene			benzo[a]pyrene			perylene		
Stage 0	5.90	± 0.68	(3)	3.22	± 0.43	(3)	0.50	± 0.06	(2)
Stage 1	4.84	± 0.45	(3)	2.68	± 0.36	(3)	0.45	± 0.03	(3)
Stage 2	8.26	± 0.45	(3)	5.60	± 0.13	(3)	0.90	± 0.07	(3)
Stage 3	11.33	± 0.87	(3)	8.99	± 0.64	(3)	1.83	± 0.23	(3)
Stage 4	30.40	± 0.50	(3)	30.05	± 0.38	(3)	6.83	± 0.47	(3)
Stage 5	46.87	± 3.72	(3)	46.00	± 2.72	(3)	8.50	± 0.34	(3)
Stage 6	58.91	± 1.21	(3)	53.36	± 1.16	(3)	10.75	± 0.80	(3)
Stage 7	44.13	± 3.26	(3)	33.53	± 2.23	(3)	6.51	± 1.14	(3)
Stage 8	31.12	± 0.96	(3)	27.35	± 0.33	(3)	4.49	± 0.13	(3)
After Filter	17.54	± 2.53	(3)	12.45	± 1.47	(3)	1.66	± 0.28	(3)
Field Blank	0.66	± 0.08	(2)	0.65	± 0.08	(2)	0.32	± 0.03	(2)
Method Blank 0	—			—			—		
Method Blank 1	—			—			—		
Method Blank 2	—			—			—		
Filter Blank	—			—			0.24		(1)
Extraction Test	1.05	± 0.19	(3)	1.03	± 0.13	(3)	0.24	± 0.00	(2)
Aging Test (Stage 2)	8.93		(1)	5.80		(1)	0.75		(1)
Aging Test (Stage 7)	46.43		(1)	34.50		(1)	6.78		(1)

Table A.6: Amounts of 276a, indeno[1,2,3-cd]pyrene, and dibenzanthracenes in Kenmore Square aerosol samples.

Sample	276a			indeno[1,2,3-cd]pyrene			dibenzanthracenes		
Stage 0	—			2.63	± 0.36	(3)	0.31	± 0.09	(2)
Stage 1	1.06	± 0.24	(3)	2.61	± 0.39	(3)	0.30	± 0.08	(3)
Stage 2	2.22	± 0.14	(3)	5.70	± 0.13	(3)	0.69	± 0.08	(3)
Stage 3	2.81	± 0.34	(3)	6.30	± 0.57	(3)	1.12	± 0.11	(3)
Stage 4	13.83	± 0.62	(3)	24.09	± 2.35	(3)	3.51	± 0.52	(3)
Stage 5	17.26	± 2.13	(3)	31.91	± 7.58	(3)	5.69	± 1.25	(3)
Stage 6	27.31	± 1.28	(3)	50.24	± 1.50	(3)	7.27	± 1.32	(3)
Stage 7	17.12	± 3.49	(3)	26.31	± 2.23	(3)	4.17	± 0.18	(3)
Stage 8	15.96	± 0.85	(3)	24.86	± 2.07	(3)	3.10	± 0.47	(3)
After Filter	16.15	± 1.97	(3)	24.43	± 3.98	(3)	1.76	± 0.30	(3)
Field Blank	—			0.59	± 0.07	(2)	—		
Method Blank 0	—			—			—		
Method Blank 1	—			0.57		(1)	—		
Method Blank 2	—			—			—		
Filter Blank	—			—			—		
Extraction Test	—			1.01	± 0.19	(3)	—		
Aging Test (Stage 2)	—			6.44		(1)	—		
Aging Test (Stage 7)	14.89		(1)	29.43		(1)	4.42		(1)

Table A.7: Amounts of benzo[ghi]perylene, and coronene in Kenmore Square aerosol samples.

Sample	benzo[ghi]perylene		coronene	
Stage 0	1.48	± 0.24 (3)	1.34	± 0.30 (2)
Stage 1	1.47	± 0.15 (3)	1.19	± 0.04 (3)
Stage 2	3.77	± 0.12 (3)	3.02	± 0.20 (3)
Stage 3	4.04	± 0.39 (3)	3.32	± 0.27 (3)
Stage 4	14.24	± 0.26 (3)	5.79	± 0.16 (3)
Stage 5	18.31	± 3.23 (3)	8.61	± 0.39 (3)
Stage 6	33.31	± 2.48 (3)	12.61	± 0.61 (3)
Stage 7	23.18	± 2.79 (3)	14.40	± 0.61 (3)
Stage 8	20.54	± 0.26 (3)	11.80	± 0.20 (3)
After Filter	35.74	± 7.54 (3)	32.90	± 7.42 (3)
Field Blank	0.35	± 0.03 (2)	0.43	± 0.00 (2)
Method Blank 0	—		0.95	± 0.21 (2)
Method Blank 1	—		0.82	(1)
Method Blank 2	—		3.70	± 4.27 (2)
Filter Blank	—		0.85	(1)
Extraction Test	0.55	± 0.11 (3)	1.31	± 0.03 (3)
Aging Test (Stage 2)	3.73	(1)	2.57	(1)
Aging Test (Stage 7)	21.19	(1)	13.56	(1)

Table A.8: Amounts of naphthalene, acenaphthylene, and acenaphthene in Quabbin Summit aerosol samples.

Sample	naphthalene	acenaphthylene	acenaphthene
Stage 0	33.78 ± 3.88 (2)	2.15 ± 0.12 (3)	8.34 ± 0.67 (3)
Stage 1	—	1.81 (1)	—
Stage 2	35.71 ± 0.54 (2)	—	2.21 ± 0.27 (2)
Stage 3	—	—	3.96 (1)
Stage 4	39.36 ± 1.80 (2)	—	2.16 ± 0.04 (2)
Stage 5	24.96 (1)	1.54 (1)	3.32 ± 0.06 (2)
Stage 6	29.15 (1)	—	—
Stage 7	—	—	—
Stage 8	33.07 ± 1.63 (2)	—	1.96 ± 0.03 (2)
After Filter	17.38 (1)	—	—
Field Blank	22.49 (1)	—	3.74 (1)
Method Blank 1	40.17 ± 1.02 (2)	1.79 (1)	20.05 ± 1.24 (3)
Method Blank 2	25.79 ± 0.79 (2)	2.80 ± 0.13 (3)	2.67 ± 0.02 (3)

Table A.9: Amounts of fluorene, phenanthrene, and anthracene in Quabbin Summit aerosol samples.

Sample	fluorene	phenanthrene	anthracene
Stage 0	40.54 ± 4.12 (3)	106.86 ± 2.59 (3)	11.08 ± 0.07 (3)
Stage 1	21.68 ± 2.22 (3)	40.42 (1)	1.36 (1)
Stage 2	17.33 ± 1.81 (3)	39.29 (1)	1.53 (1)
Stage 3	25.07 ± 5.10 (3)	46.37 ± 1.36 (2)	2.20 ± 0.19 (2)
Stage 4	18.46 ± 2.96 (3)	32.42 ± 0.41 (3)	1.47 ± 0.15 (3)
Stage 5	20.37 ± 3.27 (3)	39.66 ± 0.93 (3)	2.28 ± 0.11 (3)
Stage 6	11.48 ± 3.30 (3)	22.52 ± 0.41 (3)	1.17 ± 0.08 (3)
Stage 7	20.07 ± 4.37 (2)	28.71 ± 0.95 (3)	1.77 ± 0.09 (3)
Stage 8	10.78 ± 1.57 (2)	23.11 ± 0.96 (3)	1.95 ± 0.11 (2)
After Filter	—	11.18 ± 0.17 (3)	—
Field Blank	16.31 ± 3.79 (3)	28.55 ± 0.03 (2)	2.05 ± 0.02 (2)
Method Blank 1	57.56 ± 1.65 (3)	131.03 ± 3.33 (2)	10.43 ± 0.14 (2)
Method Blank 2	9.43 ± 1.22 (3)	19.98 ± 0.38 (3)	1.46 ± 0.15 (3)

Table A.10: Amounts of fluoranthene, pyrene, and benzo[ghi]fluoranthene in Quabbin Summit aerosol samples.

Sample	fluoranthene	pyrene	benzo[ghi]fluoranthene
Stage 0	51.49 ± 7.90 (3)	15.38 ± 2.06 (3)	0.78 ± 0.02 (2)
Stage 1	33.86 ± 4.07 (3)	10.41 ± 1.38 (3)	1.90 ± 0.03 (3)
Stage 2	23.31 ± 3.44 (3)	6.35 ± 1.00 (3)	1.18 ± 0.03 (3)
Stage 3	23.91 ± 1.15 (3)	6.13 ± 0.47 (3)	1.28 ± 0.02 (3)
Stage 4	24.89 ± 2.81 (3)	8.23 ± 1.65 (3)	2.33 ± 0.06 (3)
Stage 5	25.31 ± 0.90 (3)	8.11 ± 0.41 (3)	2.53 ± 0.05 (3)
Stage 6	21.65 ± 2.76 (3)	10.35 ± 1.43 (3)	2.82 ± 0.10 (3)
Stage 7	17.35 ± 1.74 (3)	6.32 ± 0.80 (3)	2.62 ± 0.10 (3)
Stage 8	16.56 ± 2.98 (3)	6.32 ± 1.13 (3)	1.100 ± 0.01 (2)
After Filter	2.67 ± 0.23 (2)	1.11 ± 0.01 (2)	—
Field Blank	7.80 ± 1.08 (3)	2.44 ± 0.44 (3)	—
Method Blank 1	34.03 ± 2.60 (3)	8.95 ± 1.08 (3)	0.63 ± 0.06 (2)
Method Blank 2	5.56 ± 0.63 (3)	2.23 ± 0.34 (3)	0.38 (1)

Table A.11: Amounts of benz[a]anthracene, chrysene/triphenylene, and benzofluoranthenes in Quabbin Summit aerosol samples.

Sample	benz[a]anthracene	chrysene/triphenylene	benzofluoranthenes
Stage 0	—	0.87 ± 0.02 (3)	1.76 ± 0.31 (2)
Stage 1	2.76 ± 0.12 (3)	7.40 ± 0.12 (3)	20.56 ± 2.97 (3)
Stage 2	0.51 ± 0.06 (2)	2.38 ± 0.04 (3)	1.76 ± 0.19 (3)
Stage 3	0.40 (1)	2.99 ± 0.01 (3)	1.94 ± 0.41 (3)
Stage 4	0.78 ± 0.04 (3)	3.90 ± 0.05 (3)	3.77 ± 0.47 (3)
Stage 5	0.71 ± 0.05 (2)	4.23 ± 0.07 (3)	3.41 ± 0.50 (3)
Stage 6	0.79 ± 0.04 (3)	4.05 ± 0.07 (3)	3.55 ± 0.40 (3)
Stage 7	0.83 (1)	3.89 ± 0.12 (3)	3.74 ± 0.15 (3)
Stage 8	0.61 ± 0.01 (2)	3.11 ± 0.17 (3)	2.18 ± 0.34 (2)
After Filter	—	—	1.63 (1)
Field Blank	—	—	0.35 (1)
Method Blank 1	—	1.01 ± 0.02 (3)	—
Method Blank 2	—	1.16 ± 0.03 (3)	—

Table A.12: Amounts of benzo[e]pyrene, benzo[a]pyrene, and perylene in Quabbin Summit aerosol samples.

Sample	benzo[e]pyrene	benzo[a]pyrene	perylene
Stage 0	0.65 ± 0.11 (2)	—	0.26 ± 0.06 (2)
Stage 1	7.13 ± 1.14 (3)	0.60 ± 0.05 (3)	0.10 (1)
Stage 2	0.69 ± 0.10 (3)	—	—
Stage 3	0.78 ± 0.13 (2)	—	—
Stage 4	1.49 ± 0.23 (3)	—	—
Stage 5	1.34 ± 0.22 (3)	—	—
Stage 6	1.42 ± 0.20 (3)	—	—
Stage 7	1.53 ± 0.10 (2)	—	—
Stage 8	0.83 ± 0.13 (2)	—	—
After Filter	0.91 (1)	—	—
Field Blank	—	—	—
Method Blank 1	—	—	—
Method Blank 2	—	—	—

Table A.13: Amounts of 276a, indeno[1,2,3-cd]pyrene, and dibenzanthracenes in Quabbin Summit aerosol samples.

Sample	276a	indeno[1,2,3-cd]pyrene	dibenzanthracenes
Stage 0	—	0.39 ± 0.03 (2)	—
Stage 1	1.30 ± 0.23 (3)	4.77 ± 0.69 (3)	0.57 ± 0.08 (3)
Stage 2	—	0.29 ± 0.00 (2)	—
Stage 3	—	0.27 (1)	—
Stage 4	—	0.67 ± 0.05 (3)	—
Stage 5	—	0.61 ± 0.14 (2)	—
Stage 6	—	0.59 ± 0.06 (3)	—
Stage 7	—	0.91 (1)	—
Stage 8	—	0.29 ± 0.00 (2)	—
After Filter	—	—	—
Field Blank	—	—	—
Method Blank 1	—	—	—
Method Blank 2	—	—	—

Table A.14: Amounts of benzo[ghi]perylene, and coronene in Quabbin Summit aerosol samples.

Sample	benzo[ghi]perylene		coronene	
Stage 0	0.16	± 0.03 (2)	—	
Stage 1	1.84	± 0.27 (3)	0.78	± 0.12 (3)
Stage 2	0.15	± 0.02 (3)	0.39	± 0.02 (3)
Stage 3	0.10	(1)	1.17	± 0.14 (3)
Stage 4	0.28	± 0.04 (3)	0.32	± 0.05 (2)
Stage 5	0.28	± 0.08 (2)	0.42	(1)
Stage 6	0.33	± 0.04 (3)	0.55	± 0.05 (3)
Stage 7	0.56	± 0.08 (2)	1.23	± 0.17 (2)
Stage 8	0.17	± 0.01 (2)	0.41	± 0.03 (2)
After Filter	0.29	(1)	0.93	(1)
Field Blank	—		0.15	(1)
Method Blank 1	0.13	(1)	0.39	(1)
Method Blank 2	—		—	

Table A.15: Amounts of 1,4-naphthoquinone, OPAH-168a, and OPAH-168b in Kenmore Square aerosol samples.

Sample	1,4-naphthoquinone			OPAH-168a			OPAH-168b		
Stage 1	52.11	± 5.43	(2)	26.91	± 10.04	(4)	7.06	± 0.65	(4)
Stage 2	33.03	± 7.12	(2)	16.42	± 8.77	(4)	76.98	± 16.08	(4)
Stage 3	92.19	± 21.40	(2)	25.31	± 7.47	(4)	228.08	± 35.13	(4)
Stage 4	47.91		(1)	13.93	± 4.21	(3)	27.10	± 3.33	(4)
Stage 5	60.53		(1)	8.52	± 4.27	(4)	41.75	± 4.62	(4)
Stage 6	56.13	± 4.64	(2)	11.05	± 2.61	(4)	25.67	± 2.92	(4)
Stage 7	41.84		(1)	10.19	± 5.13	(3)	7.68	± 0.46	(3)
Stage 8	33.96		(1)	5.80	± 2.86	(3)	10.16	± 0.60	(3)
After Filter	—			1.09		(1)	—		
Field Blank	—			8.19	± 0.20	(2)	64.100	± 6.67	(3)
Method Blank 1	74.18	± 1.100	(2)	10.35	± 5.25	(3)	—		
Method Blank 2	—			8.67	± 4.22	(4)	—		
Filter Blank	—			1.03	± 0.74	(2)	—		

Table A.16: Amounts of 1-acenaphthenone, 9-fluorenone, and 1,8-naphthalic anhydride in Kenmore Square aerosol samples.

Sample	1-acenaphthenone			9-fluorenone			1,8-naphthalic anhydride		
Stage 1	10.48	± 1.78	(4)	70.39	± 3.35	(4)	37.18	± 4.69	(4)
Stage 2	8.41	± 0.84	(3)	74.13	± 8.74	(4)	45.13	± 4.13	(4)
Stage 3	11.93	± 1.01	(3)	87.66	± 6.48	(4)	69.68	± 2.67	(2)
Stage 4	6.93	± 1.67	(2)	57.15	± 8.33	(4)	58.99	± 4.72	(4)
Stage 5	5.60	± 1.30	(3)	37.29	± 3.42	(4)	35.90	± 6.25	(4)
Stage 6	3.91	± 0.81	(3)	33.24	± 0.11	(2)	—		
Stage 7	5.74	± 0.02	(2)	38.23	± 0.43	(3)	76.31	± 10.80	(3)
Stage 8	2.95	± 0.41	(3)	23.43	± 1.83	(3)	29.12	± 1.71	(3)
After Filter	—			3.08	± 1.25	(2)	5.30		(1)
Field Blank	—			2.99	± 1.28	(2)	—		
Method Blank 1	—			7.66	± 0.09	(2)	—		
Method Blank 2	—			2.25	± 0.87	(3)	—		
Filter Blank	—			3.03	± 0.83	(2)	—		

Table A.17: Amounts of OPAH-208a, phenanthrenequinone, and OPAH-208b in Kenmore Square aerosol samples.

Sample	OPAH-208a	phenanthrenequinone	OPAH-208b
Stage 1	9.46 ± 0.98 (4)	4.72 ± 1.19 (3)	1.03 ± 0.10 (3)
Stage 2	10.86 ± 1.49 (4)	2.42 ± 0.26 (3)	—
Stage 3	16.03 ± 1.31 (4)	49.99 ± 2.14 (4)	3.26 ± 0.28 (4)
Stage 4	11.69 ± 1.65 (4)	2.61 ± 0.57 (3)	—
Stage 5	9.19 ± 1.24 (4)	2.00 ± 0.19 (3)	—
Stage 6	8.03 ± 0.45 (4)	3.49 ± 0.49 (3)	0.73 ± 0.04 (3)
Stage 7	5.86 ± 1.13 (3)	25.24 ± 5.94 (3)	3.80 ± 0.48 (3)
Stage 8	3.85 ± 0.14 (3)	1.48 ± 0.08 (3)	—
After Filter	0.32 ± 0.06 (2)	—	—
Field Blank	—	—	—
Method Blank 1	0.40 (1)	—	—
Method Blank 2	0.51 ± 0.09 (3)	—	—
Filter Blank	—	—	—

Table A.18: Amounts of 11H-benzo[a]fluoren-11-one, 7H-benzo[c]fluoren-7-one, and 11H-benzo[b]fluoren-11-one in Kenmore Square aerosol samples.

Sample	11H-benzo[a]fluoren-11-one	7H-benzo[c]fluoren-7-one	11H-benzo[b]fluoren-11-one
Stage 1	12.68 ± 1.16 (4)	4.74 ± 0.30 (3)	7.84 ± 0.73 (3)
Stage 2	17.42 ± 1.68 (4)	5.37 ± 1.18 (3)	10.50 ± 1.35 (4)
Stage 3	25.17 ± 1.16 (4)	9.04 ± 1.14 (3)	14.64 ± 1.77 (4)
Stage 4	27.13 ± 2.16 (4)	8.83 ± 1.19 (3)	21.30 ± 1.68 (4)
Stage 5	27.34 ± 3.18 (4)	9.43 ± 0.84 (3)	21.78 ± 3.12 (4)
Stage 6	33.81 ± 4.52 (4)	12.96 ± 2.77 (4)	34.57 ± 1.27 (4)
Stage 7	36.53 ± 0.39 (3)	16.35 ± 0.100 (3)	35.18 ± 4.90 (3)
Stage 8	15.85 ± 2.49 (3)	7.30 ± 1.36 (3)	15.98 ± 1.53 (3)
After Filter	2.90 (1)	1.57 (1)	3.51 (1)
Field Blank	—	—	—
Method Blank 1	0.70 (1)	—	—
Method Blank 2	—	—	—
Filter Blank	—	—	—

Table A.19: Amounts of benzanthrone, 5,12-naphthacenequinone, and OPAH-248a in Kenmore Square aerosol samples.

Sample	benzanthrone	5,12-naphthacenequinone	OPAH-248a
Stage 1	4.09 ± 0.07 (2)	—	—
Stage 2	6.36 ± 0.22 (2)	2.38 (1)	—
Stage 3	12.37 ± 1.82 (3)	8.25 ± 0.62 (2)	—
Stage 4	19.86 ± 2.33 (3)	6.99 ± 0.46 (3)	0.59 (1)
Stage 5	26.77 ± 6.53 (4)	8.20 ± 2.34 (2)	0.77 ± 0.10 (2)
Stage 6	50.75 ± 2.51 (4)	15.02 ± 2.46 (4)	2.65 ± 0.56 (2)
Stage 7	58.32 ± 7.14 (3)	19.82 ± 1.43 (2)	4.32 ± 0.32 (2)
Stage 8	48.57 ± 3.91 (3)	6.65 ± 0.98 (2)	1.83 ± 0.01 (2)
After Filter	8.40 (1)	5.55 (1)	2.63 (1)
Field Blank	—	—	—
Method Blank 1	1.70 (1)	—	—
Method Blank 2	—	—	—
Filter Blank	—	—	—

Table A.20: Amounts of OPAH-254a, 6H-benzo[cd]pyrene-6-one, and OPAH-230a in Kenmore Square aerosol samples.

Sample	OPAH-254a	6H-benzo[cd]pyrene-6-one	OPAH-230a
Stage 1	—	1.76 ± 0.03 (2)	2.20 ± 0.28 (3)
Stage 2	0.44 ± 0.04 (2)	3.61 ± 0.08 (2)	0.42 ± 0.01 (2)
Stage 3	0.54 ± 0.05 (2)	6.62 (1)	19.61 ± 2.64 (4)
Stage 4	1.12 ± 0.25 (3)	15.02 ± 0.76 (3)	—
Stage 5	1.76 ± 0.11 (2)	27.98 ± 1.04 (3)	—
Stage 6	2.70 ± 0.56 (4)	47.30 ± 2.47 (4)	—
Stage 7	4.23 ± 0.01 (2)	63.71 ± 9.95 (3)	3.53 ± 0.07 (2)
Stage 8	1.25 ± 0.51 (3)	30.77 ± 1.75 (3)	—
After Filter	1.42 (1)	61.99 ± 7.93 (2)	4.65 ± 3.00 (3)
Field Blank	—	—	—
Method Blank 1	—	—	—
Method Blank 2	—	—	1.33 ± 0.13 (2)
Filter Blank	—	—	—

Table A.21: Amounts of OPAH-272a, OPAH-280a, and benzo[a]pyrene-6,12-dione in Kenmore Square aerosol samples.

Sample	OPAH-272a		OPAH-280a		benzo[a]pyrene-6,12-dione	
Stage 1	—		—		—	
Stage 2	—		—		—	
Stage 3	—		1.71	(1)	2.83 ± 0.26	(2)
Stage 4	0.65	(1)	2.94	(1)	4.36 ± 1.41	(3)
Stage 5	0.58 ± 0.06	(2)	5.15 ± 1.42	(2)	4.91 ± 0.22	(2)
Stage 6	1.86 ± 0.08	(2)	8.67 ± 1.29	(2)	6.87 ± 0.14	(2)
Stage 7	2.78 ± 0.02	(2)	7.72 ± 0.80	(2)	5.47 ± 0.02	(2)
Stage 8	1.28 ± 0.31	(2)	2.72 ± 0.68	(2)	3.02	(1)
After Filter	3.95 ± 0.70	(2)	4.31	(1)	—	
Field Blank	—		—		—	
Method Blank 1	—		—		—	
Method Blank 2	—		—		—	
Filter Blank	—		—		—	

Table A.22: Amounts of OPAH-280b in Kenmore Square aerosol samples.

Sample	OPAH-280b	
Stage 1	—	
Stage 2	—	
Stage 3	1.85	(1)
Stage 4	8.11 ± 1.69	(2)
Stage 5	10.26 ± 1.38	(2)
Stage 6	17.76 ± 1.52	(3)
Stage 7	15.49 ± 1.66	(2)
Stage 8	5.08 ± 0.21	(2)
After Filter	6.96	(1)
Field Blank	—	
Method Blank 1	—	
Method Blank 2	—	
Filter Blank	—	

Appendix B

Tabulated Absorption Artifact

Experimental Data

The data generated from HPLC analysis of the absorption artifact experiment samples are presented here in tabular form. Data are presented in the form $\mu \pm \sigma(n)$; where μ is the mean amount of analyte in the whole sample in μg , σ is one standard deviation of the amount of analyte in the whole sample in μg , and n is the number of duplicate injections. Samples in which the analyte was not present in quantifiable amounts in any of the HPLC injections are indicated by “—”.

Table B.1: Amounts of Pyrene in Absorption Artifact Experiments.

Sample	6 h Absorption			24 h Absorption			73 h Absorption		
Stage 0	18.61	± 0.46	(3)	65.14	± 6.52	(3)	154.85	± 9.58	(3)
Stage 1	16.73	± 0.25	(3)	72.70	± 1.31	(3)	159.53	± 5.10	(3)
Stage 2	22.29	± 0.85	(3)	86.34	± 3.23	(3)	200.76	± 3.08	(3)
Stage 3	22.56	± 0.07	(3)	105.30	± 1.49	(3)	220.16	± 12.17	(3)
Stage 4	23.61	± 0.17	(3)	98.79	± 3.77	(3)	237.58	± 12.68	(3)
Stage 5	18.57	± 0.90	(3)	89.09	± 6.96	(3)	225.91	± 7.45	(3)
Stage 6	17.19	± 0.38	(3)	83.46	± 2.63	(3)	205.33	± 3.54	(3)
Stage 7	13.67	± 0.84	(3)	72.11	± 3.47	(3)	172.02	± 24.28	(3)
Stage 8	8.13	± 0.62	(3)	49.97	± 3.06	(3)	147.26	± 6.50	(3)
Blank	—			—			—		

Table B.2: Amounts of Pyrene in Recovery Test Samples.

Amount Added	Amount Quantified		
7.55	6.32 ^a	± 1.07	(3)
22.65	20.55	± 1.47	(3)
75.50	67.9	± 2.6	(3)

^aThis sample was not used in the calculation of average recovery efficiency because the amounts were near the lower limit of calibration

Table B.3: Amounts of Pyrene in Saturation Experiment Samples.

Sample	Original Solution Concentration (mg/mL)		
B	104.0	± 2.7	(3)
C	115.8	± 0.6	(3)

Table B.4: Amounts of Pyrene in Solvent Trap Experiment.

Sample	Amount Quantified		
Solvent Trap 1	8.05	± 0.98	(2)
Solvent Trap 2	—		
Solvent Trap Blank	—		

Appendix C

Absorption Artifact Model Code

The following code, *absart9.m*, integrates the absorption of PAH by mass transfer from impinging jets to impaction media. The functions *k_stagn.m*, *k_stagu.m*, *k_tran.m*, and *k_wall.m* are called to estimate local mass transfer coefficients. This code runs under Matlab 4.2, software for DEC OSF/1 by The MathWorks (Natick, MA).

```

% absart9.m
% Matlab script to calculate the amount of PAH which will
% absorb on a greased impaction plates of a cascade impactor.
% Grease used here is dibutyl phthalate (DBP).
%
% Governing equation:
%  $d\theta(r,\tau) / d\tau = \kappa * (1 - \zeta(\tau) - \theta(r,\tau))$ 
%
% BC:  $\theta(r,0) = 0$ ,  $\theta(r,\infty) = 1$ 
%
% where
%  $\theta = K C_l / C_g$ 
%   - dimensionless concentration of PAH in grease
%  $K = \text{vap\_press} * \text{MW}(\text{DBP}) / (\text{gas\_const} * T * \rho(\text{DBP}))$ 
%   - ratio of conc of PAH in gas at surfact to conc in grease
%   assumes ideal gas law, and small mole fraction PAH
%  $C_l$  - conc of PAH in grease
%  $C_g$  - conc of PAH in gas phase entering impactor
%  $r = x/R$  - dimensionless radial distance
%  $x$  - radial distance
%  $R$  - nozzle radius
%  $\tau = K * k_0 * t / \delta$  - dimensionless time
%  $t$  - elapsed time
%  $k$  - mass transfer coefficient
%  $k_0$  - mass transfer coefficient at  $r = 0$  for last stage
%  $\kappa = k / k_0$ 
%  $\delta$  - thickness of DBP film
%  $\zeta = 1 - C_b/C_g$ 
%   - dimensionless measure of gas phase denuding
%  $C_b$  - conc of PAH in bulk gas phase
%    $C_b = C_g$  ONLY on stage 0
%
% Units for variables are SI, unless otherwise noted.
%
% Solution method for  $C_l$  at a given  $r$  is Eulerian integration
% with a fixed step size. Total mass absorbed with time is the
% sum of  $C_l * dVol$  at each discrete value of  $r$ .
%
% revised absart7.m to make tau dimensionless
% JOA 15 Sep 96

clear;

% Ideal Gas Constants
R1 = 8.31451; % m3 Pa / mol K
R2 = 1.98589; % cal / mol K

% flag for denuding (0 = no, 1 = yes)
denuding = 1;

imp_type = 1;

if imp_type == 1

```

```

% -----
% * Cascade Impactor Parameters for MIT Micro-Orifice Impactor *
% -----

% stage 0 is index 1, stage 8 is index 9
num_jets = [1 10 10 20 40 80 900 2000 2000];
num_stages = length(num_jets);

% measured operating pressures (atm) for MOI
pressure = [1.0 1.0 1.0 0.9967 0.9833 0.9465 0.9014 0.8118 0.6748];

% D - diameter of orifice (m)
D = [ 1.00e-2, 3.80e-3, 2.47e-3, 1.37e-3, 7.20e-4, 4.38e-4, 1.36e-4, ...
      5.94e-5, 5.14e-5];
R = D / 2.0;

% H - nozzle to plate distance (m)
% S_W values from analogous stages in MOUDI manual
S_W = [0.75 1.0 1.0 1.0 1.0 1.5 6.4 10.6 11.1];
H = S_W .* D;

elseif imp_type == 2

% -----
% ***** Cascade Impactor Parameters for 10 stage MOUDI *****
% -----

% stage 0 is index 1, stage 8 is index 9
num_jets = [1 3 10 10 20 40 80 900 900 2000 2000];
num_stages = length(num_jets);

% measured operating pressures (atm) for MOUDI
pressure = [1.0 1.0 1.0 1.0 1.0 0.99 0.97 0.95 0.89 0.76 0.53];

% D - diameter of orifice (m)
D = [ 1.71e-2 0.889e-2 0.380e-2 0.247e-2 0.137e-2 0.072e-2, ...
      0.040e-2 0.0140e-2 0.0090e-2 0.0055e-2 0.0052e-2];
R = D / 2.0;

% H - nozzle to plate distance (m). guess for stage 0
S_W = [0.75 0.5 1.0 1.0 1.0 1.0 1.5 4.1 6.4 10.6 11.1];
H = S_W .* D;

end

% -----
% ***** PAH Properties *****
% -----

name = ['Naphthalene   ';
        'Phenanthrene  ';
        'Pyrene         ';
        'Benzo[e]pyrene'];

```

```

% Dab_1atm = diffusivity at T=25C, P=1atm m2/s from correlation of Fuller
Dab_1atm = [7.02e-6 5.97e-6 5.74e-6 5.12e-6];
% Dab proportional to 1/P (Reid, Prausnitz and Poling eq 11-3.2)
Dab = (1./pressure)' * Dab_1atm;

num_pah = length(Dab_1atm);

% -----
% ***** Experimental Conditions *****
% -----

T_op = 298;           % operating temperature (K)
Vdot = 5.0e-4 ./ pressure; % volumetric flow rate through impactor (m3/s)

% -----
% ***** Gas Properties *****
% -----

% N2
% mu - viscosity of gas at 298 K (Pa s)
mw_gas = 28;
mu = 1.77e-5;

% Air
% mw_gas = 29;
% mu = 1.80e-5;

% rho - density of gas (kg/m3)
rho = pressure * 101325 * mw_gas * 1e-3 / R1 / T_op;

% -----
% ***** Dimensionless parameters to calculate k *****
% -----

jetA = D.^2 * pi / 4;           % area of a single jet
u = Vdot ./ (jetA .* num_jets); % superficial velocity (m/hr)
Re = rho .* u .* D / mu;       % Reynolds number

Sc = mu ./ ((rho' * ones(1,num_pah)) .* Dab); % Schmidt number (stage,pah)

vol_dbp = 1.58e-8;             % volume of DBP (m3)
area_dbp = pi * (0.037)^2 / 4; % area DBP covers (m2)
delta = vol_dbp / area_dbp;    % thickness of DBP layer (m)

% r is dimensionless radial position, scaled with jet radius
rs = 1.5; % limit of stagnation region
rt = 3.0; % limit of transition region

% apportion plate area (m2)
% from uv micrographs, pyrene absorbs on the entire area of *all* stages
plate_area = (0.037)^2 * pi / 4;
rm = sqrt(plate_area ./ num_jets ./ pi) ./ R;

% limits of applicability of mass transfer correlations

```

```

for stage = 1:num_stages
    r_limit(1,stage) = min([rm(stage), rs]); % stagnation
    r_limit(2,stage) = min([rm(stage), rt]); % transition
    r_limit(3,stage) = rm(stage);          % wall jet
end

% correction for array of round nozzles (Martin, 1977)
k_corr = (1 + (H ./ (0.6 * D .* rm)).^6).^(-0.05);

% save constants
eval(sprintf('save absart9_%i_const', denuding));

% -----
% ***** Numerical Integration Parameters *****
% -----

tau_steps = 1000;
r_steps = 500;

% -----
% ***** Loop over PAH *****
% -----

for pah = 3:3

    % allocate memory
    zeta = zeros(1, tau_steps);
    zeta_out = zeros(1, tau_steps);
    theta = zeros(tau_steps, r_steps);
    theta_bar = zeros(num_stages, tau_steps);

    % -----
    % ***** Scale Time, Set Up Matrices *****
    % -----

    % tau_max is dimensionless time for complete absorption
    % characteristic time of problem is 1/kappa
    % kappa ~ 1 - 0.1
    tau_max = 50;
    dtau = tau_max / tau_steps;
    tau = 0:dtau:tau_max;

    % no denuding for input to stage 0
    zeta_out = zeros(1, tau_steps);

    % -----
    % ***** Loop over stages *****
    % -----

    for stage = 1:num_stages;

        % pressure drop at jet nozzle reduces PAH concentration
        if stage > 1
            zeta = 1 - (1 - zeta_out) * pressure(stage) / pressure(stage-1);

```

```

else
    zeta = zeta_out;
end

% -----
% ***** Calculate mass transfer coefficients for all r's *****
% -----

% divide area into dr steps
dr = rm(stage) / r_steps;
r_stag_idx = floor(r_steps * r_limit(1,stage) / rm(stage) + 0.5);
r_tran_idx = floor(r_steps * r_limit(2,stage) / rm(stage) + 0.5);
r_wall_idx = floor(r_steps * r_limit(3,stage) / rm(stage) + 0.5);
r = zeros(1,r_steps);
for r_idx = 1:r_steps
    r(r_idx) = r_idx * dr;
end

% stagnation region, uniform jet
k0 = k_stagu (0, Sc(num_stages,pah), Dab(num_stages,pah), ...
R(num_stages), Re(num_stages));

k = zeros(1,r_steps);
for r_idx = 1:r_stag_idx
    if stage == 1
        k(r_idx) = k_stagn (r(r_idx), Sc(stage,pah), Dab(stage,pah), ...
R(stage), Re(stage));
    else
        k(r_idx) = k_stagu (r(r_idx), Sc(stage,pah), Dab(stage,pah), ...
R(stage), Re(stage));
    end
end

% transition region
for r_idx = r_stag_idx+1:r_tran_idx
    k(r_idx) = k_tran (r(r_idx), Dab(stage,pah), R(stage), Re(stage));
end

% wall jet region
for r_idx = r_tran_idx+1:r_wall_idx
    k(r_idx) = k_wall (r(r_idx), Sc(stage,pah), Dab(stage,pah), ...
R(stage), Re(stage));
end

kappa = k * k_corr(stage) / k0;
k_dtau = kappa * dtau;

% -----
% ***** Integrate amount absorbed with time *****
% -----

% Boundary Condition - theta = 0 at t = 0
theta = zeros(tau_steps, r_steps);

```



```

if denuding == 0
    zeta_coeff = 0;
else
    zeta_coeff = 2 * pi * k0 * num_jets(stage) * R(stage)^2 ...
                / (Vdot(stage) * dtau);
end

% Euler's method
for tau_idx = 2:tau_steps
    dtheta = k_dtau .* (1 - zeta(tau_idx-1) - theta(tau_idx-1,:));
    theta(tau_idx,:) = theta(tau_idx-1,:) + dtheta;

    % calculate gas phase denuding
    sum_r_dtheta = sum(r .* dtheta) * dr;
    theta_bar(stage, tau_idx) = theta_bar(stage, tau_idx - 1) + ...
        2 * sum_r_dtheta / rm(stage)^2;
    zeta_out(tau_idx) = zeta(tau_idx-1) + zeta_coeff * sum_r_dtheta;
end

% -----
% ***** Adjust Time Steps *****
% -----

% truncate extra time steps from early stages
zeta = zeta(1:(tau_steps - num_stages + stage));
zeta_out = zeta_out(2:tau_steps);
theta = theta(1:(tau_steps - num_stages + stage),:);
tau = tau(1:(tau_steps - num_stages + stage));
tau_steps = tau_steps - 1;

% -----
% ***** Write Results to File *****
% -----

words = sprintf('save absart9_%i_p%i_s%i', denuding, pah, stage-1);
eval(words);

sprintf('absart9: done PAH %i, stage %i', pah, stage-1)

end % stage

% -----
% ***** Write Summary of Results to File *****
% -----

theta_bar = theta_bar(:,1:tau_steps+1);
eval(sprintf('save absart9_%i_p%i_sum theta_bar tau k0', denuding, pah));

end % PAH

return;

```

```

function k = k_stagn(r, Sc, Dab, R, Re)
% K_STAGN mass transfer coefficient for stagnation region of impinging jet.
% Uses correlation for non-uniform jets from Scholtz and Trass (1970).
% r - dimensionless position from center of jet.
% Sc - Schmidt number.
% Dab - Gas phase diffusivity.
% R - jet radius.
% Re - Reynolds number.
% JOA 20 Dec 94

```

```

k = (0.8242 * Sc^0.361 ...
- 1.351e-1 * Sc^0.368 * r.^2 ...
- 9.850e-3 * Sc^0.408 * r.^4 ...
+ 1.171e-3 * Sc^0.424 * r.^6 ...
+ 2.856e-4 * Sc^0.433 * r.^8 ...
+ 2.458e-6 * Sc^0.439 * r.^10 ...
- 6.352e-7 * Sc^0.442 * r.^12)' ...
* (Dab ./ R .* sqrt(Re));

```

```

function k = k_stagu(r, Sc, Dab, R, Re)
% K_STAGU mass transfer coefficient for stagnation region of impinging jet.
% Uses correlation for uniform jets from Scholtz and Trass (1970).
% r - dimensionless position from center of jet.
% Sc - Schmidt number.
% Dab - Gas phase diffusivity.
% R - jet radius.
% Re - Reynolds number.
% JOA 20 Dec 94

```

```

k = (0.3634 * Sc^0.361 ...
+ 0.03441 * Sc^0.386 * r.^2 ...
- 2.531e-3 * Sc^0.408 * r.^4 ...
- 1.741e-3 * Sc^0.424 * r.^6)' ...
* (Dab ./ R .* sqrt(Re));

```

```

function k = k_tran(r, Dab, R, Re)
% K_TRAN mass transfer coefficient for transition region of impinging jet.
% Uses correlation for non-uniform jets from Scholtz and Trass (1970).
% r - dimensionless position from center of jet.
% Sc - Schmidt number.
% Dab - Gas phase diffusivity.
% R - jet radius.
% Re - Reynolds number.
% JOA 20 Dec 94

```

```

k = (r.^(-0.86))' * (0.95 .* Dab .* sqrt(Re) ./ R);

```

```

function k = k_wall(r, Sc, Dab, R, Re)
% K_WALL mass transfer coefficient for wall jet region of impinging jet.
% Uses correlation for non-uniform jets from Scholtz and Trass (1970).
% r - dimensionless position from center of jet.
% Sc - Schmidt number.
% Dab - Gas phase diffusivity.
% R - jet radius.
% Re - Reynolds number.
% JOA 20 Dec 94

```

```

g0 = gamma(Sc+1/3)/gamma(Sc)/gamma(1/3);

```

```

k = (r.^(-1.25))' * (0.5071 .* g0 .* Re.^0.75 .* Dab ./ R);

```


Appendix D

PAH Physical Properties

D.1 Introduction

The physical properties of polycyclic aromatic hydrocarbons (PAH) determine to a large extent their fate in the atmosphere. Of particular importance to this work are the vapor pressures, solubilities and gas phase diffusivities of PAH. A review of the literature on PAH physical properties finds sometimes sparse or contradictory experimental data for these properties. This appendix attempts to compile a set of consistent physical and thermodynamic property data for PAH at atmospheric conditions ($P = 1 \text{ atm}$, $T = -5\text{--}35^\circ\text{C}$). Experimental data will be used when available. Otherwise experimental data will be extrapolated to the conditions of interest; where no reliable experimental data are available, empirical correlations will be used.

The sections of this appendix each cover a physical or thermodynamic property, beginning with simple properties and progressing onto properties which require more complex calculations. The PAH of interest are listed with their molecular structures

in Table 1.1.

D.2 Boiling Point

White compiled experimental boiling point data and predicted boiling points based on GC retention indices for PAH with molecular weights up to 278 [161]. The retention indices were taken from gas chromatography work done by Lee et al. [110]. The retention indices were calculated for a large number of PAH from GC retention time data so that the retention indices of naphthalene, phenanthrene, chrysene and picene are 200, 300, 400 and 500, respectively. For example, PAH which elute between naphthalene and phenanthrene are assigned retention indices, RI , as

$$RI = 200 + 100 * \frac{RT(\text{PAH}) - RT(\text{naphthalene})}{RT(\text{phenanthrene}) - RT(\text{naphthalene})} \quad (\text{D.1})$$

where RT are retention times. Using a similar linear temperature program described in Section 2.3, we have observed PAH retention times consistent with Lee's retention indices.

The definition of the retention index forces the ratio of retention time to retention index to vary over the range of PAH. For example, a unit retention index corresponds to 0.122 minutes between naphthalene and phenanthrene; but 0.089 minutes between chrysene and picene. Additionally, Lee's retention index data do not include PAH with molecular weights greater than 278. Therefore, we have used our own retention time data to develop a linear correlation similar to that used by White.

Table D.1: Experimental and Estimated Values of PAH Boiling Points.

PAH	T_b (°C)		
	Experimental	This Work	White ^a
Naphthalene	218	211	223
Acenaphthylene	270	272	275
Acenaphthene	279	279	281
Fluorene	294	299	298
Phenanthrene	338	336	330
Anthracene	340	338	332
Fluoranthene	383	386	378
Pyrene	393	393	386
Benzo[<i>ghi</i>]fluoranthene	432	432	427
Benzo[<i>c</i>]phenanthrene	427	431	427
Cyclopenta[<i>cd</i>]pyrene	—	438	434
Benz[<i>a</i>]anthracene	435	440	435
Chrysene	441	442	437
Triphenylene	—	440	437
Benzo[<i>b</i>]fluoranthene	481	480	483
Benzo[<i>j</i>]fluoranthene	480	479	483
Benzo[<i>k</i>]fluoranthene	481	481	484
Benzo[<i>e</i>]pyrene	493	489	493
Benzo[<i>a</i>]pyrene	496	490	495
Perylene	—	493	498
Indeno[1,2,3- <i>cd</i>]pyrene	—	525	537
Dibenz[<i>a,c</i>]anthracene	—	526	538
Dibenz[<i>a,h</i>]anthracene	—	527	538
Benzo[<i>b</i>]chrysene	—	529	541
Picene	—	529	543
Benzo[<i>ghi</i>]perylene	—	532	545
Dibenzo[<i>b,k</i>]fluoranthene	—	564	585
Dibenzo[<i>a,l</i>]pyrene	—	565	585
Coronene	—	576	597
Dibenzo[<i>a,i</i>]pyrene	—	580	604

^aReference [161]

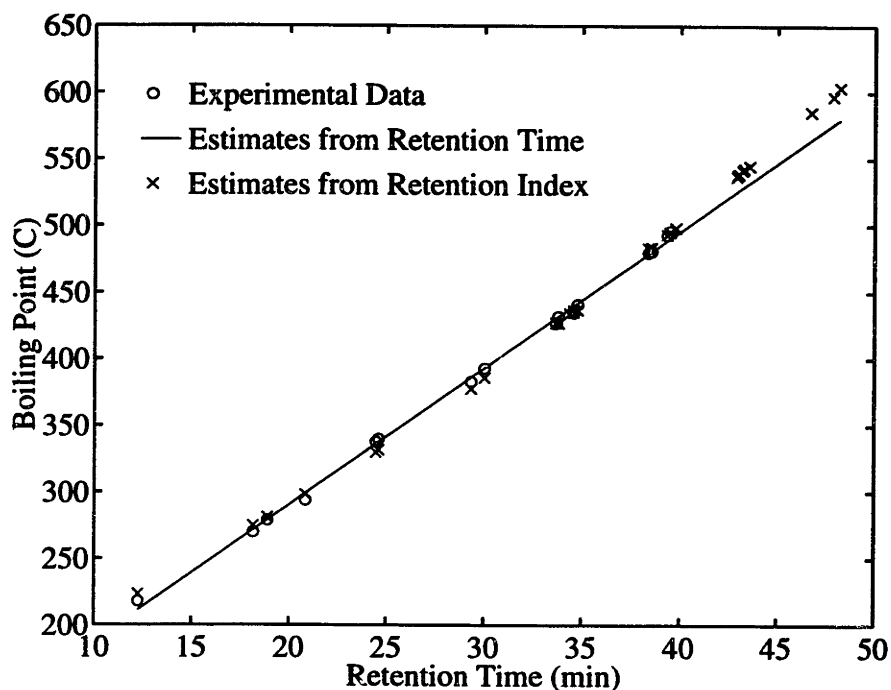


Figure D-1: Linear fit of boiling point with retention time.

A least squares linear fit of boiling points to retention times yields the relation

$$T_b (\text{°C}) = 86.6 + 10.24 RT (\text{min}) \quad (\text{D.2})$$

Figure D-1 shows this correlation with experimental data and White's calculated values. Table D.1 lists the data used to generate this figure. The boiling points calculated using retention times and retention indices are similar up to dibenz[*a,h*]anthracene. For higher molecular weight PAH, the boiling points predicted from retention time data are significantly lower than the prediction based on retention index. Because the retention indices are not uniformly scaled with GC temperature, the predictions based on retention times should be more reliable.

D.3 Critical Properties

The method of Joback was used to estimate critical temperatures, pressures and volumes for PAH [128]. The relations are

$$T_c = \frac{T_b}{0.584 + 0.965 \Sigma\Delta_T - (\Sigma\Delta_T)^2} \quad (\text{D.3})$$

$$P_c = (0.113 + 0.0032 n_A - \Sigma\Delta_P)^{-2} \quad (\text{D.4})$$

$$V_c = 17.5 + \Sigma\Delta_V \quad (\text{D.5})$$

where

T_c	critical temperature (K)
T_b	boiling point (K)
$\Sigma\Delta_T$	sum of group contributions for temperature
P_c	critical pressure (bar)
n_A	number of atoms in the molecule
$\Sigma\Delta_P$	sum of group contributions for pressure
V_c	critical volume (cm ³ /gmol)
$\Sigma\Delta_V$	sum of group contributions for volume

Reid et al. recommend using this method and expect errors in the range 5–10%. Comparison of estimated and published values for the critical properties of naphthalene, anthracene and phenanthrene show that the estimated values are within 3% of the published values.

Table D.2: Estimated Values for PAH Critical Properties and Lennard—Jones Parameters.

PAH	T_c (K)	P_c (bar)	V_c (cm ³ /gmol)	ϵ/k (K)	σ (Å)
Naphthalene	727	38.97	409.50	560	6.25
Acenaphthylene	793	36.73	473.50	610	6.55
Acenaphthene	800	35.18	487.50	616	6.62
Fluorene	824	33.76	521.50	635	6.77
Phenanthrene	872	32.43	555.50	671	6.91
Anthracene	874	32.43	555.50	673	6.91
Fluoranthene	919	30.73	619.50	707	7.17
Pyrene	928	30.73	619.50	715	7.17
Benzo[ghi]fluoranthene	959	29.16	683.50	739	7.41
Benzo[c]phenanthrene	967	27.41	701.50	745	7.47
Cyclopenta[cd]pyrene	967	29.16	683.50	745	7.41
Benz[a]anthracene	980	27.41	701.50	754	7.47
Chrysene	983	27.41	701.50	757	7.47
Triphenylene	980	27.41	701.50	754	7.47
Benzo[b]fluoranthene	1012	26.08	765.50	779	7.69
Benzo[j]fluoranthene	1011	26.08	765.50	778	7.69
Benzo[k]fluoranthene	1013	26.08	765.50	780	7.69
Benzo[e]pyrene	1024	26.08	765.50	789	7.69
Benzo[a]pyrene	1026	26.08	765.50	790	7.69
Perylene	1030	26.08	765.50	793	7.69
Indeno[1,2,3-cd]pyrene	1053	24.85	829.50	811	7.90
Dibenz[a,c]anthracene	1061	23.47	847.50	817	7.96
Dibenz[a,h]anthracene	1063	23.47	847.50	818	7.96
Benzo[b]chrysene	1065	23.47	847.50	820	7.96
Picene	1066	23.47	847.50	821	7.96
Benzo[ghi]perylene	1062	24.85	829.50	817	7.90
Dibenzo[b,k]fluoranthene	1093	22.42	911.50	842	8.15
Dibenzo[a,l]pyrene	1093	22.42	911.50	842	8.15
Coronene	1101	23.70	893.50	848	8.10
Dibenzo[a,i]pyrene	1113	22.42	911.50	857	8.15

Table D.3: Literature Values for PAH Critical Properties [128].

PAH	T_c (K)	P_c (bar)	V_c (cm ³ /gmol)
Naphthalene	748.4	40.5	413
Anthracene	869.3		554
Phenanthrene	873.0		554

Table D.4: Joback Group Contributions for Critical Properties [128].

Group	Δ_T	Δ_P	Δ_V
Ring $-CH_2-$	0.0100	0.0025	48
Ring $=CH-$	0.0082	0.0011	41
Ring $=C<$	0.0143	0.0008	32

D.4 Lennard-Jones Parameters

Parameters for the Lennard-Jones 6-12 potential are listed in Table D.2. These were estimated from critical properties as [143]

$$\epsilon/k = 0.77 T_c \quad (\text{D.6})$$

$$\sigma = 0.841 V_c^{1/3} \quad (\text{D.7})$$

D.5 Diffusivity in Air

Fuller et al. developed an empirical correlation to predict gas phase diffusivities at atmospheric pressure as follows [162]

$$D_{AB} = \frac{0.00143 T^{1.75}}{P M_{AB}^{1/2} [(\Sigma_v)_A^{1/3} + (\Sigma_v)_B^{1/3}]^2} \quad (\text{D.8})$$

where

D_{AB} binary diffusion coefficient (cm²/s)

T temperature (K)

P pressure (bar)

M_{AB} $2/(1/M_A + 1/M_B)$

M_i molecular weight of species i (g/gmol)

Σ_v sum of atomic diffusion volumes

For PAH the relevant atomic diffusion volumes are 15.9 for C, 2.31 for H and -18.3 for aromatic rings. Table D.5 shows diffusivities for PAH estimated by this method. This method is recommended because it produces the smallest average error, typically within 5%, among empirical correlations [128]. However, when compared with the experimental data for naphthalene ($D_{AB} = 0.086 \text{ cm}^2/\text{s}$) this method underestimates D_{AB} by 17% [163]. This method's inability to estimate accurately D_{AB} for PAH stems from a lack of experimental data for PAH and an assumption that colliding molecules behave as spheres.

In an attempt to predict better the diffusivities of PAH, the method of Fuller et al. was revised by changing the volume contribution of coplanar aromatic rings to match the experimental diffusivity of naphthalene. The calculated volume contribution of coplanar aromatic rings is -41.6. The revised method yields a reasonable diffusivity for benzene at STP, $0.1014 \text{ cm}^2/\text{s}$. This value compares well with experimental data, $0.0962 \text{ cm}^2/\text{s}$, and the prediction from the method of Fuller et al., $0.0899 \text{ cm}^2/\text{s}$ [162]. The diffusivity of coronene was calculated assuming 6 coplanar aromatic rings.

The 1925 results of Mack are widely cited values for PAH diffusivities [164]. Mack reported diffusivities for naphthalene and anthracene as 0.0611 and $0.0783 \text{ cm}^2/\text{s}$, respectively. Calculations of diffusivities of naphthalene and anthracene using Mack's mass loss data and modern sublimation pressure data yield diffusivities of 0.0786 and $0.2004 \text{ cm}^2/\text{s}$ at STP, respectively. This experimental value for naphthalene is similar to that obtained by Caldwell [163]. Contrary to theory and empirical correlations, the diffusivity of anthracene calculated from Mack's data is higher than that for naphthalene; therefore this value was not used.

Table D.5: Gas Phase Diffusivities for PAH Estimated by the Method of Fuller et al. and a Revised Method [162].

PAH	D_{AB} (cm ² /s)	
	Fuller et al.	Revised Method
Naphthalene	0.0702	0.0834
Acenaphthylene	0.0632	0.0726
Acenaphthene	0.0624	0.0714
Fluorene	0.0597	0.0675
Phenanthrene	0.0597	0.0731
Anthracene	0.0597	0.0731
Fluoranthene	0.0552	0.0654
Pyrene	0.0574	0.0752
Benzo[ghi]fluoranthene	0.0534	0.0669
Benzo[c]phenanthrene	0.0528	0.0660
Cyclopenta[cd]pyrene	0.0534	0.0669
Benz[a]anthracene	0.0528	0.0660
Chrysene	0.0528	0.0660
Triphenylene	0.0528	0.0660
Benzo[b]fluoranthene	0.0496	0.0601
Benzo[j]fluoranthene	0.0496	0.0601
Benzo[k]fluoranthene	0.0496	0.0601
Benzo[e]pyrene	0.0512	0.0676
Benzo[a]pyrene	0.0512	0.0676
Perylene	0.0512	0.0676
Indeno[1,2,3-cd]pyrene	0.0483	0.0614
Dibenz[a,c]anthracene	0.0479	0.0607
Dibenz[a,h]anthracene	0.0479	0.0607
Benzo[b]chrysene	0.0479	0.0607
Picene	0.0479	0.0607
Benzo[ghi]perylene	0.0483	0.0614
Dibenzo[b,k]fluoranthene	0.0454	0.0560
Dibenzo[a,l]pyrene	0.0467	0.0620
Coronene	0.0470	0.0628
Dibenzo[a,i]pyrene	0.0467	0.0620

Without reasonable data on the diffusivities of higher molecular weight PAH one cannot reasonably decide between the methods of Fuller et al. or the revised method presented here. Turpin and coworkers found PAH diffusivities equal to the values predicted by Fuller's method within the error of their measurements [129]. Because of its wide acceptance, gas phase diffusivities estimated from Fuller's method are used in this work.

D.6 Melting Behavior

Melting points and enthalpies of fusion are available for many PAH [165, 166, 167, 168, 169, 170]. At the melting point, T_m , the entropy of fusion, ΔS_{fus} , can be calculated from the experimentally measured enthalpy of fusion, ΔH_{fus} , as

$$\Delta S_{fus} = \frac{\Delta H_{fus}}{T_m} \quad (\text{D.9})$$

Measured values for T_m , ΔH_{fus} , and ΔS_{fus} are given in Table D.6. For PAH without T_m data, the method of Joback was used to estimate T_m [128]. Estimates made using this method differed from the experimental values by as much as 100 K; these estimates should therefore be used with caution. Values for ΔS_{fus} range from 31.3 to 60.0 (J/gmol K); there appears to be no general trend in ΔS_{fus} values with PAH structure or molecular weight. An average value for ΔS_{fus} of 50.0 (J/gmol K) was used for PAH without experimental data.

Table D.6: Thermodynamic Properties for PAH Melting.

PAH	T_m (K)	ΔH_{fus} (kJ/gmol)	ΔS_{fus} (J/gmol K)	Reference ^a
Naphthalene	353.45	18.99	53.73	1
Acenaphthylene	335.12	—	50.00	*
Acenaphthene	366.55	21.46	58.55	4
Fluorene	387.95	19.58	50.46	4
Phenanthrene	372.37	16.46	44.21	4
Anthracene	488.97	29.39	60.11	2
Fluoranthene	383.35	18.74	48.90	3
Pyrene	423.81	17.37	40.98	3
Benzo[ghi]fluoranthene	499.46	—	50.00	*
Benzo[c]phenanthrene	334.65	16.31	48.75	6
Cyclopenta[cd]pyrene	499.46	—	50.00	*
Benz[a]anthracene	434.25	21.38	49.23	6
Chrysene	531.35	26.15	49.22	6
Triphenylene	471.01	24.76	52.57	3
Benzo[b]fluoranthene	515.72	—	50.00	*
Benzo[j]fluoranthene	515.72	—	50.00	*
Benzo[k]fluoranthene	515.72	—	50.00	*
Benzo[e]pyrene	454.15	17.32	38.15	6
Benzo[a]pyrene	454.35	16.56	36.46	6
Perylene	550.93	31.89	57.89	5
Indeno[1,2,3-cd]pyrene	589.76	—	50.00	*
Dibenz[a,c]anthracene	531.98	—	50.00	*
Dibenz[a,h]anthracene	544.15	31.16	57.27	6
Benzo[b]chrysene	531.98	—	50.00	*
Picene	531.98	—	50.00	*
Benzo[ghi]perylene	554.15	17.37	31.34	6
Dibenzo[b,k]fluoranthene	606.02	—	50.00	*
Dibenzo[a,l]pyrene	606.02	—	50.00	*
Coronene	710.45	19.20	27.03	6
Dibenzo[a,i]pyrene	606.02	—	50.00	*

^a1 - McCullough et al. (1957), 2 - Goursot et al. (1970), 3 - Wong and Westrum (1971), 4 - Finke et al. (1977), 5 - Wong and Westrum (1980), 6 - Lide, ed. (1995), * - Estimated (see text).

D.7 Heat Capacity

Joback describes a group contribution method to estimate the ideal gas heat capacity, $C_{p,G}$, as a third order polynomial in T [128]. Table D.7 lists the polynomial coefficients and heat capacities calculated for 298 K. Values for $C_{p,G}$ calculated at 298 K by this method agree within 2% of calculations made for phenanthrene and anthracene from spectroscopic data [171].

Measurements of $C_{sat,S}$, the energy required to effect a temperature change in the solid while maintaining equilibrium with a saturated vapor, have been made for a number of PAH [166, 167, 169, 168]. As shown in Figure D-2 for a typical PAH, $C_{sat,S}$ is nearly a linear function of temperature from 250 K up to the onset of melting and can be expressed as

$$C_{sat,S} = \alpha_S + \beta_S T \quad (\text{D.10})$$

Best fit values for α_S and β_S are given in Table D.8 for these PAH. Phenanthrene exhibits a phase transition at 347 K and is the only exception to the linear dependence of $C_{sat,S}$ with T in the range 298 K to T_m . For the low reduced temperatures of interest here, $C_p \approx C_{sat}$ [128].

PAH without experimental $C_{sat,S}$ data are assumed to also exhibit a similar linear dependence of $C_{sat,S}$ on T . The experimental values for β_S are all in the range 0.784–1.006; for PAH without experimental $C_{sat,S}$ data, the average value of β_S , 0.930, is used. $C_{sat,S}$ at 298 K appears to be a linear function of molecular weight, M , within the family of PAH (see Figure D-3). $C_{sat,S}$ (298 K) for PAH without experimental

Table D.7: Ideal Gas Heat Capacities for PAH.

PAH	$C_{p,G}$ (298 K) J/gmol K	$C_{p,G}$ (J/gmol K) = $a + bT + cT^2 + dT^3$			
		a	b	c	d
Naphthalene	132.63	-71.55	0.8712	-6.88×10^{-4}	2.14×10^{-7}
Acenaphthylene	154.70	-88.05	1.0732	-9.72×10^{-4}	3.50×10^{-7}
Acenaphthene	162.36	-95.83	1.1292	-9.85×10^{-4}	3.46×10^{-7}
Fluorene	172.93	-94.08	1.1586	-9.80×10^{-4}	3.32×10^{-7}
Phenanthrene	183.50	-92.33	1.1880	-9.75×10^{-4}	3.18×10^{-7}
Anthracene	183.50	-92.33	1.1880	-9.75×10^{-4}	3.18×10^{-7}
Fluoranthene	205.56	-108.83	1.3900	-1.26×10^{-3}	4.54×10^{-7}
Pyrene	205.56	-108.83	1.3900	-1.26×10^{-3}	4.54×10^{-7}
Benzo[ghi]fluoranthene	227.62	-125.33	1.5920	-1.54×10^{-3}	5.89×10^{-7}
Benzo[c]phenanthrene	234.36	-113.11	1.5048	-1.26×10^{-3}	4.22×10^{-7}
Cyclopenta[cd]pyrene	227.62	-125.33	1.5920	-1.54×10^{-3}	5.89×10^{-7}
Benz[a]anthracene	234.36	-113.11	1.5048	-1.26×10^{-3}	4.22×10^{-7}
Chrysene	234.36	-113.11	1.5048	-1.26×10^{-3}	4.22×10^{-7}
Triphenylene	234.36	-113.11	1.5048	-1.26×10^{-3}	4.22×10^{-7}
Benzo[b]fluoranthene	256.42	-129.61	1.7068	-1.55×10^{-3}	5.58×10^{-7}
Benzo[j]fluoranthene	256.42	-129.61	1.7068	-1.55×10^{-3}	5.58×10^{-7}
Benzo[k]fluoranthene	256.42	-129.61	1.7068	-1.55×10^{-3}	5.58×10^{-7}
Benzo[e]pyrene	256.42	-129.61	1.7068	-1.55×10^{-3}	5.58×10^{-7}
Benzo[a]pyrene	256.42	-129.61	1.7068	-1.55×10^{-3}	5.58×10^{-7}
Perylene	256.42	-129.61	1.7068	-1.55×10^{-3}	5.58×10^{-7}
Indeno[1,2,3-cd]pyrene	278.49	-146.11	1.9088	-1.83×10^{-3}	6.93×10^{-7}
Dibenz[a,c]anthracene	285.22	-133.89	1.8216	-1.55×10^{-3}	5.26×10^{-7}
Dibenz[a,h]anthracene	285.22	-133.89	1.8216	-1.55×10^{-3}	5.26×10^{-7}
Benzo[b]chrysene	285.22	-133.89	1.8216	-1.55×10^{-3}	5.26×10^{-7}
Picene	285.22	-133.89	1.8216	-1.55×10^{-3}	5.26×10^{-7}
Benzo[ghi]perylene	278.49	-146.11	1.9088	-1.83×10^{-3}	6.93×10^{-7}
Dibenzo[b,k]fluoranthene	307.28	-150.39	2.0236	-1.83×10^{-3}	6.61×10^{-7}
Dibenzo[a,l]pyrene	307.28	-150.39	2.0236	-1.83×10^{-3}	6.61×10^{-7}
Coronene	300.55	-162.61	2.1108	-2.11×10^{-3}	8.29×10^{-7}
Dibenzo[a,i]pyrene	307.28	-150.39	2.0236	-1.83×10^{-3}	6.61×10^{-7}

Table D.8: Solid Heat Capacities of PAH (C_{sat} (J/gmol K) = $\alpha + \beta T$ (K)).

PAH	$C_{sat,S}$ (298 K) J/mol K	α_S	β_S	Reference ^a
Naphthalene	164.03	-69.30	0.783	1
Acenaphthylene	188.78	-88.36	0.930	*
Acenaphthene	187.53	-106.00	0.985	4
Fluorene	201.19	-98.60	1.006	4
Phenanthrene	221.75	-113.50 ^b	1.125	4
Anthracene	209.23	-24.40	0.784	2
Fluoranthene	230.20	-22.50	0.848	3
Pyrene	228.86	-60.20	0.970	3
Benzo[ghi]fluoranthene	253.05	-24.09	0.930	*
Benzo[c]phenanthrene	254.78	-22.36	0.930	*
Cyclopenta[cd]pyrene	253.05	-24.09	0.930	*
Benz[a]anthracene	254.78	-22.36	0.930	*
Chrysene	254.78	-22.36	0.930	*
Triphenylene	262.13	13.60	0.834	3
Benzo[b]fluoranthene	275.62	-1.52	0.930	*
Benzo[j]fluoranthene	275.62	-1.52	0.930	*
Benzo[k]fluoranthene	275.62	-1.52	0.930	*
Benzo[e]pyrene	275.62	-1.52	0.930	*
Benzo[a]pyrene	275.62	-1.52	0.930	*
Perylene	276.94	14.70	0.880	5
Indeno[1,2,3-cd]pyrene	296.47	19.33	0.930	*
Dibenz[a,c]anthracene	298.20	21.06	0.930	*
Dibenz[a,h]anthracene	298.20	21.06	0.930	*
Benzo[b]chrysene	298.20	21.06	0.930	*
Picene	298.20	21.06	0.930	*
Benzo[ghi]perylene	296.47	19.33	0.930	*
Dibenzo[b,k]fluoranthene	319.04	41.90	0.930	*
Dibenzo[a,l]pyrene	319.04	41.90	0.930	*
Coronene	312.38	-62.80	1.259	5
Dibenzo[a,i]pyrene	319.04	41.90	0.930	*

^a1 - McCullough et al. (1957), 2 - Goursot, Girdhar and Westrum (1970), 3 - Wong and Westrum (1971), 4 - Finke et al. (1977), 5 - Wong and Westrum (1980), * - Estimated (see text).

^bValid for 270–330 K.

Table D.9: Liquid Heat Capacities of PAH (C_{sat} (J/gmol K) = $\alpha + \beta T$ (K)).

PAH	$C_{sat,L}$ (298 K) J/mol K	α_L	β_L	Reference ^a
Naphthalene	196.75	85.0	0.3750	1
Acenaphthylene	236.43	145.6	0.3048	*
Acenaphthene	230.46	90.7	0.4690	4
Fluorene	250.94	107.3	0.4820	4
Phenanthrene	260.14	102.2	0.5300	4
Anthracene	273.37	134.2	0.4670	2
Fluoranthene	278.31	85.8	0.6460	3
Pyrene	277.87	109.8	0.5640	3
Benzo[ghi]fluoranthene	334.54	221.0	0.3810	*
Benzo[c]phenanthrene	354.65	218.4	0.4572	*
Cyclopenta[cd]pyrene	334.54	221.0	0.3810	*
Benz[a]anthracene	354.65	218.4	0.4572	*
Chrysene	354.65	218.4	0.4572	*
Triphenylene	340.86	171.6	0.5680	3
Benzo[b]fluoranthene	380.65	244.4	0.4572	*
Benzo[j]fluoranthene	380.65	244.4	0.4572	*
Benzo[k]fluoranthene	380.65	244.4	0.4572	*
Benzo[e]pyrene	380.65	244.4	0.4572	*
Benzo[a]pyrene	380.65	244.4	0.4572	*
Perylene	373.20	208.7	0.5520	5
Indeno[1,2,3-cd]pyrene	406.65	270.4	0.4572	*
Dibenz[a,c]anthracene	426.75	267.8	0.5334	*
Dibenz[a,h]anthracene	426.75	267.8	0.5334	*
Benzo[b]chrysene	426.75	267.8	0.5334	*
Picene	426.75	267.8	0.5334	*
Benzo[ghi]perylene	406.65	270.4	0.4572	*
Dibenzo[b,k]fluoranthene	452.75	293.8	0.5334	*
Dibenzo[a,l]pyrene	452.75	293.8	0.5334	*
Coronene	432.65	296.4	0.4572	*
Dibenzo[a,i]pyrene	452.75	293.8	0.5334	*

^a1 - McCullough et al. (1957), 2 - Goursot, Girdhar and Westrum (1970), 3 - Wong and Westrum (1971), 4 - Finke et al. (1977), 5 - Wong and Westrum (1980), * - Estimated (see text).

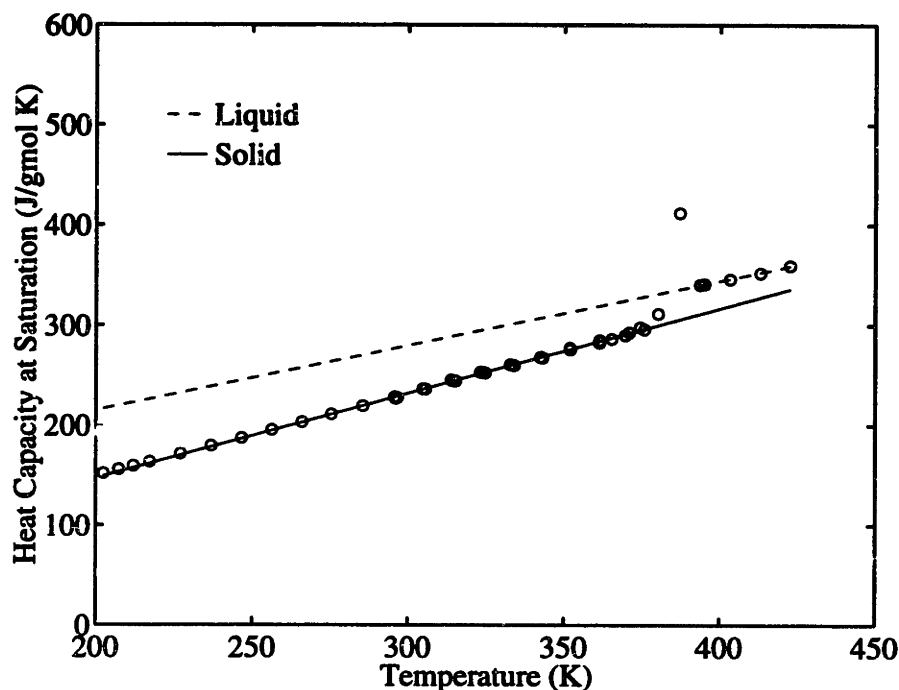


Figure D-2: Heat capacity at saturated conditions for solid and liquid fluoranthene [167].

$C_{sat,S}$ data was estimated as

$$C_{sat,S}(298K) \text{ (J/gmol K)} = 57 + 0.87 M \quad (\text{D.11})$$

Values of α_S for these PAH was calculated using these estimates of $C_{sat,S}$ (298 K).

Experimentally measured $C_{sat,L}(T)$, the energy required to effect a temperature change in a liquid while maintaining equilibrium with a saturated vapor, are also nearly linear functions of temperature from the melting point up to the highest temperatures studied (see Figure D-2). $C_{sat,L}(T)$ can be expressed as

$$C_{sat,L} = \alpha_L + \beta_L T \quad (\text{D.12})$$

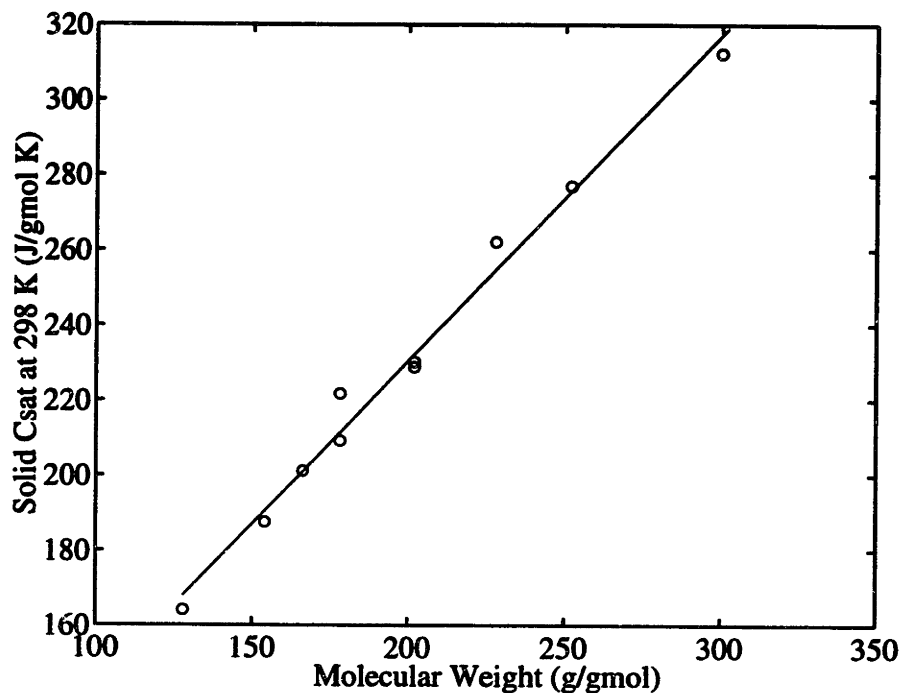


Figure D-3: Solid heat capacities, $C_{sat,S}$, of PAH at $T = 298$ K [166, 167, 169, 168, 170].

Best fit values for α_L and β_L are given in Table D.9. For PAH without experimental data, the group contribution technique of Durupt et al., which also expresses $C_{sat,L}$ as a linear function of temperature, was used to estimate α_L and β_L [172].

D.8 Sublimation Pressure

The sublimation pressures, p_S , of many PAH have been measured [173, 113, 121, 114]; these and other measurements have been compiled [20]. Selected data are collected in Table D.10 in the form

$$\log[p_S \text{ (Pa)}] = \frac{-A}{T} + B \quad (\text{D.13})$$

Where more than one sublimation pressure measurement was available in the literature, the measurement made nearest ambient temperature was selected. Purported sublimation pressure data collected from GC retention times were not considered since this technique measures the association of a species with the column material, not crystalline PAH. The failure of this technique is apparent in the case of phenanthrene and anthracene which have similar retention times but sublimation pressures which differ by a factor of 20.

Measurements made at temperatures significantly greater than ambient, must be corrected to ambient temperature (298 K). The empirical constants A and B can be related to thermodynamic properties as [114]

$$A = \frac{\Delta H_{sub}}{R \ln 10} \quad (\text{D.14})$$

$$B = \frac{\Delta S_{sub}}{R \ln 10} \quad (\text{D.15})$$

The constants A and B are generated by a least squares fit of p_S versus $1/T$, therefore the relevant average experimental temperature, T_{exp} , is the mean of the inverse experimental temperatures. Table D.10 lists experimental sublimation pressure correlations and p_S directly extrapolated to 298 K.

More accurate calculations of sublimation pressure at ambient temperature can be made by applying heat capacity corrections to the experimental data. ΔH_{sub} can

Table D.10: Sublimation Pressure Correlations for PAH at Experimental Temperatures ($\log[p_S \text{ (Pa)}] = -A/T + B$).

PAH	A (K)	B	ΔH_{sub} (kJ/gmol)	ΔS_{sub} (J/gmol K)	$\log p_S$ (Pa) (298 K)	Reference ^a
Naphthalene	3960	14.30	75.81	273.75	1.01	1
Acenaphthylene	3822	12.77	73.16	244.44	-0.06	1
Acenaphthene	4535	14.67	86.83	280.84	-0.55	1
Fluorene	4616	14.38	88.37	275.40	-1.11	1
Phenanthrene	4963	14.85	95.01	284.34	-1.80	1
Anthracene	4792	12.98	91.74	248.44	-3.10	1
Fluoranthene	4416	11.90	84.54	227.84	-2.92	1
Pyrene	4761	12.75	91.14	244.06	-3.23	1
Benz[<i>a</i>]anthracene	4247	9.68	81.30	185.40	-4.57	1
Chrysene	6210	14.91	118.90	285.37	-5.93	2
Triphenylene	6038	14.88	115.60	284.93	-5.38	2
Benzo[<i>k</i>]fluoranthene ^b	6792	15.89	130.03	304.23	-6.90	3
Benzo[<i>e</i>]pyrene	6220	14.74	119.08	282.23	-6.13	3
Benzo[<i>a</i>]pyrene	6181	14.61	118.33	279.64	-6.13	3
Perylene	7200	15.93	137.84	223.99	-8.21	4
Dibenz[<i>a,c</i>]anthracene	7266	16.13	139.10	308.86	-8.25	2
Dibenz[<i>a,h</i>]anthracene	7354	15.96	140.80	305.63	-8.72	2
Benzo[<i>ghi</i>]perylene	6674	9.52	127.77	182.24	-12.88	3
Coronene	7100	9.11	135.93	174.41	-14.72	3

^a1 - Sonnefeld et al. (1983), 2 - de Kruif (1980), 3 - Murray et al. (1974), 4 - Gigli et al. (1973)

^bPreiiminary values.

be corrected to ambient temperatures, T_a , as [121]

$$\Delta H_{sub}(T_a) = \Delta H_{sub}(T_{exp}) + \int_{T_a}^{T_{exp}} C_{sat,S} dT - \int_{T_a}^{T_{exp}} C_{sat,G} dT \quad (D.16)$$

where $C_{sat,S}$ and $C_{sat,G}$ are the energies required to effect a temperature change while maintaining the solid and gas phases, respectively, in a saturated state. For the low reduced temperatures of interest here, $C_{sat} \approx C_p$ [128]. Therefore Joback's third order polynomial for $C_{p,G}$ presented in Table D.7 was used to evaluate Equation D.16. Similarly, ΔS_{sub} can be corrected to T_a as

$$\Delta S_{sub}(T_a) = \Delta S_{sub}(T_{exp}) + \int_{T_a}^{T_{exp}} \frac{C_{sat,S}}{T} dT - \int_{T_a}^{T_{exp}} \frac{C_{sat,G}}{T} dT \quad (D.17)$$

Table D.11 lists ΔH_{sub} (298 K) and ΔS_{sub} (298 K) calculated using Equations D.16 and D.17. The corrections from T_{exp} are negligible for measurements made near ambient temperatures, but are significant for higher molecular weight PAH for which sublimation pressure measurements were made at elevated temperatures. The constants A and B presented in this table were calculated from ΔH_{sub} (298 K) and ΔS_{sub} using equations D.14 and D.15. Values of p_S (298 K) are nearly identical to the values presented in Table D.10 for all PAH with the exceptions of perylene and coronene, for which the corrected p_S are 58 and 96% lower, respectively.

Table D.11: Sublimation Pressure Correlations for PAH Corrected to 298 K
 $(\log[p_S(\text{Pa})] = -A/T + B)$.

PAH	<i>A</i> (K)	<i>B</i>	ΔH_{sub} (kJ/gmol)	ΔS_{sub} (J/gmol K)	$\log p_S$ (Pa) (298 K)
Naphthalene	3966	14.32	75.94	274.16	1.01
Acenaphthylene	3829	12.79	73.30	244.89	-0.06
Acenaphthene	4541	14.69	86.93	281.17	-0.55
Fluorene	4622	14.40	88.48	275.77	-1.11
Phenanthrene	4971	14.88	95.16	284.84	-1.80
Anthracene	4797	12.99	91.84	248.77	-3.10
Fluoranthene	4421	11.92	84.63	228.16	-2.92
Pyrene	4765	12.76	91.23	244.36	-3.23
Benz[<i>a</i>]anthracene	4251	9.70	81.38	185.66	-4.57
Chrysene	6359	15.33	121.73	293.40	-6.01
Triphenylene	6182	15.30	118.35	292.90	-5.44
Benzo[<i>e</i>]pyrene	6323	15.04	121.05	287.96	-6.18
Benzo[<i>a</i>]pyrene	6288	14.92	120.38	285.56	-6.18
Perylene	7445	16.58	142.54	235.96	-8.41
Dibenz[<i>a,c</i>]anthracene	7354	16.37	140.80	313.48	-8.31
Dibenz[<i>a,h</i>]anthracene	7453	16.23	142.69	310.69	-8.78
Benzo[<i>ghi</i>]perylene	6803	9.88	130.25	189.08	-12.95
Coronene	7442	9.97	142.48	190.80	-15.01

D.9 Vapor Pressure Above Liquid

Vapor pressures of PAH, which are all solid at room temperature, must be estimated for the sub-cooled liquid state from sublimation pressure and heat capacity data.

Pure component fugacity, f , is defined as

$$G = RT \ln f + \lambda(T) \quad (\text{D.18})$$

where G is the pure component Gibbs free energy [152]. If the gas is assumed to behave ideally, then the fugacity is equal to the partial pressure, p , and the pure component pressures over the liquid and solid at equal temperatures can be related as

$$\ln \frac{p_L}{p_S} = \frac{G_L - G_S}{RT} \quad (\text{D.19})$$

where p_L and p_S are the pure component vapor and sublimation pressures, respectively; G_L and G_S are the pure component Gibbs free energies of the liquid and solid states, respectively.

Consider the change in G for this process:

- heating the solid along the vapor—solid equilibrium line from ambient conditions, T_a , to the triple point, T_{TP} ,
- melting of the solid at T_{TP} , and
- cooling the liquid along the vapor—liquid equilibrium line from T_{TP} to T_a .

In this case

$$G_L - G_S = \int_{T_a}^{T_{TP}} \left[\left(\frac{\partial G}{\partial T} \right)_{[V-S]} - \left(\frac{\partial G}{\partial T} \right)_{[V-L]} \right] dT \quad (\text{D.20})$$

where the subscripts $[V - S]$ and $[V - L]$ designate vapor—solid and vapor—liquid equilibrium conditions. The standard state is taken to be the solid at T_{TP} . This can be shown to equal

$$G_L - G_S = \int_{T_a}^{T_{TP}} \left[\Delta S_{fus,TP} + \int_{T_{TP}}^T \frac{C_{sat,L} - C_{sat,S}}{T'} dT' + V_S \left(\frac{\partial P}{\partial T} \right)_{[V-S]} - V_L \left(\frac{\partial P}{\partial T} \right)_{[V-L]} \right] dT \quad (\text{D.21})$$

where $\Delta S_{fus,TP}$ is the entropy change of melting at the triple point. The last two terms in the integral are approximately equal to $\frac{V_S}{V_G} \Delta S_{fus,TP}$. Since $V_G \gg V_S$, these terms can be neglected. Because data at T_{TP} are not available and $T_{TP} \approx T_m$, T_m will be used in place of T_{TP} and ΔS_{fus} at T_m will be used in place of $\Delta S_{fus,TP}$ in Equation D.21. The subcooled liquid heat capacity can be assumed to follow the same temperature dependence as the liquid heat capacity, the heat capacity difference, $C_{sat,L} - C_{sat,S}$, can then be expressed in linear form as

$$C_{sat,L} - C_{sat,S} = \alpha_L - \alpha_S + (\beta_L - \beta_S)T \quad (\text{D.22})$$

Equation D.21 can now be integrated to yield an expression for p_L

$$\ln \frac{p_L}{p_S} = \frac{1}{RT_a} \left[\Delta S_{fus}(T_m - T_a) \right]$$

$$+(\alpha_L - \alpha_S) \left(T_a \ln \frac{T_m}{T_a} - T_m - T_a \right) - \frac{\beta_L - \beta_S}{2} (T_m - T_a)^2 \quad (D.23)$$

Values of p_L for -5, 5, 15, 25 and 35°C are given in Table D.12 for PAH for which both melting behavior and sublimation pressure data are available. The sublimation pressures are estimated from the ambient temperature constants in Table D.11.

Phenanthrene exhibits a phase transition at 347 K, therefore Equation D.23 cannot be applied. The vapor pressure for phenanthrene was estimated using

$$\ln \frac{p_L}{p_S} = \frac{1}{RT_a} \left[\Delta S_{fus}(T_m - T_a) + \alpha_L \left(T_a \ln \frac{T_m}{T_a} - T_m - T_a \right) - \frac{\beta_L}{2} (T_m - T_a)^2 + \int_{T_a}^{T_m} S_S(T_m) - S_S(T) dT \right] \quad (D.24)$$

The integral of S_S was evaluated numerically from the experimental data.

PAH vapor pressure data have been reported in the literature using a simplified form of Equation D.23 [174]

$$\ln \frac{p_L}{p_S} = \frac{\Delta S_{fus}(T_m - T_a)}{RT_a} \quad (D.25)$$

Some authors use actual data for ΔS_{fus} , others use a generic value of 56.52 J/gmol K. Figure D-4 shows the effect of these simplifications. For lower molecular weight PAH either simplified method yields accurate values for p_L . For PAH with $M \geq 252$, the simplified methods yield p_L estimates an order of magnitude greater than those

Table D.12: Subcooled Liquid Vapor Pressures for PAH.

PAH	$\log p_L$ (Pa)				
	-5°C	5°C	15°C	25°C	35°C
Naphthalene	0.366	0.780	1.163	1.518	1.848
Acenaphthene	-1.204	-0.724	-0.281	0.129	0.511
Fluorene	-1.762	-1.253	-0.783	-0.347	0.057
Phenanthrene	-2.820	-2.252	-1.726	-1.239	-0.785
Anthracene	-2.657	-2.162	-1.706	-1.285	-0.894
Fluoranthene	-3.626	-3.131	-2.674	-2.251	-1.859
Pyrene	-3.906	-3.358	-2.851	-2.382	-1.947
Benz[<i>a</i>]anthracene	-5.026	-4.522	-4.060	-3.636	-3.245
Chrysene	-6.430	-5.668	-4.966	-4.318	-3.717
Triphenylene	-6.216	-5.478	-4.797	-4.166	-3.581
Benzo[<i>e</i>]pyrene	-7.718	-6.897	-6.140	-5.441	-4.793
Benzo[<i>a</i>]pyrene	-7.773	-6.951	-6.194	-5.494	-4.845
Perylene	-8.851	-7.961	-7.139	-6.378	-5.672
Dibenz[<i>a,h</i>]anthracene	-9.705	-8.762	-7.894	-7.091	-6.349
Benzo[<i>ghi</i>]perylene	-14.465	-13.564	-12.734	-11.966	-11.254
Coronene	-12.860	-12.103	-11.408	-10.767	-10.175

estimated from Equation D.23. This is because higher molecular weight PAH have large values of $T_m - T_a$ and their p_S were generally measured at higher temperatures. In the case of coronene, the use of a high value for ΔS_{fus} fortuitously results in an estimate p_L near that estimated from Equation D.23.

The enthalpy of vaporization, ΔH_{vap} , for subcooled liquid PAH can be calculated by summing the enthalpy changes for this process:

- heating the liquid along the vapor—liquid equilibrium line from ambient conditions, T_a , to the triple point, T_{TP} ,
- solidifying the liquid at T_{TP} ,
- cooling the solid along the vapor—solid equilibrium line from T_{TP} to T_a , and
- subliming the solid.

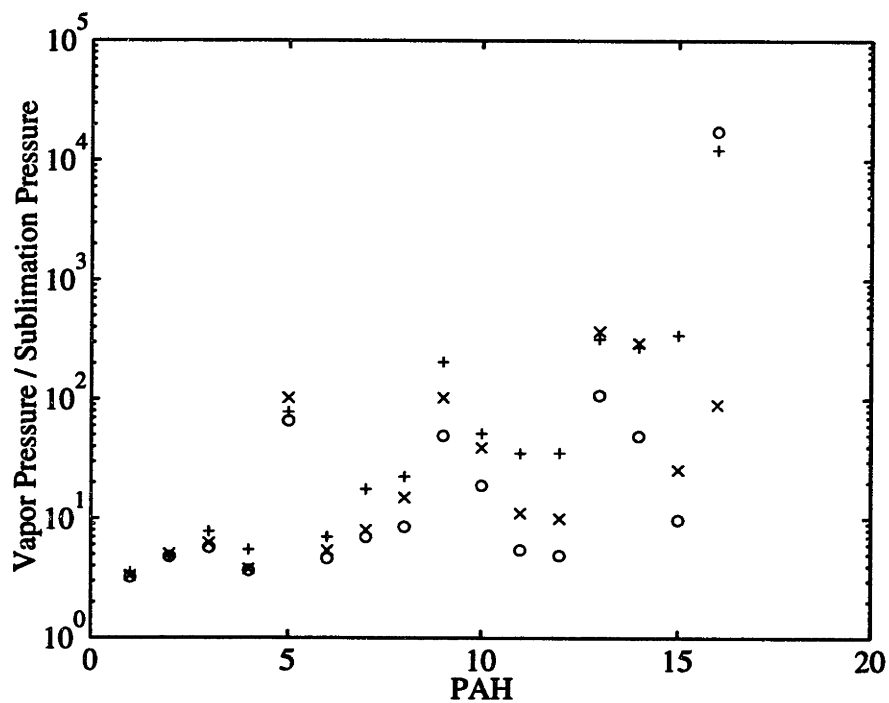


Figure D-4: Comparison of vapor pressure estimation techniques. Vapor pressures estimated by Equation D.23 (o), Equation D.25 using ΔS_{fus} data (x), and Equation D.25 using $\Delta S_{fus} = 56.52$ (J/gmol K) (+). PAH numbered sequentially in the order in which they appear in Table D.12.

ΔH_{vap} is then

$$\Delta H_{vap} = \int_{T_a}^{T_{TP}} C_{sat,L} - C_{sat,S} + V_L \left(\frac{\partial P}{\partial T} \right)_{[V-L]} - V_S \left(\frac{\partial P}{\partial T} \right)_{[V-S]} dT - \Delta H_{fus,TP} + \Delta H_{sub} \quad (D.26)$$

As above, the last two terms in the integral are approximately $-\frac{V_S}{V_G} \Delta S_{fus,TP}$. Since

$$\Delta H_{fus} \gg \int_{T_a}^{T_{TP}} \frac{V_S \Delta H_{fus}}{V_G T_{TP}} dT \quad (D.27)$$

these terms can be neglected. Application of $T_{TP} \approx T_m$ and the linear expressions for heat capacity, to Equation D.26 yields

$$\Delta H_{vap} = (\alpha_L - \alpha_S)(T_m - T_a) + \frac{(\beta_L - \beta_S)(T_m^2 - T_a^2)}{2} - \Delta H_{fus} + \Delta H_{sub} \quad (D.28)$$

Calculated values of ΔH_{vap} at 298 K are presented in Table D.13. As for the p_L calculations, the integral of the solid heat capacity was done numerically for phenanthrene.

D.10 Activity Coefficients

The solubility of many PAH in water, $C_{w,sat}$, and the equilibrium partitioning between *n*-octanol and water, K_{ow} , have been measured at 25°C [175, 20]. In this section activity coefficients, γ , are calculated from the measured concentrations of PAH in

these saturated solutions. The saturation concentration in water, rather than the Henry's Law constants, are used here because, for high molecular weight PAH, the latter require difficult measurements of very low gas phase concentrations.

For measurements made at 25°C, a temperature at which all pure PAH are solids, γ is

$$\gamma = \frac{p_S}{x p_L} \quad (\text{D.29})$$

where x is the mole fraction of PAH in a saturated solution. Generally, x is

$$x = \frac{\frac{C}{M}}{\frac{C}{M} + \frac{\rho_o}{M_o} \left(1 - \frac{C}{\rho}\right)} \quad (\text{D.30})$$

where C is the absorbate concentration, M_o is the molecular weight of the absorbent, and ρ and ρ_o are the densities of the absorbate and absorbent, respectively. If $x \ll 1$ this expression simplifies to

$$x = \frac{C M_o}{M \rho_o} \quad (\text{D.31})$$

PAH are barely soluble in water, with $x < 10^{-5}$. PAH are more soluble in *n*-octanol with x , in the approximate range 10^{-1} – 10^{-5} . Therefore the simplified expression for x can be used for aqueous solutions but not *n*-octanol solutions.

Activity coefficients in water were calculated using $C_{w,sat}$ at 25°C for C . $C_{w,sat}$ data were taken from Mackay and Shiu [175]. The activity coefficients in *n*-octanol were calculated using $K_{ow}C_{w,sat}$ at 25°C for C . K_{ow} values recommended by Mackay et al. were used for all PAH except coronene [20]. For coronene, $\log K_{ow} = 5.40$ was used; this is the only experimental value available [20]. Table D.13 presents the

Table D.13: Enthalpy of Vaporization and Activity Coefficients for PAH at 298 K.

PAH	ΔH_{vap} (298 K) (kJ/gmol)	γ water	γ <i>n</i> -octanol
Naphthalene	58.13	6.97×10^4	3.45
Acenaphthene	67.20	4.55×10^5	6.26
Fluorene	71.26	8.13×10^5	6.14
Phenanthrene	79.91	2.10×10^6	6.41
Anthracene	68.92	2.06×10^6	6.79
Fluoranthene	69.26	9.34×10^6	6.37
Pyrene	76.82	1.19×10^7	8.93
Benz[<i>a</i>]anthracene	69.22	1.06×10^8	14.90
Chrysene	106.01	1.28×10^8	20.20
Triphenylene	103.23	1.55×10^7	5.72
Benzo[<i>e</i>]pyrene	114.36	6.43×10^8	—
Benzo[<i>a</i>]pyrene	114.46	7.52×10^8	78.40
Perylene	124.50	3.25×10^8	20.90
Dibenz[<i>a,h</i>]anthracene	131.16	5.24×10^8	10.60
Benzo[<i>ghi</i>]perylene	125.60	6.06×10^9	219.00
Coronene	104.68	6.84×10^6	3.12

results of these calculations.

Appendix E

Atmospheric Partitioning Model

Code

The following code, *aer-part2.m*, calculates the evolution of PAH in an urban aerosol.

The function *transtau.m* is called to calculate characteristic times for gas—particle equilibration. This code runs under Matlab 4.2, software for DEC OSF/1 by The MathWorks (Natick, MA).

```

% aer_part2.m
% Matlab script for aerosol partitioning model.
% Lagrangian model of distribution of semi-volatile pollutants
% in urban atmosphere.
% Assumes - gas-particle mass xfer rapid
%           - inter particle mass xfer rapid
%           - uniform source emissions
%           - initial conc = 0
%           - equilb size dist like Phe in Kenmore
%           - source size dist like Cor in Kenmore
%
% JOA 9 Dec 96
%
% Added Kelvin effect and non-continuum mass transfer corrections.
% Added gas phase only emissions.
% Converted units to SI (except used g, not kg).
% JOA 5 Jan 97

clear;
more off;

% divide aerosol into size bins corresponding to MOI size cuts (um)
impactor = [19.2 6.00 3.38 1.90 1.07 0.626 0.343 0.141 0.087 0.010];
num_bins = length(impactor)-1;

for bin = 1:num_bins
    % Dp = vol avg particle size for bin (m)
    Dp(bin) = ((impactor(bin)^3 + impactor(bin+1)^3)/2)^(1/3) * 1e-6;
end

% sample results every min
num_samples = 100;
tot_time = num_samples * 60;

% Concentrations
% Co - conc organics in each bin (g/m3)
Co = zeros(num_samples+1, num_bins);
% Cp - conc particulate PAH in each bin (g/m3)
Cp = zeros(num_samples+1, num_bins);
% Cg - gas phase conc PAH (g/m3)
Cg = zeros(num_samples+1, 1);
% Ct - total conc PAH (g/m3)
Ct = zeros(num_samples+1, 1);

time = zeros(num_samples+1, 1);

% ***** Organic aerosol evolution *****

% Volume in bin / volume in PM10 for Whitby's typical aerosols
frac_rural = [0.4810 0.2917 0.1709 0.0676 0.0345 0.0623 0.0793 0.0167 0.0073];
frac_urban = [0.2043 0.1330 0.0896 0.0653 0.0863 0.1778 0.2341 0.0600 0.0378];

% total aerosol mass in each bin (g/m3)
mass_rural = 23e-6 * frac_rural;

```

```

mass_urban = 33e-6 * frac_urban;

% fraction ultrafine particle mass which is organic
% estimated from DPM extractable mass
%org_frac = 0.175;
% estimated from Hildemann's OC for gasoline engines
%org_frac = 0.5;
org_frac = 0.333;

% use size distributions of PAH presumed to be equilibrated
% for initial and final organic aerosol distributions
Ceq_qua = [7.13 0.69 0.78 1.49 1.34 1.42 1.53 0.83 0.91]; % BeP
Ceq_ken = [647.57 515.60 500.12 370.85 285.51 243.69 170.74 131.71 13.22]; % Phe
Ceq_ken = [41.51 43.87 48.27 38.85 30.92 25.63 20.23 15.41 1.51]; % Ant
% subtract blank value
Ceq_ken(1:8) = Ceq_ken(1:8) - 1.7;

% use bin 8 since with bin 9 final organic mass > urban aerosol mass

% Initial condition - use rural aerosol, Quabbin data
Co(1,8) = mass_rural(8) * org_frac;
Co(1,:) = Co(1,8) * Ceq_qua / Ceq_qua(8);

% check that organic mass < total mass
if max (Co(1,:) ./ mass_rural) > 1
    sprintf('Organic mass > rural aerosol mass');
    return;
end

% Final condition - use urban aerosol, Kenmore data
Co(num_samples+1,8) = mass_urban(8) * org_frac;
Co(num_samples+1,:) = Co(num_samples+1,8) * Ceq_ken / Ceq_ken(8);

% check that organic mass < total mass
if max (Co(num_samples+1,:) ./ mass_urban) > 1
    sprintf('Organic mass > urban aerosol mass');
    return;
end

% ***** PAH and Organic Physical Properties *****

% use values for chrysene as average PAH values
% Lennard-Jones parameters
sigma = 7.47; % angstrom
ek = 757; % K
M = 228; % g/gmol

% ambient conditions
T = 298; % K
P = 10100; % Pa

% density of organics in aerosol
rho_o = 0.8e6; % g/m3

```

```

% assuming coated particles, volume fraction organics
%phi = [0.25 0.25 0.25 0.25 0.25 0.25 0.25 0.25 0.25];
phi = [1.0 1.0 1.0 1.0 1.0 1.0 1.0 1.0 1.0];

for gas_emissions = 0:0
    % gas_emissions = 0 for no gas phase emissions
    % gas_emissions = 1 for gas and particulate phase emissions
    % gas_emissions = 2 for only gas phase emissions

for logK = 9:0.2:18
    %for logK = 12:18

    % K is organic-air equilib partition coeff
    K = 10^logK;

    % ***** Mass Transfer Characteristic Times *****

    for bin = 1:num_bins
        tau(bin) = transtau (M, sigma, ek, logK, T, P, Dp(bin));
    end

    % ***** Integration parameters *****

    dt = 0.3 * min(tau); % sec
    if dt > 1
        dt = 1;
    end
    num_tsteps = ceil(tot_time / dt);
    sample = ceil(num_tsteps/num_samples);
    num_tsteps = sample * num_samples;

    % change in organic aerosol per dt
    dCo = (Co(num_samples+1,:) - Co(1,:)) / num_tsteps;

    % ***** PAH initial conc and sources *****

    Cp(1,:) = Ceq_qua;
    Cg(1) = Cp(1,9) * rho_o / Co(1,9) / K;
    Ct(1) = sum(Cp(1,:)) + Cg(1);

    % set initial mass
    init_mass = 0.1e-9; % g/m3
    Cp(1,:) = Cp(1,:) * init_mass / Ct(1);
    Cg(1) = Cg(1) * init_mass / Ct(1);
    Ct(1) = init_mass;

    % PAH source distribution like coronene at Kenmore
    tCp = [1.19 3.02 3.32 5.79 8.61 12.61 14.40 11.80 32.90];

    if gas_emissions == 0
        % no gas phase emissions
        tCg = 0;
    elseif gas_emissions == 1
        % gas phase in equilib with smallest bin

```

```

    tCg = tCp(9) * rho_o / Co(num_samples+1,9) / K;
elseif gas_emissions == 2
    % entirely gas phase emissions
    tCp = zeros(size(tCp));
    tCg = 1.0;
end

% final mass = emission * initial mass
emission = 20;
scale = init_mass * emission / (sum(tCp) + tCg);
tCp = scale * tCp;
tCg = scale * tCg;

% source addition in each dt
if gas_emissions == 0
    % no gas phase emissions
    dCp = (tCp - Cp(1,:)) / num_tsteps;
    dCg = 0;
elseif gas_emissions == 1
    % gas phase in equilib with smallest bin
    dCp = (tCp - Cp(1,:)) / num_tsteps;
    dCg = (tCg - Cg(1)) / num_tsteps;
elseif gas_emissions == 2
    % entirely gas phase emissions
    dCp = zeros(size(tCp));
    dCg = (tCg - Cg(1)) / num_tsteps;
end

dCt = sum(dCp) + dCg;

% tC* are current conc
tCo = Co(1,:);
tCp = Cp(1,:);
tCg = Cg(1);
tCt = Ct(1);

for t = 1:num_tsteps

    % add emissions
    tCo = tCo + dCo;
    tCp = tCp + dCp;
    tCg = tCg + dCg;
    tCt = tCt + dCt;

    % mass xfer to/from gas phase for each bin
    % eCp - Cp in equilib with gas phase
    eCp = tCg * K * tCo / rho_o;
    tCp = tCp + (eCp - tCp) * dt ./ tau;

    % gas phase conc from mass balance
    tCg = tCt - sum(tCp);

    if rem(t,sample) == 0
        % save data

```

```

    t_save = t/sample+1
    Co(t_save,:) = tCo;
    Cp(t_save,:) = tCp;
    Cg(t_save) = tCg;
    Ct(t_save) = tCt;
    time(t_save) = t*dt;
end
end

% ***** Save data to file *****

words = sprintf('save aer_part2_%i_%i impactor Dp tau time Cp ...
    Cg Ct Co dCp dCg dCo', gas_emissions, round(10*logK));
eval(words);
end
end

return;

```



```

function tau_t = transtau (M, sigma, ek, logK, T, P, Dp)
% Matlab function to calculate characteristic time for mass transfer
% in transition regime for PAH in air.
%
% tau - characterisitc time (s)
% M - PAH mol wt (g/gmol)
% sigma - Lennard-Jones length for PAH (angstrom)
% ek - Lennard-Jones energy parameter (epsilon/k) (K)
% K - equilibrium partition coefficient
% T - temperature (K)
% P - pressure (Pa)
% Dp - particle diameter (m)
%
% JOA 3 Jan 97

% plank's constant (J/K)
k = 1.38066e-23;

% ideal gas const (Pa m3 / mol K)
R = 8.31451;

% collision efficiency
alpha = 1.0;

psi = kelvin(M, T, Dp);

% free molecular regime characteristic time
tau_k = Dp * 10^logK / (6 * alpha * psi) * sqrt(2 * pi * M * 1e-3 / R / T);

% properties of gas (air)
Mj = 28.966; % g/gmol
sigma_j = 3.617; % angstrom
ek_j = 97.0; % K

% ratio of molecular weights
z = M / Mj;

% Lennard-Jones parameters
sigma_ij = (sigma + sigma_j) / 2;
ek_ij = sqrt(ek * ek_j);

% lambda is mean free path (m)
lambda = k * T / (pi * P * (sigma_ij * 1e-10)^2 * sqrt(1 + z));

Kn = 2 * lambda / Dp;

beta = alpha / (2 - alpha);

Tr = T ./ ek_ij;

% collision integral, omega(1,1), from Hirschfelder et al 1964
% row 1 - reduced T, row 2 - omegall
omegall = [0.30 0.35 0.40 0.45 0.50 0.55 0.60 0.65 ...
           0.70 0.75 0.80 0.85 0.90 0.95 1.00 1.05 ...

```

```

1.10  1.15  1.20  1.25  1.30  1.35  1.40  1.45  ...
1.50  1.55  1.60  1.65  1.70  1.75  1.80  1.85  ...
1.90  1.95  2.00  2.10  2.20  2.30  2.40  2.50  ...
2.60  2.70  2.80  2.90  3.00; ...
      2.662  2.476  2.318  2.184  2.066  1.966  1.877  1.798 ...
1.729  1.667  1.612  1.562  1.517  1.476  1.439  1.406 ...
1.375  1.346  1.320  1.296  1.273  1.253  1.233  1.215 ...
1.198  1.182  1.167  1.153  1.140  1.128  1.116  1.105 ...
1.094  1.084  1.075  1.057  1.041  1.026  1.012  0.9996 ...
0.9878 0.9770 0.9672 0.9576 0.9490];

omega_ij = interp1(omega11(1,:), omega11(2,:), Tr)';

a = (1 + z).^2 ./ (3 + 5 * z);
b = (1 + 2 * z) ./ (3 + 5 * z);

Jt_Jk = Kn * (1 + Kn * 3 * beta * a / 4) ...
        ./ (8 * omega_ij ./ (3 * pi * (1 + z)) ...
        + Kn * (beta * b / pi + 1 / (2 * beta)) ...
        + 9 * Kn^2 * a / 8);

tau_t = tau_k / Jt_Jk;

return;

```

THESIS PROCESSING SLIP

FIXED FIELD: ill. _____ name _____

index _____ biblio _____

► COPIES: Archives Aero Dewey Eng Hum
Lindgren Music Rotch Science

TITLE VARIES: ► _____

NAME VARIES: ► Ostrom

IMPRINT: (COPYRIGHT) _____

► COLLATION: 346 p

► ADD. DEGREE: _____ ► DEPT.: _____

SUPERVISORS: _____

NOTES:

cat'r:

date:

► DEPT: Chem. Eng. page: F50

► YEAR: 1997 ► DEGREE: Ph.D.

► NAME: ALLEN, Jonathan O.